PARITY VIOLATION IN THE HADRONIC WEAK INTERACTION

by

Septimiu Balascuta

A Dissertation Presented in Partial Fulfillment
of the Requirements for the Degree
Doctor of Philosophy

Approved April 2012 by the
Graduate Supervisory Committee:

Ricardo Alarcon, Chair
Andrei Belitsky
Bruce Doak
Joseph Comfort
Kevin Schmidt

ARIZONA STATE UNIVERSITY

May 2012

ABSTRACT

This thesis deals with the first measurements done with a cold neutron beam at the Spallation Neutron Source at Oak Ridge National Laboratory. The experimental technique consisted of capturing polarized cold neutrons by nuclei to measure parity-violating observables from the emission of gamma rays following neutron capture. The measurements presented here for the nuclei Chlorine (^{35}Cl) and Aluminum (^{27}Al) are part of a program with the ultimate goal of measuring the asymmetry in the angular distribution of gamma rays emitted from the radiative capture of neutrons on protons ($\vec{n}+p \rightarrow d+\gamma$) with a precision better than $1 \cdot 10^{-8}$, in order to extract the weak hadronic coupling constant due to pion exchange interaction with isospin change equal with one ($h_\pi^{\ 1}$). Based on theoretical calculations the asymmetry in the $\vec{n} + p \rightarrow d + \gamma$ reaction has an estimated size of $5 \cdot 10^{-8}$. This implies that the Al parity violation asymmetry and its uncertainty have to be known with a precision smaller than $4 \cdot 10^{-8}$. The proton target is liquid Hydrogen (H_2) contained in an Aluminum vessel. Results are presented for parity violation and parity-conserving asymmetries in ^{35}Cl and ^{27}Al. The systematic and statistical uncertainties in the calculation of the parity-violating and parity-conserving asymmetries are discussed.

DEDICATION

For my parents

ACKNOWLEDGEMENTS

TABLE OF CONTENTS

LIST OF TABLES

Table   Page

LIST OF FIGURES

Chapter 1

INTRODUCTION

A system can have positive or negative parity depending on its behavior under a spatial inversion. Parity is a conserved symmetry if the Hamiltonian of the system is invariant under spatial inversion. The conservation of parity was believed to be a universal law of nature until the discovery of parity violation in the decay of K mesons [1] and in the nuclear beta decay of polarized ^{60}Co [2]. This strong experimental evidence proved that the weak interaction violates parity as it has been predicted earlier by Yang and Lee [3] who were awarded the Noble Prize in Physics in 1957 for their penetrating investigation of the parity laws which has led to important discoveries regarding the elementary particles [4]. The other three fundamental interactions of nature, the strong, electromagnetic, and gravitational forces are all believed to conserve parity. However, the strong interaction at its fundamental level is an interaction between quarks which are the fundamental constituents of visible matter. Quarks are subject to both the weak and strong interactions. At present the study of hadronic parity violation provides the only known window on weak interactions between the up and down quarks.

The range of the weak interaction between quarks is significantly smaller than the size of the nucleon, and the strong repulsion between nucleons at short distances implies that the dynamical mechanism for the weak NN interaction must involve meson exchanges, because the hadronic interaction is mediated by these. The weak force between quarks is 10^{-7} times smaller than the strong force and is responsible for parity-violating effects in the nucleon-nucleon system. This hadronic weak interaction is sensitive to the

quark-quark correlations in hadrons because the range of the W and Z bosons exchanged between quarks is small compared with the nuclear size [5–9].

The weak nucleon-nucleon interaction is needed to understand a variety of phenomena that involve parity violation in atomic, nuclear, and hadronic systems. In atomic physics, parity violation is used to quantify the effect of nuclear anapole moments, a parity-odd and time-reversal-even electromagnetic moment, on nuclear structure. Very precise measurements exist of parity violation in P-shell and light $S - D$ -shell nuclei with parity doublets, but shell model calculations converge slowly for parity- odd operators. In heavy nuclei, parity violation involves convoluted theoretical analysis that can give predictions for weak couplings. Last, but not least, parity violation in electron scattering is widely used to isolate the role of strange quarks in nucleon structure where the presence of weak quark-quark and anapole moments effects must be taken into account.

The structure of the weak quark-quark interaction is well established in the Standard Model of particle physics. However, for low energies, the parity violation in the strangeness changing quark-quark interaction is not understood due to the non-perturbative approach required for these calculations. There are two independent models that describe the quark-quark weak interaction at energies above and below the strong Quantum Chromodynamics (QCD) scale $\Lambda = 1$ GeV. At energies above Λ and below the electroweak scale, the quark-quark weak interaction is written in a current-current form that transforms under isospin as $\Delta I = 0, 1, 2$. For energies below Λ, pion exchange dominates the low energy strong interaction between hadrons due to the chiral symmetry breaking in QCD. For this low energy regime, five independent weak transition

amplitudes are present in NN elastic scattering [10–12]: the $\Delta I = 1$ transition amplitudes in $^3S_1 - \,^3P_1$ and $^1S_0 - \,^3P_0$ partial waves; the $\Delta I = 0$ transition amplitudes in $^3S_1 - \,^1P_1$ and $^1S_0 - \,^3P_0$ partial waves; and the $\Delta I = 2$ transition amplitude in the $^1S_0 - \,^3P_0$ partial wave. A quantitative calculation in the Standard Model to interpolate between these upper and lower energy limits is not possible at this time.

A deviation in the weak amplitudes of the non-leptonic weak decay of hyperons or kaons from their expected relative size, was the subject of many previous works [13]. This non-leptonic weak amplitude is isospin dependent and was seen mostly in the interaction between strange quarks. The measurements in the NN and few nucleon systems may confirm that this dependence is a characteristic of all light quarks. The source of the deviations from the expected pattern of isospin dependence of the weak amplitude in the non-leptonic weak decays can be understood by the study of the $\vec{n} + p \rightarrow d + \gamma$ reaction, i.e., the capture of polarized neutrons by protons. In this reaction the change in isospin $\Delta I = 1$ and the interaction between the charged currents is suppressed by $V_{us}^2/V_{ud}^2 \simeq 0.1$. Therefore the $\vec{n} + p \rightarrow d + \gamma$ reaction is sensitive to the neutral currents interaction. At the same time, the main contribution is due to the long range pion exchange because the deuteron is a loosely bound nuclear system. Due to the simplicity of the neutron and proton system, this reaction is free from the uncertainties present in the other nuclear many body systems.

Experimentally, the hadronic weak interaction has been observed in the non-leptonic flavor changing decays of baryons and mesons [14, 15] and in the measurement of observables that conserve flavor but violate the parity

symmetry [16,17]. Measurements have also been performed in few-body systems, such as the pp and $p\alpha$ systems, and in nuclei ranging from the P-shell nuclei like ^{18}F to heavy nuclei such as ^{133}Cs. The longest-range part of the interaction is dominated by the weak pion-nucleon coupling constant, $h_\pi{}^1$. Measurements of the circular polarization of photons in the decay of ^{18}F [18] imply a small value for $h_\pi{}^1$, while precision parity violation measurements in pp and ^{133}Cs seem to imply a large value for $h_\pi{}^1$ [19] relative to theoretical estimates [13]. The origin of these discrepancies may lie in approximations used to compute effects in nuclei, in the use of a model [13] as the basic framework in one or more of the experiments. Ideally one would like to obtain a set of numbers that are free from the uncertainties associated with many-body nuclear physics and that do not require a meson-exchange model for interpretation. Recently, a theoretical framework for such a program has been developed with the ideas of effective field theory (EFT) [20].

Carrying out a program of hadronic parity violation measurements with neutrons will allow one to arrive at a complete determination of the leading-order parity-violating operators in a way that is independent of nuclear model approximations. Central to this is the parity violation that can be related with the asymmetry in the angular distribution of the gamma rays emitted at the capture of polarized neutrons on protons. If the neutron spin is along the vertical direction then the parity violating asymmetry is proportional with the scalar product of the neutron spin and the momentum of the gamma rays $\vec{s} \cdot \vec{k}_\gamma$. Under parity transformation the gamma ray momentum changes sign but the direction of the neutron spin is not changed. The non-zero asymmetry in the angular distribution of the gamma rays is proportional with the parity violation in the weak interaction between the interacting particles. In the

4

$\vec{n} + p \rightarrow d + \gamma$ reaction, this parity-violating asymmetry is dominated by the $\Delta I = 1$ transition amplitude in the $^3S_1 - {}^3P_1$ channel of the strangeness-conserving hadronic weak interaction. The $\vec{n} + p \rightarrow d + \gamma$ parity-violating up-down asymmetry A_γ in the angular distribution of the gamma rays with respect to the neutron spin direction was measured as part of this work, in the first phase of the NPDGamma experiment at the Neutron Scattering Center LANSCE at Los Alamos National Laboratory [21]. The experimental result did not have enough statistical precision to produce a definite result. After the completion of this experiment the entire experimental setup was moved to the new intense pulsed Spallation Neutron Source (SNS) at Oak Ridge National Laboratory.

This thesis describes the installation of the NPDGamma apparatus at the SNS and its modifications, the implementation of a new way to polarize the neutrons with respect to the one used at LANSCE, the SNS commissioning measurements and calibrations at the new cold neutron beam line, and then the parity violation measurements on the nuclei of Al and Cl. In Spring, 2012, the experiment is switching to a liquid H_2 target to measure the parity violation on the $\vec{n} + p \rightarrow d + \gamma$ reaction.

The remainder of this thesis is organized as follows. In chapter 2 the physics of the parity violation in the $\vec{n} + p \rightarrow d + \gamma$ reaction is briefly discussed, followed by that related to the parity violation with polarized neutrons on the nuclei of Al and Cl. Also presented in this chapter is a brief description of the apparatus used at LANSCE and the results obtained in that experiment. The experimental setup, design and construction of the apparatus for neutron polarization, and the corresponding magnetic field measurements done at the

experiment site, are described in chapter 3. The work continues with the presentation of measurements for the neutron flux, neutron polarization and a study of the detector alignment in chapter 4. The nuclei target measurements discussed in chapter 5 were done in May and June 2011 as part of the final commissioning of the $\vec{n} + p \rightarrow d + \gamma$ experiment. The procedures involved in the data analysis and the study of the systematic and statistical errors are presented in chapter 6. A summary and outlook are presented in chapter 7.

Work has also been done to help on the preparations of two future experiments that will use cold and ultracold neutrons at the SNS. Appendices B and C present finite-element calculations done for the design of coils and magnetic shields for two experiments, namely a search for the neutron electric dipole moment (nEDM) and precise measurements of the neutron beta decay parameters (Nab). Both experiments aim to validate new theories that try to extend the Standard Model. The nEDM experiment will establish a new upper limit on the electric dipole moment of the neutron and establish possible new sources of charge conjugation and parity (CP) violation and time reversal symmetry violation. The Nab experiment aims to measure with unprecedented precision the parameters related with the neutron beta decay with a large field expansion superconducting spectrometer and state-of-the-art position sensitive silicon detectors.

Chapter 2

PARITY VIOLATION IN THE HADRONIC INTERACTION

This chapter discusses the theoretical models that explain and predict the asymmetry in the angular distribution of the gamma rays emitted from the capture of polarized neutrons on the proton and heavy nuclei. Section 2.2 outlines the calculations of the weak meson-nucleon couplings of the hadronic weak interaction and their connection with the asymmetry measured in the $\vec{n} + p \rightarrow d + \gamma$ reaction. Statistical models that are discussed in section 2.3 help to explain the amplification of the parity-odd effects in the radiative capture of polarized neutrons in Cl and the cancellation of these effects for neutrons captured in Al. Finally section 2.4 presents a summary of the measured asymmetries in Al, Cl and H_2 targets during the first phase of the experiment at LANSCE.

2.1 Theoretical Models for NN Interaction at Low Energy

The mechanism of the weak NN interaction at low energies is not completely understood due to the non-perturbative calculations required for the rigorous description of QCD problems at low energies. Some aspects of the weak interaction can be understood from experiments at the high-energy regime. To probe the weak hadronic interaction at low-energy, the experiments are usually done on complex nuclei and the weak force depends on the effective two-body operators. The matrix elements of such operators are difficult to evaluate, due to the uncertainties in the nuclear wave functions and the short-range correlations. The weak interactions can be studied when the strong and the electromagnetic interactions are forbidden due to a symmetry principle, such as the S (strangeness) and C (charm) conservation. The analysis of the

7

experimental results usually assume that the effective weak force originates from a process where one nucleon emits a meson (π, ρ, ω, ϕ) through a weak interaction and the meson is then absorbed by a second nucleon via strong interaction [22]. Two models of the parity nonconserving (PNC) interaction have been used. In the first one the matrix elements of the NN interaction are expressed in function of five S-P amplitudes. In the second model the PNC interaction is written as a potential due to the single meson (π, ρ, ω) and two meson exchange $\pi\pi$. There are several advantages of the second model over the first one. The potential description of the low-energy PNC interaction predicts correctly the energy dependence of the S-P amplitudes and the strength of transitions between higher partial waves. In addition the effect of the short range NN correlations on the PNC matrix elements can be estimated in the meson exchange model.

One process that could contribute to the PNC interaction is the direct exchange of $W^{\pm}$ and Z^0 bosons. However due to small Compton wavelengths of the bosons (about 0.002 fm) the direct exchange can occur only when the nucleons overlap. This process can not happen at low energies due to the strong repulsion forces between the two nucleons. The NN interaction takes place at distances larger than the nucleon size, through the long-range meson exchange (Figure 2.1). The long -range processes can be described without explicit reference to the structure of the nucleons.

The relation between the parity non-conserving NN potential and the theory of weak interaction between quarks can be understood from the phenomenological current-current Lagrangian of the hadronic interaction:

$$L = \frac{G_F}{\sqrt{2}}(J_w^{\dagger}J_w + J_z^{\dagger}J_z) + h.c. \tag{2.1}$$
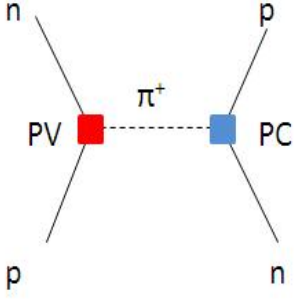
Figure 2.1: The interaction between neutron and proton through pion exchange.

The charged and neutral currents are J_w and J_z respectively. If one neglects the contribution of the heavy quarks c, b, t to the interaction, then only the contribution of the light quarks u, d, s can be considered in the expression of the charged current: $J_w = \cos(\theta_c) \cdot J_w^0 + \sin(\theta_c) \cdot J_w^1$ where θ_c is the Cabibbo angle and $\sin(\theta_c) = 0.22$ [23]. Consider ΔI and ΔS the change in isospin and strangeness of a nucleon due to the NN interaction. The current J_w^0 drives the $u \to d$ transition and transforms as $\Delta I = 1, \Delta S = 0$ while J_w^1 drives the $u \to s$ transition and transforms as $\Delta I = 1/2$ and $\Delta S = -1$. The neutral current J_z has two components J_z^0 and J_z^1 which transforms as $\Delta I = \Delta S = 0$ and $\Delta I = 1, \Delta S = 0$ respectively. The weak $\Delta S = 0$ hadronic interaction is therefore described by the sum of current-current terms:

$$
\begin{aligned}
L &= \frac{G_F}{\sqrt{2}} \cdot (\cos^2 \theta_c J_w^{0\,\dagger} J_w^0 + \sin^2 \theta_c J_w^{1\,\dagger} J_w^1 \\
&+ (J_z^{0\dagger} J_z^0 + J_z^{1\dagger} J_z^1 + J_z^{0\dagger} J_z^1 + J_z^{1\dagger} J_z^0) + h.c.
\end{aligned}
\tag{2.2}
$$

The product of currents $J_w^{0\,\dagger} \cdot J_w^0$ transforms as $\Delta I = 0, 2$, while $J_w^{1\,\dagger} \cdot J_w^1$ transforms as $\Delta I = 1$. Therefore the $\Delta I = 1$ component of the charged current interaction is suppressed by $\tan^2\theta_c$ compared to the $\Delta I = 0, 2$ component, but the contribution of the neutral-currents to the $\Delta I = 1$ is not

suppressed. The neutral current is expected to dominate the $\Delta I = 1$ component of the Parity Violating hadronic interaction. However this qualitative argument is not valid if the strong interaction between quarks can significantly alter the weak matrix elements between hadrons. The relative strength of the three isospin components $\Delta I = 0, 1, 2$ depends on the interplay between the neutral and charged current.

To disentangle the neutral- and charged- current contributions, most of the recent research was focused on determining the isospin dependence of the flavor conserving $\Delta S = 0$ hadronic weak interaction. More recently, the flavor changing decays of the mesons have been described by effective field theories like chiral perturbation theory, heavy quark and soft-collinear effective theory [24–26] . In these theories the non-perturbative QCD interaction coefficients are obtained from experiment, and the observables are calculated in the effective field theory (EFT). A precise computation of the parity-violating observables in the EFT frame needs input from a comprehensive experimental program in the few body systems. The EFT can be used to explain the simultaneous contribution of the parity-violating S-wave and parity -conserving P -wave amplitudes in the hyperonic non-leptonic decay and the anomalously large parity-violating asymmetries in the radioactive decay of hyperons. According to the SU(3) flavor symmetry in the limit of degenerate up u, down d, and strange s quarks, this asymmetry should vanish, because no apparent QCD symmetries can enhance a particular reaction channel. The dominance of the ΔI=1/2 channel over the ΔI=3/2 channel in the strangeness changing non-leptonic decays can be understood from precise measurements of the parity violation at 10^{-7} level or better, in the $\vec{p}p$ scattering, $\vec{n}\alpha$ spin rotation and polarized neutron capture on hydrogen.

2.2 Parity Violation in the $\vec{n} + p \rightarrow d + \gamma$ Reaction

A calculation of the weak meson-nucleon couplings from the Standard Model was first performed by Desplanques, Donoghue, and Holstein by using a valence quark model in 1980 [13] and more recently in reference [27]. In this model the observables are expressed in terms of six weak meson-nucleon coupling constants: h_π^1, h_ρ^0, h_ρ^1, h_ρ^2, h_ω^0, h_ω^1.

Adelberger and Haxton in 1985 [23] proposed an experimental program and performed the calculations specifying the relation between the corresponding observables and the weak coupling constants. In the $\vec{n} + p \rightarrow d + \gamma$ reaction the short range contribution is reduced due to the low energy of the initial two nucleons and the weak binding of the deuteron. Therefore, in this reaction, the long range of the $\Delta I = 1$ part of the hadron weak interaction is the most important component. The transition amplitudes of the electromagnetic part of the Hamiltonian between the initial and the final two nucleon states can be used to calculate the differential cross section. Most of the gamma rays are produced in the parity-conserving magnetic dipole *M1* transition of the strong interaction between the initial singlet and triplet S-wave states $^1S_0$, $^3S_1$ and the deuteron bound state.

The weak interaction induces electric dipole *E1* gamma transitions between states of opposite parity such that the P-wave components $^3P_1$, $^3P_0$, and $^1P_1$ are mixed with the initial and final states. The interference between the *E1* and *M1* transitions gives rise to a parity-odd asymmetry in the gamma ray angular distribution. In the NPDGamma ($\vec{n} + p \rightarrow d + \gamma$) experiment [28] the neutrons are polarized in the vertical direction normal to the beam axis. In the differential cross section (eq. 2.3), the up-down asymmetry A_γ multiplies the

parity-violating scalar product of the neutron spin $\hat{s}_n$ and the direction of the gamma ray $\hat{k}_\gamma$ emitted after neutron capture $\hat{s}_n \cdot \hat{k}_\gamma$. The left-right asymmetry B_γ multiplies the parity-conserving observable $\hat{k}_\gamma \cdot (\hat{s}_n \times \hat{k}_n)$ where $\hat{k}_n$ is the momentum of the neutron. The parity-violating term is therefore maximum for gamma rays emitted along the neutron spin direction parallel with the direction of the magnetic field. There is very little mixing between the two asymmetries if the misalignment angle between the vertical axis of the detector and the direction of gravity is smaller than $1°$ ([29]).

The differential cross section for the capture of polarized neutron by nuclei is proportional with the factor:

$$\frac{d\sigma}{d\Omega} \propto \frac{1}{4\pi} \left(1 + A_\gamma \cos\theta + B_\gamma \sin\theta \right) \qquad (2.3)$$

In the above equation θ is the angle between the neutron spin direction and the gamma ray initial momentum. In the absence of any systematic effects, a non-zero asymmetry A_γ in the angular distribution of the gamma rays with respect to the neutron spin direction comes from the small parity non-conserving admixture of the P-wave states in the initial S -wave singlet and the final S-wave triplet states:

$$\epsilon = \frac{\langle \psi_{k'} | W | \psi_k \rangle}{\Delta E} \ . \qquad (2.4)$$

The allowed quantum numbers for the transition are $k = \{J, L, S, p\}$ $(p = \mathrm{parity})$. The gamma ray asymmetry for this reaction has a simple form in terms of the matrix elements between initial and final states:

$$A_\gamma \propto \mathrm{Re} \, \frac{\epsilon \langle {}^3P_1 | E1 | {}^3S_1 \rangle}{\langle {}^3S_1 | M1 | {}^1S_0 \rangle} \ . \qquad (2.5)$$

The parity-odd amplitudes $\langle \psi_{k'} | W | \psi_k \rangle$ can be treated as perturbations. These amplitudes can be estimated in the meson exchange picture and can be

parametrized by using effective field theory, or calculated in the lattice gage theory. As mentioned earlier in the meson exchange picture the hadronic weak interaction can be expressed completely in terms of six weak meson-nucleon coupling constants $O_{PV} = a_\pi^1 h_\pi^1 + a_\rho^0 h_\rho^0 + a_\rho^1 h_\rho^1 + a_\rho^2 h_\rho^2 + a_\omega^0 h_\omega^0 + a_\omega^1 h_\omega^1$. The coefficient $a^{\Delta I}$, with ΔI being the change in the isospin, are determined from the evaluation of electromagnetic matrix elements for the $\vec{n} + p \rightarrow d + \gamma$ reaction. The only significant contribution to the NPDGamma asymmetry comes from the weak pion exchange. The measured asymmetry and the weak meson couplings are related [9, 23, 27, 30–32] with three coupling constants:

$$A_\gamma = -0.1069 h_\pi^1 - 0.0014 h_\rho^1 + 0.0044 h_\omega^1 . \tag{2.6}$$

The interaction is therefore almost purely $\Delta I = 1$. The effect of the D- wave state admixture in the deuteron ground state on these coefficients is negligible.

The $\Delta I = 1$ part has been calculated before and the predicted best value for h_π^1 is 4.7×10^{-7} [22]. The most sensitive experiments designed to measure the parity violation in the $\Delta I = 1$ channel used the ^{18}F gamma ray circular polarization [18]. The results of these experiment and the arguments of the meson model [33] suggest that $h_\pi^1 \leq 1.2 \times 10^{-7}$. The non-zero measurement of the anapole moment of ^{133}Cs [19] has been used to calculate $h_\pi^1 = (9.6 \pm 2.2 \, (\text{exp.}) \pm 3.6 \, (\text{theor.})) \times 10^{-7}$ [34]. Because the two values do not agree in the limits of experimental errors, the $\Delta I = 1$ part of the hadronic weak interaction remains undetermined.

2.3   Parity Violation in Neutron Radiative Capture in Complex Nuclei

The compound nuclei produced after the neutron capture have a large number ($>10^6$) of possible states with different parities and angular momenta. The

structure of the excited states in the compound nuclei can amplify the parity-odd asymmetry in the angular distribution of prompt gamma rays emitted from the nuclear transition to the ground state. The Fock space components of the compound nuclear states are treated by statistical techniques as independent random variables to calculate the root mean square of the distribution of expected observables. This approach helped in the understanding of certain global features of the nuclei structure [35], of the distribution of the neutron resonance widths [36] and the isospin violation in heavy nuclei [37].

2.3.1 Enhancement of Parity Violation in Compound Nuclei

Flambaum and Gribakin [38] suggested that the parity non-conservation and time invariance can be enhanced 10^6 times in compound nuclei. They described the problem of the correlations in the (n, γ) radiative capture in terms of the mixing in the transient amplitudes. Two effects contribute about equally (10^3) to this factor: (i) the significant difference between the S-wave amplitude and the much smaller P-wave neutron capture amplitude (kinematic enhancement) and (ii) the very large density of compound states which provides mixing of opposite parity states at very small energy separations (dynamical enhancement). Because of the complex structure of the compound state, the dynamical enhancement is proportional with $1/\sqrt{D}$ where D is the mean level spacing. The parity non-conserving effects in nuclear fission and (n, γ) reactions requires a resonance enhancement up to a factor D/Γ where Γ is the compound state width. In the (n,γ) reaction, the parity-odd effect is due to the mixing between the compound states either in the initial or final nuclear states [39]. In heavy nuclei a neutron can capture in the S- or P- wave states close to the neutron separation energy. The weak interaction mixes the

14

two transition amplitudes from these states to lower states.

The relative magnitude of the weak interaction in the nuclear forces is $G \cdot m_\pi{}^2 = 2 \cdot 10^{-7}$. The reaction amplitudes for the capture of the slow neutron in the S- and P- wave states, without the parity violation are presented in Figure 2.2 below.
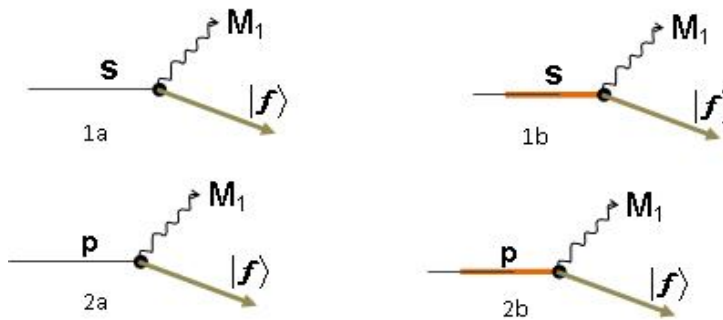
Figure 2.2: The reaction amplitudes for slow neutron capture in S- and P- wave states without parity violation.

The first pair of diagrams (1a, 2a) corresponds to the direct radiative neutron capture in S- or P -wave states followed by the transition into the final state $|f\rangle$. The average distance between the compound levels in the region of neutron threshold and of the final state respectively are $D_i = D(E \approx E_i)$ and $D_f = D(E \approx E_f)$. The number of the principal components in the wave function of the final, initial and capture states are N_f, N_i and N_c respectively. The numbers of principal components in the wave functions of the initial and final states are inversely proportional with the mean level of spacing: $N_f \approx$ 1MeV $/D(E_f)$ and $N_i \approx$ 1MeV $/D(E_i)$, respectively. The diagrams (1a, 2a) have one vertex of electromagnetic interaction proportional with $1/\sqrt{N_f}$. The second pair of diagrams (1b and 2b) represents the resonance neutron capture. These diagrams correspond to neutron capture in the intermediate

compound state (c=S or P) and contain the neutron capture vertex ($1/\sqrt{N_c}$), the Green function of the compound state $N_c D/(E - E_c + i \cdot \Gamma_c/2)$ and the photon emission vertex $1/\sqrt{N_c}$. The mean-square estimate of the amplitudes was calculated in [38] and the ratio between the resonance and the direct capture amplitudes indicates that the resonance mechanism in the (n, γ) reaction dominates the transitions into the complex final state ($N_c \gg 1$). Consider E the neutron energy; E_c and Γ_c, the energy and width of the nearest resonance and D(E_c) the average distance between the compound levels with fixed quantum numbers at energy close to E_c. The ratio of the resonance capture amplitude f_a and the direct capture amplitude f_b ([38]) is equal with:

$$\frac{f_a}{f_b} = \sqrt{N_f} \frac{D(E_c)}{E - E_c + \frac{i\Gamma_c}{2}} \tag{2.7}$$

The direction and the resonant state amplitudes are comparable only if the transition is in the final state. To calculate the amplitude of the transition to the ground state, both the direct and resonance transitions are taken into account. The amplitudes for the capture in the S and P- wave states are given by the relations:

$$f_1 = -\frac{1}{2k} \left\{ \sum_s \frac{\langle f, \gamma | H_{EM} | s \rangle \langle s | H_s | n \rangle}{E - E_S + \frac{i\Gamma_S}{2}} + \langle f, \gamma | H_{EM} | n \rangle \right\} \tag{2.8}$$

$$f_2 = -\frac{1}{2k} \left\{ \sum_s \frac{\langle f, \gamma | H_{EM} | p \rangle \langle p | H_s | n \rangle}{E - E_P + \frac{i\Gamma_P}{2}} + \langle f, \gamma | H_{EM} | n \rangle \right\}. \tag{2.9}$$

For complex nuclei, the resonance capture state dominates the parity-violating amplitude for transitions to the final state. The diagrams with the weak mixing compound states give the dominant CP violating effects.

Consider R the radius of the nucleus. The mean square estimates of
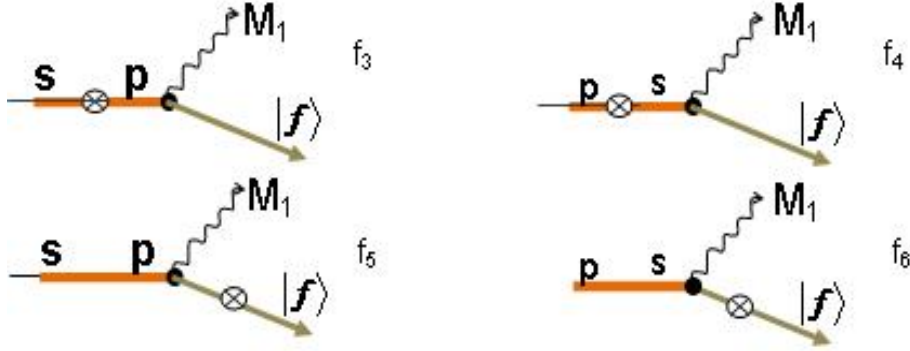
Figure 2.3: The amplitudes for slow neutron capture in the complex states or simple final states.

the amplitudes are given by [11, 17]:

$$f_3 \sim \frac{1}{\sqrt{kR}} \sqrt{N_i} \frac{D_i}{\left(E - E_S + \frac{i\Gamma_S}{2}\right)} \frac{D_i}{\left(E - E_P + \frac{i\Gamma_P}{2}\right)} \qquad (2.10)$$

$$f_4 \sim \sqrt{kR}\sqrt{N_i} \frac{D_i}{\left(E - E_S + \frac{i\Gamma_S}{2}\right)} \frac{D_i}{\left(E - E_P + \frac{i\Gamma_P}{2}\right)} \qquad (2.11)$$

$$f_5 \sim \frac{\sqrt{N_f}}{\sqrt{kR}} \frac{D_i}{\left(E - E_S + \frac{i\Gamma_S}{2}\right)} \cdot \frac{D_f}{\left(E - \omega - E'_f + \frac{i\Gamma'_f}{2}\right)} \qquad (2.12)$$

$$f_6 \sim \sqrt{kR}\sqrt{N_f} \frac{D_i}{E - E_p + \frac{i\Gamma_S}{2}} \cdot \frac{D_f}{E - \omega - E'_f + \frac{i\Gamma'_f}{2}}. \qquad (2.13)$$

The amplitudes f_5 and f_6 can be neglected because they are $\sqrt{N_f}/\sqrt{N_i}$ smaller than f_3 and f_4 respectively. The amplitude f_4 is due to the P-wave capture and is suppressed by the factor $1/(kR) \sim 10^2 - 10^3$ in comparison with f_3.

After a neutron is captured on ^{27}Al, the excited ^{28}Al nucleus makes a transition to the ground state with emission of prompt gamma rays in a cascade. The contribution of the gamma cascade to the parity mixing in the final state can be calculated in terms of the reaction amplitudes of the neutron capture in S-wave or P-wave states.

17

The contribution of the diagrams with P-wave mixing in the final state is $\sqrt{N_i}/\sqrt{N_f}$ times smaller than the contribution of the diagrams with mixing in the initial states. Therefore the mixing in the final state can be neglected for the transitions to the low-lying states with N_f=1.

If the gamma ray transition does not go to the ground state after the neutron capture, then at least one more gamma ray will be emitted. The number of gamma quanta exceeds 2 or 3 times the number of captured neutrons. The secondary gamma quanta influence the magnitude of the correlations in the integral spectrum. In the presence of parity-odd mixing in the initial state, only the first gamma quanta in the cascade contribute to the correlation. In the case of a neutron capture in the S-wave and two gamma ray transition with a weak interaction in the intermediate state, the four possible diagrams are presented in Figure 2.4.
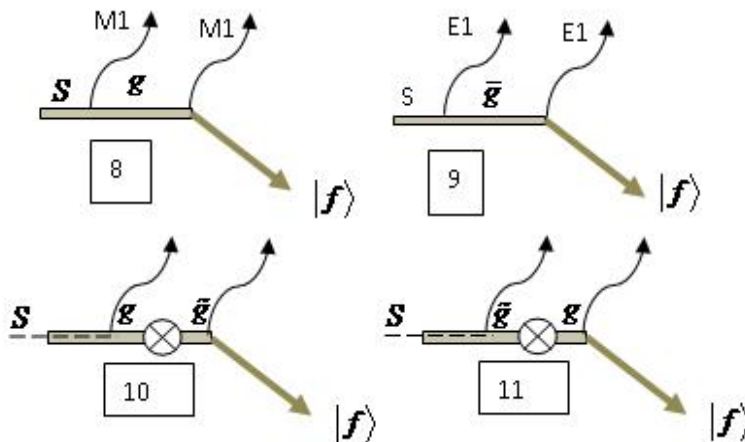
Figure 2.4: The diagrams for two quanta transitions with a mixing in the intermediate states.

In this figure the gamma ray transitions from the capture state $|s\rangle$ to the intermediate states with opposite parities $|g\rangle$ and $|\tilde{g}\rangle$ are magnetic *M1* and electric *E1* dipole transitions respectively. These are the transitions

18

$|g\rangle \rightarrow |f\rangle + |M1\rangle$ and $|\tilde{g}\rangle \rightarrow |f\rangle + |E1\rangle$ with amplitudes f_8 and f_9. The P-odd mixing in the final state corresponds to the parity violation at the emission of the first gamma quantum and comes from the interference between f_8 with f_{11} and f_9 with f_{10}.

The interference of f_8 with f_{11} and of f_9 with f_{10} leads to parity violation related with the first gamma quantum and corresponds to P-wave mixture in the final state. The new effect due to the cascade is the interference of f_8 with f_{10} and f_9 with f_{11}. The amplitude of this interference is reduced by a factor $\sqrt{N_i/N_g}$ compared with the contribution of the amplitudes with mixing in the initial state. The probability of the population in the intermediate states are given by W_g and $W_{\tilde{g}}$:

$$W_g = \left| -\frac{1}{2k} \frac{\langle g|M_1| s\rangle \langle s|H_s| n\rangle}{E - E_s + i\Gamma_s/2} \right|^2 \tag{2.14}$$

$$W_{\tilde{g}} = \left| -\frac{1}{2k} \frac{\langle \tilde{g}|E_1| s\rangle \langle s|H_s| n\rangle}{E - E_s + i\Gamma_s/2} \right|^2 . \tag{2.15}$$

There is a partial compensation between the terms $f_8^* f_{10}$ and $f_9^* f_{11}$. This can be seen by writing the contribution of the weak force to the cross section:

$$\int \frac{d\omega}{2\pi} \frac{2}{(2k)^2} Re\{f_8^* f_{10} + f_9^* f_{11}\} \propto 2W_g \frac{\langle g|H_w|\tilde{g}\rangle}{E_g - E_g} \cdot \frac{\langle f|M_1|\bar{g}\rangle \langle \bar{g}|E_1|f\rangle}{\Gamma_g} +$$
$$2\tilde{W}_g \frac{\langle \tilde{g}|H_w|g\rangle}{E_g - E_{\tilde{g}}} \cdot \frac{\langle f|E_1|g\rangle \langle g|M_1|f\rangle}{\Gamma_{\tilde{g}}} = 2\frac{\langle \tilde{g}|H_w|\tilde{g}\rangle}{E_g - E_g} \langle f |M_1| g\rangle \langle \tilde{g} |E_1| f\rangle \left(\frac{W_g}{\Gamma_g} - \frac{W_{\tilde{g}}}{\Gamma_{\tilde{g}}}\right).$$
$$\tag{2.16}$$

The amplitudes of the electric $E1$ and magnetic dipole $M1$ transitions differ by a phase factor equal with i. The above contribution to the cross section will be zero if:

$$\left| \frac{W_g}{\Gamma_g} \right| = \left| \frac{W_{\tilde{g}}}{\Gamma_{\tilde{g}}} \right| . \tag{2.17}$$

19

The appearance of the widths of the state g and $\tilde{g}$ is the only effect of the secondary gamma quanta. Neither the contribution of the mixing in the final state nor that of the cascade have the resonance enhancement factor $D/(E - E_p)$. For this reason there is an additional suppression of these contributions with about two orders of magnitudes.

2.3.2   Parity Violation in Chlorine and Aluminum

Because of the large number of possible electromagnetic transitions in heavy nuclei, the calculation of the parity-violating asymmetry from matrix elements of the strong and weak Hamiltonian is not possible. However, statistical arguments can be used to calculate the root mean square of the asymmetry close to the neutron separation energy because of the large number of uncorrelated random amplitudes in the calculation of the mean square matrix elements. In reference [40] the authors calculated a root mean square gamma ray asymmetry for ^{27}Al equal with $1.3 \cdot 10^{-7}$. This indicates a small enhancement of the parity-odd effects for Al. This result was explained by the random sign of the asymmetry for the different highly degenerate levels close to the neutron capture level. The incoherent mix of the transition produces a $1/\sqrt{N}$ suppression.

The spin of ^{27}Al is 5/2. Therefore in the capture state the Al nucleus can be in the 2^+ or 3^+ state. The energy levels of ^{28}Al have been determined mainly from the (d, p) reaction. The energy of the nuclear levels were determined from measurements of the gamma rays energies emitted at the transition of excited ^{28}Al nucleus to the ground state [41]. Their measured Q value for this nucleus is 7725.5 keV $\pm$ 1 keV. The density level above 5 MeV is considerable. Excited states with well known spin and parities are very few [42]. The available spin

and parity assignments are based upon beta decay and (d, p) reaction data. Definite assignments exists: 3^+ for the ground state, 2^+ for the state at 31 keV and 1^+ for the state at 1373 keV. The gamma rays originate from both the neutron captured and neutron inelastic scattering in Al and have energies between 7.726 MeV and 0.3998 MeV. The lines at 844, 1014, 2212 and 2731 keV are due to the inelastic neutron scattering in ^{27}Al. The ^{28}Al nucleus, in the ground state, beta decays to ^{28}Si in excited 2^+ state. A 1.78 MeV quanta is emitted in the transition of excited ^{28}Si to its ground state 0^+.

The parity violation in the radiative neutron capture in ^{35}Cl was measured before [43]. The neutron can be captured in a 2^+ state located 130 eV below threshold or in a second state 2^- that lies at 398 eV above threshold.The big parity-violating asymmetry is due to the mixing of these two states. Theoretical calculation of the parity-violating correlation $\vec{s_n} \cdot \vec{k_\gamma}$ in Cl were done in the reference [44]. The predicted asymmetry: $A_\gamma = -(37 \pm 18) \cdot 10^{-6}$ is in agreement with the measured Cl asymmetry [45, 46]. The decay scheme for ^{36}Cl from references [47, 48] is presented in Figure 2.5.
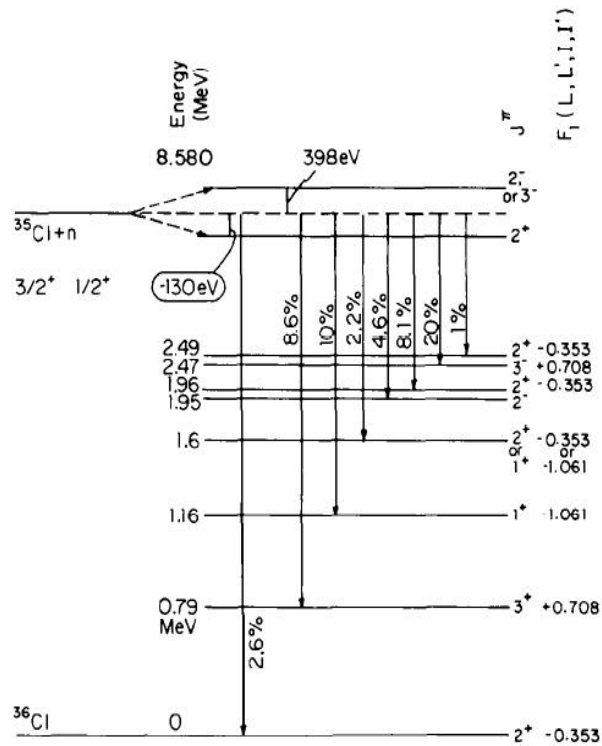
Figure 2.5: The decay of ^{36}Cl

2.4   The NPDGamma Experiment at LANSCE

The first phase of the NPDGamma experiment was completed at the Manuel

Lujan Jr. Neutron Scattering Center (LANSCE) at Los Alamos National

Laboratory in 2006. The experimental setup is discussed in [21] and is

reproduced in Figure 2.6. The linear accelerator delivers 800 MeV proton

beam to a proton storage ring where the beam is compressed to 250

nanoseconds wide pulses at the base and transported to a tungsten target.

The resulting spallation neutrons were cooled by a H_2 moderator. The

backscattered neutrons from the moderator were transported through an

$m = 3$ supermirror guide to the NPDGamma experiment [49]. The supermirror

guide is covered with a multilayer of substrates that have different scattering

length densities [50, 51]. The multilayer is an aritifical one dimensional lattice that allows for Bragg reflection of the neutron wave on the substrates for the appropriate neutron momentum transfer. The neutrons incident on the multilayer coating are totally reflected up to a critical angle θ_c. For an angle of incidence $\theta > \theta_c$ the neutron wave propagates in the material and can be reflected at the interface between two layers. For this reason the material reflectivity property is defined in terms of the momentum transfer $q = 4\pi/\lambda \cdot \sin\theta$. The m value of the supermirror is the ratio of the momentum transfer of the supermirror and of the natural Nichel: $m = q_c/q_{c,Ni}$ with $q_{c,Ni} = 0.217$ (1/nm).

The distance from the moderator to the target was about 22 meters. After the guide exit, the neutrons were transversely polarized by transmission through a polarized ^{3}He cell. The polarization of ^{3}He atoms, monitored through NMR measurements, was reduced by the intense neutron flux [52]. The neutron polarization was calculated for each run, from the fit of the transmission spectrum with the expression $P = \tanh(\sigma_c \cdot n \cdot L \cdot P_{He})$ where σ_c is the neutron capture cross section in ^{3}He, P_{He} is the Helium cell polarization, L is the length of the cell in the direction of the beam and n is the volume concentration of ^{3}He atoms in the cell. The neutron cross section in ^{3}He is given by $\sigma_c = \sigma_0 \sqrt{(E_0/E_n)}$ where σ_0 =5333 barns is the neutron cross section at thermal energy E_0 =25.3 meV.

The neutron spin direction was reversed on a pulse by pulse basis by passing through a radio frequency spin rotator (SR). After exiting the SR, the neutrons entered in the 16-liter liquid H_2 target, where 60% of the polarized neutrons are captured on protons [53].The gamma rays emitted from the
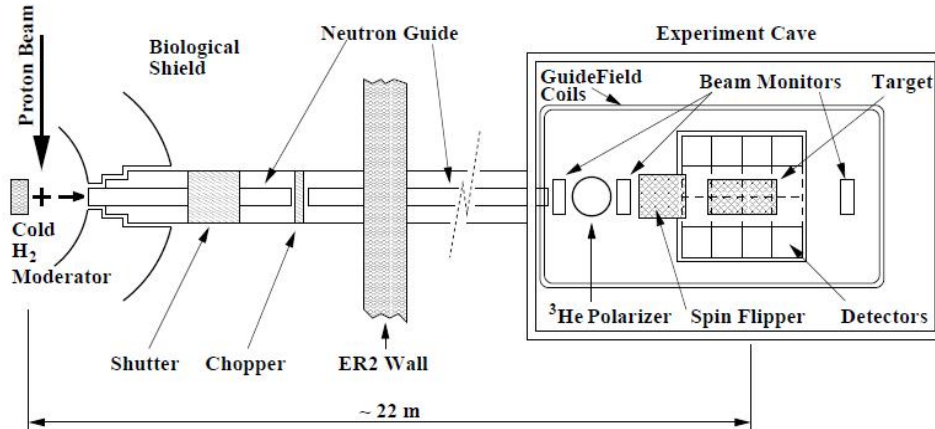
Figure 2.6: The schematic view of the flight 12 and the NPDGamma aparatus at LANSCE.

neutron capture were detected in an array of 48 CsI(Tl) detectors operated in current mode [28, 54]. Each crystal was viewed by a vacuum photodiode. Because of the high neutron flux, the gamma rays detectors had to be operated in current mode. Three ^{3}He parallel-plate ion chambers were used to monitor the beam intensity and polarization. Two pairs of horizontal guide coils and two pairs of vertical shim coils generated a vertical magnetic field of 9.8 Gauss over all the NPDGamma apparatus to maintain the polarization of the ^{3}He cell and the polarization of the neutron beam. The gradient of this field was smaller than 1 μT/cm such that the Stern Gerlach steering of the polarized neutron beam was negligible, according to the calculations presented in section 6.4.

The target cryostat built from non-magnetic materials (Al, Cu) , consisted of an isolation vacuum chamber with neutron beam entrance and exit windows, a Cu shield for thermal radiation and the target itself, covered with thin sheets of Lithium Fluoride that absorbed almost completely the neutrons scattered from the liquid H_2 but was transparent for the high energy gamma rays. The target triple containment boundaries between liquid H_2 and

24

the outside air were in place to prevent the mixing of H_2 gas with the air above the Low Explosion Limit and for a more efficient thermal isolation. Feedback electric circuits with temperature and pressure sensors provided the stable operation of the target during the data collection.

A chopper and a shutter were placed along the beam line between the neutron source and the exit of the neutron guide. The shutter was closed during the background measurements. The chopper was rotated with the frequency of the beam (20 Hz). The opening angle of the chopper allowed to select neutrons with energy between 2 and 15 meV. The beam was closed by about 6 ms before the end of each neutron pulse to allow for the collection of detector pedestals and background studies [49]. For neutrons with energy 3.3 meV the moderator brightness was 1.25×10^8 n/(s $\cdot$ cm^2 $\cdot$ sr $\cdot$ meV $\cdot$ μA). The integrated neutron flux at the end of the guide was 1.0×10^9 (n/cm^2) when the average proton current was 100 μA.

To ensure that the neutrons are not depolarized by inelastic scattering about 99.98% of the liquid H_2 has to be in "para" state in which the spins of the two protons in the molecule are opposite.The neutron energy was too low to excite the para-hydrogen molecules to the ground state of ortho-hydrogen [55]. During the filling of the target, the H_2 gas cooled down to about 20 K, condensated in liquid phase and was converted from ortho- to para- state by passing through an Ortho-Para converter with Fe_2O_3 catalysis to speed up the conversion.

The parity-violating and the parity-conserving asymmetries in the angular distribution of the gamma rays were extracted from the signals of the 48 detectors mounted annularly around the liquid H_2 target [40]. For the

$\vec{n} + p \to d + \gamma$ reaction the measured parity-violating and parity-conserving left-right asymmetries were $A_{\gamma,UD} = (-1.2 \pm 2.1 \text{ stat.} \pm 0.2 \text{ sys.}) \times 10^{-7}$ and $A_{\gamma,LR} = (-1.8 \pm 1.9 \text{ stat.} \pm 0.2 \text{ sys.}) \times 10^{-7}$, respectively. The precision was limited by the low average power of the neutron beam (800kW) and the decrease in the polarization efficiency of the ^{3}He cell. Measurements with the Al target were done in preparation of the H_2 runs. The up down and left right asymmetry for Al were $A_{\gamma,UD} = (-0.02 \pm 3) \times 10^{-7}$ and $A_{\gamma,LR} = (-2 \pm 3) \times 10^{-7}$. The known parity-odd asymmetry for Cl was used to verify the geometrical dependence of the detector pair asymmetries. The up-down and left right asymmetries measured for Cl were $A_{\gamma,UD} = (-19 \pm 2) \times 10^{-6}$ and $A_{\gamma,LR} = (-1 \pm 2) \times 10^{-7}$.

Chapter 3

EXPERIMENTAL SETUP

The second phase of the NPDGamma experiment is being carried out at the

Spallation Neutron Source (SNS) at Oak Ridge National Laboratory (ORNL).

At this facility (figure 3.1) the fast neutrons are produced by a pulsed proton

beam sent into a Hg target. For each proton striking the nucleus, between 20

and 30 neutrons are expelled in addition to the daughter nucleus and

neutrinos. The phenomena is called spallation (or nuclear evaporation). In this

manner a neutron beam with an average power of 1.2 MW is produced by the

incidence of a pulsed, 60 Hz, 1 GeV proton beam on a Hg target.

Figure 3.1: Conceptual Design of the SNS site.

In the first section (front-end systems) of the linear accelerator,

negatively charged hydrogen ions are produced. Each ion consists of a proton

orbited by two electrons. The ions are accelerated and close to the end of the

accelerator they pass through a foil which strips off each ion's two electrons

converting them to protons. The protons are then stored in a ring where they

accumulate in bunches that are released from the ring as proton pulses at 60

Hz. The fast neutrons produced by spallation in the target are slowed down by a cold liquid H_2 moderator to less than 50 meV and then transported through a curved $m = 3$ supermirror neutron guide (see section 2.4) to the experiment located at the Fundamental Neutron Physics Beam Line (BL13). A schematic of the layout of this experimental area within the SNS is shown in Figure 3.2.
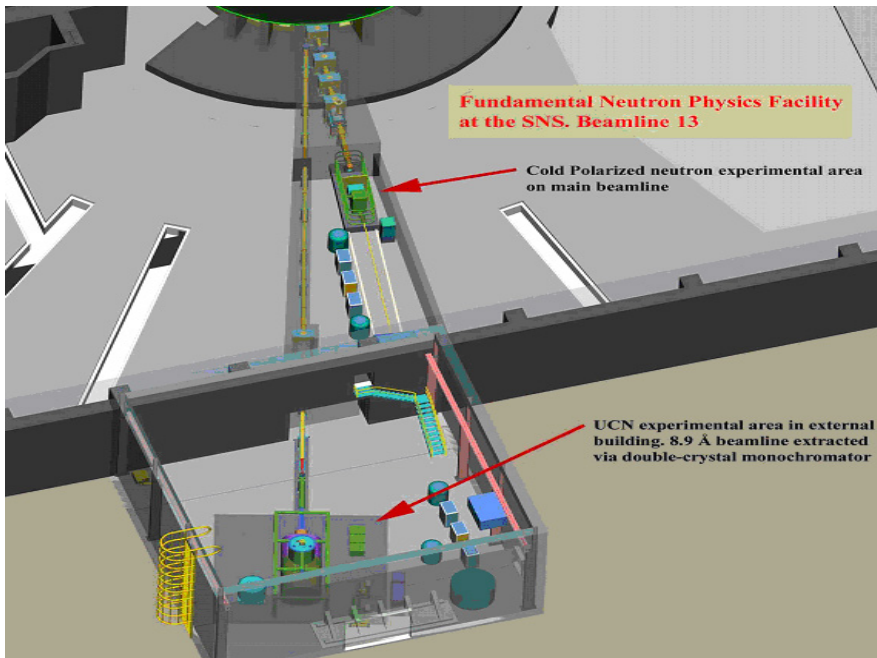
Figure 3.2: The Fundamental Neutron Physics Facility at beam line 13.

The BL13 area is the only one at the SNS that is designed to do experiments with cold and ultra-cold neutrons. The transport of these neutrons through the curved guide reduces the gamma ray flux and the fast spallation neutron components in the beam delivered to the experiment. The beam line is equipped with two choppers and primary and secondary shutters. The opening time window of the two choppers was adjusted to select only neutrons with energies between 2.3 meV and 13.2 meV. All the main components of the experiment are described in section 3.1. The magnetic coils and shielding is

described in section 3.1.1.

During the data collection only the secondary shutter was operated. The primary shutter was left opened until the end of a complete measurement cycle. The pulsed structure of the neutron beam allows precise measurements of the neutron time of flight and energy. However slow neutrons in two narrow intervals centered at 14 Å and 28 Å could also pass through the chopper windows and increased the detector signal near the start and end of each pulse. The beam intensity was monitored for each pulse with two ionization chambers located in front and after the SMP. The ionization chambers are described in the section 3.1.2. Any false asymmetry due to the pulses that do not have slow neutrons, was eliminated with proper cuts placed on the monitor signal.

Because the neutron flux at BL13 is about 30 times of the flux of the FP12 at LANSCE, it was decided to use a multi-channel Supermirror Polarizer (SMP) [56–58] to avoid the decrease in the ^{3}He spin filter efficiency with neutron beam irradiation, that was observed at LANSCE. Neutron polarization after the SMP depends weakly on the neutron wavelength and is predicted to be larger than 95% if the internal magnetic field in the SMP is bigger than 300 G. The SMP is described in section 3.1.3.

The experiment uses a Spin Rotator (SR), described in subsection 3.1.4. The spin of the neutrons is reversed by passing through the SR that is switched on during four pulses in each spin sequence of eight pulses. The order for the switch on and off signals for the SR eliminates the false asymmetry related with the drift in electronic pedestal and detector gains.To measure the angular distribution of the gamma rays emitted from the capture of

neutrons in the target, an array of 48 detectors was placed in a cylindrical geometry around the target. Due to the high rate of gamma rays the detectors have to work in current mode (subsection 3.1.5).

Some of the neutrons will capture in the SMP and will produce gamma rays. To decrease the background contribution from the SMP, two lead walls were placed downstream from the SMP and before the Spin Rotator (SR). The upper limit of the SMP residual fields over the detector and the target is given by the tight requirements on magnetic field gradients and direction. A Compensation Magnet (CM) was placed around the SMP to cancel their combined fringe magnetic field at the position of the detector [59]. Furthermore the combined fields of SMP, CM, and the four main coils of the apparatus have to change sufficiently slowly over the length of the neutron path so that the neutron spin can adiabatically follow the field direction. The magnetic field configuration was designed by using a comprehensive finite element model of the entire magnetic environment of the NPDGamma experiment at the BL13, including the steel walls of the experimental shielding enclosure. This is described in detail in section 3.2. Calculations have been done with the code Opera13 to establish operational parameters and to design the CM and the additional field correction coils, the shim coils.

Section 3.3 presents the magnetic field measurements carried out at the BL13 and the calculation of the field direction, field gradient and the neutron transport in the static field of the coils in order to address the field requirements needed to decrease the systematic effects below the limit of the statistical errors. Most of the magnetic field measurements were done inside the area of the guide coils by moving manually two magnetic probes along vertical and

horizontal Al rails. The field was measured over all the volume of the beam before the installation of the NPDGamma apparatus inside the guide coils.

3.1 Main Components of the Experiment

A layout of the experiment main components and a three dimensional model view of the experimental set-up are presented in Figure 3.3 and a downstream model view in Figure 3.4. The four main coils produce a vertical field over the volume of the target and spin rotator (SR). The currents in the right, left, front and back shim coils produce a magnetic field that corrects the angle of the main field. Current directions in the coils are indicated by arrows. The origin of the coordinate system (x, y, z) is in the center of the detector. The center of the detector is at 185 cm from the end of the super mirror polarizer (SMP). A compensation magnet (CM) is placed around the SMP. After the SMP the neutrons are polarized with their spin aligned with the vertical main magnetic field. The direction of the neutron spin is reversed only in the SR, only during four pulses in each sequence of eight pulses. The two radiological lead walls decrease the background due to the gamma rays emitted from neutron capture in the iron multilayer films of the SMP.

3.1.1 Magnetic Coils and Magnetic Shielding

The four main coils produced a vertical field over the volume of the target and spin rotator. The currents in the outer pair and the middle pair of the main coils are I_1 and I_2 respectively in Figure 3.3. The two middle and two outer (top and bottom) main coils have 18 and 39 windings respectively, with nominal operating current of 23 A. Inside each of the four main coils cases there are 12 additional windings powered by separate auxiliary power supply with 3.3 A. The main coils and additional windings provide a homogeneous magnetic field

31
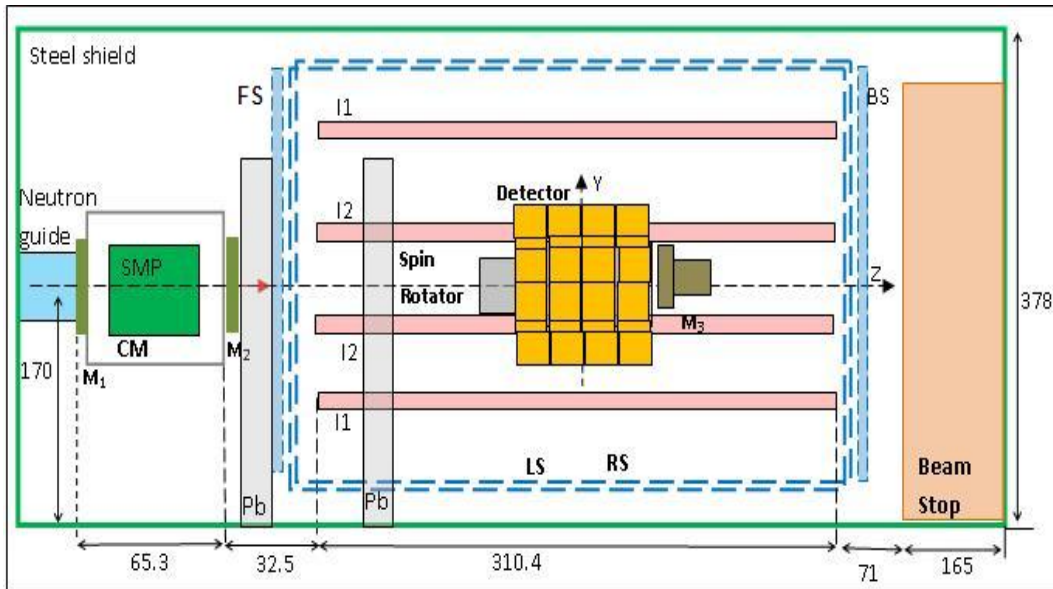
Figure 3.3: A sketch of the main components at the SNS BL13. All dimensions are in centimeters.

of 9.4 Gauss in the center of the main coils.

In addition, there are two pairs of vertical shim coils attached to the Al support frame. These coils are labeled FS (front shim), BS (back shim), RS (right shim) and LS (left shim) coils in Figure 3.3 and are the red coils in Figure 3.4. Current directions in the coils are indicated by arrows. The center of the coordinate system is defined by the intersection of the vertical axis of the main coils with the axis of the beam. The origin of the coordinate system is in the middle of the detector array.The coils in each pair have identical geometry and the same number of turns. There are 28 windings in each side shim coils and 37 windings in each front and back shim coils. The two shim coils in one pair are attached to the lateral vertical sides of the Al support structure of the main coils. The function of this pair of coils is to produce a small magnetic field along the x axis near the center of the main coils and to decrease the overall

32
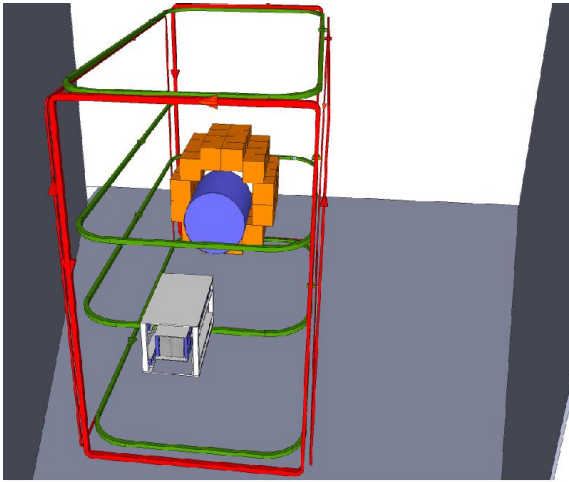
Figure 3.4: The NPDGamma main field coils (green), shim coils (red), gamma detector array (yellow), spin rotator (blue), steel shield without roof (gray), SMP and CM assembly (white) at BL13.

magnetic field component B_x by adjusting currents in the coil. The other two shim coils are the two vertical coils installed on the upstream and downstream ends of the main coils support structure. By adjusting the currents in this pair of coils, the field component B_z, related with the neutron depolarization through the field rotation in the (z, y) plane, can be decreased.

The floor, ceiling and the lateral walls of the BL13 enclosure are lined with soft low-carbon steel plates to provide magnetic and radiological shielding. These plates also form a return yoke for the field flux and attenuate residual fields outside the BL13 enclosure to less than 25 mG to meet the facility requirement. Furthermore, they attenuate the changing magnetic fields generated outside the enclosure that otherwise could change the field parameters in the experiment. The steel shield is asymmetric relative to the main coils causing a misalignment in the direction of the magnetic field of the main coils relative to the y direction inside the detector volume. For the same reason, the field profiles along the x and y directions do not have a minimum

located on the beam axis (the z axis). The finite-element calculations were used to estimate the optimum ratio of the currents in the main coils. A goal was to minimize the average field gradient in the y direction, dB_y/dy over the volume between the SR and the end of the liquid H_2 target.The polarized neutrons move through the magnetic field of the guide coils to the Spin Rotator and to detector array where the target is located.

3.1.2   Beam Monitors

The neutron beam intensity was monitored by two parallel-plate ionization chambers, called the monitors M_1 and M_2, filled with a mixture of ^{3}He and N_2 gas.The first monitor M_1 is located immediately after the beam guide. The second monitor is mounted on the surface of the first radiological wall located just after the polarizer. Each monitors had 1 - mm -thick entrance and exit Al windows and three internal copper grids. The central grid (the anode) is connected to 5 kV voltage. The other two grids (the cathodes) are supplied with -5 kV voltage. When the neutron beam passes through a monitor, some neutrons are captured in ^{3}He and produced alpha particles, tritium and gamma rays that further ionize the N_2 gas. The electrons and the positive ions drift to anode and to the cathodes respectively and produce an electric current that is amplified in a preamplifier circuit. The output signal is the voltage drop on a resistor at the output of the preamplifier circuit.

For monitor M_1, the partial ^{3}He and N_2 pressures are 14.8 torr and 736.8 torr respectively. Inside monitor M_2, the partial ^{3}He and N_2 pressures were 10 torr and 766.9 torr respectively. The calculated densities of Helium and Nitrogen are 0.0022 kg/m^3 and 1.176 kg/m^3 respectively for M_1, and 0.0033 kg/m^3 and 1.129 kg/m^3 for M_2. Relative to the total mass of the monitor gas,

34

the concentration of ^{3}He inside M_1 and M_2 are 0.0018 and 0.0029 respectively.

A third monitor M_3, used only for the beam profile and polarization measurements, had a B$_4$C plate located just in front of a CsI crystal. The crystal was a cylinder with 3.81 cm radius and 7.62 cm length, placed inside a thin Al cylindrical housing 0.8 mm thick with a front glass window 0.5 mm thick. The neutrons are captured in $^{10}_5B$ inside the plate and produce alpha particles, ^6_3Li and gamma rays that are detected in the CsI crystal behind the plate. For the asymmetry calculation, the cuts were placed on the M_1 and M_2 signals to eliminate the spin sequences that can potentially introduce systematic errors in the data analysis. A CAD model of the second monitor is presented in Figure 3.5
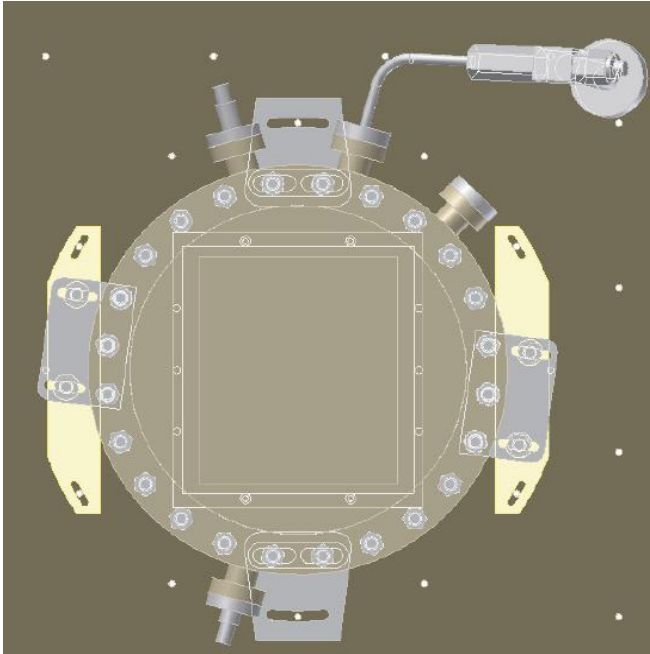
Figure 3.5: The CAD model of the second monitor mounted on the first radio-logical Pb wall is seen along the neutron beam axis.

3.1.3   Super Mirror Polarizer

The Super Mirror Polarizer (SMP) is made from 46 thin parallel and vertical glass films with 0.1 cm distance between them. The stack of glass films is 40 cm long with a curvature radius of 9.6 m, and an active cross sectional area of 10 cm wide and 12 cm high. The magnetic field inside the SMP is between 300 and 380 Gauss.The two vertical surfaces of the glass films are covered with reflecting layers of Fe/Si with an $m = q_c/q_{c,Ni}$ number equal with 3 ([56]). The SMP has no anti-reflecting layers; instead neutrons with the wrong spin state are absorbed in the 0.3 -mm -thick borofloat glass film substrate. The Fe/Si coating was preferred over Fe/Co/V due to a reduced activation produced by cold neutrons. For the magnetic field calculation over the volume of the SMP, it is convenient to introduce a local system of reference x_1, y_1, z_1 centered in the center of the SMP. The z_1 axis is the SMP axis and the vertical axis is y_1. The axis of the neutron beam after the SMP, is the z axis of the NPDGamma experiment. The y axis is vertical and the x is horizontal and points to the beam left wall as looking downstream. Because the neutrons are reflected on the Fe/Si reflecting layers on the surface of the slightly bended glass films, the $z1$ of the SMP is not parallel with the z of the beam but makes a small angle of about one degree. The intensity of the reflected beam has a maximum when the axis of the incident beam makes a $1.15°$ angle with the z_1 axis of the SMP.

The polarization of the transmitted neutron beam is above 95% if the magnetization of the iron films is aligned within $3°$ with the vertical plane of the film. The magnetization of the film is saturated when the vertical component of the magnetic field, applied parallel to the film surface, is bigger than 300 G. This strong field in the SMP is produced by 12 pairs of NdFeB permanent

36

magnet bars with 16 cm height and with square cross section of 1.5×2.0 cm^2. The bars are mounted to the right and left sides of the polarizing volume and the field from the bars is then yoked with two steel plates, see Figure 3.8. The polarizer and magnets are inside a 47.5 -cm -long gas tight steel enclosure.

3.1.4 Spin Rotator

The efficiency of the detectors will change slowly due to temperature and crystal activation. In addition, the asymmetry cannot be calculated to the required accuracy by measuring the signal in a detector for one spin state and then for a later pulse with reversed spin state, due to the pulse-to-pulse beam fluctuations. To reduce the false asymmetry generated by drift in the detector gains, electronic pedestals and beam fluctuations, the direction of the neutron spin is rotated by 180° in a resonant RF Spin Rotator (SR) [60] located before the target. The Spin Rotator is turned off during the 1st, 4th, 6th and 7th pulses and is switched on during the other four pulses in the spin sequence of eight pulses. The spin is rotated by 180° only when the SR is turned on. The sequence of the spin reversal was chosen to cancel the effects of the linear and the second-order drift in the electronic pedestal or detector gain.

The SR operates according to the principle of Nuclear Magnetic Resonance. A 27.5 - kHz magnetic field oscillates along the axis of the beam while the static field of the four guide coils is normal to the axis of the SR. The axis of the RF field is surveyed with the beam axis and it is normal to the main static magnetic field. The RF field of the SR is produced by a 30 -cm -diameter and 30 -cm -long solenoid held inside a 42 -cm -long and 42 -cm -diameter Al cylinder with 0.1 -cm- thick entrance and exit windows and 0.25 -cm -thick wall. The axis of the Al cylinder is coincident with the axis of the solenoid. The

function of the Al cylinder is to shield the experiment against RF power of the SR. For each pulse, the neutrons with different energies arrive to the detector at different times. For this reason the amplitude of the RF field has to be inversely proportional with the time of flight of each neutrons, in order to flip all the neutron spins with maximum efficiency. It was proven [60] that the RF field is well confined inside the SR due to the skin effect in Al walls, and the RF control signals do not couple with the detector signal.

3.1.5   Detector System

The gamma rays from neutron capture on liquid para-hydrogen are detected by the 48 detectors grouped in four rings, with 12 detectors in each ring (Figure 3.6). The liquid Hydrogen target is also presented in this figure. The axis of the beam is coincident with the axis of the detector array and liquid Hydrogen cryostat. Each detector is made from two optically coupled, rectangular CsI crystals doped with Thallium. Thin Al walls cover the six facets of each cubical $15.2 \times 15.2 \times 15.2$ cm^3 detector that contains two identical CsI crystals. The mean free path of 2.2 MeV gamma rays in CsI is about 5.5 cm such that 84% of the incident gamma ray energy is absorbed. The eight surfaces of the crystals are covered with Teflon and Al walls. The gamma rays produced in the target interact with the CsI crystals by Compton scattering or photoelectric effect, and produce optical photons. Each detector has a glass window and a vacuum photodiode mounted on the back side of the detector, away from the target. The optical grease between the crystals and the optical window, and the aluminum housing protects the slightly hygroscopic CsI crystals. The optical photons generated in the CsI crystals are reflected on the lateral and front walls and are transmitted through the glass window on the back side of a detector and enter into the S20 Hamamatsu vacuum photo-diode, producing an electric

current. Because of the high neutron flux the gamma detector has to be operated in current mode.
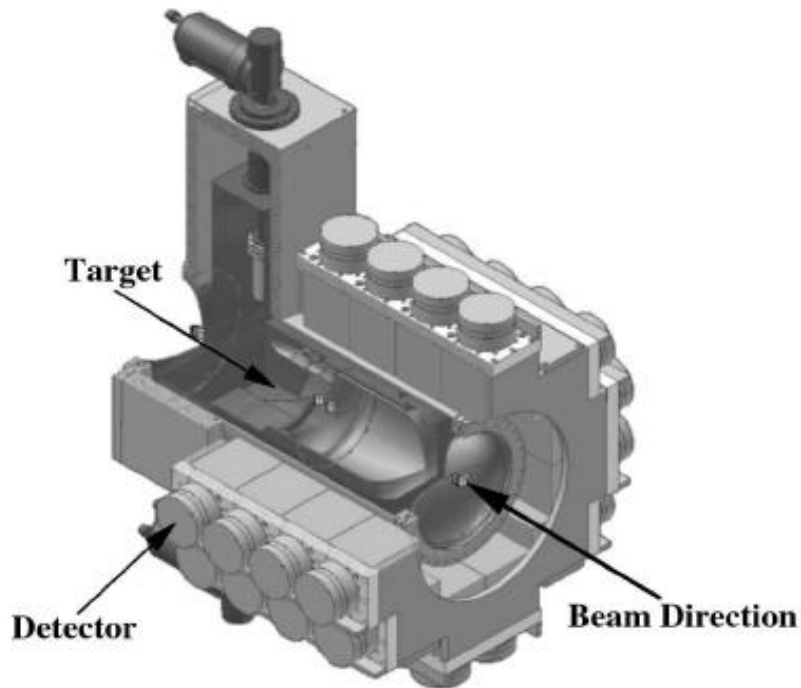
Figure 3.6: A view of the 48 detectors assembly and liquid H_2 target cryostat.

The Al target placed in the center of the detector array is seen along the beam, in the two dimensional sketch of Figure 3.7. In this figure only twelve detectors in the first ring are seen. The detectors are numbered clockwise, as looking downstream from the exit of the polarizer. In this figure only the 12 detectors in ring 0 can be seen.

The vacuum photo-diode current is amplified by a three stage low noise current-to-voltage preamplifier circuit. Two 45 -Volt batteries apply a 90 -Volt bias across the vacuum photo-cathodes. The electronic noise in the preamplifier is reduced to the level of Johnson noise by different filter stages
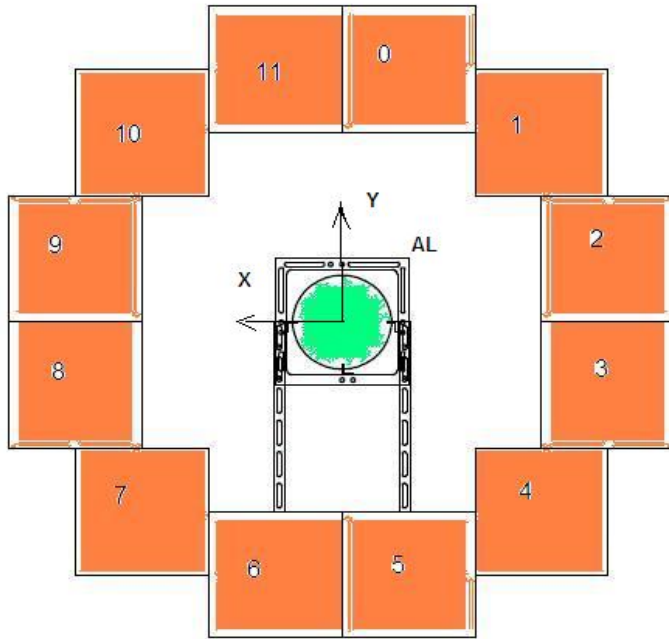
Figure 3.7: The sketch of the 12 detectors in the first ring and the Al target (green) and the Al support are seen along the beam axis as looking downstream.

and ground isolation such that the time to measure the asymmetry to $1 \cdot 10^{-8}$ limit is limited only by the counting statistics and beam intensity fluctuations.

3.2 Compensation Magnet Design and Implementation

The overall sensitivity of the NPDGamma experiment requires stringent control of systematic effects [61]. In particular, the magnetic field requirements are such that: (a) a field uniformity in the volume of the SR has to be better than 1% to assure a spin-flip efficiency bigger than 95% and to prevent a change in the neutron kinetic energy; (b) the gradient of the vertical component of the field dB_y/dy has to be less than 3 mG/cm over the volume of the SR and liquid H_2 target in order to decrease the systematic error due to the Stern-Gerlach effect for neutrons with spin up or down moving in a non-uniform magnetic field; (c) inside the volume of the liquid H_2 target the average angle of the field

$|\theta| = |B_x/B_y|$ has to be less than 2 mrad, which is half of the accuracy of the effective alignment of the detector array and (d) the overall change in magnetic field vector, in the frame of the neutron, has to be small enough such that the the neutron's spin can follow adiabatically the change in the direction of the field and that the depolarization is less than 1%. There is no tight specification on $|B_z/B_y|$, because false effects in the NPDGamma experiment due to a z component of the magnetic field are insignificant.

The Compensation Magnet (CM) placed around the Polarizer was designed to cancel the fringe field of the SMP downstream at the position of the SR and liquid H_2 target while at the same time assuring a minimum decrease in the magnetizing field inside the SMP. The combined field of SMP, CM, and the main coils of the experiment has to change sufficiently slowly over the length of the neutron path so that the neutron spin can adiabatically follow the field direction. The design of the CM and the calculation of the optimum position of the guide coils was done by using a comprehensive finite element model of the entire magnetic environment of the NPDGamma experiment at the BL13. The optimum number of NdFeB magnets and the geometry of the CM that achieves the magnetic field requirements were determined by finite-element calculations in Opera 3D model of the SMP and CM.

The geometry of the CM and SMP is presented in Figure 3.8. The red arrows indicate the direction of the magnetization in the NdFeB magnets (green) located between steel plates. The steel yokes and the Al plates are presented in black and white colors, respectively. Figure 3.9 shows a schematic cross sectional view of the CM along the beam axis of the SMP and the CM, indicating the four Al posts at the corners of the CM and eleven small

41

Al rectangular spacers (white) located between the NdFeB magnet bars (black).
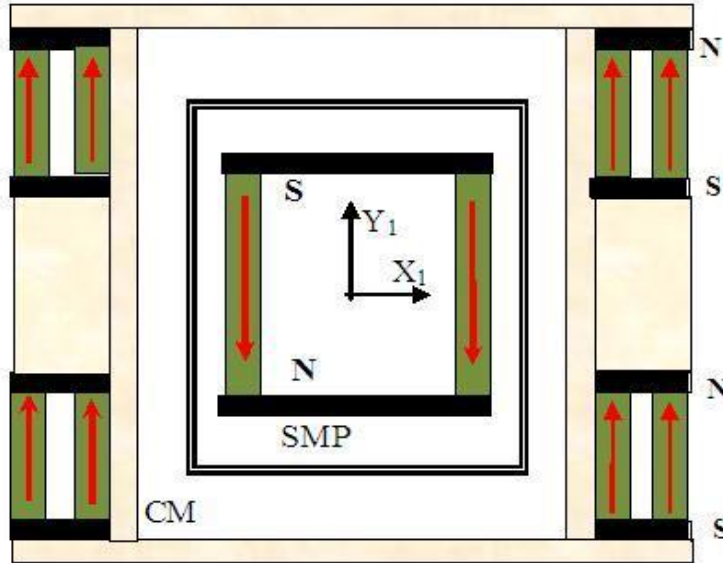
Figure 3.8: A schematic cross sectional of the SMP and the surrounding CM is seen as looking upstream.

The CM is built from carbon-free steel and Al. The magnetic field in the CM is produced by small NdFeB permanent bar magnets [62] with square cross sections of 1.12×1.12 cm^2 and with height of 5 cm. The SMP is 17.6 cm high, 17.2 cm wide, and 47.6 cm long. The bent glass films with Fe/Si supermirror coating are not shown. The CM is 27.8 cm high, 28.4 cm wide and 50 cm long. The 44 magnets are installed in two pairs of rows; a pair on the right side and the other pair on the left side of the CM z_1-axis. The magnets are grouped in four rows, two on each lateral side. This distribution of the magnets provides a smaller decrease in the average field magnitude and uniformity in the volume of the SMP compared with a CM with only two rows. The direction of magnetization in the bar magnets of the CM is opposite to the magnetization

42

in the SMP. The spacing between the top and bottom rows of magnets in the CM was done to keep sufficiently uniform field bigger than 300 Gauss over the entire volume of the SMP, while still generating a large enough magnetic dipole moment to oppose that of the SMP.
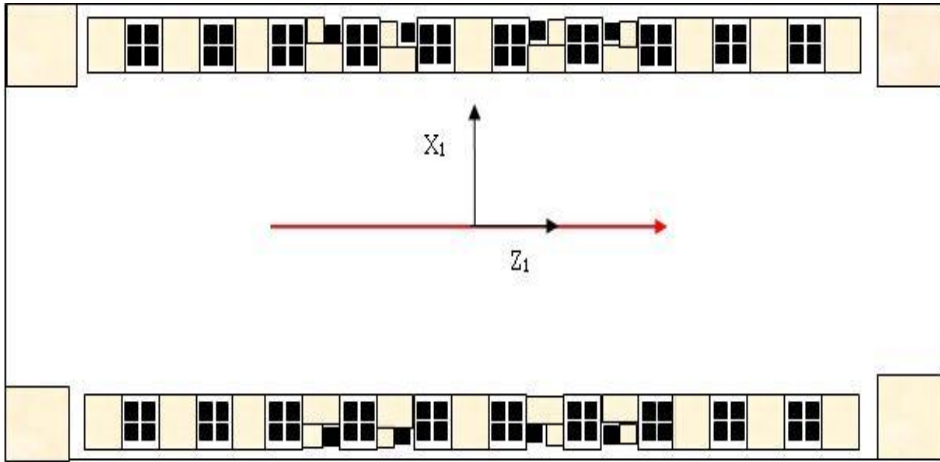
Figure 3.9: The schematic cross sectional top view of the compensation magnet (CM) where z_1-axis is the common axis of the SMP and CM.

Figure 3.10 shows the calculated average magnitude of the magnetic field produced by the SMP and the CM along their common z_1 axis.The origin of the coordinate system (x_1, y_1, z_1) is in the SMP center.The average field is calculated along twelve lines parallel to the axis of the CM and SMP intersecting the x_1, y_1 plane at x_1 =0, 1, 2, 3 cm and y_1=0, 1, 2 cm.

The smallest residual field inside the SR and the detector is obtained for N = 44 NdFeB magnets in each row. Results are shown for a SMP without the CM and then with a CM that has different number of permanent magnets to create the compensating field. The field is measured along 12 lines parallel to the beam axis and downstream from the exist of the SMP (z_1>25 cm). The neutrons are polarized in the SMP centered at z_1=0 cm. The field profile along

43

the negative and positive directions of the z_1 axis are expected to be symmetric, because the change in the Earth magnetic field inside the NPDGamma shielded enclosure is very small. The field is calculated from the center of the SMP to the end of the detector. This is the region of interest where the fringe field of the SMP and CM in the volume of the SR and the detector has to be small enough, to decrease the field - related systematic errors to a minimum.

The average over several lines parallel to the beam axis is done to account for the width and height of the neutron beam. In these calculations, the main guide coils field and the shim fields are zero. The magnitude of the remaining fringe field depends on the number of permanent magnets N in the CM. The fringe fields of the SMP and CM partially cancel each other on the beam axis in the experiment close to center of the SR. The magnitude of the measured field component, corrected for the ambient field in the BL13 cave is shown along a line parallel with z_1 axis and at 0.8 cm above it. The other lines show the fields produced by the SMP and the CM with a different number N of permanent magnets used for each side of the CM. The locations of the SR and the photon detector array on the z_1 axis are indicated.

The results of the calculations of the magnetic field inside the SMP with and without the compensation field are presented in Figure 3.11. The currents in the main and shim coils are zero. In the two top graphs, the average field magnitude is calculated over 25 lines parallel to x_1 axis, at $y_1 = 0, \pm 3, \pm 5$ cm and $z_1 = 0, \pm 10, \pm 20$ cm and over 35 lines parallel to z_1 axis, at $x_1 = 0, \pm 2, \pm 4, \pm 5$ cm and $y_1 = 0, \pm 3, \pm 5$ cm. Inside the volume of the SMP glass films (x_1 from -4 cm to 4 cm and z_1 from -20 cm to 20 cm) the magnitude of the field inside the SMP is reduced by less than 35 Gauss by the CM leaving

44
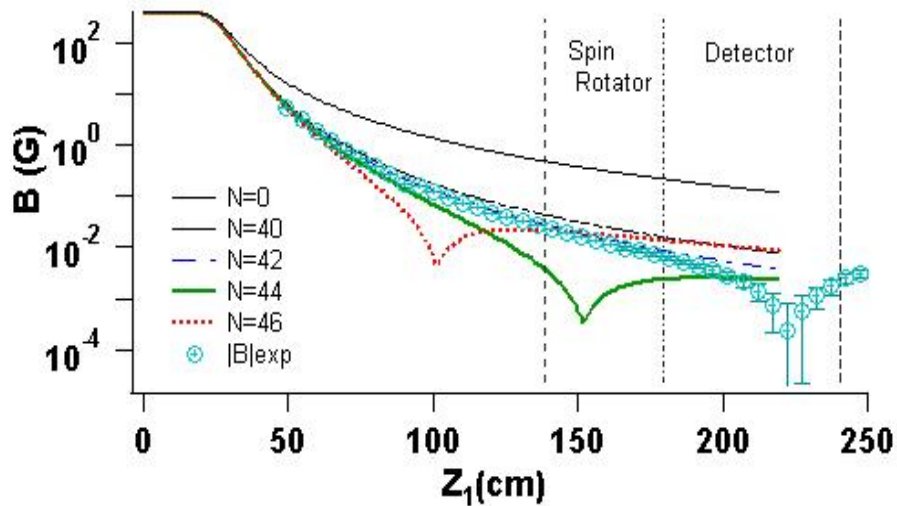
Figure 3.10: The average magnitude of the field is calculated along twelve lines parallel to the axis of the CM and SMP. The black line, denoted N = 0, shows the field produced by the SMP alone.

the total field strength larger than 300 G. This assures that the magnetization of the Fe/Si layers is saturated as required for the maximum neutron polarization efficiency. Without the CM the calculated field strength in the center of the SMP is 415 G. The bottom graphs in this figure show the average angle between the field direction and the y_1 axis, $\text{acos}(B_y 1/B)$ in radians, as a function of x_1 and z_1 calculated along the same directions as above, for zero current in the main coils and shim coils. The results suggest that the field of the CM changes the small angle B_{y_1}/B less than 0.05 rad in the volume of the SMP. Therefore the direction of the field is still almost parallel with the vertical surface of the Fe/Si films as required.

The neutron beam polarization and the beam transmission through the SMP both depend on the beam glancing angle on the surface of the reflecting vanes. Because the neutron beam travels along the curved channels of the

45
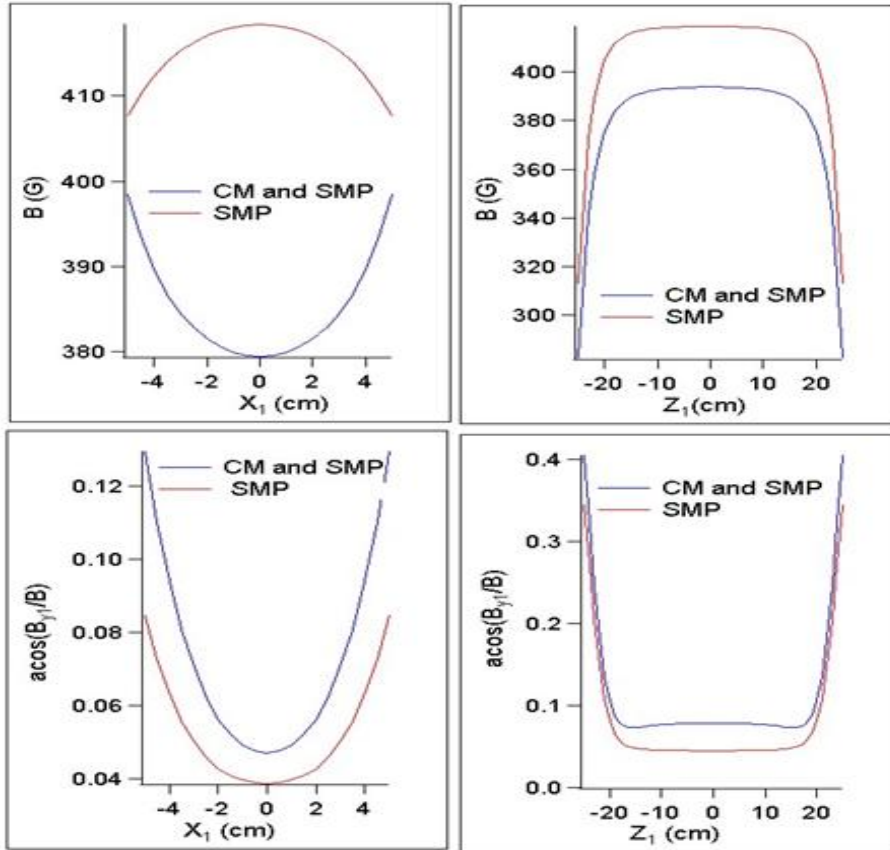
Figure 3.11: The average magnetic fields (top figures) and the angle between the field and y_1 axis (bottom figures) are calculated inside the SMP with and without the CM.

SMP, the axis of the transmitted neutron beam (z) will be rotated relative to the axis of the SMP z_1. To maximize the neutron polarization and the polarizer transmission, the SMP and CM are mounted on the adjustable table that can be rotated around a vertical axis passing through a pivot point located under the entrance face of the SMP. The rotation angle determines the angle between the SMP z_1 axis and the z axis of the experiment, and can be chosen within a $\pm 2.4^o$ range. Furthermore, the table can be translated in the y_1 and x_1 directions. The rotation angle was optimized by studying the neutron flux and polarization after the SMP. The changes in the field direction and in the field

gradients over the SR and detector volume were calculated for two extreme rotation angles of the SMP. The results suggest that the changes in the field gradient dB_y/dy and in the field angle θ are smaller than 0.05 mG/cm and 0.04 rad respectively. Figure 3.12 demonstrates the function of the shim coils. The gradient of dB_y/dy and the angle of the field projected in the (x, y) plane, $\theta = B_x/B_y$, calculated for four currents in the right shim coils in the region of the SR and the detector, are averaged over 12 lines parallel to the beam axis and passing through $y=$ 0, 3, 6 cm and x = 0, 2, 4, 5 cm. In the model the angle between z and z_1 axes is 2.3^o and the current in the right shim coil is varied.
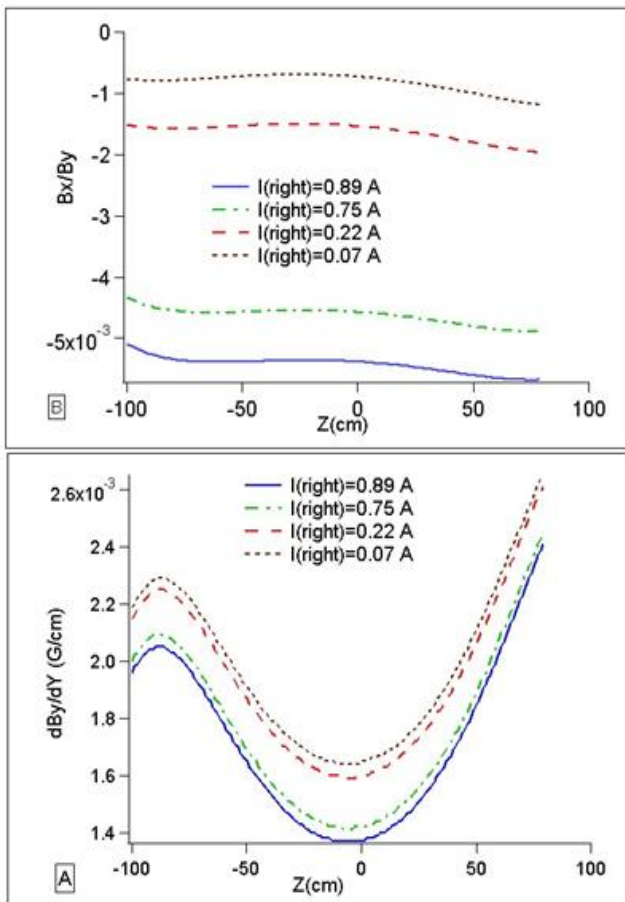
Figure 3.12: The calculated field ratio B_x/B_y (top figure) and the field gradient (dB_y/dy) (bottom figure) are averaged over 12 lines parallel to the beam axis.

47

3.3   Magnetic Field Measurements

After installation of the most of the SMP, CM, guide and shim coils at the BL13, the magnetic fields were measured over the entire volume of interest. The three components of the magnetic field, B_x, B_y and B_z, were measured with a 3-axis magnetic flux-gate probe (model Mag03-MS, Bartington Instruments) attached with three screws to an Al frame on a dove-tail table that could slide through the channel of a long Al extrusion supported by the main coils. For measurements of the vertical component B_y, the Al frame was translated on the surface of a vertical Al post mounted on a platform with three adjustable feet. The level of the horizontal plate supporting the Al frame or the direction of the vertical post could be adjusted relative to the direction of the gravity with an accuracy of 0.9 mrad or less.

Because the steel shielding is not symmetric with respect to the beam axis, the profile of the B_y component does not have a minimum on the beam axis. To minimize the field gradient dB_y/dy inside the beam volume between the SR and the liquid H_2 target, the distance between of the top main coil and the steel floor was set equal to the optimum distance found from the finite-element calculations. Figure 3.13 shows the results of these measurements along three directions parallel to the beam axis at $x = y = 0$ cm, $x = 4$ cm, $y = 0$ cm and $x =$-4 cm, $y =$0 cm, with a 2.5 cm step. The field in the center of the main coils was about 9.8 G. The calculated field components are indicated by solid lines in the same figure for comparison. The end of the SMP is at $z =$-185 cm when the center of the detector array is at $z =$0 cm. The center of the liquid H_2 target is at 3.8 cm downstream from the detector center.

The neutron depolarization probability increases with the rate of the change in the magnetic field direction. In the measured field, the largest change in the field direction takes place in the region of the field minimum. To control the depolarization in the transition region between the end of the SMP and the start of the guide coils, where the B_y component has a minimum (Figure 3.13, bottom left), the main coils were mounted as close to the SMP as allowed by radiological shielding. One of the criteria for the design of the CM was to keep the depolarization of neutrons after the SMP small. The depolarization probability on trajectories from the end of the SMP to the end of the liquid H$_2$ target, depends on the rate of change of the field direction compared to the Larmor frequency of the spin in the field B. The depolarization probability is described by the adiabatic factor λ equal with the ratio of the Larmor frequency of the neutron spin, $\omega_L = \gamma \cdot B$, to the angular frequency of the field rotation, ω_B. It can be shown that the depolarization probability is negligible if the adiabatic factor λ is much larger than one [63, 64], where

$$\lambda = \frac{\omega_L}{\omega_B} = \frac{\gamma B}{\frac{1}{B^2}\left|\vec{B} \times \frac{d\vec{B}}{dt}\right|}.$$

(3.1)

Here B is a static field and gamma is the neutron gyromagnetic ratio. The adiabatic factor is calculated from the three measured field components shown in Figure 3.13 for neutrons with kinetic energy of 20 meV, the upper limit for the neutron energy in the NPDGamma experiment. At the field minimum $\lambda \approx 20 \gg 1$ and because ω_B is proportional with the neutron energy, the depolarization probability is negligible. The electric currents in the right, left, front and back shim coils were 0.54 A, 0.22 A, 0.47 A and 0.7 A respectively. As seen from the figure at $z = $ -146 cm, the field magnitude has a minimum of

about 5 G.
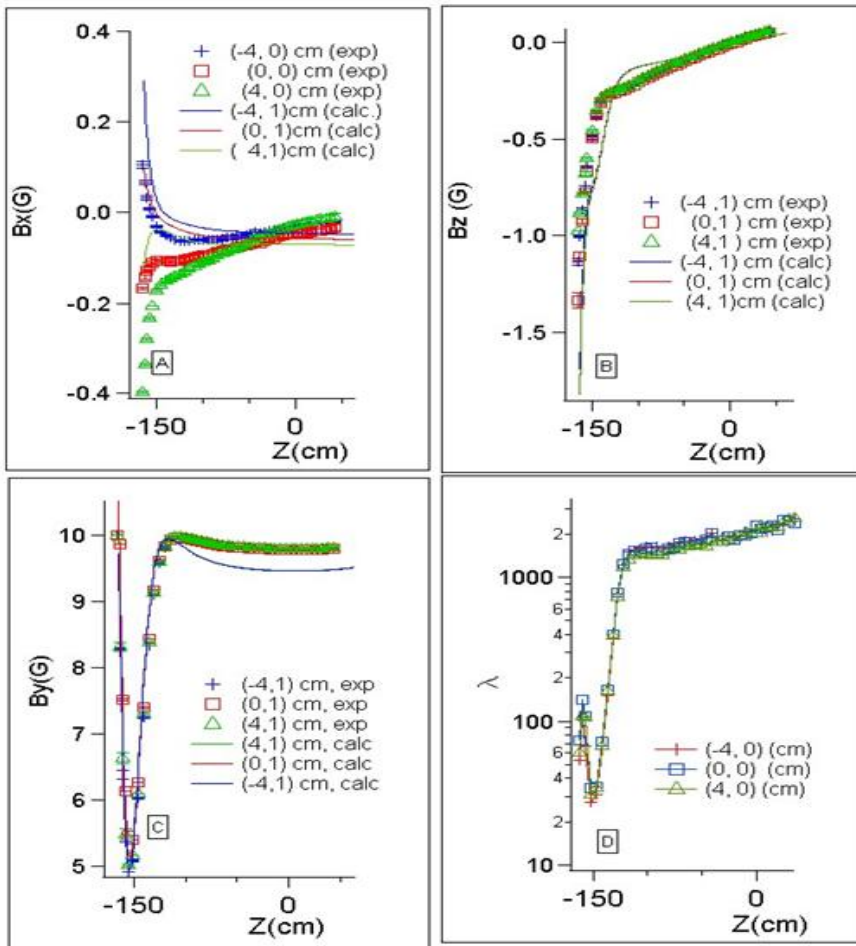
Figure 3.13: The magnetic field components measured and calculated along three lines parallel to the beam axis and the adiabatic factor λ for 20 meV neutrons.

To match the resonance frequency 27.4 kHz of the SR fixed by the internal inductance and capacitance of its electric circuit, the static field for the NPDGamma experiment was later set to 9.4 G. One possible source of a false up-down asymmetry in the experiment is a shift in the center of the neutron beam up or down relative to the center of the target, causing a change in the acceptance solid angle of the detectors. This up-down shift is due to the Stern-Gerlach steering effect, the neutron spin interaction with the field

gradient dB_y/dy. The size of the effect depends again on the neutron energy

and the size of the field gradients over the beam volume between the SR and

the end of the liquid H$_2$ target. The measured gradients are shown in Figure

3.14 on the z axis at $x = 0$ cm and at four different y axis values. The left panel

shows the field gradient, dB_y/dy calculated from the measured B_y field along

four lines parallel with z axis, at $x = 0$ cm and four y coordinate values. The

right panel shows the angle $\theta = B_x/B_y$ on the beam axis, measured for 0.54

Amp current in the right shim coil. The solid lines in both plots show the field

gradient and angle θ from the calculated field components by using a complete

model of the main coils, SMP, CM and magnetic shields.

The average gradient $dB_y/dy \leq 3$ mG/cm in the beam volume of

interest, less than the specification limit. In the same figure, the center of the

detector and liquid H$_2$ target are at z=3.8 cm and 0 cm respectively and the

end of the SR is at about $z = -40$ cm.

For the up-down gamma asymmetry measurement, the axes of

symmetry of the detector array and the magnetic field have to be aligned

accurately to the y-direction. Because the efficiencies and gains of each 48

detectors are different, the effective locations of the detectors had to be

determined with a sealed gamma source placed in the center of the detector

array. The detector signals were measured when the gamma source was

moved at known positions on a grid in the (x, y) plane. On the basis of these

measurements, the up-down orientation of each detector is defined with the

accuracy of less than 4 mrad [65]. In order not to increase the systematic error

due to the alignment accuracy, the average angle $\theta = B_x/B_y$ of the magnetic

field over the volume of the beam and the target has to be between ± 2 mrad of
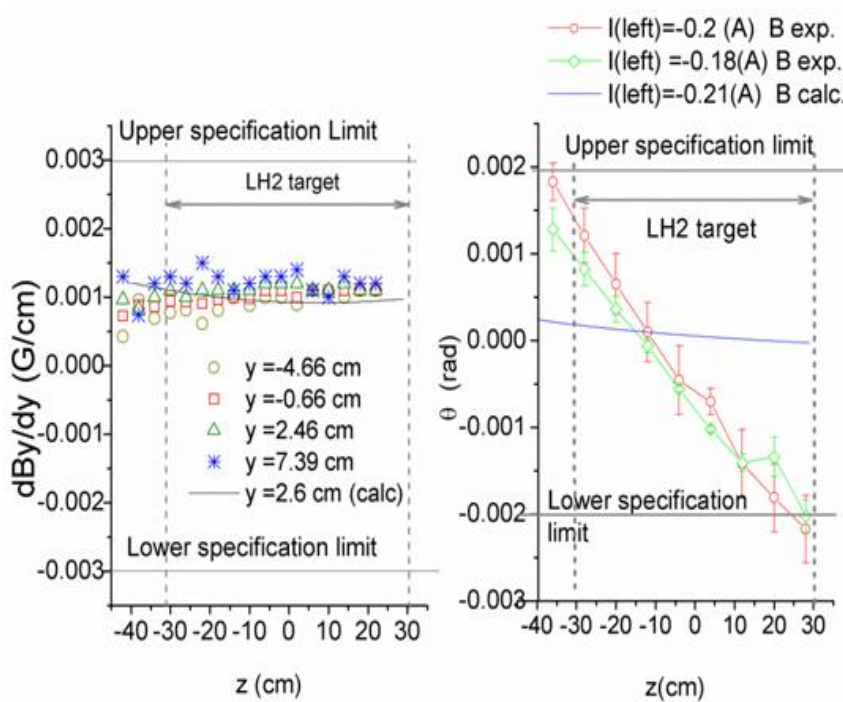
Figure 3.14: The field gradient dB_y/dy and the angle $\theta = B_x/B_y$, measured for a 0.54 Amp current in the right shim coil, are compared with the calculated field gradient and angle θ.

the vertical direction. Figure 3.14 shows the field angle $\theta = B_x/B_y$ on the beam axis for two different currents on the left shim coil. The average value for the angle θ meets the field specifications.

In section 6.4 the contribution to the false asymmetry from the Stern Gerlach effect is calculated from the measured magnetic field gradients. The measurements presented here confirm that the field gradient inside the beam volume and between the SR and the end of the detector is smaller than 3 mG/cm. The volume average of the magnetic field direction in the target region was measured to be aligned with the direction of the gravity, the y-axis, within ± 2 mrad which is in agreement with the specification limit.

Chapter 4

DETECTOR ALIGNMENT AND BEAM CHARACTERIZATION

MEASUREMENTS

This chapter presents the results of the preparatory measurements done with

the apparatus and the cold neutron beam at the SNS Fundamental Neutron

Beam Line 13. Section 4.1 presents the measurements of the misalignment in

the center of each detector, with a ^{137}Cs radioactive source that was moved

over different points of a grid located in the vertical plane normal to and

centered with the beam axis. The techniques for the measurement and

calculation of the neutron flux incident on the target are presented in section

4.2 which is followed by beam profile measurements described in section 4.3.

The measurements of the neutron beam polarization are presented in section

4.4.

4.1 Alignment of the Photon Detector Array

Each of the 48 detector elements that form the detector array is made from two

identical CsI crystals $7.4 \times 7.4 \times 15$ cm^3 assembled side by side (Figure 4.1).

In this figure, U and D are the first pair of opposite detectors in a ring. The

precise knowledge of the real position of each of the detector geometrical

centers is crucial for a reliable calculation of the geometry factors that enter in

the determination of the experimental asymmetries. At least two factors may

cause the geometrical center to change from the ideal position. First, due to

radiation exposure over the years, either to different levels of radiation or being

affected differently by it, the two crystals that form a detector element can have

slightly different optical properties and efficiency and this could displace the

center of the active volume from the geometrical center. Second, the change in

53
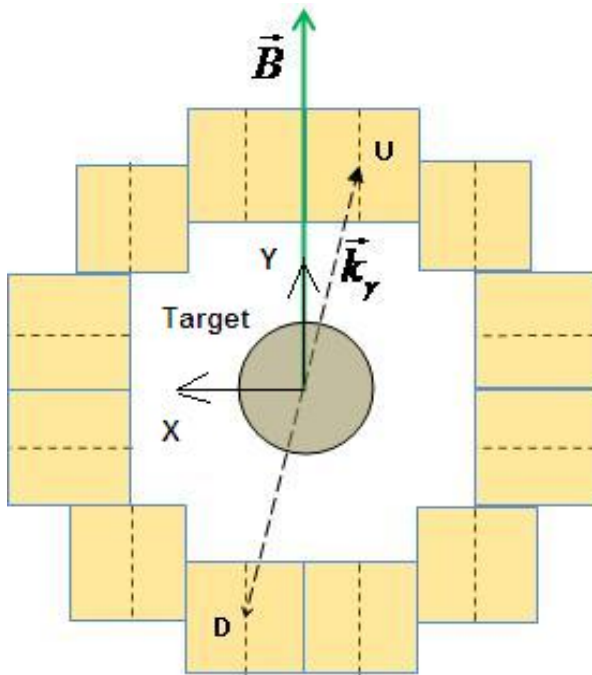
Figure 4.1: The 12 detectors in a ring, the direction of the magnetic field and the position of the two CsI crystals in each detector

the expected position of the detector element center can also be due to mechanical reasons: for example, bending or shifting in the Al support of the detector assembly because the tolerance in the position of the detectors due to mechanical stress is about 1 mm. Both of these contributions are expected to change the angle of the detector center from its ideal position expected from the geometry of perfect crystals and in the absence of mechanical stresses.

The position of the detector center relative to the center of axes is given by the distance r and the two angles θ and φ measured relative to the beam axis (z) and to the x horizontal axis. To measure the misalignment in the centers of the detectors and for a more precise calculation of the geometry factors, the detectors signals were recorded in the presence of a ^{137}Cs source that was moved with an automatic scanner over a grid in the vertical plane

normal to the beam axis and passing though the center of each detector array ring. There are 12 detectors in each ring and the measurements were repeated for all four rings. The location of the grid plane is such that the nominal detector element angle θ is always 90°. If there is a change in the detector center along z axis then the angle θ would become 90° + $\delta\theta$, and $\sin\theta$ becomes $\sin(90° + \delta\theta) = \cos(\delta\theta) = 1 - (\delta\theta)^2/2$. Therefore a small change in the angle θ enters as a second order correction in the geometry factors of the 12 detectors located in the ring with the source in its center. The angle φ between the radial distance r to the geometrical center of the detector and the x axis is never close to 90° or 0°. For this reason, when the source is moved in different points in the vertical plane, the geometry factors for the 12 detectors in that ring depend mainly of the angle φ. The detector element misalignment is assumed to be equivalent to a small rotation of the detector center about the z axis with an angle δ in the expected detector angle φ. This allows for a simple correction of the geometry factors. The rotation angle φ was calculated from the fit of the detector signals measured for all the (x, y) positions of the source. The detector signals were measured several times for a scan along the x axis at positions (0, 1, 2, 2, 1, 0, -1, -2, -2) inches and in the same positions along the vertical y axis. In addition the measurements were done at (1, -1) , (-1, 1), (-1, -1) and (1, 1) inches.

For ideal detectors the geometry factors are equal with the detector energy weighted scalar product of the initial momentum of the gamma ray and the unit vector of the vertical $\hat{y}$ and horizontal $\hat{x}$ axes:

$$G^{ud} = \left\langle \hat{k}_\gamma \cdot \hat{y} \right\rangle = \left\langle \sin\theta \sin(\varphi) \right\rangle \tag{4.1}$$

$$G^{lr} = \left\langle \hat{k}_\gamma \cdot \hat{x} \right\rangle = \left\langle \sin\theta \cos(\varphi) \right\rangle \tag{4.2}$$

The dependence of the detector signal on the coordinates of the source can be modeled in MCNPX by computing the energy deposition in the detectors for each position of the source. The MCNPX output for the energy deposition in a detector is given in MeV/gram, normalized to the number of source particles.

The coordinates of the detector element center in the ideal position (x, y) and the real position (x', y') are related through the rotation angle δ about the z axis:

$$x' = x \cos(\delta) - y \sin(\delta) \; ; \quad y' = x \sin(\delta) + y \cos(\delta) \tag{4.3}$$

The change in the detector signal is expected to be the same when the two directions of scanning (x, y) are rotated with an angle $-\delta$ while the center of the detector is not changed. Therefore the MCNPX model was built for detectors located in their ideal positions. The model was used to derive the dependence between the energy deposition in each detector in a ring and the (x, y) coordinates of the source moved in the vertical grid. The energy deposition in each detector was calculated for each location of the source in the 441 points of a 25.4×25.4 cm^2 grid, larger than the real scan grid [65]. The energy deposition in a detector was fit with an eight order polynomial in x and y:

$$f(x, y) = \sum_{k+l=0}^{k+l=8} p_{k,l} x^k y^l \tag{4.4}$$

The fitting coefficients p_{kl} were calculated for each detector. The detector rotation angle δ was estimated from the fit of the measured detector signal $Y(d)$ with the fitting function $f(x', y')$ that depends on the rotated axes of coordinates. The relation between the two quantities involve the scaling constant h and the misalignment angle δ:

$$Y(d) = h \cdot f(x \cos \delta - y \sin \delta, x \sin \delta + y \cos \delta) \tag{4.5}$$

56

The scaling factor and the misalignment angle δ are calculated from the minimization of the χ^2 function. The geometry factors $G^{ud} = <\vec{k} \cdot \vec{y}>$ and G^{lr} $= <\vec{k} \cdot \vec{x}>$ are calculated first for the ideal position of the detectors. The adjusted geometry factors are then calculated from the ideal geometry factors by using the misalignment detector angles:

$$G^{ud'} = \left\langle \hat{k}_\gamma \cdot \hat{y}' \right\rangle = \langle \sin\theta \sin(\varphi + \delta) \rangle = \left\langle \hat{k}_\gamma \cdot \hat{x} \right\rangle \sin\delta + \left\langle \hat{k}_\gamma \cdot \hat{y} \right\rangle \cos\delta \quad (4.6)$$

$$G^{lr'} = \left\langle \hat{k}_\gamma \cdot \hat{x}' \right\rangle = \langle \sin\theta \cos(\varphi + \delta) \rangle = \left\langle \hat{k}_\gamma \cdot \hat{x} \right\rangle \cos\delta - \left\langle \hat{k}_\gamma \cdot \hat{y} \right\rangle \sin\delta \quad (4.7)$$

For any detector the correction angle is smaller than 0.04 (rad) as this is illustrated in Fig. 4.2. The uncertainties come from the errors in the fit. The estimation of the systematic errors due to these effects are discussed in Sec. 6.3.

4.2 Neutron Flux Measurements

Measurements of the neutron flux in the center of the detector were done with a Boron Carbide B_4C placed at the center of the detector array at $45°$ relative to the beam axis as shown in Fig.4.3. The MCNPX calculations of the neutrons interaction with the plate were used to calculate the average energy deposition in each detector divided with the number of neutrons incident in the plate. Also the calculation of the fraction of neutrons captured in the plate indicated that about 99% of the neutrons are captured in the plate. When neutrons are captured in ^{10}B the excited ^{11}B nucleus splits into ^{7}Li and ^{4}He. With (94%) probability the excited ^{7}Li nucleus decays to the ground state emitting a 0.48 MeV gamma ray. With 6% probability ^{7}Li is produced in its ground state with no gamma ray emission. For each neutron captured, one gamma ray is emitted with a probability given by the branching ratio.
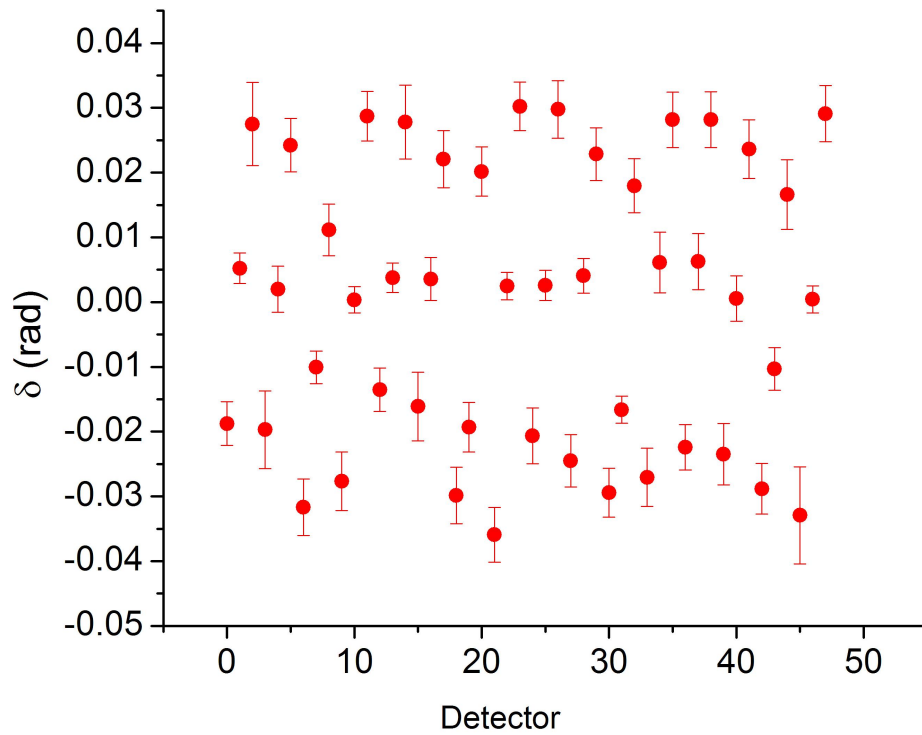
Figure 4.2: Misalignment angles for each of the 48 detectors

The neutrons captured in the plate produce gamma rays that are detected in the 48 detectors. At the end of these measurements the B_4C plate was removed and a small cylindrical ^{137}Cs gamma source was placed on the beam axis and close to the center of a detector array. By taking the ratio of the detector signals recorded from the two measurements, the integrated neutron flux (n/s) and the spectral flux n/s/Å/cm^2 were calculated. The calculation of the neutron flux spectrum from the ratio of the time bin detector voltages measured with the B_4C plate and then with the Cs source, will be presented in the subsections 4.2.1 and 4.2.2.

4.2.1 The Boron Carbide Plate Method

In the absence of any collimator the neutron beam after the Super Mirror polarizer is incident on a B_4C plate (12 inches long, 7.25 inches high and 0.07 inches thick). The plate is placed in the center of the detector such that the normal to the B_4C plate makes an angle of $45°$ with the axis of the beam. The setup is schematically shown in Fig. 4.3. The distances are measured from the inner surface of the downstream Al wall.
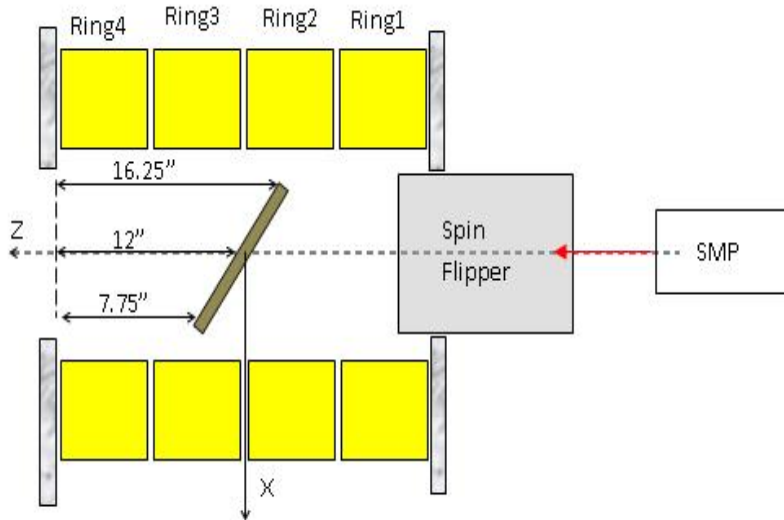
Figure 4.3: A cross section through the center of the detector and B_4C plate in the horizontal plane of the beam axis. The red arrow indicates the beam direction.

The detector signal is recorded in 40 time bins for each pulse. Because the frequency of the neutron pulses is 60 Hz, the time bin interval is $\Delta t_B = 0.417$ ms. The detector signal is therefore a function of the neutron time of flight t_F. For each time of flight the DAQ reads a detector signal that is the product of the number of neutrons $\Delta N(t_F)$ hitting the B_4C plate in a time bin interval Δt_B, the solid angle $\Omega_{B,i}$ of the detector, the energy of the gamma

59

radiation emitted from the neutron capture $E_{\gamma,B}$ and the detector gain (G_i).

Thus, the number of neutrons per pulse incident on the plate at the time of

flight t_F is the integral of the neutron flux spectrum over the time bin t_B and the

corresponding wavelengths, divided by 60 because there are 60 neutron

pulses in each second:

$$\frac{\Delta N(t_F)}{\Delta t_B} = \frac{\Delta N_\lambda}{60} = \frac{1}{60} \int_{t_F}^{t_F + \Delta t_B} \int_{\lambda(t_F)}^{\lambda(t_F + \Delta t_B)} \frac{d^2 N}{dt \cdot d\lambda} d\lambda dt \tag{4.8}$$

Because there are 40 time bins in each pulse, the detector signal is measured

for 40 neutron times of flight. The detector voltage V_B at a time of flight t_F is

equal with the product of the branching ratio (0.94) and the number of neutrons

hitting the B$_4$C plate per pulse, divided by the time bin interval:

$$V_B(t_F) = 0.94 \frac{\Delta N_\lambda}{60 \cdot \Delta t_B} \Omega_{B,i} E_{\gamma,B} G_i \tag{4.9}$$

The number of neutrons per second is related with the number of neutrons per

one time bin:

$$\frac{\Delta N_\lambda}{\Delta T} = \frac{\Delta N_\lambda}{\Delta t_B} \frac{\Delta t_B}{\Delta T} = \frac{\Delta N_\lambda}{\Delta t_B} \frac{1}{40 \cdot 60}. \tag{4.10}$$

The detector voltage in the presence of the B$_4$C plate is measured for each

time bin to calculate the neutron flux for each time bin:

$$V_B(t_F) = 0.94 \frac{40 \cdot 60}{60} \frac{\Delta N_\lambda}{\Delta T} \Omega_{B,i} E_{\gamma,B} G_i \tag{4.11}$$

4.2.2   The Cesium Source Method

In these measurements the ^{137}Cs source was placed on a 38 cm long Al bar at

about 0.64 cm downstream from the center of the detector array. The source

activity measured in 2002 was $5.2 \cdot 10^{-3}$ Ci. Because the half life for ^{137}Cs is

30.12 years, the source strength at the time of this experiment (July, 2011) is

$4.2 \cdot 10^{-3}$ Ci. The radioisotope ^{137}Cs with atomic number Z=55, undergoes

(100%) beta decay to ^{137}Ba with atomic number Z=56). The mean beta energy

is 187.1 keV and the most intense gamma ray (0.662 MeV) is emitted in a

transition that has a branching ratio of 94.7%. With a probability of 85.1% from

the total number of disintegrations, the 0.662 MeV gamma rays are emitted at

the transition of the excited Ba nucleus to its ground state. The detector signal

in the presence of the source is independent of the neutron time of flight and is

equal with the product of the branching ratio (0.851), the activity of the source

S, the detector gain G_i, the gamma rays energy and the solid angle $\Omega_{Cs,i}$:

$$V_{Cs} = 0.851 \cdot S \cdot E_{\gamma,Cs} \cdot \Omega_{Cs,i} G_i \tag{4.12}$$

The ratio of the two signals from the two methods is given by the ratio of

equations 4.12 and 4.11:

$$\frac{V_{Cs}}{V_B(t_F)} = 0.9053 \frac{S \cdot E_{\gamma,Cs}\Omega_{Cs}}{40 \frac{\Delta N_\lambda}{\Delta T} \cdot E_{\gamma,B}\Omega_B} \tag{4.13}$$

so that:

$$\frac{\Delta N_\lambda}{\Delta t} = 0.9053 \frac{V_B(t_F)}{V_{Cs}} \frac{S \cdot E_{\gamma,Cs}\Omega_{Cs}}{E_{\gamma,B}\Omega_B} \frac{1}{40} \tag{4.14}$$

The spectrum distribution of the neutrons (n/Å/s) can be obtained by

dividing the neutron flux per unit time (n/s) with the wavelength interval for one

time bin that can be calculated from the measured path length of the cold

neutron from the center of the H$_2$ moderator (just after the Hg target) to the

center of the detector L=17.58 m, the Planck constant $h = 6.626 \cdot 10^{-27}$ (erg $\cdot$

s) and the mass of the neutron $m = 1.6749 \cdot 10^{-24}$ (g), namely

$$\Delta\lambda = \frac{d\lambda}{dt}\Delta t_B = \frac{2\pi\hbar}{mL}\frac{1}{40 \cdot 60} = 0.0937 \cdot 10^{-8} c(m) \tag{4.15}$$

4.2.3   MCNP Simulations

In order to calculate the ratio $E_{\gamma,Cs}\Omega_{Cs}/E_{\gamma,B}\Omega_B$ Monte Carlo calculations were

done with the code MCNPX . The code calculates the energy deposition in

each detector divided by the mass of the detector and the number of source particles. For a model with the Cs source the code tracked only the photons and all the photon cross sections libraries were used. The calculations were done for a point source placed in the center of the detector array and also displaced by 0.5, 1, 1.5, 2 and 2.5 cm downstream along the beam axis. The agreement of the measured detector signal and the calculated energy deposition is better for an offset of about 2.5 cm. For the model with the B_4C plate the trajectories of both neutrons and photons were calculated and the neutron cross sections were used. In the MCNPX model the neutrons were emitted at the exit of the SMP. The lead walls, polarizer, Al flange between the lead walls, the concrete blocks and the two monitors were not modeled. The flux in the center of the detector from the B_4C plate has to be normalized to the number of neutrons that hit the plate. By default the energy deposition tally is normalized to the number of primary neutrons N_s generated in the code. For the calculation of the neutron flux at the B_4C plate, it was necessary to calculate the energy deposition per number of neutrons captured in the plate (N_c).

$$E\left(\frac{MeV}{g \cdot N_c}\right) = E\left(\frac{MeV}{g \cdot N_s}\right)\frac{N_s}{N_c} \qquad (4.16)$$

The energy deposition in the detectors was also calculated in MCNP for a 0.662 MeV gamma point source placed in the center of the detector array. From the MCNP model of the B_4C plate, the energy of the gamma rays deposited in the detectors was calculated for four neutron energies (4, 8, 10 and 14 meV) and for the 0.014 rad divergence of the beam, as calculated in McStas [66]. The number of neutrons captured in the plate divided with the number of source neutrons emitted is between 0.83 and 0.87 depending on the neutron energy (from 4 meV to 14 meV). From the same model but without the

B$_4$C plate, the expected background due to the gamma rays emitted from the Al stand or SR windows was calculated.

In each ring with 12 detectors there are four lateral detectors: 2 on the left and 2 on the right of the beam. For example in the first ring (figure 3.7) the beam-right and beam-left lateral detectors are (2, 3) and (8, 9) respectively. Therefore there are eight pairs of lateral detectors for all four rings of detectors. The flux was calculated from the signal of the 8 lateral detectors located on beam-right (2, 3 ,14, 15, 26, 27, 30, 31) and 8 detectors on beam-left (8, 9, 20, 21, 32, 33, 44, 45) because for these detectors the flux of the gamma rays emitted at the neutron capture in the B_4C target is maximum.

The MCNP calculations were used to estimate the ratio of the gamma rays energy deposition in each detector with and without the B$_4$C plate, and in the presence of the Cs source placed on the detector axis. The energy deposition in a detector without the B$_4$C plate is the calculated background. The average energies deposited in the lateral detectors are calculated for five initial energies of the neutron (4, 6, 8, 10 and 12 meV), for a model with and without the B$_4$C plate located in the center of the detector array (the green and the red curve respectively in Figure 4.4). Their difference of the gamma ray energy lost in the detectors with and without the plate ($E_2 - E_1$) is the gamma rays energy deposition due to the neutron captured on the B$_4$C plate.

To compare the calculation of the flux in the center of the detector with the flux at the exit of the beam guide, the neutron transmission through the materials located between the exit of the guide and the center of the detector was calculated from MCNPX. The transmission factors through the two monitors (M1 and M2), 2 meters of air and the SR are 0.97, 0.97 , 0.25, 0.9
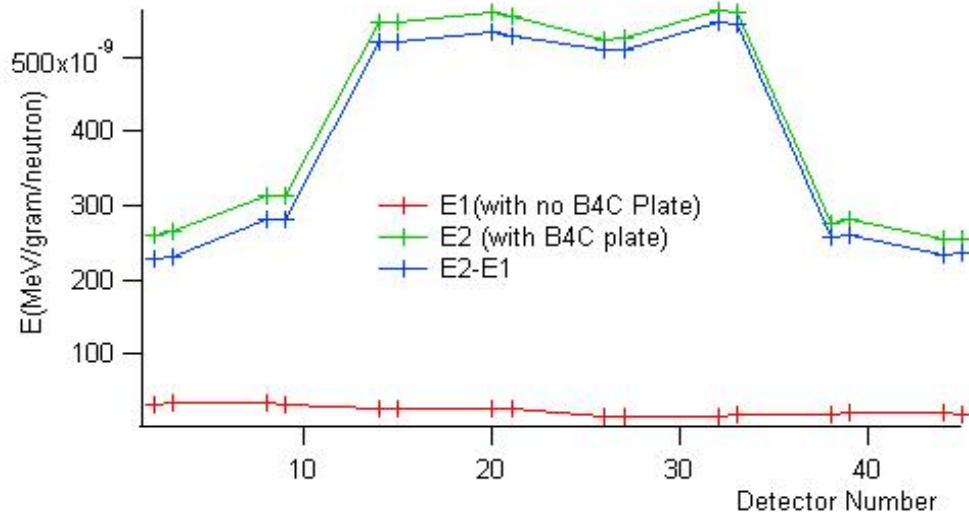
Figure 4.4: The average gamma ray energies deposited in each pair of lateral detectors is calculated for five neutron energies, for a model with and without the B$_4$C plate (E_2 and E_1 respectively).

and 0.99, respectively. With no collimator in the front of the SR only 0.5% of the neutron beam flux is absorbed in the Lithium sheet with a rectangular hole 16×16 cm ^{2}, placed on the entrance window of the SR at 102 cm from the exit of the polarizer. According to the McStas [66] calculations this rectangular hole decreases the flux of the neutron beam with only 0.5%. The area of the beam at the exit of the SMP is 120 cm^2. From the measured beam divergence in the x and y directions $11 \cdot 10^{-3}$ rad and $14 \cdot 10^{-3}$ rad respectively, the beam profile in the vertical plane of the SR entrance window was calculated in McStas [66]. The beam profile calculations with boundaries defined by the projected surface of B$_4$C plate in the vertical plane normal to the beam (8.48×7.25) inch^2 proved that about 0.6% of the beam flux passes above, below or around the lateral sides of the plate.

The relative transmission of the neutrons through the monitor was calculated in MCNPX from a tally of the number of neutrons passing through

the entrance and exit windows of the monitor. The dependence of the transmission on the neutron wavelength comes from the neutron energy dependence of the ^{3}He cross section.

$$T_1 = 0.99216 - 0.011705\lambda \qquad (4.17)$$

$$T_2 = 1.0039 - 0.007744\lambda \qquad (4.18)$$

The transmission through the air depends only weakly on the neutron wavelength. For a distance d measured in cm, the average transmission for neutrons with energies from 3 meV to 13 meV is equal with:

$T_3 = 100 - 0.03 \cdot d \quad (\%)$

The number of neutrons captured in the two monitors normalized to the number of source neutrons generated in MCNP is calculated for different wavelengths in Figure 4.5. The transmission of the neutrons through the two monitors can be seen in figure 4.6.

In the MCNPX model the detector center is at 242 cm distance from the exit of the first monitor. The distance from the exit of Monitor 1 and the entrance of Monitor 2 is 51 cm. The center of the detector is at 180 cm from the exit of the CM and the Polarizer such that the transmission through the air is 94.6%. The decrease in the neutron flux due to the Lithium sheet and the Al windows of the SR is 2%. To calculate the neutron transmission through the SR, the number of the neutrons passing through the entrance and the exit surfaces of the SR were recorded in MCNP for three neutrons energies. The thickness of the SR windows is 1 mm and the front thin window is covered on both sides with Lithium sheet that has a square opening (16 cm $\times$ 16 cm). The SR copper coils are winded on the surface of a plastic (polyethylene) hollow
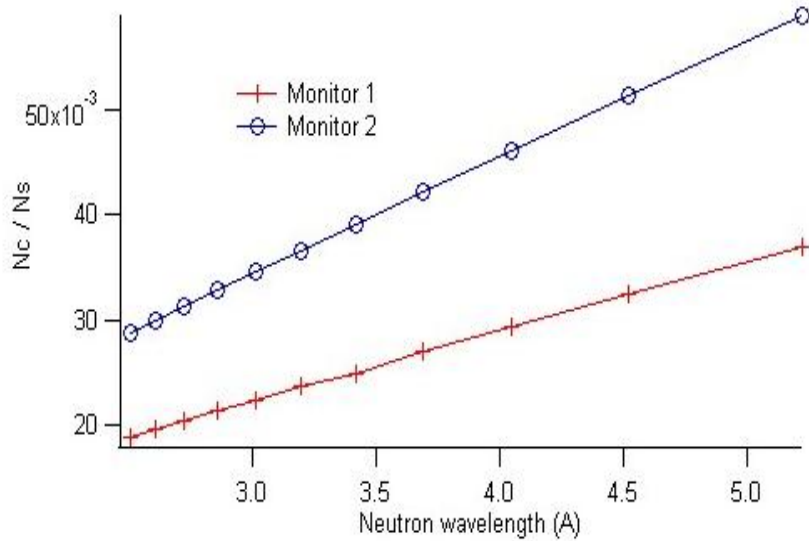
Figure 4.5: The number of neutrons captured in the two monitors (M1, M2) divided with the number of source neutrons is calculated versus the wavelength.
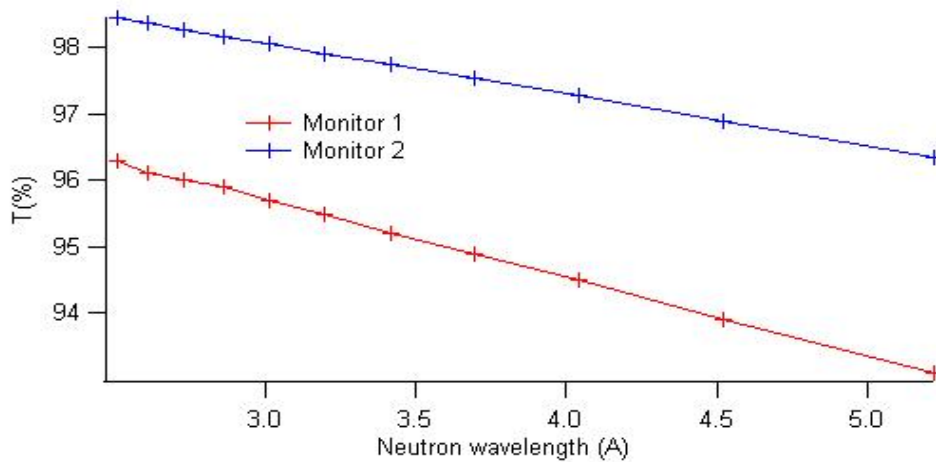
Figure 4.6: The transmission of the neutrons through the two monitors is calculated for neutrons wavelengths from 2.5 to 5.5 Å.

cylinder with inner radius 11.8 cm. The inner surface of the plastic cylinder is covered with Lithium sheet 0.32 cm thick. The composition of the Lithium sheet in the model was $^{6}Li_3$ (27%), $^{12}C_6$ (15.9%), $^{16}O_8$ (20.86%) $^{1}H_1$ (4.18%), Si (27.88%), Zn (0.15%) and $^{7}Li_3$ (3%). The exit window of the SR is in contact

with a Lead cylindrical wall with radius 21.7 cm and a square hall with dimensions 21.82 cm × 21.91 cm. The transmission of the neutron beam from the entrance window of Monitor 1 to the end of the detector stand is calculated in MCNP for four neutron energies and presented in Figure 4.7. The neutron transmission is the ratio of the neutrons crossing a surface normal to the beam and the number of source neutrons generated in the code.
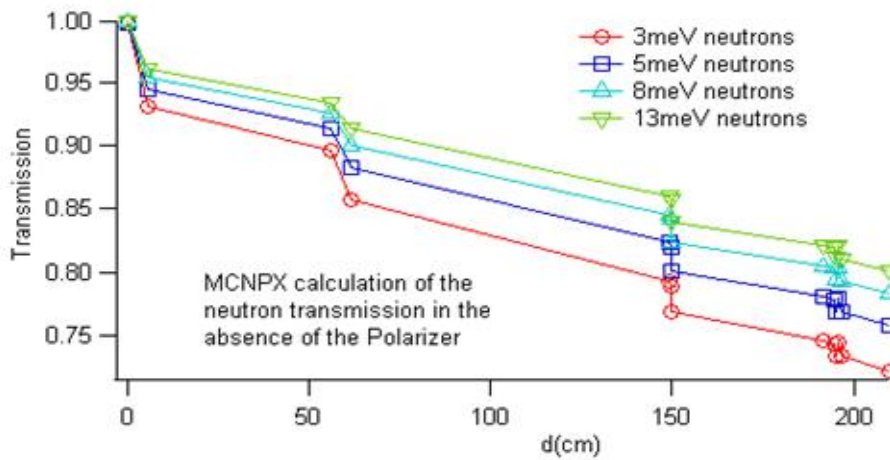
Figure 4.7: The neutron beam transmission is calculated along the neutron beam axis from the entrance in the first monitor (d=0.4 cm) to the center of the detector (d=221 cm) for four neutron energies.

The total transmission is the ratio of the neutrons crossing the vertical surface through the center of the detector and the total number of neutrons generated. In the absence of the SMP the total transmission calculated in MCNP is 80% for 13 meV neutrons and 75% for 5 meV neutrons. For neutron wavelength in Å, the total transmission depends almost linearly on the neutron wavelength:

$$T = 0.8755 - 0.02938 \cdot \lambda \tag{4.19}$$

67

4.2.4 Neutron Flux and Transmission Results

The detector signals were measured in the presence and in the absence of the B_4C plate placed at the center of the array , at $45°$ relative to the beam axis. The corrected detector signal is the difference between the signal measured with the B_4C plate and in the absence of the plate. The ratio of the corrected detector signal measured with the B_4C plate and with the Cs source was calculated.
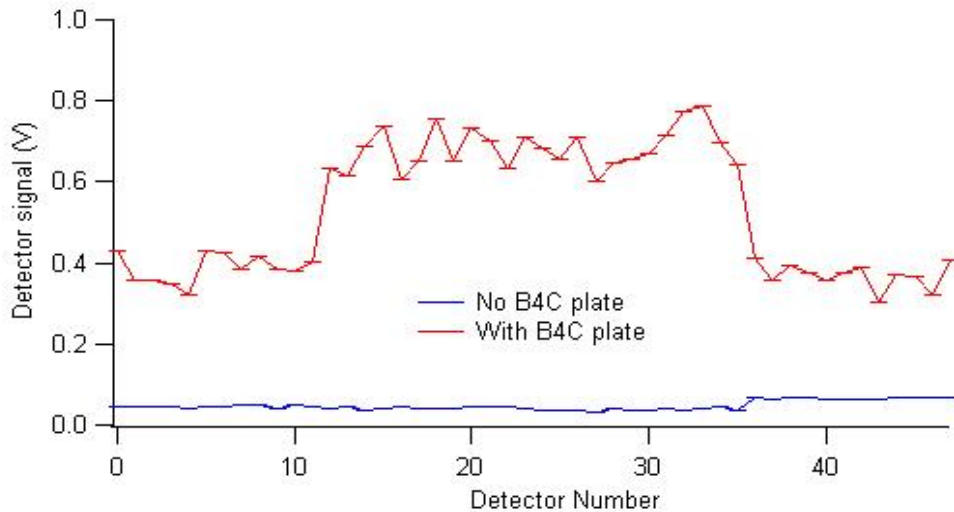
Figure 4.8: The detector signals averaged over runs and all time bins in a spin sequence, was measured in the presence of the B_4C plate (10 runs, red curve) and without the plate (3 runs, blue curve).

The 48 detectors signals were measured for 10 runs, each run had 2500 spin sequences (see FIg. 4.8). The background is the detector signal measured in the absence of the B_4C plate for three runs with the same length (blue line).The average detector signals in the absence of the B_4C plate were subtracted from the average detector signals measured with the plate. There was no collimator in front of the SR. The measurements for both Cs source and

68
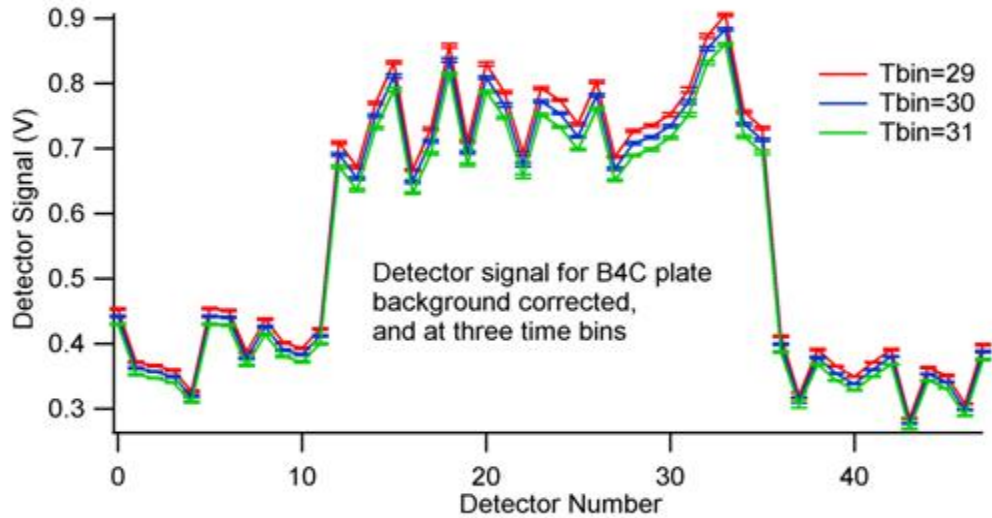
Figure 4.9: The difference between the 48 detector signals measured with and without the B_4C plate, for three time bins (29, 30, 31).

B_4C plate were done for the same detector gains.

For all runs the pedestal is calculated from the detector signals during a missing pulse that occurs when a proton pulse is not delivered to the Hg target but is dumped such that no neutrons are produced. The average detectors voltage was calculated for each of the 40 time bins in a pulse and for all the missed pulses in a run to get a run average pedestal. The average pedestal was subtracted from the beam-on detector voltages. The average of detector signals for the three runs with beam off is the background due to the gamma rays coming mostly from the Al wall. The background corrected detector signal for three time bins (29, 30, 31) is the difference between the detector signals measured with and without the B_4C plate, at these time bins (Fig. 4.9).

The detector signals were recorded for the Cs source placed in the center of the detector array. The measurements were done 10 times with the Cs source and 11 times in the absence of the source. The 11 pedestal

69
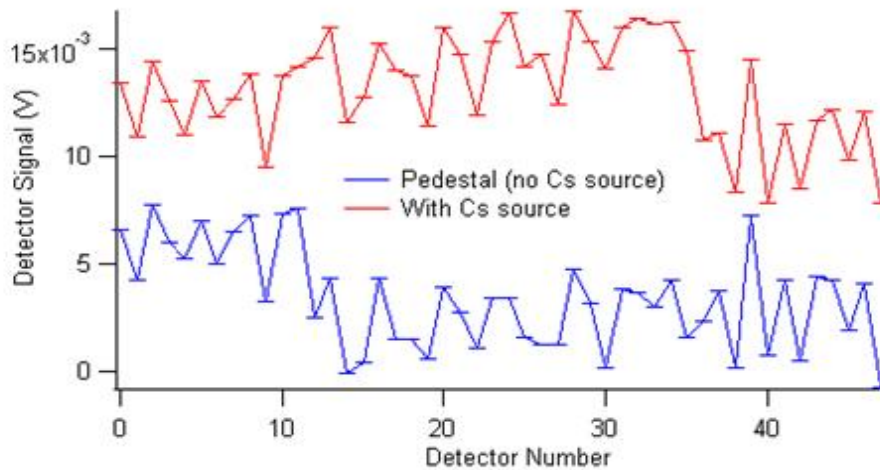
Figure 4.10: The average detectors signals with the Cs source (red curve) and in the absence of the Cs source (blue curve) versus the detector number.

measurements were done with no Cs source before and after each measurement with Cs source. The detector signals with the source, averaged over 10 runs, and in the absence of the source, averaged over 11 runs, are presented in Figure 4.10.

The detector signal, background corrected, for a Cs source placed in the center of the detector array, Figure 4.11, shows slight bigger detector signals in ring 4 (detectors 36 to 47) compared to ring 1 (detectors 0 to 11).

This difference is related to the average offset in the position of the Cs source along the direction of beam axis relative to the center of the detector array. For 1.5 cm displacement in the position of the Cs source, in the direction of the beam and downstream from the detector center, the calculated data agrees better with the measurements.

The flux in neutrons/ second is calculated from the average of the detector signal over all 40 time bins in a pulse with B_4C plate and Cs source

70
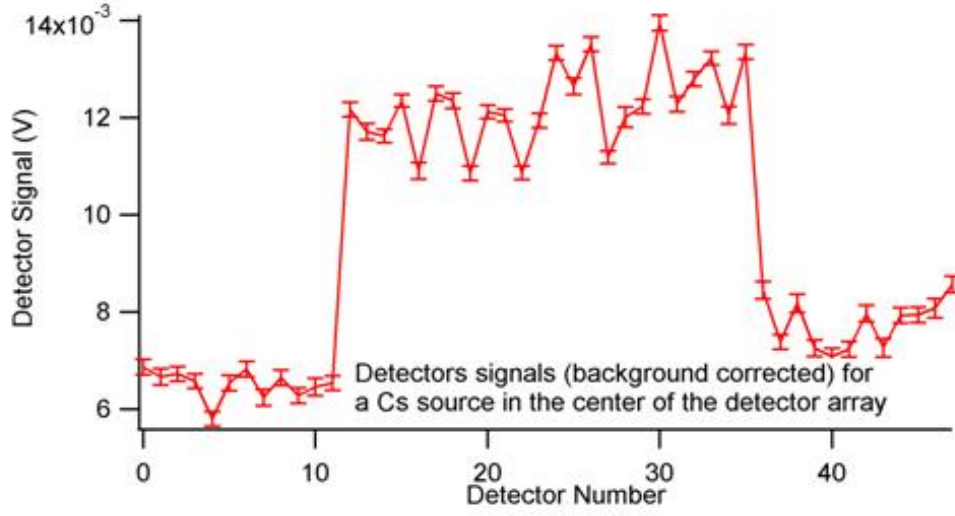
Figure 4.11: The detector signals background corrected for a Cs source placed in the center of the detector array.

according to the equation 4.14. From the ratio V_B/V_{Cs} the average neutron flux (over the 40 time bins) is calculated with the source strength S=$4.2 \cdot 10^{-3}$ Ci =$15.54 \cdot 10^7$ (1/s), E_g = 0.662 MeV, E_B=0.48 MeV and Ω_B= Ω_{Cs} in the relation:

$$F_0' = \frac{1}{N_B} \sum_{i=1}^{N_B} \frac{0.9053}{40} \frac{v_{B,i}}{v_{Cs}} \frac{S E_{\gamma,Cs} \Omega_{Cs}}{E_{\gamma,B} \Omega_B} = 4.85 \cdot 10^6 \frac{\{v_B\}}{v_{Cs}} \tag{4.20}$$

The ratio of the energies deposited in each detector can be calculated in MCNPX for the B$_4$C plate and for the ^{137}Cs source E(Cs)/ E(B). This ratio enters in the calculation of the neutron flux:

$$F_0 = 0.9053 \frac{\{v_B\}}{40 \cdot v_{Cs}} \frac{S \cdot E(Cs)}{E(B)} \tag{4.21}$$

$$F_0 = 1.407 \cdot 10^8 \frac{\{v_B\}}{40 \cdot v_{Cs}} \frac{E(Cs)}{E(B)} \tag{4.22}$$

The relation between the time bin and the neutron wavelength can be calculated from the de Broglie relation and the time (t_s=10.68 ms) spent by the fastest neutron (with wavelength λ_S) to travel the distance L=17.56 m from the

71

H_2 moderator to the center of the target. Consider the time t measured from the start of the data acquisition frame and t_B the bin number (from 0 to 40). The relation between wavelength and the time bin becomes:

$$\lambda = \frac{h}{mL}(t + t_d) = \frac{h}{mL}(t_B \cdot 0.0004166 + t_d) \tag{4.23}$$

The wavelength of the fastest neutrons that are not cut by the chopper is equal with:

$$\lambda_S = \frac{h}{mL}t_d = 2.4 \ \overset{o}{A} \tag{4.24}$$

$$\lambda = \lambda_S \left(\frac{t_B}{0.01068} 0.0004166 + 1 \right) = \lambda_S (0.039t_B + 1) \tag{4.25}$$

To calculate the flux of neutrons per unit area, unit time and Å, the wavelength correspondence for one time bin can be calculated:

$$d\lambda = 0.0937 \cdot dt_B \tag{4.26}$$

Therefore dividing the neutron flux (n/s) with the wavelength width of one time bin 0.0937Å, one can calculate the flux per unit time and per neutron wavelength.

In table 4.1, the flux is calculated for time bins 29, 30 and 31 or neutrons with wavelengths from 5 Å to 5.2 Å, for each of the lateral detectors in rings 2 and 3. The MCNPX calculations are done for a 2.5 cm offset of the ^{137}Cs source downstream from the center of the detector array. The flux F_0' was calculated with equation 4.20. The flux F_0 was calculated from MCNPX calculations of the ratio of the energies deposit in the detector in the presence of the ^{137}Cs source or the B_4C plate. The flux per unit time and wavelength $F'_{\lambda,0}$ and $F_{\lambda,0}$ are calculated by dividing the flux intensity F_0', F_0 with area of the beam at the center of the detector (320 cm^2) and with the wavelength interval for a time bin (0.0916 Å). The beam power was 0.82 MW.

Table 4.1: The ratio of the lateral detector signals measured with B_4C plate (V_B) and with ^{137}Cs source (V_{Cs}) is averaged for three neutron wavelengths (5, 5.1, 5.2Å).

Det#	Ring	V_B/V_{Cs}	F_0' (n/s) 10^8	$F_{\lambda,0}'$ n/s/Å 10^9	E_{Cs}/E_B D=2.5 cm	F_0 (n/s) 10^8	$F_{\lambda,0}$ n/s/Å 10^9
14	2	87.8	4.26	4.63	1.33	4.11	4.46
15	2	87.7	4.25	4.62	1.32	4.08	4.43
20	2	86.6	4.20	4.57	1.30	3.95	4.29
21	2	82.6	4.01	4.36	1.29	3.76	4.09
26	3	88.9	4.31	4.69	1.52	4.77	5.18
27	3	90.1	4.37	4.75	1.49	4.73	5.15
32	3	94.0	4.56	4.96	1.41	4.65	5.05
33	3	93.5	4.54	4.93	1.40	4.60	5.00

From the measured detector signals and the MCNPX calculation of the ratio of the energy deposition with the ^{137}Cs source and the energy deposition with the B_4C plate, the flux per unit time, unit wavelength and 5.1 Å neutrons, averaged over the eight lateral detectors in rings 2 and 3 is equal with:

$$F_0' = (4.71 \pm 0.15) \cdot 10^9 (\text{n/s Å}) \text{ for } \lambda_n = 5.1 \text{ Å} \tag{4.27}$$

For each of the 40 time bins in a neutron pulse, the ratio of the detector signal measured with a B_4C plate and the detector signals measured with a ^{137}Cs source placed in the center of the detector array was calculated. The measurements of the pedestal were done before and after each measurement with the ^{137}Cs source. The ROOT NPDGamma libraries [67] were used to read the binary data in trees and branches. The detector signal was read first for all dropped pulses in a run to calculate the pedestal for each time bins. The "dropped" pulse is detected if the time average of the monitor 2 (M_2) signal for a pulse is smaller than 0.25 Volts. For each pulse with beam on and for each time bin the pedestal was subtracted from the beam-on detector signal. The

final mean and the error of the mean over all the runs were calculated for each time bin and for the lateral detectors. The ratio of the detector signals for a B_4C plate and a ^{137}Cs source placed in the center of the detector is presented in Figure 4.12 for the lateral detectors in ring 2 and 3. The deeps in the plot occur at the Al Bragg edges (4.0 Å and 4.6 Å) where the neutron scattering cross section increases.
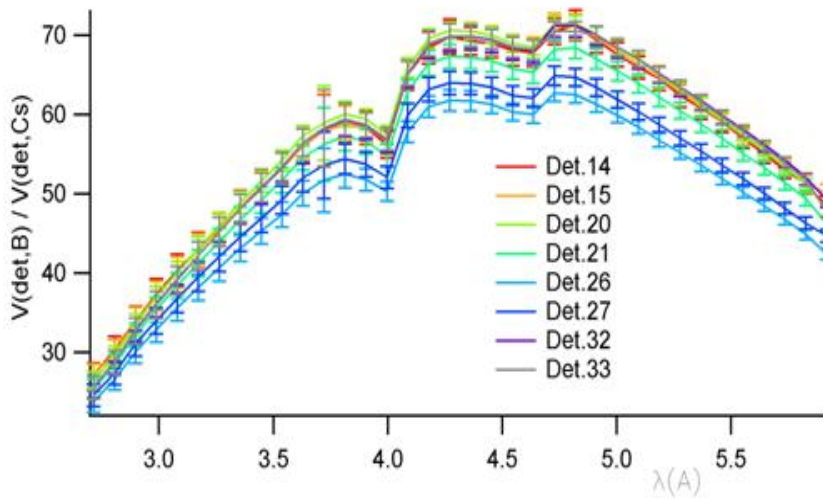
Figure 4.12: The ratio of the detector signals measured with a B_4C plate and a ^{137}Cs source placed in the center of the detector is calculated for wavelengths between 2.7 Å and 5.9 Å.

The neutron flux was calculated from detector signals for each time bin and the MCNPX calculation of the energy deposition in the detectors for a ^{137}Cs and a B_4C plate according to the relation:

$$F_{0,I} = \frac{S \cdot 0.85}{0.94} \frac{V_{B,I}}{V_{Cs,I}} \frac{\langle E_{Cs,I}\Omega_{Cs,I}\rangle}{\langle E_{B,I}\Omega_{B,I}\rangle} \frac{1}{40} \tag{4.28}$$

The average of these eight values of the neutron per unit time and wavelength is calculated for each neutron wavelength inside the useful range in Figure 4.13. The neutron flux spectrum per unit time, area, wavelength and beam

power, for neutrons with wavelength between 2.7 Å and 5.9 Å , or time bins from 6 to 36, can be seen in Figure 4.14.
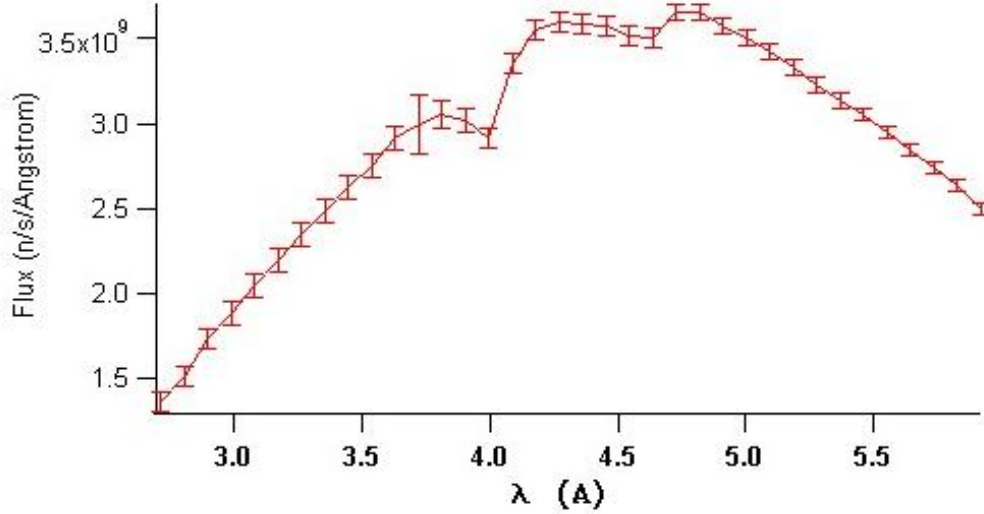
Figure 4.13: The neutron flux spectrum is calculated per neutron wavelength and unit time for neutron between 2.7 Å and 5.9 Å, from the measured detector signals with ^{137}Cs source and B_4C plate.

The average flux per unit time can be calculated from the neutron flux versus time bin by summing the fluxes for each time bin and dividing with the number of time bins (N=36 for these calculations).

$$\bar{F} = \frac{1}{N} \sum_i F(\lambda_i) = \frac{(9.6 \pm 0.03) \cdot 10^9}{36} = 0.27 \cdot 10^9 (\text{n/s}) \qquad (4.29)$$

All these results can be used to compare the flux measurements at the end of the beam guide with the flux measured in the center of the NPDGamma detector with the ^{137}Cs source and B_4C plate (Figure 4.15). Because the effective cross section area of the beam in the center of the detector is not known, the flux measured at the exit of the guide was multiplied with the cross section area of the polarizer, 120 cm^2, such that both fluxes in this figure are in units of n/s/Å/MW.

75
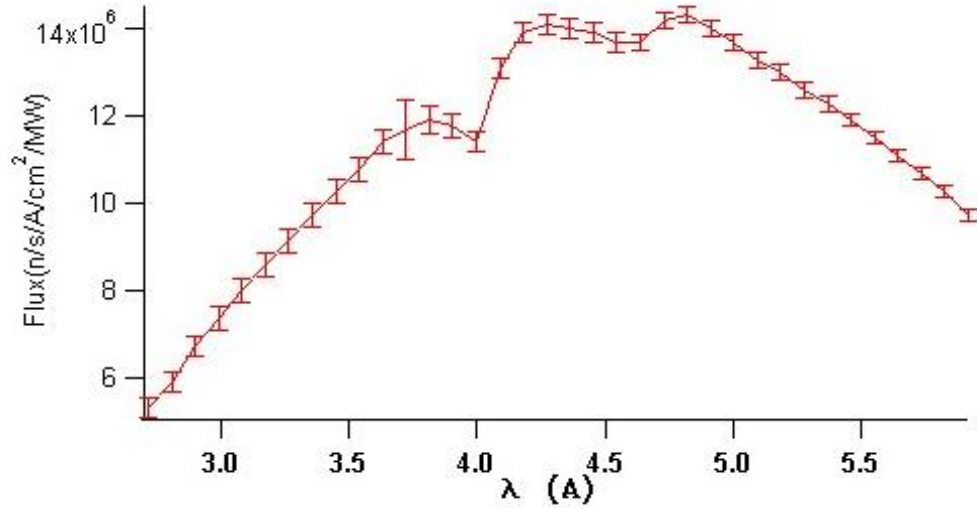
Figure 4.14: The neutron flux spectrum per neutron wavelength, area, time and beam power is calculated for 2.7 Å to 5.9 Å neutrons, from the detector signals measured with ^{137}Cs source and B$_4$C plate.

The ratio of the two fluxes and the MCNP calculation of neutron transmission through the two monitors, air and SR, was used to calculate the neutron transmission T_P through the polarizer (SMP) for wavelengths between 2.6 and 6.0 Å (see table 4.2 and Figure 4.16). In table 4.2 the transmission of the SMP is calculated from the ratio of the neutron fluxes in the center of the detector array (ϕ_2) and at the exit of the beam guide (ϕ_1).

$$\frac{\Phi_2}{\Phi_1} = T_1(\lambda) \cdot T_P \qquad (4.30)$$

The average transmission of the polarizer is 25.8% in agreement with the McStas calculations [66].
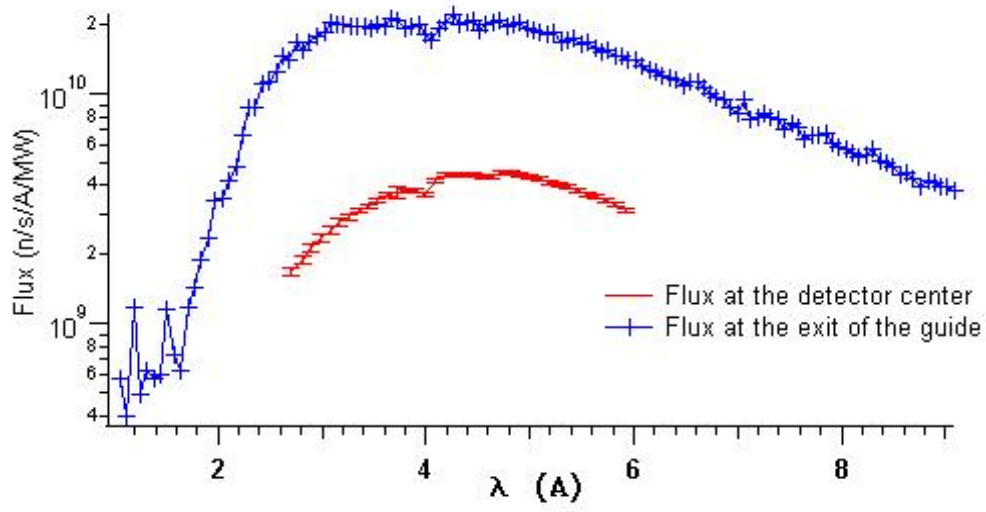
Figure 4.15: The neutron flux spectrum measured at the exit of the beam guide (the blue curve) and at the center of the detector (red curve).

Table 4.2: The transmission of the neutrons T1 in the absence of the SMP, calculated in MCNPX, versus neutron wavelength.

λ Å	Φ_2 / Φ_1	T_1	T_P
2.77	10.56	0.781	0.135
3.16	14.184	0.769	0.184
3.48	16.173	0.759	0.213
4.20	20.416	0.737	0.277
4.98	22.17	0.712	0.311
5.50	22.81	0.696	0.328
6.28	24.34	0.671	0.363

4.3   Beam Profile Measurements

The beam profile was measured by using two Cadmium (Cd) pinholes and a [6]Li glass detector connected to a photomultiplier tube [68]. The neutrons are captured in [6]Li and produce alpha and tritium particles, with 4.8 MeV energy release. Each of the two particles deposit their energy in the scintillator material and the light of the scintillator is detected in the PMT. The first pinhole
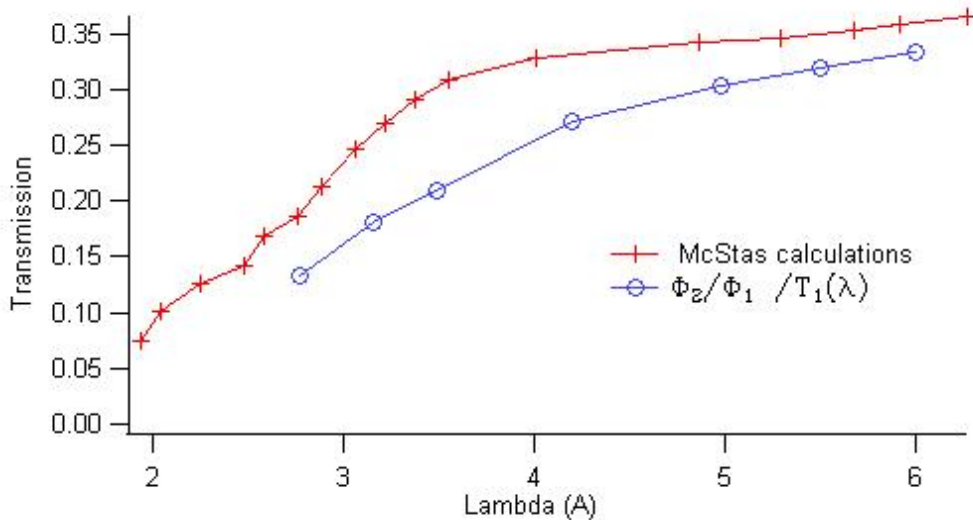
Figure 4.16: The transmission of the SMP is calculated from the ratio of the flux in the center of the detector and at the exit of the beam guide, divided with the transmission through the monitors, air and SR.

(0.58 cm radius) was installed in front of the SR at 45 cm upstream from the detector shield and at 1.5 inches below the beam axis. The second pinhole (0.07 cm radius) was located just in front of the ^{6}Li detector that was mounted with the PMT tube on the XY scanner placed in front of the Beam Stop at 144 cm from the end of the detector shield (Figure 4.17). The areas of the pinholes were measured with a high resolution scanner. The data were taken with counting electronics coupled to the NPDGamma data acquisition. The photo-multiplier tube was connected to a group of high pass and low pass filters, a discriminator, a logic gate and a counter.The beam profile measurements were used to calculate the neutron flux at the beam stop.

The counts were measured first for a translation of the ^{6}Li detector in the x direction (Figure 4.18) and then along the y direction at the x-position of the peak (Figure 4.19). In these figures the distances are measured in the local coordinates of the scanner with the origin at the center of the scanner's
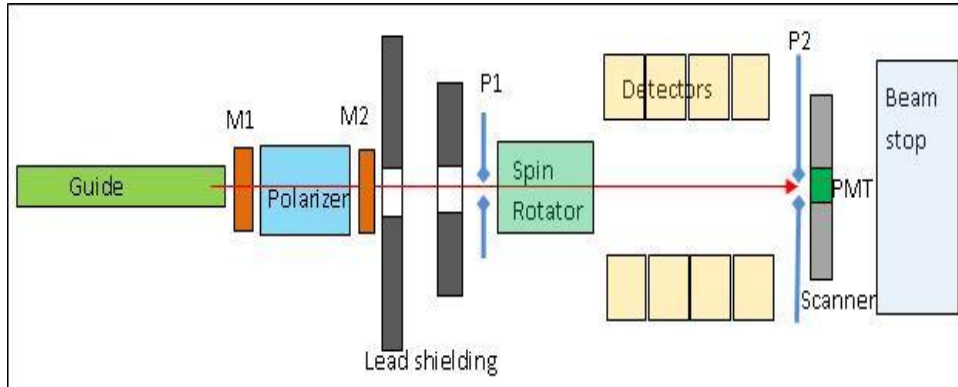
Figure 4.17: The experimental set-up for the beam profile measurements.

travel. The beam profile along the y direction has two peaks. The structure in the y scan was supposed to be caused by the incomplete opening of the shutter and the location of the first pinhole at 3.81 cm below the beam center coupled with a displacement in the neutron moderator with 1 cm in the vertical direction. When the shutter is completely open the angle of the shutter blade edge relative to the vertical axis is $0°$. This angle is not zero when the shutter is not completely open. The beam profile was calculated by modeling the geometry of the BL13 beam guide in McStas [69] for different rotation angles of the shutter located at 11 m downstream from the target. For a shutter rotation angle of $5°$ the distance between the peaks in the simulated and the measured beam profile are about the same. However because the tolerance in controlling the angle of the shutter when it is fully open is smaller than $0.5°$, such big misalignment angle was ruled out.

The first pinhole decreases the raw neutron flux measured in neutrons per second with a factor equal with the ratio of the areas of the pinhole 1 and the neutron beam guide $A_g = 120$ cm^2. The areas of the first and second pinholes are $A_1 = 0.529 \pm 0.007$ cm^2 and $A_2 = 0.0077 \pm 0.0004$ cm^2 respectively. If F_0 and F_1 are the neutron fluxes before and after the pinhole 1

79
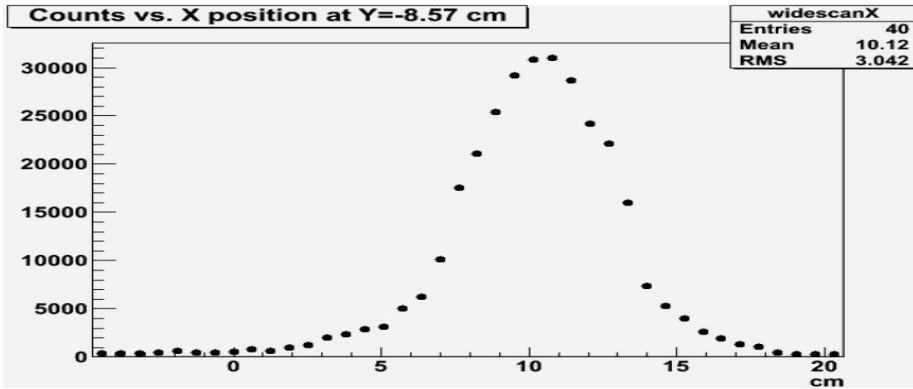
Figure 4.18: The neutron beam profile measured along the x direction. The origin is at the center of the scanner's travel.
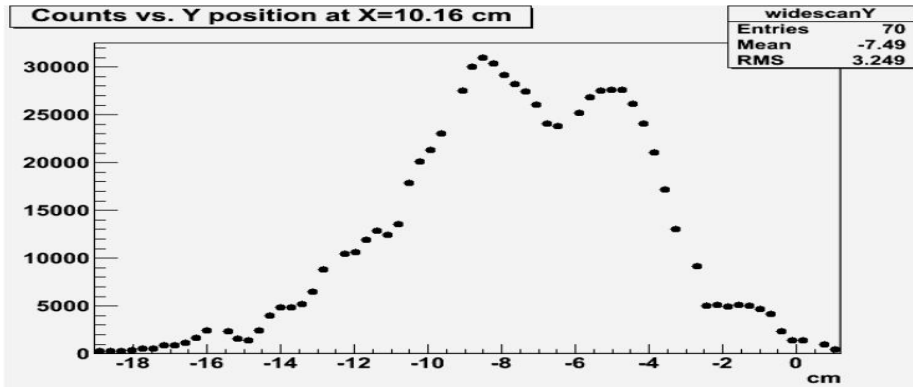
Figure 4.19: The neutron beam profile measured along the y direction. The origin is at the center of the scanner's travel

then one can write the relation:

$$F_0 = \frac{A_g}{A_1} F_1 \tag{4.31}$$

The flux after the second pinhole F_2 is measured at the position of the ^{6}Li glass detector for different positions for the scanner. The ratio of the fluxes after and before the second pinhole, F_2/F_1, is equal with the product of the integrated areas under the x and y scanning histograms $S_x \cdot S_y$ and the product of the scanning steps $\Delta x \cdot \Delta y$, divided with the product of the pinhole 2 area A_2 and the number of peak reading (counts/s) m_0. The logic gate received a signal T_0

for each proton pulse that was delivered in the Hg target. Each point in the histogram is a reading of the counter after 999 T_0 signals. The number of counts were divided by 60 to get the number of counts for one neutron pulse. The step sizes along the two directions were $\Delta x = 1/4$ (inches) and $\Delta y = 1/8$ (inches).

$$F_0 = \frac{A_g}{A_1} F_1 = \frac{A_g}{A_1} \frac{S_x \cdot S_y \cdot \Delta x \Delta y}{A_2 \cdot m_0} \tag{4.32}$$

According to this formula the calculated neutron flux was $(2.78 \pm 0.18)10^9$ (n/s) at 800 kW power, in the wavelength range 4.26 Å to 5.26 Å. With the expected attenuation of the neutron beam in air (25%), beam monitors M1 (2.44%), M2 (1.7%) the discriminator level (7.9%) and detector efficiency (0.1%) the calculated neutron flux at the exit of the Polarizer was $(5.7 \pm 0.37) \cdot 10^9$ (n/s/MW). To calculate the polarizer transmission this result is divided with the flux measured at the exit of the beam guide $2 \cdot 10^{10}$ (n/s/MW). The ratio of the neutron flux after and before the Polarizer is 28% as expected for the Polarizer transmission for neutrons in the above wavelength range.

4.4 Measurement of the Neutron Polarization through Transmission

The polarization of the neutron beam was measured by transmission through a Helium cell. After passing through the Helium cell the neutrons were captured in the B_4C plate at the entrance of monitor M_3, producing gamma rays that were detected in a CsI crystal inside the same monitor, after the plate. The CsI crystal was optically coupled with the B_4C plate. The M_3 signal was measured for each time bin. Monte Carlo calculations of the energy of the gamma rays deposited in the CsI crystal per incident neutron were performed to calibrate the M_3 monitor. To derive the relation of the neutron polarization let's consider that a neutron beam with cross section A is incident on a ^{3}He cell with

81

thickness dx and N_+ and N_- the numbers of neutrons with spin up and down, passing through area A in unit time. The beam polarization is given by:

$$P_n = \frac{N_+ - N_-}{N_+ + N_-}$$ (4.33)

The polarized neutron beam can be described by a two dimensional vector [70, 71]. The components of the vector are the relative number of neutrons in the two polarization states:

$$|B_{pol}\rangle = \begin{pmatrix} 1 + P_n \\ 1 - P_n \end{pmatrix}$$ (4.34)

For a completely unpolarized beam the two dimensional vector $|B_0\rangle$ is obtained from the above relation with P_n=0. The neutrons are polarized by passing through the channels between two thin glass films of the SMP. Only the neutrons with spin direction parallel with the direction of magnetization in the Fe/Si films on the surface of the glass films can pass through the SMP. If P_{SM} is the SMP polarization efficiency then the effect of SMP on the neutron spin state can be described with the matrix:

$$B_{SM} = \begin{pmatrix} 1 + P_{SM} & 0 \\ 0 & 1 - P_{SM} \end{pmatrix}$$ (4.35)

The off diagonal terms related with the neutron spin flip in the polarizer are very small. The neutron beam incident on the SMP is not polarized. The polarization of the beam after passing through the SMP is equal with

$$B_{SM}|B_0\rangle = \begin{pmatrix} 1 + P_{SM} \\ 1 - P_{SM} \end{pmatrix}$$ (4.36)

In the NPDGamma experiment the neutron beam also passes through a SR that rotates the spin with $180°$ for each neutron in the beam. If ε is the SR

efficiency then the SR efficiency matrix is given by:

$$P_{sf} = \begin{pmatrix} 1 - \varepsilon & \varepsilon \\ \varepsilon & 1 - \varepsilon \end{pmatrix} \tag{4.37}$$

The polarization state of the neutron beam after passing through the SMP and SR is given by:

$$P_{sf}B_{SM}|B_0\rangle = \begin{pmatrix} 1 + P_{SM}(1 - 2\varepsilon) \\ 1 - P_{SM}(1 - 2\varepsilon) \end{pmatrix} \tag{4.38}$$

The ^{3}He cell is placed in a magnetic field aligned with the vertical direction. Consider n the total concentration of ^{3}He atoms in the cell and n_1 , n_2 the concentration of the atoms with spin up and down respectively. The cross sections of the ^{3}He atoms with spins parallel and opposite to the neutron spin are σ_1 and σ_2 respectively. The thermal cross section for ^{3}He and neutron with parallel spins is essentially negligible compared with the cross section for the two particles with opposite spins (10,666 b at neutron speed 2200 m/s) [72]. The neutron beam was polarized in the vertical direction of the field with the neutron spin pointing up. In this case the decrease in the flux of neutrons incident on polarized ^{3}He cell is proportional with the concentration if ^{3}He with spin down (n_2), with their cross section σ_2 and with the thickness of the cell dx in the direction of the beam:

$$\frac{dT_+}{T_+} = -n_2\sigma_2 dx \tag{4.39}$$

Depolarized ^{3}He has equal number of atoms with spin-up and spin-down. The average cross section of depolarized ^{3}He for a completely polarized neutron beam is equal with:

$$\sigma = \frac{\sigma_1 + \sigma_2}{2} \cong \frac{\sigma_2}{2} \tag{4.40}$$

83

The polarization of the ^{3}He is given by the equation:

$$P_{He} = \frac{n_1 - n_2}{n_1 + n_2} \tag{4.41}$$

The transmission of the spin-up neutrons that passed through a cell of thickness l can be calculated after integration of equation 4.39.

$$T_+(l) = T_+(0) \exp(-n\sigma(1 - P_{He})l) \tag{4.42}$$

$$T_-(l) = T_-(0) \exp(-n\sigma(1 + P_{He})l) \tag{4.43}$$

The relative numbers of the spin-up and spin down neutrons incident on the ^{3}He cell are equal with:

$$T_\pm(0) = \frac{N_\pm}{N} \tag{4.44}$$

The transmission of a neutron beam through the ^{3}He cell is related with the polarization of the beam (P), the cell polarization (P_{He}) and transmission through the empty cell T_g:

$$T(l) = T_g \left[\frac{1 + P_n}{2} \exp(-n\sigma(1 - P_{He})l) + \frac{1 - P_n}{2} \exp(-n\sigma(1 + P_{He})l) \right] \tag{4.45}$$

$$T(l) = T_g e^{-n\sigma l} \left[\cosh(n\sigma l P_{He}) + P_n \sinh(n\sigma l P_{He}) \right] \tag{4.46}$$

For the calculation of the neutron polarization, the transmissions of the neutron beam through depolarized ^{3}He cell and a cell polarized in the same direction and in the opposite direction of the neutron spins were measured.

The transmission of the beam through depolarized ^{3}He cell is given by:

$$T_0(l) = T_g e^{-n\sigma l} \tag{4.47}$$

The transmission of a fully depolarized neutron beam through a polarized ^{3}He cell was calculated from the average of the two neutron beam transmissions

measured with SR on and off:

$$T_{pn0}(l) = T_g e^{-n\sigma l} \cosh(n\sigma l P_{He})$$

The relative transmission of a polarized beam through the ^{3}He cell with the polarization direction opposite to the direction of the neutrons is given by the relation:

$$R_1 = T_1(l)/T_0(l) = \cosh(n\sigma l P_{He}) - P_n \sinh(n\sigma l P_{He}) \qquad (4.48)$$

After the direction of the Helium spins is reversed by using Adiabatic Fast Passage, the transmission of the polarized neutron beam is given by:

$$R_2 = T_2(l)/T_0(l) = [\cosh(n\sigma l P_{He}) + P_n \sinh(n\sigma l P_{He})] \qquad (4.49)$$

The factor $n\sigma l$ can be written as a function of the neutron wavelength (λ, Å), the cell length (l, cm) and the Helium pressure (P, atm) in the cell at room temperature: $n\sigma l = 0.0733 \cdot P \cdot \lambda \cdot l$

The flipping ratio is the ratio of the neutron transmission through the cell when the neutron and Helium spins are parallel and antiparallel respectively. This ratio can be measured by flipping the neutron spin direction with the SR turned on, while the direction of the ^{3}He spin is fixed (AF coils off) or the ^{3}He spins are flipped with the AFP coils and the SR is off. Both methods were used to calculate the neutron polarization and the results compared. The flip of the ^{3}He spins with the AFP coils allows the calculation of the neutron polarization without knowledge of the SR efficiency. In this case the neutron polarization is calculated from the quantities R_1 and R_2 for each time bin:

$$P_n = \frac{R_2 - R_1}{\sqrt{(R_2 + R_1)^2 - 4}} \qquad (4.50)$$

For the second method the SR is turned successively on and off for all eight pulses in the spin sequence. The transmission of the neutron beam

through the Helium cell was measured with the SR turned on (T_{on}) and off (T_{off}) and normalized with the transmission of the neutron beam through depolarized cell (T_0). In the experiment the direction of ^{3}He polarization and the direction of the neutron spin before the SR are opposite. With the SR switched on the relative neutron flux measured after the cell is given by:

$$R_{\text{sf}} = \frac{T_{\text{sf}}}{T_0} = \cosh(n\sigma \cdot l \cdot P_{He}) - (1 - 2\varepsilon)P_n \sinh(n\sigma \cdot l \cdot P_{He}) \qquad (4.51)$$

By combining the neutron beam transmission when the SR is turned off (4.48) and on (4.51) the relation between the neutron polarization and the efficiency of the SR can be derived:

$$P_n = \frac{R_{sf} - R_1}{\sqrt{((2\varepsilon - 1)R_1 + R_{\text{sf}})^2 - (2\varepsilon)^2}} \qquad (4.52)$$

The above equation is used for the calculation of the SR efficiency after the measurement of the two flipping ratios R_1 and R_{sf} with the SR off and on respectively. This was done for the ^{3}He cell centered in 9 points of a grid in the vertical plane xy normal to the beam, with a 4 cm distance between the points. On axis the efficiency of the SR is 99 ± 1 % and decreases to 94± 1 % at 3.5 cm from the axis [60].

The transmission measurements through a polarized ^{3}He were also used to adjust the RF current amplitude, and the current in the guide field. For these measurements the SR was turned on and off on pulse by pulse bases such that there were 4 pairs of pulses with spin off and on in each spin sequence. The experimental set-up used for all polarization measurements is presented in Figure 4.20

For the calculation of the flipping ratio the pedestal signal was measured with the same monitor M_3 and the secondary shutter closed T_{ped}. In
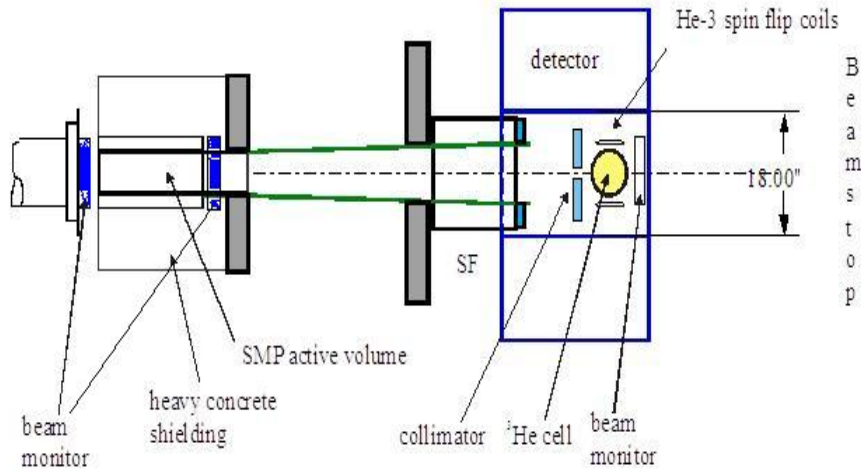
Figure 4.20: The experimental set up used for the ^{3}He cell measurements.

this case the flipping ratio is the ratio of the background corrected transmission with the SR turned on and off:

$$R_{\mathrm{sf}} = \frac{T_{\mathrm{on}} - T_{\mathrm{ped}}}{T_{\mathrm{off}} - T_{\mathrm{ped}}} \qquad (4.53)$$

The amplification level of the current in the SR coils was adjusted for the maximum flipping ratio. For the optimum RF current in the SR, the flipping ratio was measured for different currents in the guide coils such that the guide fields was changed between 9.2 Gauss and 9.6 Gauss 4.21. The maximum is close to 9.4 Gauss as expected for the characteristic RF resonance frequency 27.4 kHz of the SR.

The polarization measured with the SR to reverse the direction of the neutron spin is in very good agreement with the polarization measured with SR off and by flipping the spin of the ^{3}He atoms with the AFP coils as in Figure 4.22 ([73]).

87
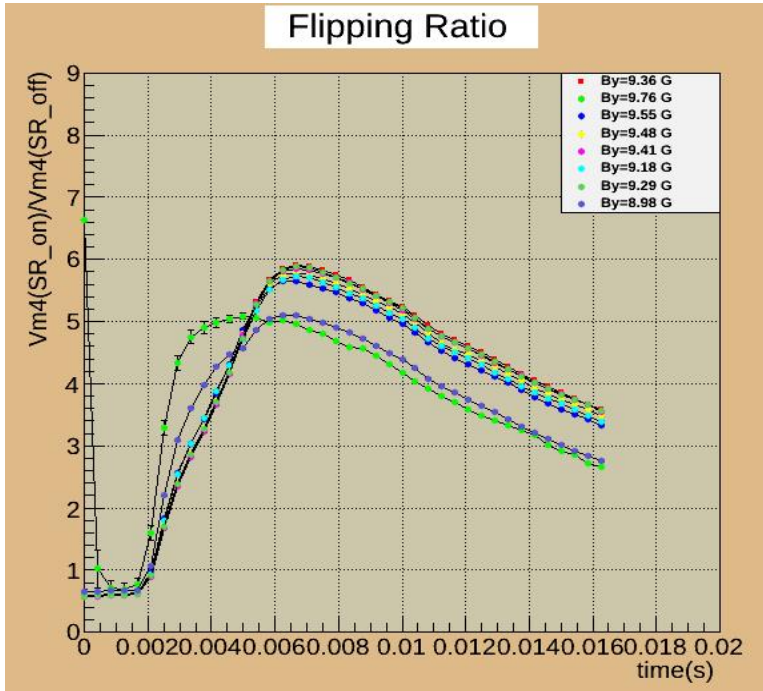
Figure 4.21: Flipping ratio as a function of the time bin and the magnitude of the magnetic field of the coils.

The polarization was measured for different concentrations of ^{3}He to calculate the uncertainty in polarization due to uncertainty in the concentration of ^{3}He (Figure 4.23). In this figure the polarization is corrected for the electronic pedestal and for the efficiency of the SR. The average polarization decreases from 0.944 at 51% ^{3}He polarization to 0.939 at 22% ^{3}He polarization.
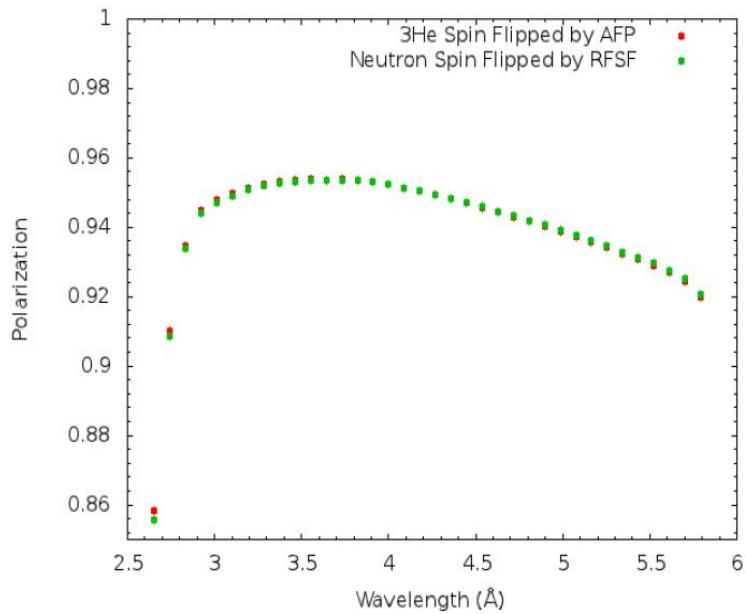
Figure 4.22: The polarization measured when SR is off and the ^{3}He spin is flipped with AFP coils (red dots) and when the AFP coils are off and the SR is on (green dots) to flip the neutron spin.
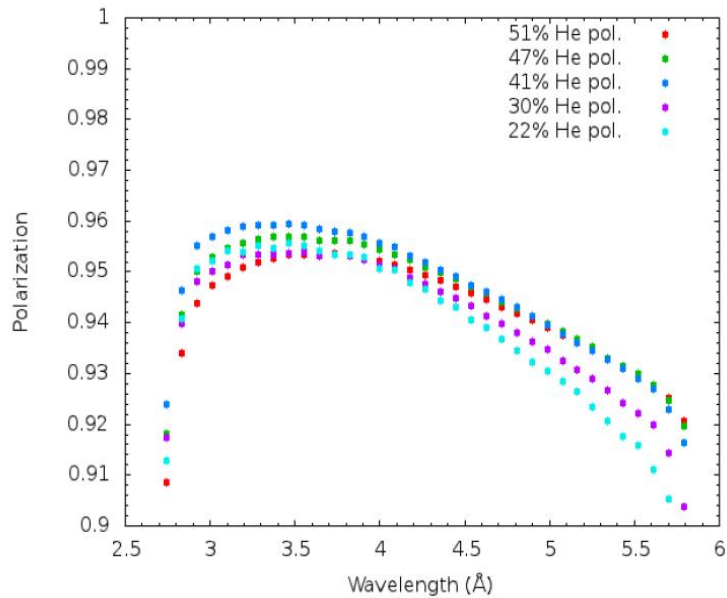
Figure 4.23: The polarization was measured at different concentrations of ^{3}He in the cell. The neutron spin is flipped with the SR.

Chapter 5

PARITY MEASUREMENTS FOR ALUMINUM AND CHLORINE

This chapter describes the properties of the Al and Cl targets, the data
collection process and the initial cuts used in the data analysis.

5.1   The Aluminum and Chlorine Targets

The Cl target is a thin hollow cylinder, 0.56 cm thick along the beam axis with
inner and outer radius equal with 5.72 cm and 6.15 cm, respectively. The
upstream and downstream faces of the Cl target are 0.76 mm and 2.67 mm
thick, respectively. The target was filled with liquid carbon tetrachloride CCl_4.
The natural Cl contains two isotopes ^{35}Cl and ^{37}Cl with natural abundances
75.53% and 24.47%, respectively. The thermal neutron capture cross sections
are 45 barns for ^{35}Cl and 0.005 barns for ^{37}Cl. After the neutron capture in ^{35}Cl
the radioactive isotope ^{36}Cl with a lifetime of $3 \cdot 10^5$ years is produced. The
center of the Cl target was on the neutron beam axis and at 1.25 inches
downstream from the center of the detector stand.

The Al target is a stack of 35 parallel disks (Al 6061) placed in the slots
of an Al holder. Each disk is 5.72 cm in diameter, 0.25 cm thick and the gap
between two disks is 0.35 cm. The target was aligned with the z axis. The
center of the Al target was close to the center of the detector array. The
distance from the last disk to the outside surface of the end Al plate of the
detector stand was 17.6 cm. The total length of the target is 27.1 cm. Disk 35
is the farthest disk downstream from the end of the SR and disk 1 is the
closest. The center of the detector stand is very close to the center of the Al
target as seen in Figure 3.7 in section 3.1.

5.2   Data Acquisition and Electronics

The data acquisition user interface at BL13 was installed on the control computer (Clover) that had the data acquisition user interface. Clover was connected by an Internet cable with the Hazel computer that communicated with the three VME crates (VME1, VME2, VME3) telling them to take data. The communication between the networked computers was done through SSH a network protocol for secure data communication, remote shell services and command execution (Figure 5.1). The Cyclonus computer had two network cards and was the bridge machine for DAQ. The first network card was connected to the ORNL network. Cyclonus could be logged in remotely by a user with both ORNL and Cyclonus account. The second network card was connected to the private network of the Hazel, Clover, H_2 target DAQ and B-Field computers. The data were transfered first to Clover where it was stocked on removable hard drives. When a predefined number of spin-sequences per run were read in Clover, the run with a given name was copied back to Hazel and then transfered over the Internet to a remote computer (Basestar). A diagram of the link between the three modules and the computers is presented in Figure 5.1.

When the Al and Cl data were collected, the H_2 target DAQ, and the Hydrogen alarm computer did not exist. The magnetic field was recorded in LabView running on the B-Field computer that was not connected to the Hazel computer. The data from each pulse was written to three data files, corresponding to each of the three VME modules that it came from. The proton current and the T0 signal from accelerator control, were recorded in the VME1 module. The detector signals were digitized in ADC counts. Instead of
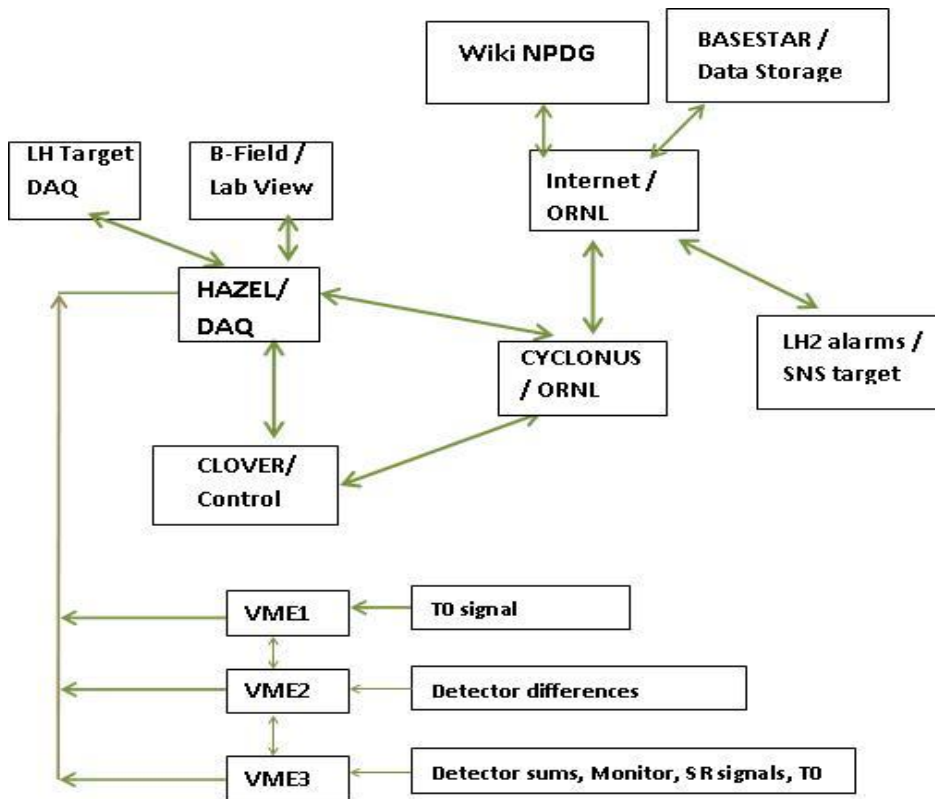
Figure 5.1: A diagram of the data acquisition network for the NPDGamma experiment.

collecting the signal for each detector,and for each pulse, the data acquisition

recorded four average signals, one for each detector ring and 48 difference

signals relative to the ring average, one for each detector. The average and

difference signals were recorded in 100 time bins with each time bin summed

over 20 difference and 25 sum samples. The sum and the difference signals

are read in the ADC channels in the VME3 and VME2 crates, respectively. The

detector signal was reconstructed by adding the average and the difference

signal. The reconstructed detector signal was copied into the data stream that

was eventually written on the removable hard drive in Clover.

In addition to the sum signals, the current and the voltage of the SR,

and the output voltages of the two beam monitors M_1, M_2 were read into the VME3 crate. The detector signals were digitized in ADC counts. The VME3 recorded the four sum signals, one for each of the four detector rings. The 48 difference detector signals relative to the sum signal was recorded in VME2 module. The reconstructed detector signal (the sum plus the difference signal) was calculated in the on-line Root data analysis program installed on Clover.

The first VME1 crate received a TTL pulse (T0) from the accelerator with a 60 Hz frequency, when the proton pulse was incident on the Hg target. The signal was transmitted to a delay module and to a logic coincidence module. The output signal from the coincidence module was transmitted to the VME2 and VME3 crates triggering the reading of the three monitors, SR and detector signals (Figure 5.2). In this diagram different kinds of modules are depicted with different colors. Each module is labeled with two numbers $X.Y$ where X is for the location of the module inside the crate and Y denotes a submodule.

The VME2 crate collected the 320 x 48 difference detector signals: each spin sequence has 320 time bins for each detector. The data collection was triggered by the T0 signal received by the VME3 crate. For each pulse, the Joerger clock generates 1000 pulses to trigger the ADC that digitized the detector signals. A diagram of the VME2 crate is presented in Figure 5.3.

VME3 contained one ADC unit with 12 channels. A diagram of the VME3 crate is presented in Figure 5.4. The first 4 channels received the average detector signal from each ring. The three monitor signals were recored in the next 3 channels. The other 5 channels were not used for data collection. The VME3 data stream had ADC data with 12 entries and each entry had 320

93
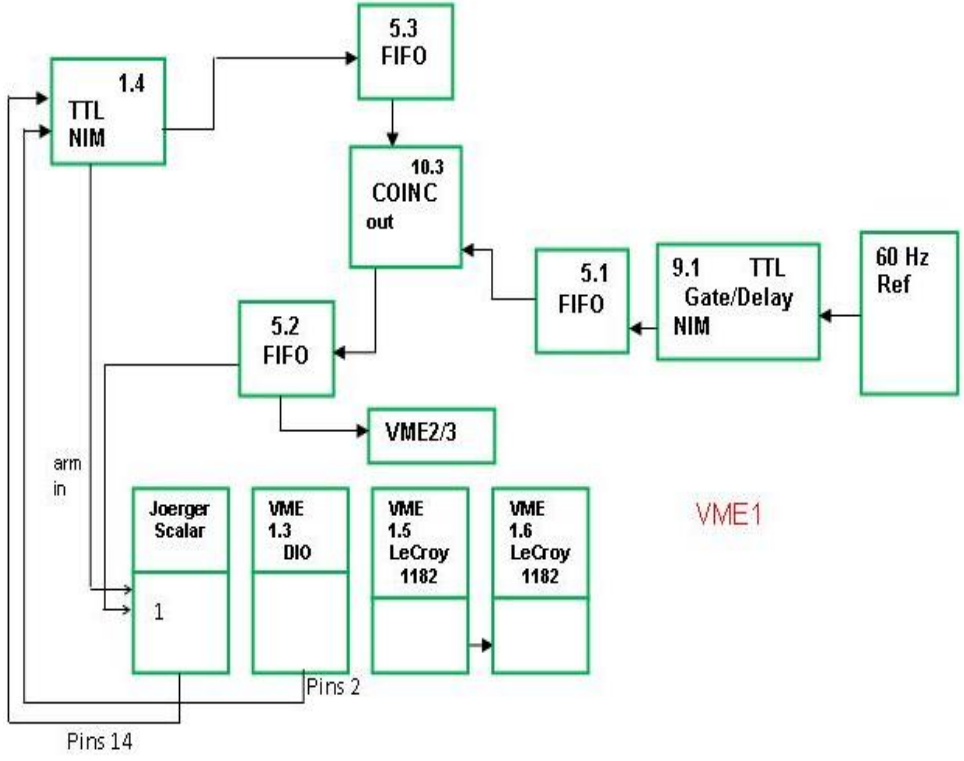
Figure 5.2: The electronic diagram of the VME1 module

time bins.

The digital acquisition timing diagram for VME3 crate is presented in Figure 5.5. The T0 signal from accelerator, at the beginning of each pulse, triggered the Joerger module to start generating pulses. The output pulses from Joerger triggered the ADC module that read the detector sums and the differences. Instead of reading the data after each pulse, the data were accumulated during eight pulses and read out to the disk during the 9th pulse. The blank pulse was received by the VME3 crate every 9th pulse. This pulse stopped the reading of the data and generated the data transfer from the ADC unit in the VME3 crate to the data stream and eventually to the hard drive on Clover.

94
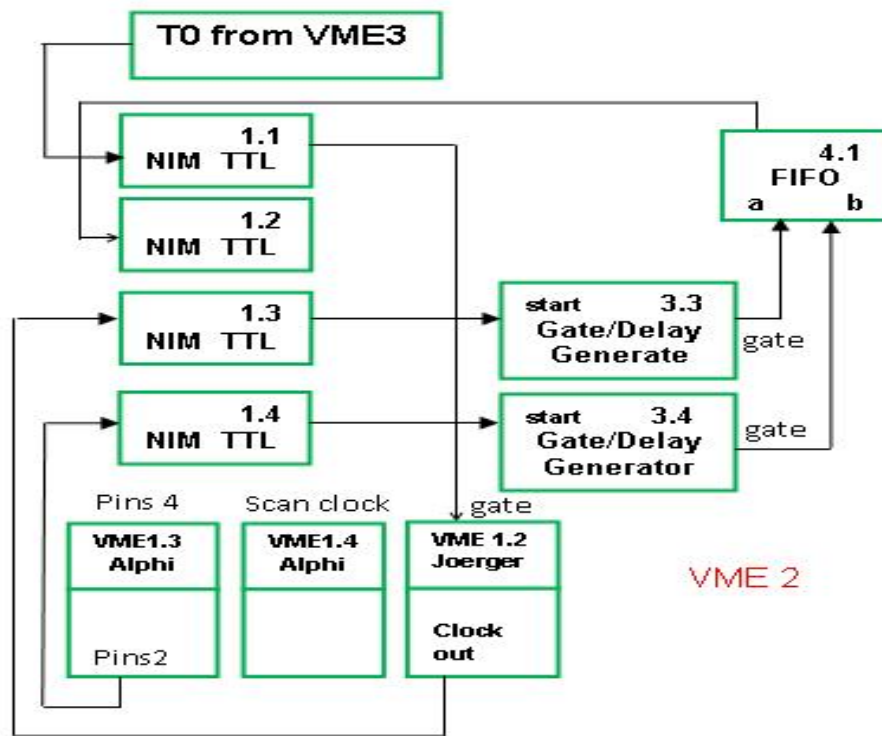
Figure 5.3: The electronic diagram of the VME2 module

Data for each spin sequence is preceded by a header that included: the date and time, the time in microseconds since the last pulse , the pulse number, the Spin Sequence information, time since the last writing of the data and the number of records written. For the future H_2 data collection the transient seen in the Al and Cl data will have to be eliminated. This will be accomplished by alternating the spin sequences in the pattern A B A B, where A= 0, 1, 1, 0, 1, 0, 0, 1 and B=1, 0, 0, 1, 0, 1, 1, 0. Moreover the old Spin Sequencer was replaced with a new one that was built at Los Alamos in Spring 2012.

The magnetic field was read by the two magnetic probes located above and below the SR . Each probe had three flux gates to measure the three field components. The six field components will be written during the H_2 data runs into the data stream of the NPDGamma data acquisition. The asymmetry in
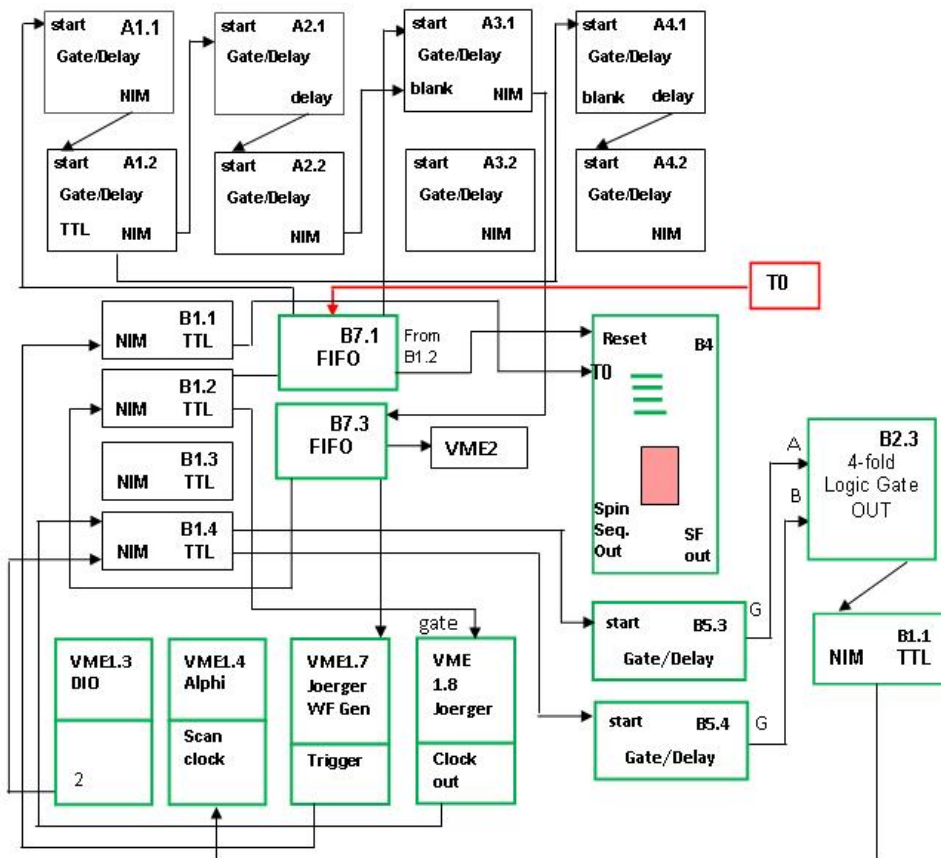
Figure 5.4: The electronic diagram of the VME3 crate

the angular distribution of the gamma rays was measured for about 2000 good

data runs, with 3750 spin sequences in each run. The data runs were

transfered to a remote computer (Fiver) over the net. After the measurements

were completed, Fiver was replaced with a new and faster computer

(Basestar).

5.3 Calculation of the Geometry Factors

The geometry factors for the Al target were calculated first with two models in

GEANT4 and MCNPX. GEANT4 was used to simulate the gamma rays emitted

from the target. The capture and scattering of the neutrons was simulated in

MCNPX. GEANT4 is written in C++ and the source code can be modified to
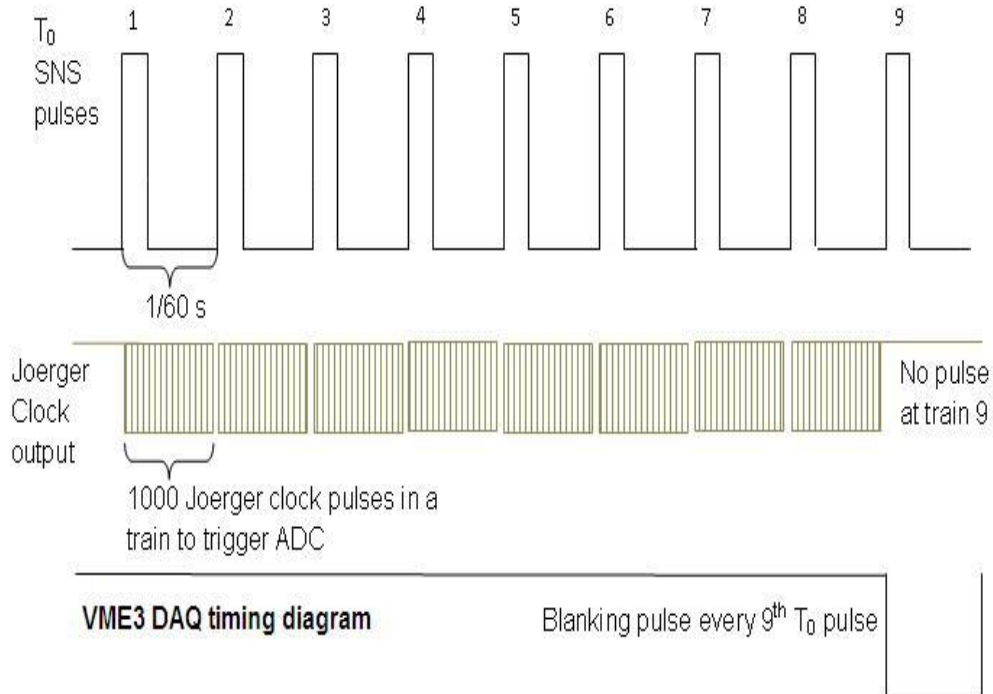
Figure 5.5: The digital aquisition timing diagram

save in files any quantities that are needed at the end of the calculations.

However because GEANT4 does not have cross section libraries for the cold

neutron capture and scattering in Al, it was decided to write special MCNPX

subroutines for recording the initial direction the emitted gamma rays and their

energy deposition in each detector. These quantities are necessary for the

calculation of the energy weighted average sums of the scalar products of the

gamma ray momentum and the x or y directions. For the final MCNPX

calculations both the neutrons and the photons were simulated [65]. The

results of the two calculations of the geometry factors (in GEANT4 and

MCNPX) were very similar. The MCNPX model of the target and detector

assembly is presented in Figure 5.6. The center of the axes of coordinate is in

the center of the detector assembly. The z axis is along the beam axis,

indicated by the red arrow.
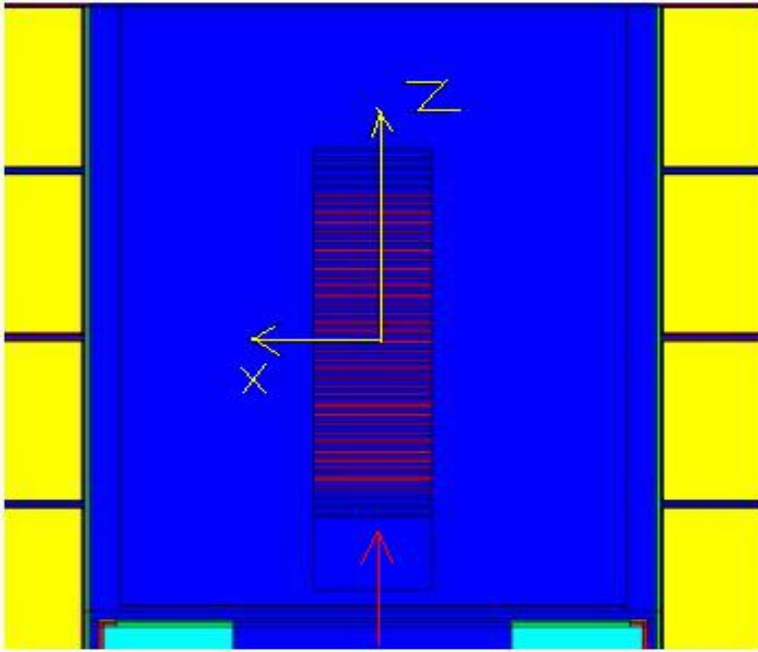
Figure 5.6: The MCNPX model of the Al target located inside the detector assembly is seen in the horizontal plane xz of the beam axis.

The number of neutrons captured in each disk divided with the number of source neutrons is calculated for neutron energies between 2 meV and 13 meV in Figure 5.7. The center of the target is at z=0 cm. The data were fitted with an exponential decay with three fitting parameters y_0, A_1, z_1:

$$N_c/N_0 = y_0 + A_1 \cdot exp(-z/z_1) \tag{5.1}$$

The relative number of the gamma rays emitted from a disk is equal with the relative ratio of the number of neutron captured in a disk. This ratio is maximum for 2 meV neutrons and for the first disk center at z=-14 cm.

The ratio of the neutron flux $N(z)$ passing through a disk centered at (0,0,z) and the neutron flux in the first disk N_1 is calculated in MCNP for each
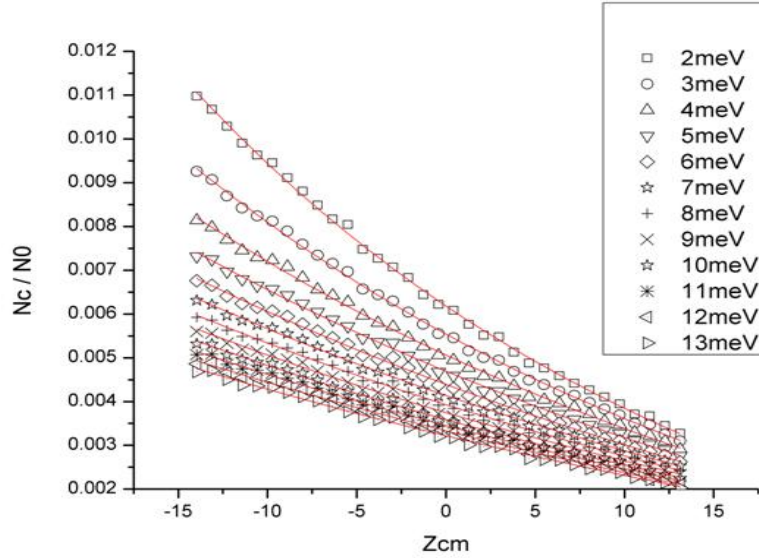
Figure 5.7: The number of neutrons emitted from a disk centered at z divided with the number of neutrons emitted in the first disk N_0 is calculated along the z axis of the target.

disk. The exponential fitting function is equal with:

$$N(z)/N_1 = -0.674 + 1.690 \cdot e^{(z-1.548)/62.255} \qquad (5.2)$$

The errors in the calculation of the geometry factors are related with the uncertainty in the position of the target along the beam axis $\pm\, 0.2$ cm and with the modeling of the energy distribution of the neutrons in the beam. The geometry factors are calculated for gamma rays with an initial energy of 2 MeV in Figures 5.8 and 5.9.

The geometry factor in the up-down (UD) or left-right (LR) directions are the average scalar product of the unit vector of the initial momentum of the gamma-ray emitted from the target and the unit vector of the vertical y axis or horizontal x axis respectively. The average of the scalar product is weighted

with the gamma ray energy deposition in the detectors :

$$G_d^{UD} = \left\langle \hat{k} \cdot \hat{y} \right\rangle = \frac{\sum_{j=1}^{N} E_j (\hat{k}_j \cdot \hat{y})}{\sum_{j=1}^{N} E_j} \;\; ; \;\; G_d^{LR} = \left\langle \hat{k} \cdot \hat{x} \right\rangle = \frac{\sum_{j=1}^{N} E_j (\hat{k}_j \cdot \hat{x})}{\sum_{j=1}^{N} E_j} \quad (5.3)$$
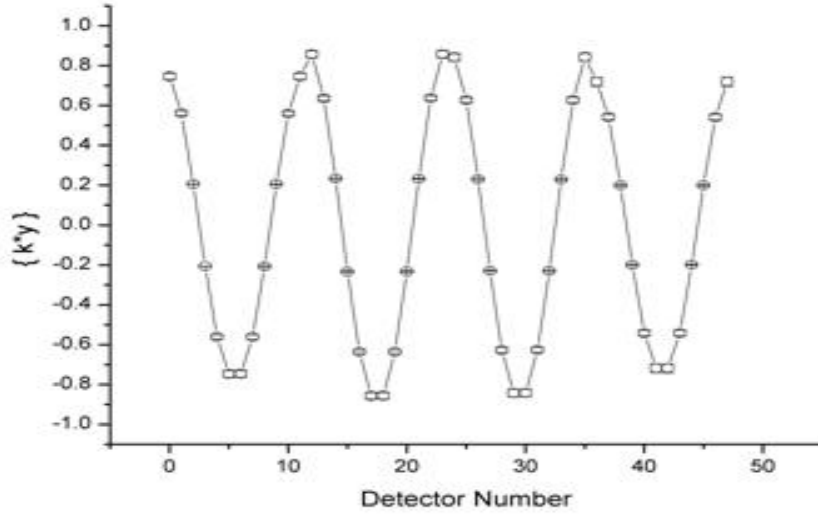
Figure 5.8: The geometry factor G_d^{UD} is calculated for Al target and each of the 48 detectors.

A Root and C++ code was used for reading the binary data ([67]). The binary data, organized in groups of eight pulses (a spin sequence), was read in branches and trees. For the Al and Cl runs only the raw data read from the three VME crates are written in branches. The subsequent branches in the data tree were created from the raw data. The branches for the 48 detector signals in ADC counts and volts, with 320 time bins for each spin sequence, were calculated from the detector sum and differences. The header quality bit constructed from the VME2 and VME3 headers was set to zero if the spin sequence was right and data were not corrupted. The asymmetry branch was calculated for 24 pairs of detectors and 40 time bins.

100
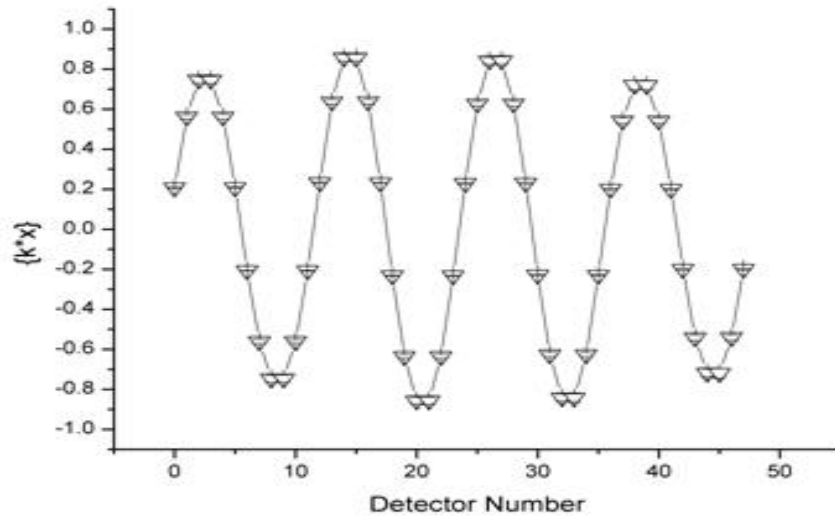
Figure 5.9: The geometry factor G_d^{LR} calculated for Al target and each of the 48 detectors.

5.4 Upper Cuts on Monitor and Detector Signals

The eight pulses in a spin sequence are counted from 0 to 7. The SR is turned off during pulses 1,2, 4 and 7 and is turned on during pulses 0, 3, 5 and 6. The time frame for one pulse was 1/60 seconds. The SR ramp signal was generated in the Joerger module located in the VME3 crate after a predefined delay time relative to the start of the T0 signal. The ramp was triggered at the starting edge of the Delay Generator gate. Due to jitter in electronic signal there was a drift between the start of the gate and the T0 pulse. In this case the SR signal could shift in time and the spin sequence was changed. These sequences had a non-zero header quality bit at the start of the data tree and were eliminated from analysis. A run was rejected if it was corrupted during the data transfer or the beam was off during the run.

During some pulses the proton beam was not delivered to the Hg target

101

such that no neutrons were generated in the spallation target. The sequences with dropped pulses were eliminated from analysis. This was done by calculating the average monitor M2 signal for each pulses (CUT1). If all eight average values are bigger than 0.11 Volts then the spin sequence did not have dropped pulses. The synchronization of the two choppers located upstream on the beam guide and their opening angle allowed a small fraction of slow neutrons with wavelength in two narrow windows centered at 14 Åand 28Å to mix with the neutrons in an earlier pulse. The dropped pulses close to the end of a spin sequence will cause the slow neutrons in the first two pulses of the next spin sequence to be absent. The pulses with missing slow neutrons can be a source of false asymmetry if they occur at the same position in a spin sequence. A second cut (CUT2) was used to eliminate the spin sequences with such pulses. The sum of the monitor M2 signal from time bins 30 to 35 in a pulse, was calculated for each eight pulses in a spin sequence. The difference between the maximum $V2_{max}$ and minimum $V2_{min}$ of the eight sums was divided with the average of the eight sums between time bins 17 and 20 (V_{S2}). The second cut selected only the spin sequences for which the ratio of the difference $V2_{max} - V2_{min}$ and the average V_{S2} is smaller than 0.12:

$$(V2_{max} - V2_{min})/V_{S2} < 0.12$$

The upper limit CUT2 was estimated from the histogram of the above ratio for all spin sequences with no dropped pulses (Figure 5.10). The third cut (CUT3) eliminated the spin sequences with pulses that had the average monitor signal very different compared with the average monitor signal for the other pulses in a spin sequence. Therefore CUT3 eliminated the spin sequences with unacceptable drops in the beam intensity for one or more
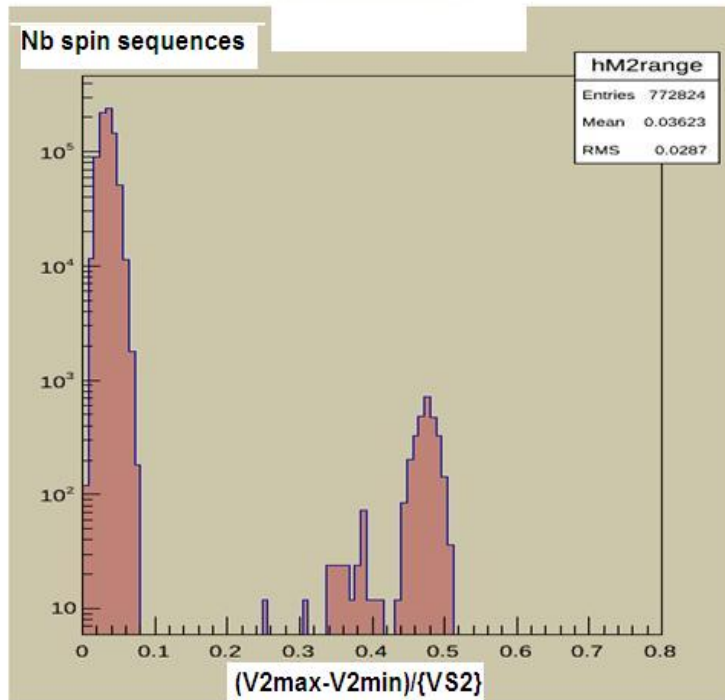
Figure 5.10: The histogram of the ratio $(V2_{max}\text{-}V2_{min})/\{V_{S2}\}$ is calculated for all spin sequences that do not have dropped pulses.

pulses in a spin sequence. Like the dropped pulses, these drops in the beam intensity occurred usually at the same pulse position in the spin sequence. For this cut the pulse areas of the eight monitor M2 pulses were calculated for each spin sequence that passed the first two cuts. The difference between the maximum and the minimum of the eight pulse areas ($S_{2max}\text{-}S_{2min}$) was divided with the time average $\{V_{m2}\}$ of all eight monitor M2 pulses in the spin sequence. A histogram of this ratio over all spin sequences for 20 runs that passed the first and second cut is presented in Figure 5.11. Because the shoulder in this histogram is located at values bigger than 0.35 the upper limit of the second cut was chosen equal with 0.35. For the fourth cut, the maximum and the minimum area (D_{max}, D_{min}) of the eight detector pulses, were calculated for each spin sequence that passed the first three cuts. The
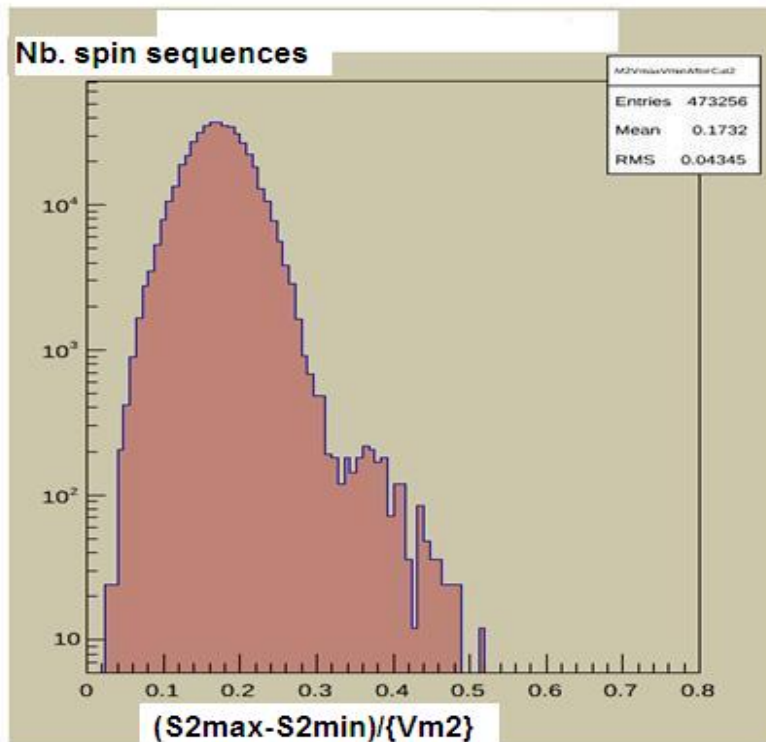
Figure 5.11: The histogram of the ratio $(S_{2max}\text{-}S_{2min})/\{V_{m2}\}$ is calculated for all spin sequences that do not have dropped pulses and passed the second cut.

difference $D_{max} - D_{min}$ was divided with the time average detector signal over all spin sequence D_{ss}. The histogram of these ratios for all spin-sequences that passed the Monitor cuts is presented in Figure 5.12. The histograms has two peaks. The presence of the second peak is due to transient signals from Spin Sequencer that are overlapped with the detector signals recorded in the presence of the beam. As a consequence a fourth cut was placed on the ratio CUT4= $(D_{max} - D_{min})/D_{ss}$. If CUT4=0.4 then this cut eliminates about 0.5% of the spin sequences. The detector pair asymmetries for Al target were calculated for CUT4 between 0.2 to 1 in section 6.8.

In summary, the first cut on spin sequences with bad header eliminated 0.22% from the total 3750 number of spin sequences in each run. The second

104
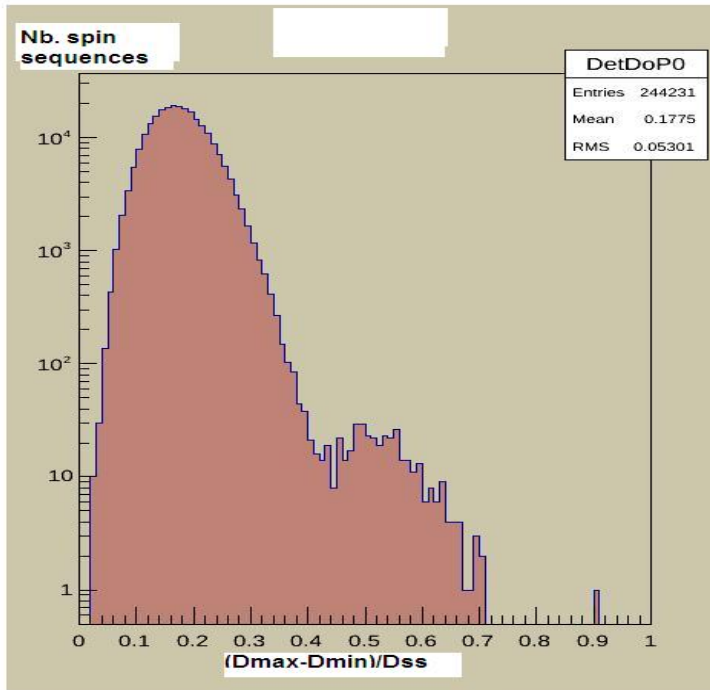
Figure 5.12: The histogram of the ratio $(D_{max} - D_{min})/D_{ss}$ is calculated from all spin sequences in 100 runs that passed the first three monitor cuts.

and third cut eliminated 5.93 % , 0.62% respectively. The fourth cut on detector signal, for CUT4 =0.5, eliminated 0.3% spin sequences.The total fraction of spin sequences rejected was 6.98%.

For each time bin and each accepted spin sequence, the detector electronic pedestal was subtracted from the detector signal. The spin sequences with dropped pulses were used to calculate the pedestals. The average detector signal between time bins 16 and 35 was calculated from the dropped pulse (V_{ped}). From the beam-on pulse preceding the dropped pulse, the time average detector signal between the time bins 16 and 35 (V_{top}) and the average in the first 9 time bins of the pulse V_{start} were calculated. These

105

three quantities can be used to calculate the g factor:

$$g = \frac{V_{start} - V_{ped}}{V_{top} - V_{start}} \qquad (5.4)$$

The average of this ratio calculated for a few runs with dropped pulses is between 0.9 and 1.3 for all detectors [74]. All three average signals V_{top}, V_{start} and V_{ped} are calculated for positive detector signals. It is expected that the shift in the electronic pedestal will increase the three average signals with the same amount. However when the gamma background is low, i.e. the beam just starts to ramp up after a long beam-off period, the pedestal V_{ped} calculated with the table of g factors, and measured average V_{top} and V_{start} can be negative:

$$V_{ped} = V_{start} - g \cdot (V_{top} - V_{start}) < 0 \qquad (5.5)$$

This can happen at the beginning of the target irradiation when the gamma background is small such that V_{start} is close to the detector pedestal. To avoid this problem, the histograms of the g-fraction $g_F = g(V_{top}/V_{start} - 1)$ were accumulated over 1000 runs, for each detector, from spin-sequences with dropped pulses. The average values of the 48 histograms were saved in a file. These values were later read from the file to calculate the pedestal V_{ped} for a spin sequence that passed all the cuts. The ratio V_{top}/V_{start} is always bigger than one and $g_F = g \cdot (V_{top}/V_{start} - 1)$ is a number between 0 and 1 such that $V_{start} (1 - g_F)$ is always positive if the average detector signal in the first 9 time bins of a pulse (V_{start}) is positive. For each detector the change in the g-fractions g_F from one run to another is negligible. The root mean square of the histograms of the 48 detector's pedestals is between $1.4 \cdot 10^{-4}$ and $3 \cdot 10^{-4}$ and the average pedestal values V_{ped} are between 0.68 and 0.74.

For each pulse i in a spin sequence, the detector pedestal was calculated from the average detector voltage over the first 9 time bins at the

106
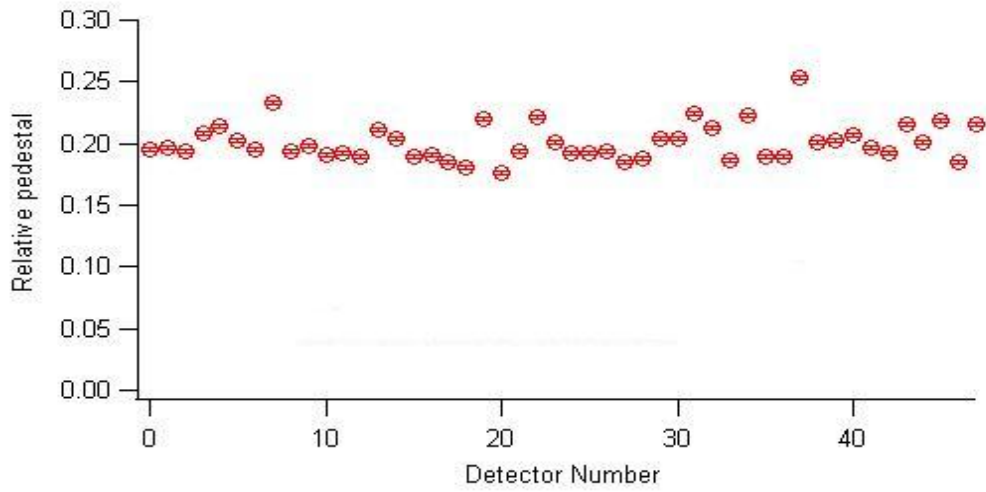
Figure 5.13: The pedestal divided with the pulse average of the detector signal is calculated for each detector number.

start of the pulse V_{start} and from the detector g-fraction g_F read from the file. In figure 5.13 the pedestal for the spin sequence is the average of the eight pedestals calculated for each pulse:

$$V_{ped}[i] = V_{start}[i](1 - g_F)\mathrm{i} = 0 \ldots 7 \qquad (5.6)$$

Chapter 6

DATA ANALYSIS

This chapter describes the analysis of the ^{35}Cl and ^{27}Al data. The detector
signals are read during the time interval of a group of eight neutron pulses
called spin sequence. The data is transfered to the disk during the 9th neutron
pulse. Each neutron pulse is divided in 40 time bins and the detector signal is
read at each time bin. For accepted spin sequences the asymmetry is
calculated for each time bin in the range $[T_1, T_2]$. The first time bin T_1 is given
by the switch-on time of the SR. The last time bin T_2 has to be smaller than the
last time bin in the pulse when the chopper is closed. The analysis results
presented here were done for T_1=8 and T_2=38, respectively, in order to avoid
the calculation of the asymmetry during the SR ramp up and during the last
time bin when the chopper is closed. Section 6.1 describes two methods used
to calculate the experimental asymmetries. Sections 6.2 and 6.3 present a
discussion of the main contributions to the statistical and systematic
uncertainties, respectively. Additional sources of false asymmetries are
discussed in sections 6.4 and 6.5. The technique for the correction of
electronic transients in the detector signals are discussed in sections 6.7 and
6.1. The results for the parity-violating and parity-conserving asymmetries are
discussed in section 6.8 for ^{27}Al and section 6.9 for ^{35}Cl.

6.1   The Procedures for Asymmetry Calculation

The asymmetry can be calculated for each of the 48 detectors or for each of
the 24 opposite detector pairs in all four rings. There are two methods used for
the asymmetry calculation, called the arithmetic mean and the geometry mean.
The asymmetry per detector can be calculated only from the arithmetic mean.

Both the arithmetic and geometry means can be used for the calculation of the 24 detector pairs asymmetry. The calculation of transient parameters and of the corrected asymmetry were done starting from the ratio of opposite detector signals at each time bin.

6.1.1 Arithmetic Mean Asymmetry

Consider D_1 and D_2 the signals of two opposite detectors (1, 2) in a ring and (k, l) two pulses with the neutron spin up and down respectively. After the SMP and before the SR, the neutron spin is pointing up, in the direction of the main field. After passing through the RF field of the SR the neutron spin is flipped down during the pulses with the SR turned on and is up for the other pulses. In each sequence the SR is on during pulses 0, 3, 5, 6 and it is switched off during pulses 1, 2, 4 and 7. The sign of the asymmetry in the angular distribution of the gamma photons emitted from the target depends on the direction of the neutron spin. For this reason the asymmetry term $P_d(t) = (A_1 G_d{}^{UD} + A_2 G_d{}^{LR})$, with the geometry factors $G_d{}^{UD}$ and $G_d{}^{LR}$, in the time bin depending detector signal (eq. 6.1) is multiplied by a constant s_k equal with +1 or -1 for pulses with neutron spin up or down respectively. The detector d has a gain factor f_d. In the absence of transient signals, the detector output is proportional with the gamma rays energy lost in the detector $I_k(t)$ (in the absence of the asymmetry term) times a factor that depends on the asymmetry:

$$D_{k,d}(t) = f_d I_k(t)(1 + (A_1 G_d{}^{UD} + A_2 G_d{}^{LR}) \cdot s_k) \qquad (6.1)$$

During the analysis of the Al data, it was observed that the asymmetry computed for each detector is always shifted to negative values such that the average detector asymmetries were between -10^{-7} and -10^{-5}. This

109

unexpected result was explained by performing beam-off measurements of the monitor and detector signals with their power source cables disconnected from the power source in the VME3 module and connected to a battery. The output of the two monitors, four detector-ring sums and 48 detector differences read in the ADC were mixed with a much smaller transient signal output from the Spin Sequencer located in VME3 module. The transient was generated at the end of each spin sequence, during the 9th pulse when the data were transfered to the computer. According to the monitor measurements the transient is a simple exponential decay. The asymmetry depends on detector number d and only weakly on the time bin due to the wavelength dependence of the SMP polarization efficiency. To calculate the asymmetry term in the presence of transient signals that are not related with the neutron beam, the formula of the detector signal for each time bin has to include the time dependence of the transient signals in addition to the detector yield due to the gamma rays from the neutron capture in the target.

$$D_{k,d}(t) = f_d I_k(t)(1 + P(t) \cdot s_k) + V \cdot e^{-(t+k \cdot T)/\tau} \tag{6.2}$$

The asymmetry factors A_1 and A_2 are proportional with the parity-violating and parity-conserving asymmetries, A_{UD} and A_{LR} respectively through the neutron polarization P_n and the efficiency ε of the SR:

$$A_{UD} = A_1/(P_n\varepsilon) \; ; \;\; A_{LR} = A_2/(P_n\varepsilon) \tag{6.3}$$

The asymmetry ratio at each time bin and for each detector can be calculated from the ratio of the difference and the sum of the detector signal measured at the same time bin, for two pulses with neutron spin up (k) and

spin down (l):

$$P_d(t) = \left(\frac{D_{k,d}(t) - D_{l,d}(t)}{D_{k,d}(t) + D_{l,d}(t)} \right)$$ (6.4)

In the asymmetry calculated with the above formula, the transient signals not related with the neutron beam give rise to a false additive asymmetry. At the same time the beam intensity fluctuations contribute to the errors in the calculated asymmetry. To avoid these problems the asymmetry has to be calculated for detector pairs. In addition, to reduce the noise contribution to the asymmetry, the average detector signals over the four pulses with spin up and four pulses with spin-down is calculated at each time bin:

$$D_{\downarrow,d}(t) = \frac{\sum_{k=0,3,5,6} D_{k,d}(t)}{4}; \quad D_{\uparrow,d}(t) = \frac{\sum_{l=1,2,4,7} D_{l,d}(t)}{4}$$ (6.5)

Neglecting the small change in the ideal position of the detector center due to the small differences in the efficiencies of the two halves of CsI crystals in a detector, the geometry factors for any pair of opposite detectors in a ring, have opposite sign:

$$G^{UD}(d_1) = -G^{UD}(d_2); \quad G^{LR}(d_1) = -G^{LR}(d_2)$$ (6.6)

In consequence the asymmetry for two opposite detectors are also expected to have opposite signs. In the absence of the transient the beam intensity $I_k(t)$ exactly cancel in the ratio of opposite detector signals recorded at the same time bin. In the presence of the transient the ratio depends on the beam intensity through the factor $V/I_k(t)$ where the amplitude of the transient V is 10^{-4} smaller than the pulse average detector signal. For this reason the contribution of the beam intensity fluctuation to the asymmetry calculated from opposite detectors ratio is negligible. The difference of the asymmetries for a pair of opposite detectors divided with two is named the detector pair

111

asymmetry. The statistical errors due to counting statistics and beam fluctuations are expected to be smaller when the asymmetry is calculated for the ratio of detector signals compared with the asymmetry calculated from the ratio of the detector signals differences and detector signals sums.The detector pair asymmetry is calculated for each time bin with the relation:

$$P_{1,2}(t) = \frac{P_1(t) - P_2(t)}{2} = \frac{D_{\uparrow,1}(t) - D_{\downarrow,1}(t)}{2(D_{\uparrow,1}(t) + D_{\downarrow,1}(t))} - \frac{D_{\uparrow,2}(t) - D_{\downarrow,2}(t)}{2(D_{\uparrow,2}(t) + D_{\downarrow,2}(t))} \quad (6.7)$$

The detector signals for a time bin at two different pulses in a spin sequence are about the same: $D_{k,2}(t) + D_{l,1}(t) \sim D_{k,1}(t) + D_{l,2}(t)$ and the above equation becomes:

$$P_{1,2}(t) = \frac{(D_{\uparrow,1}(t) - D_{\downarrow,1}(t)) - (D_{\uparrow,2}(t) - D_{\downarrow,2}(t))}{(D_{\uparrow,1}(t) + D_{\downarrow,1}(t)) + (D_{\uparrow,2}(t) + D_{\downarrow,2}(t))} \quad (6.8)$$

The time average of the pair asymmetry ratio is calculated over time bins (from T_1 to T_2) in a the spin sequence and over all N_s accepted spin-sequences for all runs.

$$\bar{P}_{1,2} = \frac{1}{N_s} \sum_{s=1}^{N_s} \sum_{t=T_1}^{T_2} \frac{1}{2} (P_{s,1}(t) - P_{s,2}(t)) \quad (6.9)$$

The calculations are done for about 2000 good Al runs and each run has about 3750 spin sequences. In average about 7% of the spin-sequences are rejected for each run. The final asymmetry ratio for each detector is the average over time bins and over the number of accepted spin sequences.

6.1.2   The Geometry Mean Asymmetry

The correction of the transient signal is possible only in the ratio of opposite detector signals for each time bin. Two geometry mean methods , presented in appendix A, were used to calculate the Al asymmetry. For clarity only the second method is presented here. The Al asymmetries were calculated with both methods and agree with each other in the limit of the statistical errors.

In the following equations, $D_d(k, t)$ and f_d are the detector signal at time t and pulse k and the detector gain. $I_k(t)$ is the average gamma yield in each of the 48 detectors. Therefore $I_k(t)$ is a function of the neutron beam intensity at pulse k and time bin t. The transient amplitude and decay times are V_d and τ respectively. The detector asymmetry $P_d(t)$ has a weak time dependence due to the wavelength dependence of the SMP polarization efficiency. For a neutron pulse k with spin up the ratio of the signals for two opposite detectors in a ring is equal with:

$$\frac{D_0(k, t)}{D_6(k, t)} = \frac{f_0 I_k(t)(1 + P_0(t)) + V_0 \cdot e^{-(t+kT)/\tau}}{f_6 I_k(t)(1 + P_6(t)) + V_6 \cdot e^{-(t+kT)/\tau}} \tag{6.10}$$

To cancel the multiplicative detector gains, the above ratio is multiplied with the inverse of the signal ratio for the same pair of detectors for a neutron pulse j with spin down:

$$\frac{D_6(j, t)}{D_0(j, t)} = \frac{f_6 I_j(t)(1 - P_6(t)) + V_6 \cdot e^{-(t+jT)/\tau}}{f_0 I_j(t)(1 - P_0(t)) + V_0 \cdot e^{-(t+jT)/\tau}} \tag{6.11}$$

The above ratios can be written in terms of the relative transient amplitudes $v_0 = V_0/\bar{D}_0$ and $v_6 = V_6/\bar{D}_6$. The relation is simplified by introducing the time dependent functions $u_0(t)$ and $u_6(t)$:

$$u_{0,6}(t) = v_{0,6} e^{-t/\tau} \frac{\bar{D}_{0,6}}{f_{0,6} I_k(t)} \tag{6.12}$$

For clarity the following notations are introduced:

$$q^k = e^{-kT/\tau} \; ; \; q^j = e^{-jT/\tau} \tag{6.13}$$

The transient decay parameter is $q_1 = \exp(-1/\tau)$ with the decay time in units of time bins. With this notation $T = 40$ is the number of time bins in one pulse.

113

The product of the opposite detector ratios at two pulses k and j is equal with:

$$\frac{D_0(k,t)}{D_6(k,t)} \cdot \frac{D_6(j,t)}{D_0(j,t)} = \frac{1 + P_0(t) + u_0(t)q^k}{1 + P_6(t) + u_6(t)q^k} \cdot \frac{1 - P_6(t) + u_6(t)q^j}{1 - P_0(t) + u_0(t)q^j} \qquad (6.14)$$

To decrease the computing time the detector ratio is averaged over the four spin up and the four spin down pulses in a spin sequence. The product of the two average ratios is calculated at each spin sequence.

$$R_{0,6}(t) = \left\langle \frac{D_{0,\uparrow}(t)}{D_{6,\uparrow}(t)} \right\rangle \cdot \left\langle \frac{D_{6,\downarrow}(t)}{D_{0,\downarrow}(t)} \right\rangle \qquad (6.15)$$

The calculation of the raw and the corrected asymmetry from the product $R_{0,6}(t)$ is presented in appendix A.2. The uncorrected asymmetry for each time bin in the time interval $[T_1, T_2]$ is the ratio $Q_{0,6}(k,t) = (\sqrt{R_{0,6}(t)} - 1)/(\sqrt{R_{0,6}(t)} + 1)$. The corrected asymmetry P for each detector pair is considered constant over the time bins $[T_1, T_2]$. The corrected asymmetry P, the relative transient amplitudes v_0, v_6 and the transient decay rate q_1, are calculated from the minimization of the χ^2, for each accepted spin sequence:

$$\chi_e^2 = \sum_{t=T_1}^{t=T_2} \left(Q_{0,6}(t) - P - \frac{u_0(t) - u_6(t)}{16} \left(\sum_{k,\uparrow} q^k - \sum_{j,\downarrow} q^j \right) \right)^2 \qquad (6.16)$$

The time average of the asymmetry over the time bins from T_1 to T_2, $\bar{P}$, is calculated for each accepted spin -sequence and each detector and saved in a histogram. The calculations are done for the detector pair asymmetry. The asymmetries of the two opposite detectors $P_6 = -\bar{P}$ and $P_0 = \bar{P}$ are saved in the histograms for detectors 0 and 6. At the end of all the runs the average and the standard deviation of the 48 histograms are read. The transient contribution is reduced in the asymmetry ratio and the offset calculated over all 24 pair asymmetries is much smaller than the fitting errors. The relative

114

transient amplitudes, the asymmetry term and the transient decay parameters are the four fitting parameters that can be determined from the minimization of the χ^2 function for each spin sequence. The weights used in this function are the variances of the asymmetry ratios $Q_{0,6}(t)$ and can be calculated at the end of each run.

The number of degrees of liberty is $(T_2\text{-}T_1 + 1) - 4$. This procedure was used to calculate the corrected asymmetry for Al and Cl. The results are presented in section 6.1.

6.2 Statistical Errors

The fluctuation in the beam intensity and in the number of gamma rays per time bin detected in two opposite detectors contribute to the statistical errors in the calculation of the asymmetry. These two sources of statistical uncertainty are much bigger than the contribution of the electronic noise in the detectors preamplifier circuits. The fluctuation in the beam intensity cancels out in the ratio of the two detector signals averaged over the same pulse. Because the precision in the calculation of the fitting parameters is related with the standard deviation of the ratio $\bar{I}_k/\bar{I}$ it is important to determine the standard deviation in the ratio of the time average over a pulse and over a spin sequence of the detector signals $\bar{D}_k/\bar{D}$. This ratio is affected by fluctuations in the beam intensity from pulse to pulse in the same sequence. The statistical errors from the counting statistics of the gamma rays detected in opposite detectors in a time bin, are calculated from standard deviation of the ratio of two opposite detector signals averaged over the same pulse. The root mean square of the histogram of this ratio can be calculated for each pulse in a spin sequence, for all good spin sequences in a run. The ratio of the average opposite detector signals calculated for one run and for 20 run, in Figure 6.1, is proportional with

the ratio of the detector gains. According to these results, the detector gains were matched with a precision better than 15%. If the asymmetry is calculated
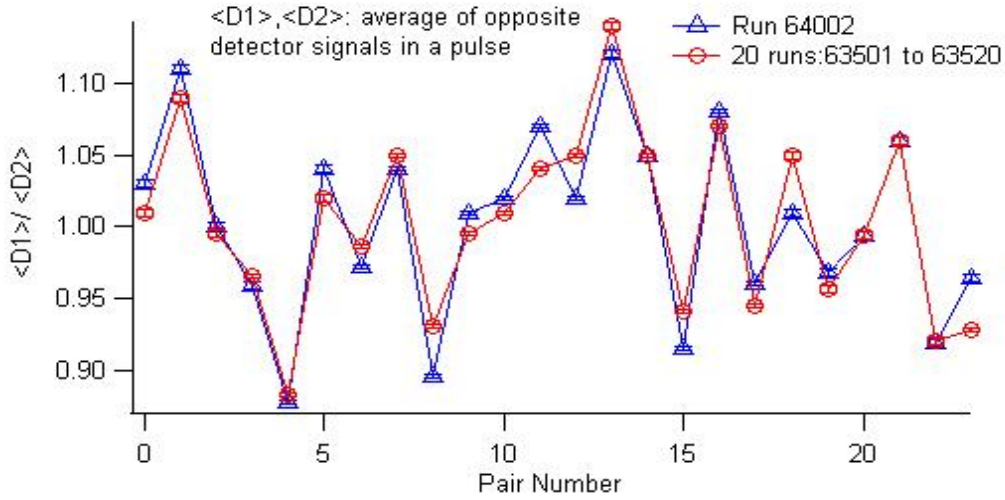
Figure 6.1: The ratio of the pulse average of two opposite detectors signals is calculated for each detector pair for one run and for 20 runs.

for detector pairs with the geometry mean of the ratio of two opposite detector signals then the errors due to beam fluctuations cancel in the difference of the asymmetries for pairs of opposite detectors. In contrast the counting statistics uncertainties due to the number of gamma rays per time bin detected in two opposite detectors will add in quadrature in the difference of the asymmetries. For this reason it is important to know how much is the contribution of the two sources of statistical errors. A quick way to estimate the statistical errors from counting statistics is to calculate the ratio of the pulse average detector signal for two opposite detectors (d_1 and d_2), for each accepted spin sequence (s) in a run (r). The pulse index k runs from 0 to 7.

$$\bar{D}_{d_1,k} = \frac{1}{T_2 - T_1 + 1} \sum_{t=T_1}^{T_2} D_{d_1}(k,t) \; ; \;\; \bar{D}_{d_2,k} = \frac{1}{T_2 - T_1 + 1} \sum_{t=T_1}^{T_2} D_{d_2}(k,t) \quad \text{(6.17)}$$

$$R_{d_1,d_2,k} = \frac{\bar{D}_{d_1,k}}{\bar{D}_{d_2,k}} \tag{6.18}$$

Because the contribution of the transient is negligible in the last four pulses of the spin sequence, the average ratio U_{d_1,d_2} is calculated over pulses k=4, 5, 6 and 7:

$$U_{d_1,d_2} = \frac{1}{4}\sum_{k=4}^{7} R_{d_1,d_2,k} \tag{6.19}$$

For each spin sequence the relative squared standard deviation in the ratio R_k is calculated. The average over all good spin sequences in a run

$$\sigma_{d_1,r}^2 = \frac{1}{N_r}\sum_{s=1}^{N_r}\frac{1}{2}\cdot\frac{4}{3}\sum_{k=4}^{7}\frac{(R_{d_1,d_2,k} - U_{d_1,d_2})^2}{4U_{d_1,d_2}^2} \tag{6.20}$$

To calculate the variance for the other detector d_2 in the pair it is justified to change the order of the detector indexes in equations 6.19 and 6.20:

$$R_{d_2,d_1,k} = \frac{\bar{D}_{d_2,k}}{\bar{D}_{d_1,k}} U_{d_2,d_1} = \frac{1}{4}\sum_{k=4}^{7} R_{d_2,d_1,k} \tag{6.21}$$

$$\sigma_{d_2,r}^2 = \frac{1}{N_r}\sum_{s=1}^{N_r}\frac{1}{2}\cdot\frac{4}{3}\sum_{k=4}^{7}\frac{(R_{d_2,d_1,k} - U_{d_2,d_1})^2}{4U_{d_2,d_1}^2} \tag{6.22}$$

The factor $4/3$ accounts for the removal of one degree of freedom taken by the calculation of the average ratio U. Because two opposite detectors contribute equally to the uncertainties of the counting statistics the factor of $1/2$ is introduced.

The final variance due only to counting statistics is the weighted sum of the inverses of the variances calculated at each run.

$$\frac{1}{\sigma_R^2} = \sum_{r=1}^{NR}\frac{N_r}{\sigma_{d,r}^2} \tag{6.23}$$

The sum is over all the good runs analyzed and N_r is the number of accepted spin sequences in a run. The average standard deviation over pulses 4, 5, 6, 7 and all accepted spin sequences is calculated for each detector presented in
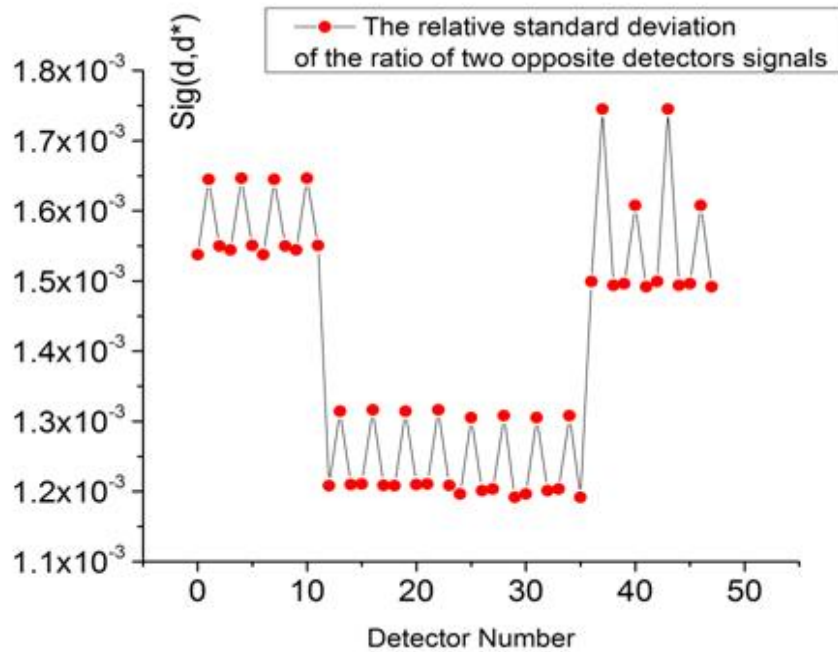
Figure 6.2: The relative standard deviation σ (d, r) averaged over 4 pulses (4, 5, 6, 7) and over all good spin sequences in 587 runs, is calculated for each detector.

Figure 6.2. The standard deviation does not depend on the number of runs.

The fractional standard deviation given by equation 6.23 is presented in Figure

6.3. Because there are about 2000 good Al runs, the fractional standard

deviation due to the counting statistics is expected to be between $5 \cdot 10^{-7}$ and

$6 \cdot 10^{-7}$. A plot of the variances of the square of the ratio of opposite detector

signals averaged over pulses 4, 5, 6 and 7 is presented in Figure 6.4.

6.3   Systematic Errors in the Calculation of the Asymmetry

The systematic errors can be instrumental or can arise from the observables

correlated with the direction of the neutron spin neutron spin that contribute to

the false asymmetry in the angular distribution of the gamma rays. The

instrumental systematic errors could be the spin-flipper correlated electronic

pick-up systematic effects, or transient signals from the spin sequencer that is

118
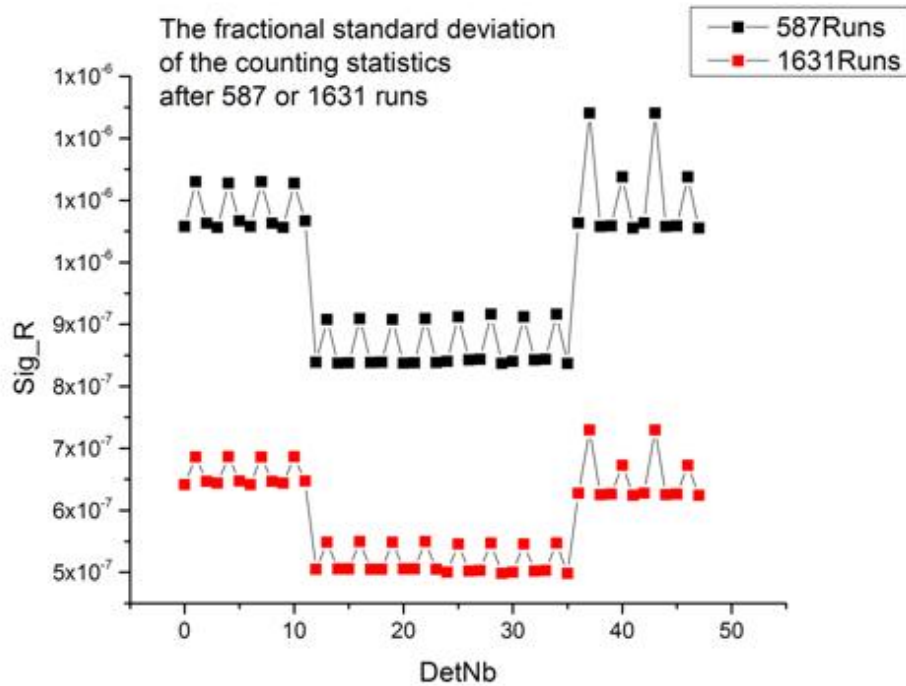
Figure 6.3: The fractional standard deviation due only to the counting statistics is calculated after 587 and 1631 runs for each detector.

mixed with the real detector signal. The upper limit of the spin-flipper electronic pick-up effects can be measured by illuminating the detectors with LED signal and operating the SR in the same conditions like those for beam-on measurements.

The systematic errors that arise from the interaction of the polarized neutrons with nuclei other than H_2 (Al, Lithium, steel shield) or with magnetic field can give rise to additional contribution to the asymmetry measured with the H_2 target. The Al left-right parity-conserving asymmetry involves the correlation between the vector product of neutron spin and momentum of incident neutron $\vec{S}_n \times \vec{k}_n$ with the momentum of the neutron after interaction $\vec{k'_n}$ (the spin-orbit coupling) or with the momentum of the gamma ray after

119
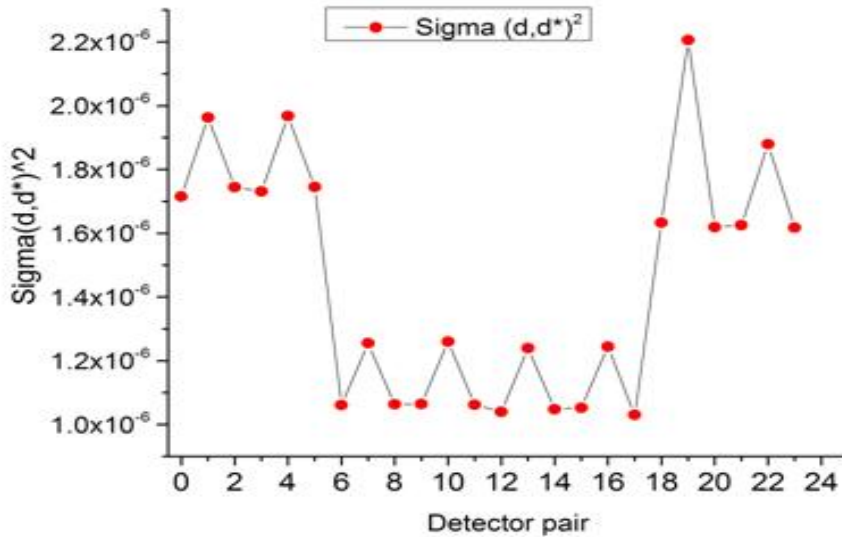
Figure 6.4: A plot of the variances of the relative difference in the detector signals averaged over pulses 4, 5, 6, 7 and over all spin sequences

.

scattering $\vec{k_\gamma^l}$ (the parity-allowed asymmetry in the direct neutron capture). The direction of the gamma rays emitted from the neutrons captured in Al, the direction of the momentum of the electron emitted in the beta decay of ^{28}Al, and the angular distribution of the prompt gamma rays emitted from Al are all correlated with the incident neutron spin. The bremsstrahlung radiation emitted by the accelerated beta particles in the electric field of the parent nucleus ^{28}Si (internal bremsstrahlung) or of the other Al nuclei in the material (external bremsstrahlung) contribute to the background asymmetry. Also the momentum of the electrons or photons emitted in the beta decay of the free polarized neutrons is correlated with the spin of the neutrons. All these effects were calculated and in some cases measured. Their magnitude is smaller or equal with 10^{-8} with the biggest contribution coming from the external bremsstrahlung in Al.

120

The first systematic errors in the Al and Cl asymmetry is related with the transient signal from the Spin Sequencer in the VME3 data acquisition module. The presence of the transient signals mixed with the detector beam signal was discovered after the collection of the Al and Cl data. The calculation of the asymmetry from the ratio of the difference and the sum of detector signals at each time bin showed a negative shift of the 48 detector asymmetries to about $-4 \cdot 10^{-7}$. The signal of the monitor M_1 was measured with a 9 Volts battery connected to the M_1 channel to understand the source of the external signals overlapped with the detector signal (Figure 6.5). The transient signal is generated during the 9th pulse at the end of each spin sequence, when the data were transfered to the disk. During this short time a transient signal with an exponential time decay is generated in the Spin Sequencer and mixed with the detector beam signal collected during the next spin sequence. The relative amplitude of the transient relative to the detector signal is between $-2 \cdot 10^{-5}$ and $-1 \cdot 10^{-4}$ and the decay time is about 0.01 seconds or 24 time bins. The instrumental systematic errors that are not correlated with the neutron spin can only shift the center of the asymmetry for all 12 detectors in each ring with the same quantity. The shift is smaller than 10^{-8} if the asymmetry is calculated for detector pairs. The up-down and left-right asymmetries are calculated after dividing the two fitting parameters (A_1, B_1) in the chi2 function with the neutron beam polarization P and SR efficiency ϵ_{sf} and neutron spin flip scattering in the target Δ_{dep}. The fitting parameter also depend on the geometry factors $G_d{}^{UD}$ and $G_d{}^{LR}$. The non-random errors in the calculations of the neutron polarization, SR efficiency, neutron spin flip scattering and geometry factors are the source of systematic errors in the calculation of the asymmetry. The systematic error in the asymmetry calculation is proportional with the

121

asymmetry and therefore are smaller than the statistical errors expected from

beam intensity fluctuations and counting statistics:

$$\frac{\sigma_{sys}}{A_\gamma} = \sqrt{\left(\frac{\sigma_P}{P}\right)^2 + \left(\frac{\sigma_{sf}}{\epsilon_{sf}}\right)^2 + \left(\frac{\sigma_G}{G}\right)^2 + \left(\frac{\sigma_{dep}}{\Delta_{dep}}\right)^2} \qquad (6.24)$$

The uncertainties in the measured beam polarization and SR efficiency

are 2% and 1% respectively. The spin flip depolarization in the target was

estimated from the geometry of the Al and Cl target to be 1%. The average

uncertainty in the geometry factors for the 48 detectors is 5.27%. Therefore the

relative systematic errors for the four contributions is equal with 5.8%. The

most important sources of systematic errors are therefore related with the

interference of transient signals with the detector signals and the physical

processes due the external bremsstrahlung and strong and electromagnetic

spin-orbit neutron scattering in Aluminum.
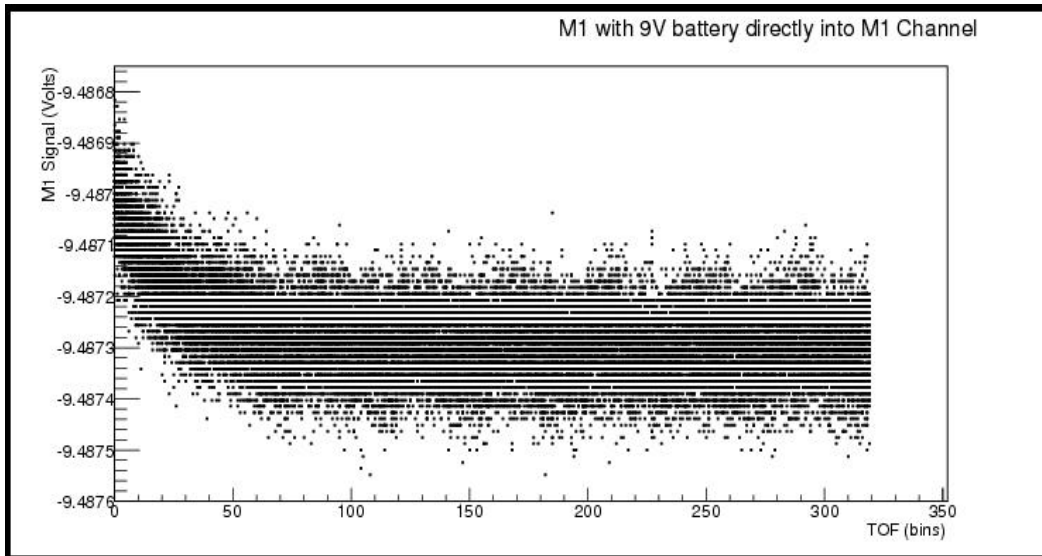
Figure 6.5: The standard deviation of the ratio of two opposite detector signals averaged over a pulse was calculated from the histograms for each pair.

If the asymmetry is calculated for each detector with the arithmetic

122

mean, then the shift in the asymmetry averaged over 48 detectors is between -10^{-7} and $-8 \cdot 10^{-7}$. When the asymmetry is calculated for detector pairs with the geometry mean, the average shift in the asymmetry is smaller than 10^{-8}. The analytical calculation of the ratio of opposite detector signals (section 6.1) the false asymmetry due to the transient signal is reduced with two orders of magnitude in this case.

The second source of instrumental systematic errors were discovered from the measurements of the detector signal when the pair of light emission diodes (LEDs, located inside each detector) were turned on. The measurements were done with the SR turned on or off and in the absence of the beam. The results indicate the presence of a second transient additive signal that seems to be ring dependent and is due to the mixing between output signal of the Spin Sequencer and the signal from the sum and difference for the four detector rings. The decay time and the amplitude of the transient signal relative to the pulse average detector signal is calculated in the next section. To calculate the parity in the presence of the transient it is necessary to calculate all three fitting parameters (the transient amplitude, decay time, and parity) by the minimization of the χ^2 function. In order to cancel the beam intensity fluctuations the ratio of the signals of the two opposite detectors in a ring is calculated at each time bin. In section 6.7 the average detector signal is calculated for each pulse in the spin sequence and is divided with the spin sequence average of the detector signal. This procedure does not eliminate the fluctuations in the beam intensity at each pulse. However the procedure can be used to calculate the relative transient signal and the transient decay time for each spin sequence. The calculation of the asymmetry from the ratio of the opposite detectors signals at each time bin,

averaged over four pulses with spin up, multiplied with the inverted detector ratio average over four pulse with spin down is presented in section 6.1.

The Al asymmetry ratio is calculated for each sequence that passed the four cuts described in section 5.4. Most Al data runs had 3750 entries except the first few data runs that had 2500 entries. Each entry in the data run is a record of the detector signal for eight pulses. Each pulse is 1/60 seconds long such that the time for one data entry is 9/60 seconds. The first bit in each 9 pulse entry is the header quality bit that is equal with zero for the correct SR sequence. The entry was not analyzed if the header quality bit was not zero.

6.4 The Stern-Gerlach Contribution to the False Asymmetry

The neutrons are moving in the static field of the main and shim coils from the exit of the SMP to the beam stop. The field gradient interacts with the neutron magnetic moment to shift the neutron position. The displacement of the neutron beam center along the vertical and horizontal axes normal to the beam is the source of a false asymmetry because the gamma yield in a detector depends on the position of the neutron beam center. The neutron has spin $1/2$ and a magnetic moment $\mu_n = -9.6623 \cdot 10^{-27}$ (J/T). Considering $\mu_N = 5.0508 \cdot 10^{-27}$ (J/T) , g_n=-3.826 the neutron g-factor and $\vec{S}$ the neutron spin, the force acting on the neutron with magnetic moment $\vec{\mu} = g_n(\mu_N/\hbar)\vec{S}$ moving in a non-uniform magnetic field is given by the relation:

$$\vec{F} = -\frac{2\mu_n}{\hbar}\vec{\nabla}(\vec{S} \cdot \vec{B}) \tag{6.25}$$

The magnetic moment of the free neutron along the vertical y direction is $\mu_y = g_n\mu_N \cdot m_s = \pm\mu_n$ where $m_s = \pm 1/2$ is the neutron magnetic number. For simplicity consider the vector $\vec{\sigma} = 2\vec{S}/\hbar$ along the direction of the neutron

124

spin. The three components of $\vec{\sigma}$ can be ± 1. The force components along the x, y and z axes are given by the relations:

$$F_x = -\mu_n(\sigma_x \cdot \frac{\partial B_x}{\partial x} + \sigma_y \cdot \frac{\partial B_y}{\partial x} + \sigma_z \cdot \frac{\partial B_z}{\partial x}) \qquad (6.26)$$

$$F_y = -\mu_n(\sigma_x \cdot \frac{\partial B_x}{\partial y} + \sigma_y \cdot \frac{\partial B_y}{\partial y} + \sigma_z \cdot \frac{\partial B_z}{\partial y}) \qquad (6.27)$$

$$F_z = -\mu_n(\sigma_x \cdot \frac{\partial B_x}{\partial z} + \sigma_y \cdot \frac{\partial B_y}{\partial z} + \sigma_z \cdot \frac{\partial B_z}{\partial z}) \qquad (6.28)$$

The force components F_x and F_y displace the beam center in the x and y directions such that the false asymmetry will add to the measured left-right and up-down directions. Due to the neutron spin precession about the static magnetic field aligned with the vertical axis, the time average of the components of the neutron spin in the horizontal plane xz is zero. In general the angle between the magnetic field vector and the z axis is θ and the angle between the field projected in the xy plane and the x axis is ϕ. In this semi-classical approach the neutron spin is aligned with the direction of the field such that:

$$\langle F_x \rangle = -\mu_n(\frac{B_x}{B} \cdot \frac{\partial B_x}{\partial x} + \frac{B_y}{B} \cdot \frac{\partial B_y}{\partial x} + \frac{B_z}{B} \cdot \frac{\partial B_z}{\partial x}) = -\mu_n \frac{\vec{B}}{B} \cdot \frac{\partial \vec{B}}{\partial x} \qquad (6.29)$$

$$\langle F_y \rangle = -\mu_n(\frac{B_x}{B} \cdot \frac{\partial B_x}{\partial y} + \frac{B_y}{B} \cdot \frac{\partial B_y}{\partial y} + \frac{B_z}{B} \cdot \frac{\partial B_z}{\partial y}) = -\mu_n \frac{\vec{B}}{B} \cdot \frac{\partial \vec{B}}{\partial y} \qquad (6.30)$$

The F_z component of the force cannot produce a false asymmetry in the gamma ray angular distribution relative to two directions normal to the beam axis. The average angles of the field and the average magnetic field gradients were calculated from the magnetic field measurements. The average field

125

Table 6.1: The relative field components and the field gradients along the three axes and the components of the Stern Gerlach force.

B_x/B 10^{-3}	B_y/B	B_z/B 10^{-3}	dB_x/dx 10^{-5} T/m	dB_y/dx 10^{-5} T/m	dB_z/dx 10^{-5} T/m
3.63	0.9998	1.13	0.40 $\pm$ 0.12	1.01 $\pm$ 0.03	0.41 $\pm$ 0.02
dB_x/dy T/m 10^{-5}	dB_y/dy T/m 10^{-5}	dB_z/dy T/m 10^{-5}	dB_x/dz T/m 10^{-5}	dB_y/dz T/m 10^{-5}	dB_z/dz T/m 10^{-5}
1.41 $\pm$0.29	1.68 $\pm$0.11	1.47 $\pm$ 0.36	0.40 $\pm$ 0.01	0.048 $\pm$ 0.007	1.67 $\pm$ 0.01
F_x/μ_n T/m 10^{-5}	F_y/μ_n T/m 10^{-5}	F_z/μ_n T/m 10^{-5}	a_x m/s^2 10^{-5}	a_y m/s^2 10^{-5}	a_z m/s^2 10^{-5}
1.02 $\pm$0.03	1.69 $\pm$0.11	0.052 $\pm$0.001	5.84 $\pm$0.17	9.70 $\pm$0.63	0.30 $\pm$0.01

inside the coils was 9.77 Gauss. After passing the SR the neutron spin was rotated with 180 degrees. The average field gradients were calculated from the measured gradients along horizontal and vertical directions in the limits of the beam volume and between SR and detector. The absolute values of the average field gradients and the components of the Stern-Gerlach force are calculated in the table 6.1.

The neutron displacements Δx and Δy were calculated for a distance $l = 1$ meter between the center of the SR and the center of the detector array and for neutrons with wavelengths between 2.3 Åand 6Å. If the neutron is moving parallel with the beam axis then the displacements are equal with:

$$\Delta x = \frac{\langle F_x \rangle}{m} \frac{l^2}{2 \cdot v^2} \tag{6.31}$$

$$\Delta y = \frac{\langle F_y \rangle}{m} \frac{l^2}{2 \cdot v^2} \tag{6.32}$$

$$\frac{\langle F_x \rangle}{m} = \frac{9.6623 \cdot 10^{-27}}{1.6749 \cdot 10^{-27}} \left(\frac{B_x}{B} \cdot \frac{\partial B_x}{\partial x} + \frac{B_y}{B} \cdot \frac{\partial B_y}{\partial x} + \frac{B_z}{B} \cdot \frac{\partial B_z}{\partial x} \right) \tag{6.33}$$

The maximum displacement occurs for neutrons with the smallest speed $v = 590$ m/s:

$$\Delta x = \frac{\langle F_x \rangle}{m} \frac{l^2}{2 \cdot v^2} = 0.83 \cdot 10^{-10} \tag{6.34}$$

$$\Delta y = \frac{\langle F_y \rangle}{m} \frac{l^2}{2 \cdot v^2} = 0.15 \cdot 10^{-9} \tag{6.35}$$

The false asymmetry for each detector is equal with the difference of the acceptance solid angles for the two directions of the neutron spin divided with the sum of the two solid angles:

$$A_f = \frac{\Omega_{up} - \Omega_{down}}{\Omega_{up} + \Omega_{down}} \tag{6.36}$$

The distance from the detector center on the beam axis to the center of any detector is approximately $r_0 = 0.286$ m. The false asymmetry will be calculated for pair detector D_1 centered at (x_c, y_c, z_c). To calculate the contribution to the left-right asymmetry, consider first the displacement in the x direction. The solid angles for the two directions of the neutron spin are:

$$\Omega_{up} = \frac{\Delta A}{r_0^2 - 2x_c\Delta x + \Delta x^2} \cong \frac{\Delta A}{r_0^2}\left(1 + \frac{2x_c\Delta x}{r_0^2}\right) \tag{6.37}$$

$$\Omega_{down} = \frac{\Delta A}{r_0^2 + 2x_c\Delta x + \Delta x^2} \cong \frac{\Delta A}{r_0^2}\left(1 - \frac{2x_c\Delta x}{r_0^2}\right) \tag{6.38}$$

In general the displacement vector is $\Delta \vec{r} = \Delta x \cdot \hat{x} + \Delta y \cdot \hat{y}$ such that the false asymmetry is equal with:

$$A_f = \frac{\Omega_{up} - \Omega_{down}}{\Omega_{up} + \Omega_{down}} = \frac{2\vec{r}_0\Delta\vec{r}}{r_0^2} \leq \frac{2\Delta r}{r_0} \tag{6.39}$$

Therefore the false asymmetry due to the Stern-Gerlah effect is expected to be $0.12 \cdot 10^{-8}$. This values is smaller than 10^{-8}, the experimental limit due to the statistical errors.

6.5 The Contribution of the Spin-Orbit Interaction

Spin orbit interaction appear in both strong and electromagnetic NN interactions. The center of a neutron beam polarized along the vertical axis is displaced along the horizontal direction normal to beam axis, after interacting with the nuclei in a target. The direction of the displacement depends on the initial direction of neutron spin. The effect was explained for the first time by Schwinger [75]. The calculation of the false asymmetry in the measurement of the parity conserving asymmetry was done for liquid para H_2, Al and other nuclei in [61]. The neutron capture cross section is proportional with $1/v$ and at low neutron energies the contribution of the strong interaction to the interference between elastic and inelastic processes (n, n') (n, α), (n, γ) becomes relevant.

Consider the neutron moving along the z axis with momentum $\vec{p}_1$ and the target nucleus fixed at a distance b from the z axis. The distance b is smaller than the atomic radius a but bigger than the radius of the nucleus R such that the neutron and the nucleus interact only through electromagnetic forces. After scattering the neutron has momentum $\vec{p}_2$. The spin of the neutron
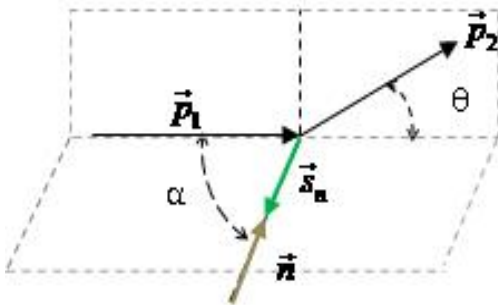
Figure 6.6: The direction of the initial and final neutron moment, the neutron spin and the scattering angles are presented in three dimensions.

128

$\vec{s_n}$ (Figure 6.6) is along the direction of the vector $\vec{n} = (\vec{p_1} \times \vec{p_2})/|\vec{p_1} \times \vec{p_2}|$ normal to the reaction plane of the neutron. The analyzing power is the relative difference in the cross sections when the spin of the neutron is aligned parallel (+) or opposite (-) to the direction of the vector $\vec{n}$. In the frame of the neutron, the nucleus is moving with a velocity $\vec{v}$. The moving electric field generates a magnetic field at the position of the neutron:

$$\vec{B} = \frac{\vec{E} \times \vec{v}}{c^2} \tag{6.40}$$

If ϕ is a spherical symmetric effective potential, then the electric field is $\vec{E} = -\nabla\phi$ and the electric potential $V(r) = -e\phi$. In this case the magnetic field is equal with $\vec{B} = \frac{1}{e}\frac{dV}{dr}\left(\frac{\vec{r}}{r} \times \frac{\vec{v}}{c^2}\right)$. In general b can be smaller than the radius of the nucleus such that the interaction involves both strong and electromagnetic forces. In this case the scalar product of the neutron magnetic moment and the magnetic field is added to the strong potential V_s in the total Hamiltonian of the spin-orbit interaction:

$$H = V_s - \vec{\mu} \cdot \vec{B} \ . \tag{6.41}$$

With the neutron g-factor $g_n = -3.826$ and M_p the mass of the proton, the relation between the neutron magnetic moment $\vec{\mu}$ and neutron nuclear spin $\vec{S}$ is given by:

$$\vec{\mu} = -g_n \frac{e}{2 \cdot M_p}\vec{S} \ . \tag{6.42}$$

With the ratio $g_n/2$= - 1.913 and the nuclear magneton $\mu_N = (e\hbar)/(2M_p)$, the electromagnetic part of the interaction is equal with:

$$H_{em} = \frac{g_n}{2M_pM_n \cdot r \cdot c^2}\frac{dV}{dr}(\vec{S} \cdot \vec{L}) \tag{6.43}$$

In the above equation M_n and M_p are the mass of the neutron and proton respectively. Due to the screening of the electrons in the atom, the effective

129

charge Q of the nucleus seen by the neutron is smaller than the charge of the protons in the nucleus $Z \cdot e$. If the electric potential of the nucleus has spherical symmetry then $V(r) = -(e \cdot Q)/r$ and the electromagnetic spin-orbit interaction is inversely proportional with r^3. The waves scattered at an angle θ are generated at a distance r from the nucleus such that $2p \cdot r \cdot sin(\theta)/2 \approx \hbar$ with $p = \hbar k$. Therefore the electromagnetic scattering occurs for the range of scattering angles [75]: $1/(k \cdot R) \gg 2\sin(\theta/2) \gg 1/(k \cdot a)$.

The calculation of the strong and electromagnetic contributions to the analyzing power was done in [61] to provide an estimate of the left-right asymmetry. Their analysis of the spin -orbit scattering of low energy neutrons is presented here. The analyzing power is the difference between the neutron capture cross section for the two states of the neutron spin:

$$A(r) = \frac{d\sigma/d\Omega_+ - d\sigma/d\Omega_-}{d\sigma/d\Omega_+ + d\sigma/d\Omega_-} \tag{6.44}$$

The analyzing power can be expressed as a function of the coherent $g(\theta)$ and incoherent $h(\theta)$ scattering lengths. Because the strong interaction is spin dependent, the total coherent scattering length $g(\theta)$ is a sum of the scattering lengths for all the nuclear spin states. The inelastic and the capture processes are more probable at low energy of the neutron because the cross section varies like $1/v$. The inelastic processes contribute to the imaginary part of the scattering length of the strong interaction:

$$g(\theta) = g_{el}(\theta) + g_{in}(\theta) \tag{6.45}$$

At low energy the most relevant contribution to $g(\theta)$ is only from the neutrons in S wave state. Consider $P(0)$ and $P(1)$ the projection operators onto the spin state $S = 0$ and $S = 1$ respectively. The phase shift in the neutron scattered

130

wave in singlet and triplet S wave states are $\delta_0(^1S_0)$ and $\delta_1(^3S_1)$ respectively. For a neutron with momentum k the elastic contribution to the scattering length of the strong interaction is equal with:

$$g_{el}(\theta) = \frac{1}{k} \left[\begin{array}{c} P_0[\delta_0(^1S_0) + i\delta_0^2(^1S_0)] + \\ P_1[\delta_1(^3S_1) + i\delta_1^2(^3S_1)] \end{array} \right] \tag{6.46}$$

If the amplitude of the neutron capture is a_c then the contribution of the inelastic channels to the cross section is given by:

$$\sigma_{in}(\theta) = \frac{4\pi a_c}{k} \tag{6.47}$$

The inelastic scattering length can be calculated from the optical theorem : $g_{in}(\theta) = i \cdot a_c \cdot P(1)$. For Al the contribution of the electromagnetic part of the spin-orbit interaction to the analyzing power is between $2 \cdot 10^{-8}$ and $6 \cdot 10^{-8}$. The bound coherent and incoherent scattering lengths are $b_c = 3.45$ fm and $b_{ic} = 0.26$ fm respectively, where 1 fm = 10^{-15} m. The analyzing power due to both strong and electromagnetic interaction for 9 meV neutron and a $45°$ neutron scattering angle is $1.4 \cdot 10^{-7}$. There is also an additional contribution from the left-right parity-conserving asymmetry due to direct neutron capture [29, 76]. This contribution was not calculated yet for low energy neutrons captured in Al. The calculated spin-orbit analyzing power for Aluminum is about 30% smaller than the left-right asymmetry extracted from the Aluminum data (section 6.8).

6.6   Asymmetry Contribution of the Bremsstrahlung Radiation

After the capture of polarized neutron in ^{27}Al the excited ^{28}Al is partially polarized in the direction of the incident neutron spin. A fraction of the ^{28}Al polarization is carried away by the prompt gamma rays emitted at the transition to the ground state. The asymmetry in the angular distribution of the promt

gamma rays is the main source of the background contribution to the asymmetry measured with the H_2 target. In the ground state ^{28}Al beta decays in ^{28}Si. Because the weak interaction does not conserve parity, the direction of the emitted electron is correlated with the spin of the polarized ^{28}Al nucleus. The radiation emitted from the accelerated beta particle in the electric field of the parent nucleus ^{28}Si (internal bremsstrahlung) or from the beta particle moving through the material (external bremsstrahlung) is correlated with the direction of the momentum of the beta particle and with the direction of the neutron spin due to the weak interaction. In addition some of the free neutrons in the beam can decay into protons, electrons and neutrinos. The direction of the electron is correlated with the neutron direction due to the parity violation in the neutron decay. The delayed gamma radiation emitted at the transition of excited ^{28}Si in its ground state can also have an asymmetry in its angular distribution because the Si nucleus has a small polarization. All these three contributions to the false asymmetry are expected to be smaller for the NPDGamma experiment at SNS compared with LANSCE because the frequency of the neutron pulses (60 Hz) is three times bigger than that at LANSCE (20Hz). However previous calculations indicated that the external bremsstrahlung in Al is only one order of magnitude smaller than the predicted size of the $\vec{n} + p \rightarrow d + \gamma$ parity-odd asymmetry [21].

The half life of ^{28}Al (2.4 minutes) is large relative to the time interval (1/60 s) between two neutron spin flips. In addition the electromagnetic transition further reduces the correlation between the neutron spin and the spin of the compound ^{28}Al nucleus. The spin of ^{27}Al in its ground state is 5/2. The state has positive parity. Therefore the S-wave capture state of ^{28}Al can have an angular momentum of 2 or 3. After the polarized neutron is captured the

132

^{28}Al is also polarized. The polarization of ^{28}Al in the ground state was estimated by calculating the population of the magnetic states in the capture state and modeling the gamma decay process by assuming either three , four or five transitions [21] . The estimated polarization of ^{28}Al is 0.16+/-0.03. The interaction with the magnetic field of the conduction electrons and the spin-lattice interaction decreases the relaxation time of polarized ^{28}Al. It was found that the main contribution to the systematic error due to the Al asymmetry comes from external bremsstrahlung (10^{-8}) in the ^{28}Al beta decay while the internal bremsstrahlung in the same process is small, $0.2 \cdot 10^{-9}$. The asymmetry of the prompt gamma rays emitted at the transition of exited ^{28}Al to the ground state was measured and the results are presented in section 6.8. The asymmetry in the distribution of the delayed gamma rays emitted at the transition of ^{28}Si in the ground state is negligible. The neutrons spin-electron correlation in the free beta decay is A_{s_n,k_β} =-0.117 [77]. At LANSCE the fraction of neutrons that decay before stopping in the H$_2$ target was $2.5 \cdot 10^{-7}$ [21] such that the contribution of the external and internal bremsstrahlung from the free neutron beta decay to the false asymmetry were $3 \cdot 10^{-11}$ and $2.4 \cdot 10^{-11}$, respectively.

6.7 Transient Correction in the Pulse Average Detector Signals

The detector signal is the sum of the neutron beam signal (at 60 Hz) due only to the gamma rays from the neutrons captured or inelastically scattered in the Al target, and a transient exponential signal. The weak time dependence of the parity $P(t)$ due to the small neutron time of flight dependence of the polarization efficiency of the Super Mirror Polarizer is neglected. The time t and the decay time τ are considered to be in units of one time bin (1/60/40 seconds). The signal for each detector, during a spin sequence number S, and

time bin t in a pulse number (k=0...7) is given by:

$$D_{s,k}(t) = f \cdot I_k(t)(1 + P \cdot s_k) + V \cdot e^{-(t+k\cdot T)/\tau} \qquad (6.48)$$

In the above relation f is the detector gain, the transient amplitude and decay time are V and τ, and s_k is +1 or -1 for pulses with neutron spin up or spin down respectively. For the SR sequence used during the Al data runs (June, July 2011) the array of eight integers is equal with:

$$s_k = \{-1; 1; 1; -1; 1; -1; -1; 1\} \qquad (6.49)$$

The pulse average detector signal is different for each pulse due to the beam fluctuations. The fitting function is obtained from the right hand side of equation 6.48 with the approximation:

$$f\bar{I}_k \cong h\bar{I} = W \qquad (6.50)$$

The other fitting parameters are the parity P, the decay parameter q and the relative transient amplitude v:

$$v = \frac{V}{f\bar{I}} \qquad (6.51)$$

The fitting parameters were calculated for each spin sequence from the derivatives of a χ^2 function with no weights:

$$\chi_e^2 = \sum_{k=0}^{7} \left(\bar{D}_k - W(1 + Ps_k + vs_t q^k)\right)^2 \qquad (6.52)$$

The fitting parameters w, P, v , q do not change if the above χ^2 function is divided with a constant like for example the square of the average detector signal in a spin sequence. Because the detector signal is read in ADC counts, D_k is a big number but the ratio D_k/D_s is a number close to unity. The normalized χ^2 function is given by:

$$\chi_n^2 = \sum_{k=0}^{7} \left(R_k - w(1 + P \cdot s_k + v \cdot s_t q^k)\right)^2 \qquad (6.53)$$

$$R_k = \frac{\bar{D}_k}{\bar{D}_s} \tag{6.54}$$

After the fitting parameters are calculated, w is multiplied back with D_s to get its value in the original (not normalized) χ^2 function.

From the derivatives of the χ^2 function (eq. 6.53) the equations for P, v are given by:

$$w = \frac{\sum_{k=0}^{7} R_k(1 + Ps_k + vs_t q^k)}{\sum_{k=0}^{7}(1 + Ps_k + vs_t q^k)^2} \tag{6.55}$$

$$\frac{\sum_{k=0}^{7} R_k s_k}{8 \cdot w} = P + vs_t \frac{\sum_{k=0}^{7} s_k q^k}{8} \tag{6.56}$$

$$\frac{\sum_{k=0}^{7} R_k q^k}{8w} = \frac{\sum_{k=0}^{7} q^k}{8} + P\frac{\sum_{k=0}^{7} s_k q^k}{8} + vs_t \frac{\sum_{k=0}^{7} q^{2k}}{8} \tag{6.57}$$

The sums calculated for each detector are:

$$S_0 = \frac{\sum_{k=0}^{7} R_k}{8} \quad S_1 = \frac{\sum_{k=0}^{7} R_k s_k}{8} \quad S_2 = \frac{\sum_{k=0}^{7} s_k q^k}{8} \tag{6.58}$$

$$S_3 = \frac{\sum_{k=0}^{7} q^k}{8} \quad S_4 = \frac{\sum_{k=0}^{7} R_k q^k}{8} \quad S_5 = \frac{\sum_{k=0}^{7} q^{2k}}{8} \tag{6.59}$$

The equations can be solved exactly. The parity is calculated first from the relation:

$$P = \frac{(S_2 S_4 - S_1 S_5)S_1 - (S_0 S_2 - S_1 S_3)S_1 S_3}{(S_2 S_4 - S_1 S_5)S_0 - (S_0 S_2 - S_1 S_3)(S_4 - S_1 S_2)} \tag{6.60}$$

The relative transient amplitude v and w are then calculated:

$$v \cdot s_t = \frac{S_1 S_3 - P(S_4 - S_1 S_2)}{S_2 S_4 - S_1 S_5} \tag{6.61}$$

$$w = \frac{S_0 + P \cdot S_1 + v \cdot s_t S_4}{1 + 2v \cdot s_t \cdot P \cdot S_3 + P^2 + v^2 s_t^2 S_5 + 2P \cdot v \cdot s_t S_2} \tag{6.62}$$

The corrected Al asymmetries for each detector are presented in Figure 6.7. A positive shift in the average over all detector asymmetries indicate that there are additional transient signals not included in the fitting function. When
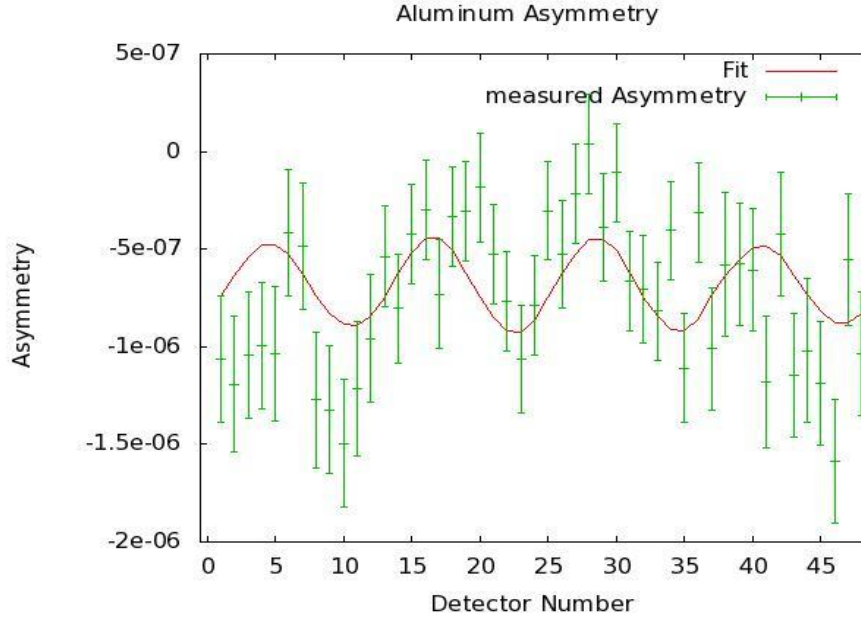
Figure 6.7: The asymmetry ratio for Al, for each detector is averaged over all good spin sequences in 2000 runs. The red line is the fit with the 48 detector geometry factors.

the detector asymmetry was calculated for fitting functions with an extra constant or a linear time depending term in addition to the exponential transient, the asymmetry shift was still present.

Figure 6.7 presents the average relative transient amplitude and its standard error that are read from 48 histograms at the end of the loop over runs. The fitting parameters are $A_1 = (-1.31 \pm 0.693) \cdot 10^{-7}$, $B_1 = (2.33 \pm 0.69) \cdot 10^{-7}$ and $C = (-6.85 \pm 0.42) \cdot 10^{-7}$, for a reduced χ^2=1.49 and goodness of the fit Q=0.017 . The error bars are calculated from the error matrix at the end of the runs. The up-down and left-right asymmetries are $A_{ud} = (-1.42 \pm 0.75) \cdot 10^{-7}$ and $A_{lr} = (2.53 \pm 0.75) \cdot 10^{-7}$. The relative transient amplitude v and the decay parameter ($q_1 = exp(-1/\tau)$) are calculated also from the fit , for each spin sequence. The results agree with the

136
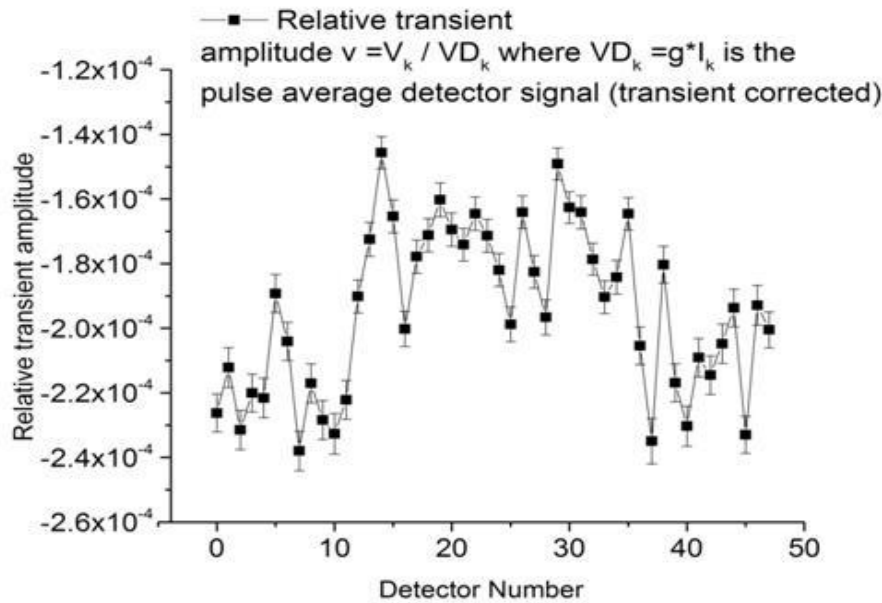
Figure 6.8: The relative transient amplitude is calculated for each accepted spin sequence and each detector number from the minimization of the χ^2 function.

transient amplitude and decay times extracted from the fit of the measured transient signal when a 9 Volts battery was connected to the ADC inputs of the 12 sum/difference modules for a detector ring [78].

The uncertainty in the relative transient amplitude is due to both the beam fluctuations and the counting statistics. The beam fluctuations hide out the transient signal making the fit calculations at each spin sequence not reliable. In Figure 6.9 the decay parameter is calculated for each detector and each accepted spin sequence in the 2000 runs and saved in a histogram.

A plot of the pulse average detector voltage can be seen in Figure 6.10. The average is done over all eight pulses in a spin sequence. For each good spin sequence the fitting parameters w, P, v and q were calculated from the minimization of the normalized χ^2 function. After the four fitting parameters are calculated, the relative fitting constant w was then multiplied with the average

137
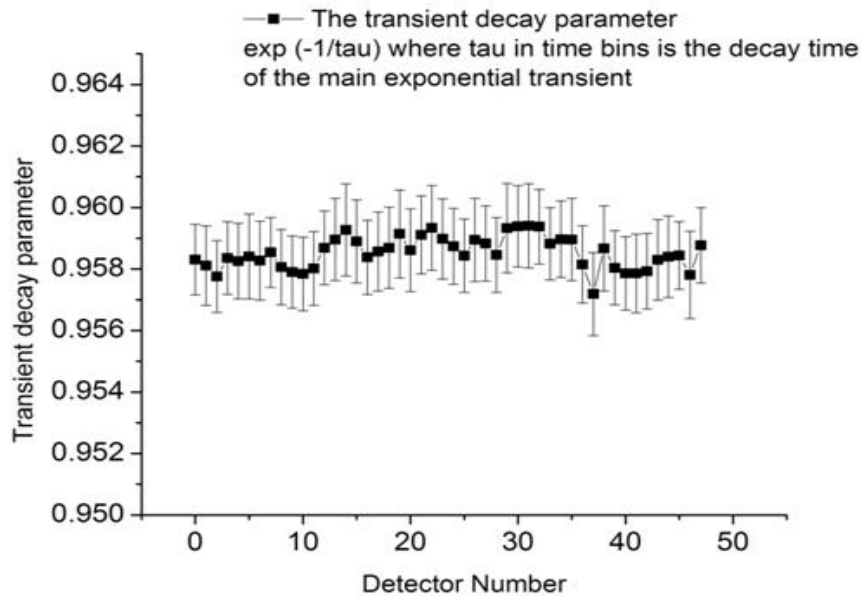
Figure 6.9: The average decay parameter over all accepted spin sequences is calculated from 48 histograms.

detector signal in the spin sequence to calculate W in units of volts. This was done for all good spin sequence in all runs.

One could conclude that the beam fluctuations makes the extraction of the asymmetry from the fit not reliable. The scatter plot of the relative amplitude calculated for each spin sequence is presented in Figure 6.11. The addition of another linear transient term to the fitting function did not decrease the spread in the relative transient amplitude.

The effect of the transient signals mixed with the detector rings sum and difference signals cannot be eliminated from the fit of the eight pulse average detector signals. A complete correction is possible in the ratio of opposite detector signals for each time bin, if all the transient signals are included in the fitting model. This procedure was described in the section 6.1.
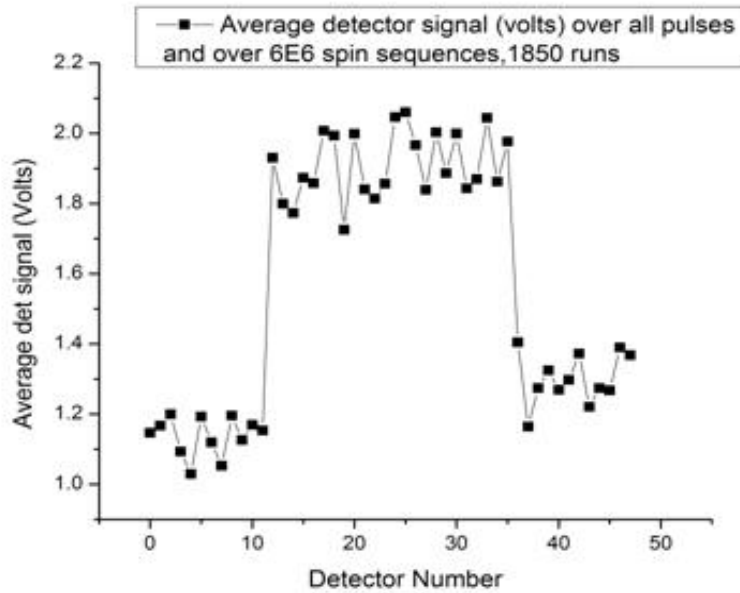
Figure 6.10: The average detector signal in volts is calculated over all good spin sequences in 1850 Al runs.
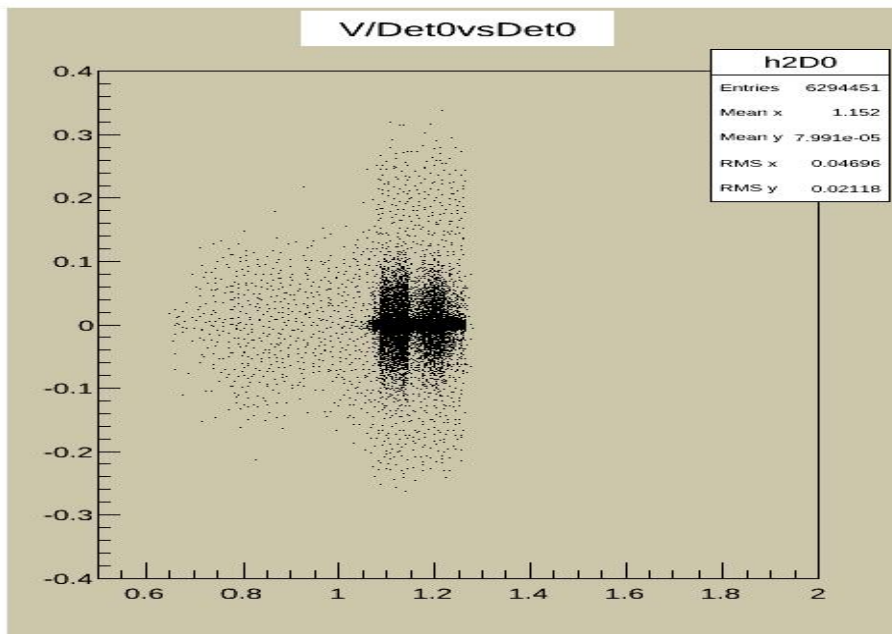
Figure 6.11: A scatter plot of the relative transient amplitude versus the average detector voltage in a spin sequence, is accumulated over $6.29 \cdot 10^6$ accepted spin sequences.

139

6.8 Asymmetry Measurements for Aluminum

The most important background contribution to the measurement of the asymmetry in the $\vec{n} + p \rightarrow d + \gamma$ reaction are the gamma rays emitted from the neutrons captured in the Al walls of the liquid H_2 target and on the windows of the SR. From the MCNP calculations done for the H_2 target at SNS, the background is expected to be about 15% of to the total measured asymmetry with the H_2 target ([65]). The shift in the measured asymmetry due to the background can be calculated if the asymmetry in Al is known.The Al asymmetry is subtracted from the total asymmetry measured with the liquid H_2 target. To measure the asymmetry in liquid H_2 with an uncertainty better than $1 \cdot 10^{-8}$ the measurement of the Al asymmetry have to be done with a precision better than $4 \cdot 10^{-8}$. If N_p and N_b are the gamma rays yields from neutron capture on H_2 and Al walls respectively, then the total measured asymmetry is equal with:

$$A_{raw} \cdot (N_p + N_b) = A_p \cdot N_p + A_b \cdot N_b \qquad (6.63)$$

The fraction of background signal divided with the proton signal is given by $\epsilon = N_b/N_p$. This fraction can be calculated from MCNPX simulation and is expected to depend on the ring number. After the Al asymmetry is measured, the H_2 asymmetry can be calculated:

$$A_{raw} = A_p \cdot (1 - \epsilon) + A_b \cdot \epsilon \qquad (6.64)$$

The statistical error in the asymmetry measured with the H_2 target is also increased due to the background asymmetry:

$$\sigma_p{}^2 = \frac{\sigma_{raw}^2}{(1 - \epsilon)^2} + \sigma_b^2 \cdot \frac{\epsilon^2}{(1 - \epsilon)^2} \qquad (6.65)$$

The statistical errors in the asymmetry measured with the H_2 target and Al target runs are σ_{raw} and σ_b respectively. The required precision in the measurement of the $\vec{n} + p \rightarrow d + \gamma$ asymmetry is $\sigma_p = 10^{-8}$. The statistical errors for Al are $\sigma_b = 3.5 \cdot 10^{-8}$. To get the required limit of statistical uncertainty $\sigma_p < 10^{-8}$ in the measurement of the asymmetry in $\vec{n} + p \rightarrow d + \gamma$ reaction, the statistical uncertainty in the asymmetry measured with the liquid H_2 target has to be $0.67 \cdot 10^{-8}$, or smaller. This requires about 6 months of continuous data collection.

The Al asymmetry is calculated for each accepted spin sequence, each pair of opposite detectors and for each time bin in the range $[T_1, T_2]$. At each spin sequence the asymmetry is averaged over time bins from $T_1 = 8$ to $T_2 = 38$. If $P = (P_0 - P_6)/2$ is the parity calculated for a pair of opposite detectors then P and $-P$ are the asymmetries that were computed in the two detector histograms, because the geometry factors for two opposite detectors have opposite signs. The first and second detectors in a pair are always located in the first half of the ring (beam right) and in the second half of the ring (beam left) respectively. At the end of the runs the average asymmetry ratio and the standard errors are read from the histograms. A number of 1957 good Aluminum runs were analyzed. The asymmetry for Aluminum, not corrected for the transient, is computed with the first geometry method and a detector signal cut equal with 0.4 and presented in Figure 6.12. The three fitting parameters in Figure 6.12 are: $A_1 = (-6.62 \pm 3.26)10^{-8}$, $B_1 = (2.08 \pm 0.33)10^{-7}$ and the offset C=$(0.06 \pm 1.9)10^{-8}$, for a reduced $\chi^2 = 1.49$ and a goodness of the fit Q=0.198. For a SR efficiency 0.98 ± 0.02 and a neutron polarization 0.94 ± 0.02, the up-down and left right asymmetries are equal with:

$A_{ud} = (-7.19 \pm 3.55)10^{-8}$, $A_{lr} = (2.25 \pm 0.36)10^{-7}$
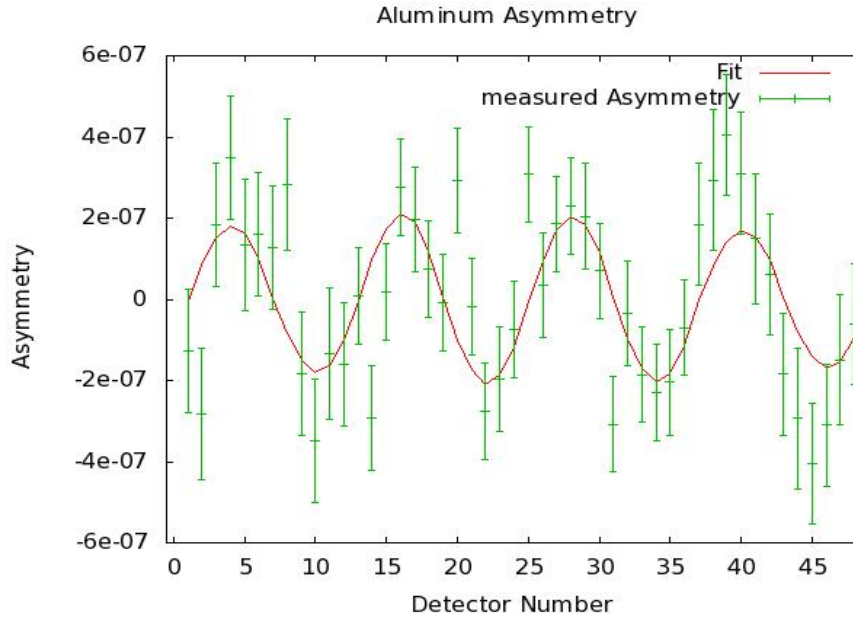
Figure 6.12: The raw asymmetry for 1900 Al runs is calculated from the ratio of the opposite detector signals with the first geometry mean method.

The transient corrected asymmetry was calculated from the fit at each good spin sequence. The standard deviation in the ratio of opposite detector signals was calculated for each pulse and over all accepted spin sequences. The counting statistics contribution to the uncertainty in the asymmetry was calculated from the ratio of opposite detector signals (equation 6.23), and were used for the weights in the χ^2 function. The corrected asymmetry for 1800 Al runs are presented in Figure 6.13. The two asymmetries calculated with transient correction, averaged over CUT4=0.4, 0.6 and 0.8 are equal with:

$A_{ud} = (-7.21 \pm 1.06(\text{stat}) \pm 0.74(\text{sys})) \cdot 10^{-8}$,

$A_{lr} = (2.82 \pm 0.13(\text{stat}) \pm 0.07(\text{sys})) \cdot 10^{-7}$.

The asymmetry ratio was calculated for each time bin, before the correction of the transient, and averaged over all good spin sequences (Figure 6.14). As expected the time bin asymmetry ratio oscillates about zero in

142
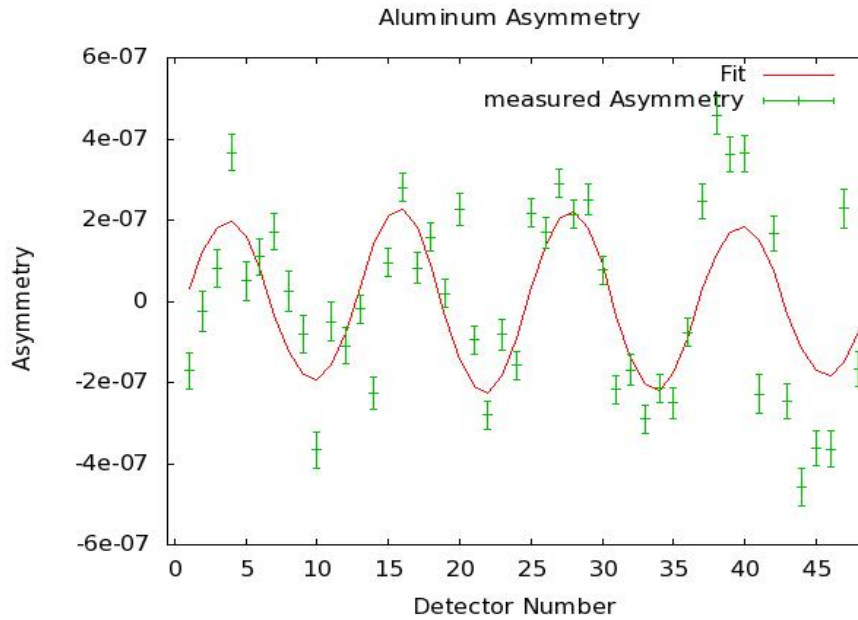
Figure 6.13: The corrected asymmetry for 1800 Aluminum runs is calculated from the ratio of the opposite detector signals with CUT3 equal with 0.3.

contrast with the time depending behavior of the asymmetry ratio calculated from the arithmetic mean (the ratio of detector differences over detector sums). This means that this procedure can correct the transient contribution. The parity violating and parity conserving asymmetries in Al, not corrected for the transient, is calculated for different values for the CUT4 on detector signal and for 1943 runs, in figures 6.15 and 6.16 respectively.

For a CUT4 equal with 0.3 about 50% of the spin sequences are rejected from analysis. Both up-down and left-right asymmetry decrease when CUT4 is decreased below 0.35, because more spin sequences are eliminated from analysis.

Between 0.4 and 0.6, the reduced χ^2 is about 1.45. When CUT4 is 0.3 the reduced $\chi2$ is 1.17. The quality of the fit is worse when CUT4 is equal or bigger than 0.8. Therefore the contribution of the instrumental systematic
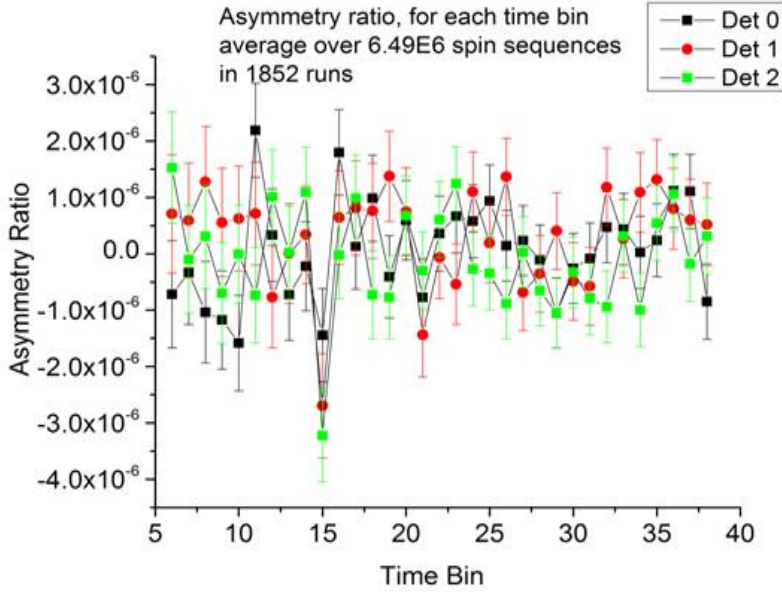
Figure 6.14: The asymmetry ratio calculated for each time bin (from 6 to 38) and averaged over all 6.49E6 spin sequences in the 1852 Al runs.

errors from the transient signals, becomes important in the absence of the cuts placed on detector signal. The average of the two Al asymmetries is calculated for detector cuts 0.35, 0.4, 0.6 and 0.8. The standard deviation of the four asymmetries is the systematic error due to the transient signals:

$A_{ud} = (-6.98 \pm 3.6(\text{stat}) \pm 0.9(\text{sys})) \cdot 10^{-8}$ and

$A_{lr} = (2.11 \pm 0.36(\text{stat}) \pm 0.3(\text{sys})) \cdot 10^{-7}$.

The up-down and left-right Al asymmetry were calculated also with the first geometry mean for CUT4=0.3, 0.4, 0.6, 0.8 and 1. The averaged over the three pairs of asymmetries calculated for CUT4 equal with 0.4, 0.6 and 0.8 are in agreement with the average asymmetries calculated with the second geometry mean: $A_{ud} = (-6.43 \pm 3.26(\text{stat}) \pm 0.81(\text{sys})) \cdot 10^{-8}$ and

$A_{lr} = (1.98 \pm 0.33(\text{stat}) \pm 0.26(\text{sys})) \cdot 10^{-7}$.
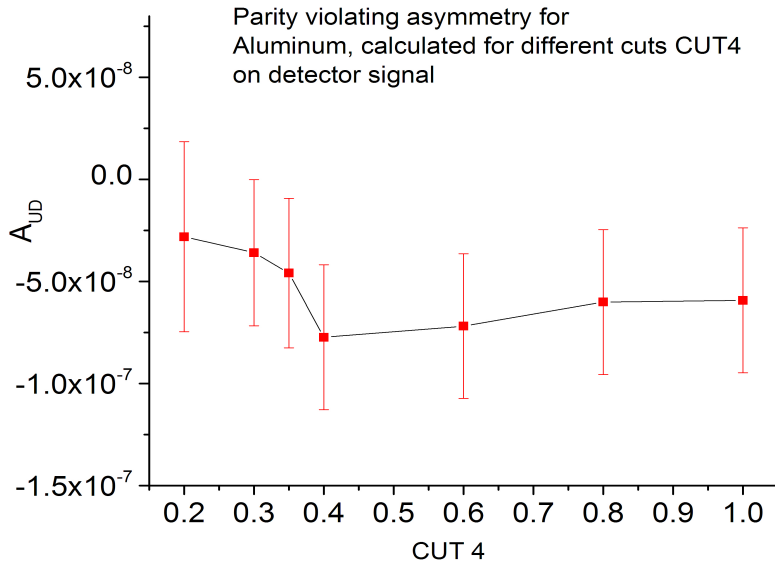
Figure 6.15: The up-down asymmetry for Aluminum calculated for different cuts on detector signals.
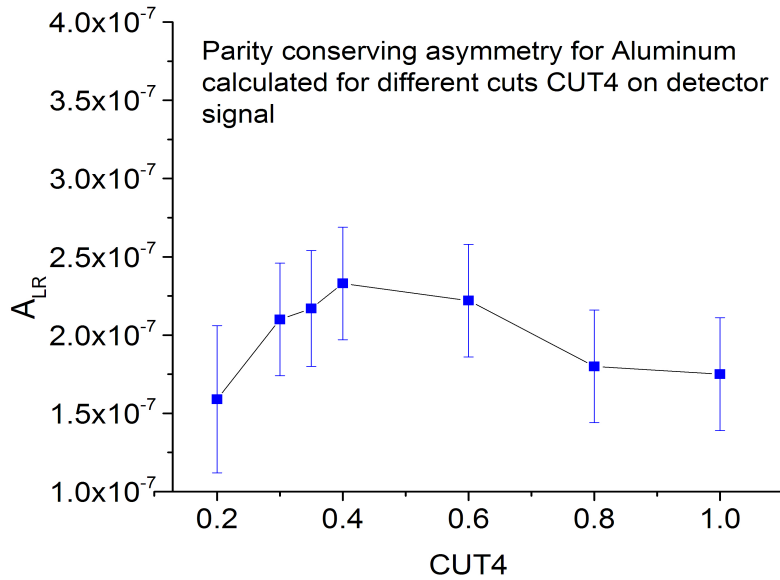
Figure 6.16: The left-right asymmetry for Aluminum calculated for different cuts on the detector signal.

145

6.9   Asymmetry Measurements for Chlorine

The parity-violating asymmetry for Cl was measured before at ILL [43], Saint Petersburg [46] and Los Alamos [45]. The measured parity violating asymmetries were:

$(-21.2 \pm 1.7) \cdot 10^{-6}, (-27.8 \pm 4.9) \cdot 10^{-6} and (-19.2 \pm 1.2) 10^{-6}$, respectively.

In this work the calculations were done for the 96 Cl data runs (from run number 63098 to 63189). The Cl measurements were done before the Al measurements (93 runs) and then close to the end of the Al data runs (132 runs). It was noticed that the asymmetry measured with the CCl_4, gradually decreased in time due to target leaks and evaporation. The parity-odd (PV) and the parity-allowed (PC) asymmetries are calculated here for a neutron polarization P=0.94 $\pm$ 0.02 and a SR efficiency e=0.98 $\pm$ 0.02.

First the Cl asymmetry are calculated for each detector with the arithmetic mean procedure, Figure 6.18). The fitting parameters were calculated from the minimization of the χ^2 function with the detector geometry factors for Cl: $A1 = (-2.25 \pm 0.03) \cdot 10^{-5}$, $B1 = (3.12 \pm 3.15) \cdot 10^{-7}$ and $C = (3.61 \pm 1.90) \cdot 10^{-7}$

The up-down and left-right asymmetries are:

$A_{ud} = (-2.44 \pm 0.08) \cdot 10^{-5}, \ \ A_{lr} = (3.42 \pm 3.42) \cdot 10^{-7}.$

In addition, the geometry mean procedure was used to calculate the two asymmetries for detector pairs with the Cl target (Figure 6.17). The fitting parameters are:

$A1 = (-2.23 \pm 0.02) \cdot 10^{-5}, B1 = (4.31 \pm 1.93) \cdot 10^{-7},$
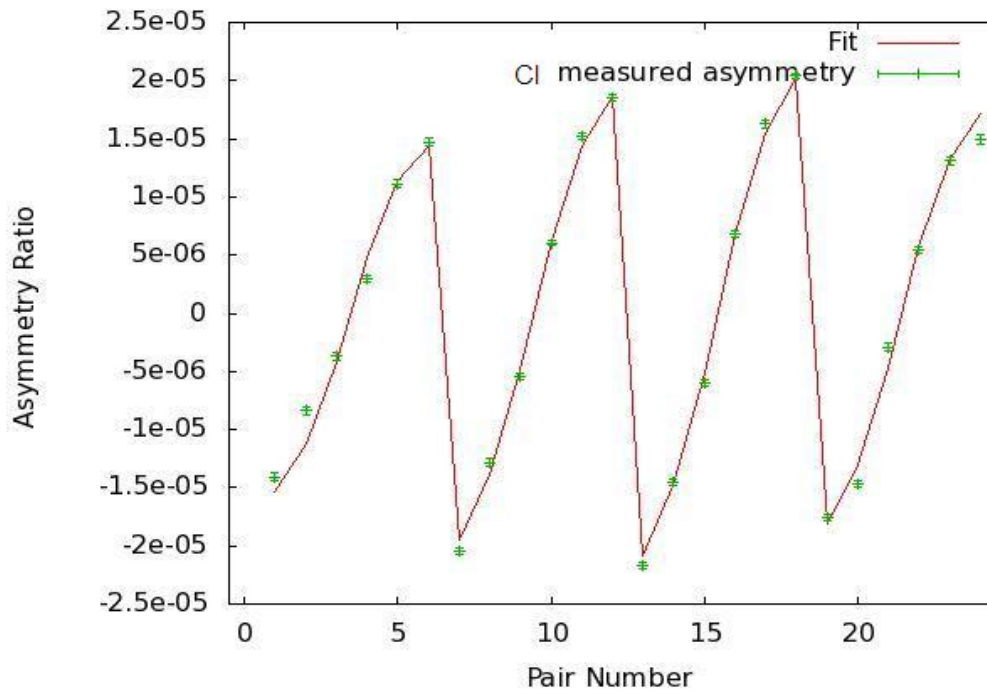
Figure 6.17: The asymmetry ratio for the CCl_4 target is calculated for each of the 24 pairs of detectors with the geometry mean method.

$C = (0.55 \pm 1.12) \cdot 10^{-7}$, with the reduced χ^2=1.56, goodness of the fit 0.904. The two fitting parameters are divided with the neutron polarization and SR efficiency to get the parity-odd (up-down) and the parity-allowed (left-right) asymmetries in Cl: $A_{ud} = (-2.42 \pm 0.07) \cdot 10^{-5}$ $A_{lr} = (4.68 \pm 2.10) \cdot 10^{-7}$

For the Cl target the correction of the false asymmetry due to the transient was done in the ratio of each pair of opposite detectors. The parity, the transient amplitudes, and the decay rate are calculated for each pair and each spin sequence and written in four histograms. The average fitting parameters are read from the histograms at the end of the loop over runs.The uncertainty in the fitting parameters is calculated from the curvature matrix. If a_k and a_j are fitting parameters and A(x) is the fitting function for the

147
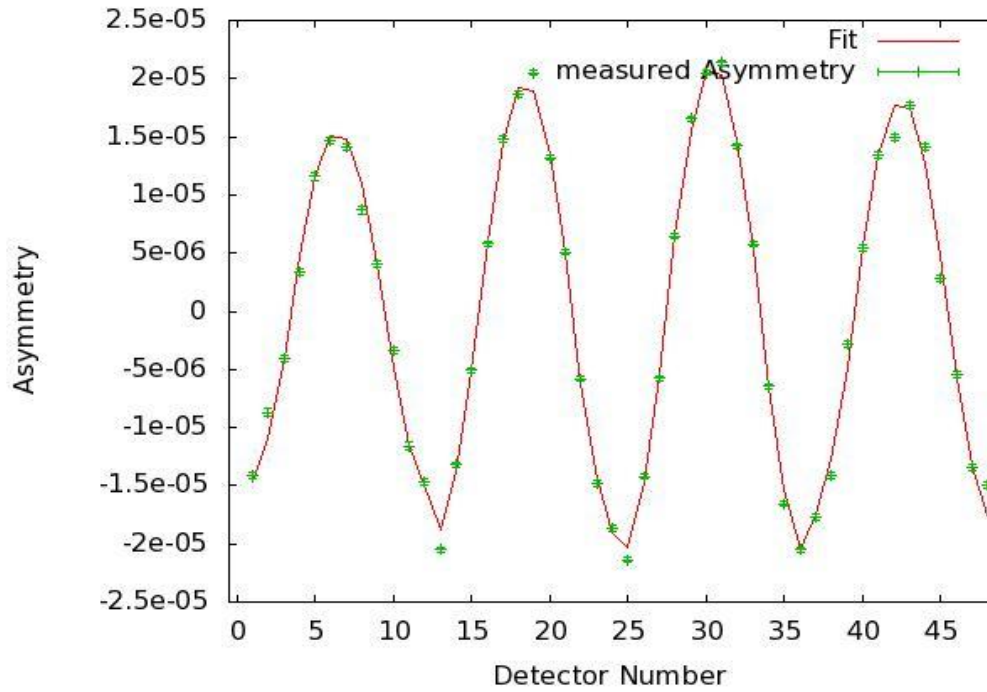
Figure 6.18: The asymmetry ratio for the CCl$_4$ target is calculated for the 48 detectors with the arithmetic mean method.

asymmetry then the elements of the curvature matrix are given by the relation:

$$\alpha_{k,j} = \sum_{i=1}^{N} \frac{1}{\sigma_i^2} \cdot \frac{dA(x_i)}{da_k} \cdot \frac{dA(x_i)}{da_j} \tag{6.66}$$

The summation is over all time bins in the interval [T1, T2] and over all pairs of pulses (k, j) with opposite spin, a total of (T2-T1+1)*16 points. In this relation σ_i is the standard deviation of the measured asymmetry $A_{k,j,t}$. The uncertainties in the fitting parameters are the square root of the diagonal elements in the error matrix. From the χ^2 function with the 48 detector geometry factors the three fitting parameters are: $A_1 = (-22.65 \pm 0.20)10^{-6}$, $B_1 = (5.30 \pm 1.98)10^{-7}$, $C = (-0.56 \pm 1.20)10^{-7}$.

Chapter 7

SUMMARY AND OUTLOOK

This work described the installation, commissioning and first asymmetry measurements for the $\vec{n} + p \rightarrow d + \gamma$ experiment at the SNS, ORNL. The first phase of this experiment was carried out at LANSCE. Some of the main modifications needed to run the experiment at the SNS were presented in this thesis: the polarization of the neutrons by transmission through a Super Mirror Polarizer, and the building of a Compensation Magnet around the Super Mirror Polarizer to decrease their total fringe field at the center of the detector array [59].

Two procedures were used to calculate the asymmetry for detector pairs for both Al and Cl targets. The most important systematic errors come from the overlap of the Spin Sequencer transient signals with the detector signals related to the neutron beam. The contribution of the transient to the false asymmetry was identified in the calculation of the asymmetry from the ratio of the difference and the sum detector signals in the arithmetic procedure. When the asymmetry is calculated for a pair of opposite detectors the contribution of the beam intensity fluctuations cancels out. The contribution of the transient is significantly reduced when the asymmetry is calculated for each time bin from the geometrical mean of the product of opposite detector signal ratios.

The measurements of the asymmetry for the Cl_4C target were done to check the sensitivity of the apparatus and the detector alignment relative to the beam axis. The asymmetry was extracted from 96 data runs collected with a thin Cl_4C target placed in the center of the detector array. The results are presented in table 7.1. The up-down asymmetry is two order of magnitudes

bigger than the left-right asymmetry. For this reason the asymmetry for Cl can be calculated with both arithmetical and geometrical methods. The present result agrees well with previous measurements and it is the most precise measurement up to now.

Table 7.1: Parity-violating (up-down) and parity-conserving (right-left) asymmetries for Cl.

Method	Target	A_{ud} 10^{-5}	A_{lr} 10^{-7}	χ^2 reduced	Reference
Geometry	Cl	-2.42 ± 0.07	4.68 ± 2.10	1.2	this work
Arithmetic	Cl	-2.44 ± 0.08	3.42 ± 3.42	2.21	this work
Arithmetic	Cl	-2.12 ± 0.17	-	-	[43]
Arithmetic	Cl	-2.78 ± 0.49	-	-	[46]
Arithmetic	Cl	-1.9 ± 0.2	-1 ± 2	-	[40]

For the Al target the parity-violating up-down asymmetry is about eight times smaller than the parity-conserving, left-right asymmetry. In table 7.2 the asymmetries obtained in the present work are compared with those measured in previous experiments. Because the up-down asymmetry for Al is smaller than 10^{-7} the contribution of the transients had to be greatly reduced. To this end the asymmetry was calculated only for detector pairs from the geometry mean of the ratio of detector signals at each time bin. Two contributions to the false asymmetry were identified from the measurement of the sum and difference of module detector signals. The first contribution is related with the exponential transient decay and was corrected from the fit of the detector ratio signals. The second contribution was discovered in the measurements of the detector signals exposed to the two detectors LEDs in the absence of the neutron beam. The asymmetry calculation of Al was derived from the fit of the detector signal ratio written as a function of time bins and for each spin sequence. The systematic errors related with the interaction of the neutron

spin with the magnetic field were calculated both in the vertical and horizontal direction.

Table 7.2: The raw and the corrected asymmetry ratio for Al. The corrected asymmetry is Geometry1 (stat.only)

Method	Target	A_{ud} 10^{-8}	A_{lr} 10^{-7}	χ^2 reduced	Reference
Geometry2	Al	-6.98 ± 3.60	2.11 ± 0.36	1.45	this work
Geometry2 (stat.only)	Al	-7.21 ± 1.06	2.82 ± 0.13	21	this work
Geometry1	Al	-6.43 ± 3.26	1.98 ± 0.33	1.46	this work
Arithmetic	Al	-8.0 ± 28	-2.0 ± 3.0	-	[40]

The present Al results for the parity violation up-down asymmetry are consistent with previous measurements and they are significantly more precise. The statistical errors for this observable are smaller than $\sigma_b = 4 \cdot 10^{-8}$. If the asymmetry with the H_2 target is be measured with an uncertainty smaller than 10^{-8} then the uncertainty in the calculated proton asymmetry would be $\sigma_p = 1.35 \cdot 10^{-8}$. Thus, this will allow the first statistically significant measurement of the asymmetry in the $\vec{n} + p \rightarrow d + \gamma$ reaction with the present apparatus at the SNS.

Three physical processes can contribute to the left-right asymmetry related with the parity-conserving scalar $\vec{k_\gamma} \cdot (\vec{s_n} \times \vec{k_n})$. The first process is due to the interaction of the neutron spin with the magnetic field gradients (the Stern Gerlach effect). Due to this interaction the center of the neutron beam is displaced along the positive or negative direction of the vertical axis depending on the direction of the spin. The displacement was calculated for all energies of the neutrons, from the measured field gradients in the detector volume. The false asymmetry due to this displacement is smaller than 10^{-8} and is therefore negligible compared with the statistical uncertainties. The second process,

called the Mott- Schwinger effect, is due to the spin-orbit interaction of the

neutron spin with the electric field of the nucleus that is moving in the reference

frame of the neutron. In this case the spin dependent shift in the beam center

is due to both the electromagnetic and the strong spin-orbit interactions [61].

For Al the electromagnetic part of the left-right asymmetry is between $2 \cdot 10^{-8}$

and $6 \cdot 10^{-8}$ for neutron energies between 2 meV and 14 meV. However for this

energy range the inelastic scattering dominates the imaginary part of the

scattering amplitude and the contribution of the strong spin-orbit interaction is

important. The interference between the electromagnetic spin-orbit scattering

and the strong spin-orbit elastic and inelastic scattering amplitudes in Al

increases the total analyzing power to $1.4 \cdot 10^{-7}$ [61]. The third contribution is

due to the parity-conserving part in the direct neutron capture in Al. This

contribution has not been calculated for Al. For the $\vec{n} + p \to d + \gamma$ reaction the

asymmetry due to this contribution [29] is equal with $0.67 \cdot 10^{-8}$. For Al the

direct capture mechanism for slow neutrons was considered in the calculation

of the cross section [76]. It is expected that the present result will stimulate

further theoretical work.

REFERENCES

Bibliography

[1] J. Orear, G. Harris, and S. Taylor. Spin and parity analysis of bevatron τ Mesons. *Phys. Rev.*, 102, 1956.

[2] C. S. Wu *et al.* Experimental test of parity conservation in beta decay. *Phys. Rev*, 105, 1957.

[3] T. D. Lee and C. N. Yang. Question of parity conservation in weak interaction. *Phys. Rev.*, 104, 1956.

[4] Nobel Foundation. *Nobel Lectures, Physics 1942-1962*. 1964.

[5] M. J. Ramsey-Musolf and S. A. Page. Hadronic parity violation: a new view through the looking glass. *Ann. Rev. Nucl. Part. Sci.*, 56, 2006.

[6] J. Erler and M. J. Ramsey-Musolf. Low energy tests of the weak interaction. *Prog. Part. Nucl. Phys.*

[7] W. M. Snow. Neutron measurements and the weak nucleon-nucleon interaction. *J. Res. Natl. Inst. Stand. Technol.*, 110(3), 2005.

[8] J.S. Nico and W.M. Snow. Fundamental neutron physics. *Ann. Rev. Nucl. Part. Sci.*, 55, 2005.

[9] C.-P. Liu. Parity-violating observables of two-nucleon systems in effective field theory. *Phys. Rev. C*, 75, 2007.

[10] G. S. Danilov. Circular polarization of γ quanta in absorption of neutrons by protons and isotopic structure of weak interaction. *Physics Letters*, 18, 1965.

[11] G. S. Danilov. Dispersion approach to the investigation of the weak nucleon-nucleon interaction. *Physics Letters B*, 35, 1971.

[12] G. S. Danilov. *Sov. J. Nucl. Phys.*, 14, 1972.

[13] J. F. Donoghue, E. Golowich, and B. Holstein. Low-energy weak interactios of quarks. *Phys. Rep.*, 131, 1986.

[14] M. Neubert. Heavy - quark symmetry. *Phys.Rep.*, 245, 1994.

[15] A. Ali, G. Kramer, and Cai-Dian LU. Cp-violating asymmetries in charmless nonleptonic decays $B \rightarrow PP, PV, VV$ in the factorization approach. *Phys. Rev. D*, 59, 1998.

[16] J. Kambor, J. F. Donoghue, B. R. Holstein, J. Missimer, and D. Wyler. Chiral symmetry tests in nonleptonic K decay. *Phys. Rev. Lett.*, 68, 1992.

[17] S. Herrlich and M. Kalinovski. Direct CP violation in $K, B \rightarrow \gamma\gamma$ with heavy top quark. *Nucl. Phys. B*, 381, 1992.

[18] C. A. Barnes et al. Search for neutral-weak-current effects in the nucleus ^{18}F. *Phys. Rev. Lett.*, 40, 1978.

[19] C.S. Wood *et al.* Measurement of parity nonconservation and an anapole moment in Cesium. *Science*, 275, 1997.

[20] D. R. Phillips, M. R. Schlinder, and R. P. Springer. An effective-field-theory analysis of low energy-parity-violation in nucleon-nucleon scattering. *Nucl. Phys. A*, 822, 2009.

[21] M.T. Gericke, R. Alarcon, S. Balascuta, L. Baron Palos, C. Blessinger, and J.D. Bowman. *Phys Rev C*, 83, 2011.

[22] B. Desplanques. Parity-non-conservation in nuclear forces at low energy: phenomenology and questions. *Phys. Rep.*, 297, 1998.

[23] E. G. Adelberger and W. C. Haxton. Parity violation in the nucleon-nucleon interaction. *Ann. Rev. Nucl. Part. Sci.*, 35, 1985.

[24] L. J. Hall. Flavor changing Higgs boson couplings. *Nucl. Phys. B*, 187, 1981.

[25] Steven Weinberg. Effective gauge theories. *Physics Letters B*, 91, 1980.

[26] P. Langacker and H. Pagels. Applications of chiral perturbation theory: mass formulas and the decay $\eta \to 3\pi$. *Phys. Rev. D*, 10, 1974.

[27] B. Desplanques. About the parity-non-conserving asymmetry in $n + p \to d + \gamma$. *Phys. Lett. B*, 512, 2001.

[28] W. S. Wilburn, J. D. Bowman, M. T. Gericke, and S. I. Penttilä. *Nucl. Instr. Meth. Phys. Res. A*, 540, 2005.

[29] A. Csoto, B. F. Gibson, and G. L. Payne. Parity conserving γ asymmetry in $n - p$ radiative capture. *Phys. Rev. C*, 56, 1997.

[30] R. Schiavilla, J. Carlson, and M. Paris. Parity Violating interaction effects exchange in the np system. *Phys. Rev. C*, 70, 2004.

[31] Chang Ho Hyun, Tae Sun Park, and Dong-Pil Min. Asymmetry in $\vec{n} + p \to d + \gamma$. *Phys. Lett. B*, 516, 2001.

[32] C. H. Hyun, S. J. Lee, J. Haidenbauer, and S. W. Hong. Parity-nonconserving observables in thermal neutron capture on a proton. *Eur. Phys. J. A*, 24(1), 2005.

[33] W. C. Haxton. Parity nonconservation in ^{18}F and meson-exhange contributions to axial charge operator. *Phys. Rev. Lett.*, 46, 1981.

155

[34] V. V. Flambaum and D. W. Murray. Anapole moment and nucleon weak interaction. *Phys. Rev. C*, 56, 1997.

[35] S. S. Wong. Nuclear statistical spectroscopy. 1986.

[36] C. E. Porter. Statistical theory of spectra: Fluctuations. 1965.

[37] H. L. Harney, A. Richter, and H. A. Wedenmuller. *Rev. Mod. Phys.*, 58, 1986.

[38] V. V. Flambaum and O. P. Sushkov. Theory of neutron reactions and weak interaction in heavy nuclei. *Nucl. Phys. A*, 412, 1984.

[39] V. V. Flambaum and G. F. Gribakin. Enhancement of parity and time invariance violating effects in compound nuclei. *Progress in particle and nuclear physics*, 35, 1995.

[40] M. T. Gericke *et al. Phys. Rev. C*, 74, 2006.

[41] R. Hardell, S.O.Idetjarn, and H. Ahlgren. Thermal-neutron capture gamma rays from the $^{27}Al(n,\gamma)^{28}Al$. *Nucl. Phys. A*, 126, 1969.

[42] P. M. Endt and C. van der Leun. Energy levels of Z=11-21 nuclei IV. *Nucl. Phys A*, 105, 1967.

[43] M.A. Avenier, G. Bagieu, H. Benkoula, and J. F. Cavaniac. Parity non-conservation in the radiative capture of polarized neutrons by ^{35}Cl. *Nucl. Physics A*, 436, 1985.

[44] V. E. Bunakov et al. Parity violation in the radiative neutron capture in Chlorine.

[45] Christopher Blessinger. *Measurement of the Parity Violating Gamma Ray Asymmetry in Polarized Neutron Capture on ^{35}Cl, ^{113}Cd and ^{139}La*. PhD thesis, Indiana University Bloomington, 2001.

[46] V. A. Vesna et al. *JETP Lett.*, 36, 169.

[47] Richard B. Firestone and Virginia S. Shirley. *Table of isotopes*. John Wiley, New York, 7 edition, 1978.

[48] A. M. J. Spits and J. Kopecky. The reaction $^{35}Cl(n,\gamma)^{36}Cl$ studied with non-polarized and polarized thermal neutrons. *Nucl. Phys A*, 264, 1976.

[49] P.-N. Seo *et al.* . *Nucl. Instr. Meth. Phys. Res. A*, 517, 2004.

[50] F. Mezei and P. A. Dagleish. Novel polarized neutron devices: supermirrors and spin component amplifiers. *Communications on Physics*, 1, 1976.

[51] J. B. Hayter and H. A. Mook. Discrete thin film multilayer design for X-ray and neutron Supermirrors. *J. Appl. Cryst.*, 22, 1989.

[52] M. Sharma *et al.* Neutron beam effects on spin-exchange-polarized ^{3}He. *Phys. Rev. Letters*, 101, 2008.

[53] S. Santra *et al.* A liquid parahydrogen target for the measurement of a parity-violating gamma asymmetry in $n + p \rightarrow d + \gamma$. *Nucl. Instr. Meth. Phys. Res. A*, 620, 2010.

[54] M. T. Gericke *et al.* . *Nucl. Instr. Meth. Phys. Res. A*, 540, 2005.

[55] L. Barrón-Palos, R. Alarcon, S. Balascuta, C. Blessinger, J. D. Bowman, T. E. Chupp, S. Covrig, C. B. Crawford, M. Dabaghyan, J. Dadras, M. Dawkins, W. Fox, M.T. Gericke, R. C. Gillis, B. Lauss, M.B. Leuschner, B. Lozowski, R. Mahurin, M. Masin, and J. Mei. Determination of the parahydrogen fraction in a liquid hydrogen target using energy-dependent slow neutron transmission. *Nucl. Instr. Meth. Phys. Res. A*, 659, 2011.

[56] M. Schneider, J. Stahn, and P. Boni. Focusing of cold neutrons: Performance of a laterally graded and parabilically bent multilayer. *Nucl. Instr. Meth. Phys. Res. A*, 610, 2009.

[57] A. Ashfaq and J. Stahn. Some improvement in Fe/Si multilayered neutron polarizor by modified sputtering geometry. *Applied Surface Science*, 255, 2009.

[58] Swiss-Neutronics AG. `http://www.swissneutronics.com/`.

[59] S. Balascuta, R. Alarcon, S. Baessler, G. Greene, A. Mietke, C. Crawford, R. Milburn, S. Penttila, J. Prince, and J. Schadler. The implementation of a super mirror polarizer at the SNS fundamental neutron physics beamline. *Nucl. Instr. Meth. Phys. Res. A*, 137, 2012.

[60] P.-N. Seo et al. High-efficiency resonant rf spin rotator with broad phase space acceptance for pulsed polarized cold neutron beam. *Phys. Rev. Special Topic-Accelerator Beam (ST-AB)*, 11, 2008.

[61] M. T. Gericke, J. D. Bowman, and M. B. Johnson. Mott - Schwinger scattering of polarized low energy neutrons up to thermal energies. *Phys. Rev. C*, 78, 2008.

[62] Ningbo Zhaobao Magnet Co. Ltd. `http://www.zhaobao-magnet.com/`, address=No. 355 Datong Road Zhenhai Ningbo, 315200, Zhejiang China.

[63] V. V. Vladimirkii. Magnetic mirrors, channels and bottles for cold neutrons. *Soviet Physics JETP*, 12, 1961.

[64] R. G. Littlejohn and Stefan Weigert. Adiabatic motion of a neutral spinning particle in an inhomogenous magnetic field. *Phys. Rev. A*, 48, 1993.

[65] Kyle Grammer. Calculation of the geometrical factors for chlorine, aluminum and hydrogen target and measurement of the detector misalignment angles. `http://battlestar.phys.utk.edu/wiki/images/1/16/Npdg_geofactors.pdf`, 2012.

[66] Christopher Crawford and Robert Mahuring. Opening angles for the $fnpb$ choppers. `http://battlestar.phys.utk.edu/wiki/images/3/38/SNS_choppers_opening_angles.pdf`.

[67] Christopher Crawford Nadia Fomin. NPDGamma online analysis at sns. `http://battlestar.phys.utk.edu/wiki/images/5/55/Online_package.pdf`, 2011.

[68] Josh Hamblen, Daniel Parson, and Jeremy Stewart. First results from beam intensity scans. `http://battlestar.phys.utk.edu/wiki/`, July 2011.

[69] P. Willendrup, E. Farhi, and K. Lefmann. McStas 1.7 - a new version of the flexible Monte Carlo neutron scattering package. *Physica B*, 350, 2004.

[70] H. Nastoll *et al.* Precise determination of the degree of polarization of a cold neutron beam. *Nucl. Inst. Meth. A*, 306, 1991.

[71] A.P. Serebrov *et al.* New method for precise determination of neutron beam polarization. *Nucl. Inst. Meth. A*, 357, 1995.

[72] T. R. Gentile *et al.* Polarized ^{3}He spin filters for slow neutron physics. *J. Res. Natl. Inst. Stand. Technol.*, 110(3), 2005.

[73] Mathew Musgrave. Polarimetry update. `http://battlestar.phys.utk.edu/wiki/index.php/Offline_Analysis/Polarimetry`, 2011.

[74] S. Kucuker. The calculation of the dynamic pedestals. `http://battlestar.phys.utk.edu/wiki/`, 2010.

[75] J. Schwinger. On the polarization of fast neutrons. *Phys. Rev.*, 73, 1948.

[76] S. Raman, S. Kahane, and J. E. Lynn. Direct thermal neutron capture. *J. Phys. G: Nucl. Phys.*, 14, 1988.

[77] C. Amsler and Particle Data Group. Review of particle physics. *Physics Letters B*, 667, 2008.

[78] Mark McCrea. A study of transients in detector Sum/Difference signals. `http://http://battlestar.phys.utk.edu/wiki/images/a/a7/TransientReport.pdf`, 2012.

[79] A. Perez Galvan, B. Plaster, J. Boissevain, R. Carr, B. W. Fillipone, M. P. Mendenhall, R. Schmid, R. Alarcon, and S. Balascuta. High uniformity magnetic coil for search of neutron electric dipole moment. *Nucl. Instr. Meth. Phys. Res. A*, 660, 2011.

[80] D. Pocanic, R. Alarcon, L. P. Alonzi, S. Baessler, S. Balascuta, J.D. Bowman, M. A. Bychkov, and J. Byrne. Nab: Measurement principles, apparatus and uncertainties. *Nucl. Instr. Meth. Phys. Res. A*, 611, 2009.

APPENDIX A

Asymmetry Calculation from the Ratio of Detector Signals

A.1   Introduction

Two geometry mean procedures for the calculation of the asymmetry are discussed in this appendix. The correction of the transient signal is based on the minimization of the χ^2 function derived from the ratio of opposite detector signals for each time bin from T_1=8 to T_2=38. From the minimum of the χ^2 function, the parity, the transient amplitude and the transient decay rate are calculated for each spin sequence and for each detector. At the end of all the runs the uncertainty in the fitting parameters are calculated from the error matrix. The contributions of the counting statistics to the statistical uncertainty is calculated from the relative standard deviation of the opposite detector signals.

A.2   The First Geometry Mean

There are six pairs of opposite detectors in each ring. In this section the calculations are done for the two opposite detectors 0 and 6 , in ring 0. The results are valid for any pair of opposite detectors. For each accepted spin sequence the ratio of opposite detector signals $D_0(k,t)/D_6(k,t)$ is calculated at each time bin t between T_1 and T_2 and each pulse k in the spin sequence. The ratio is multiplied with the inverted ratio of the detector signals $\bar{D}_6(t)/\bar{D}_0(t)$ at the same time bin, where $\bar{D}_{0,6}(t)$ are the average of the detector signals at time t over the eight pulses in the spin sequence.

Consider f_d the detector gain and $I_k(t)$ the average gamma flux (at pulse k and time bin t) over all directions of the initial gamma ray momentum. The transient model is a simple exponential decay. The transient amplitude and decay times are V_d and τ respectively. The procedure presented in here allows the calculation of the corrected detector asymmetry $P_d(t)$ at each time t.

$$\frac{D_0(k,t)}{D_6(k,t)} = \frac{f_0 I_k(t)(1 + P_{0,t} \cdot s_k) + V_0 \cdot e^{-(t+kT)/\tau}}{f_6 I_k(t)(1 + P_{6,t} \cdot s_k) + V_6 \cdot e^{-(t+kT)/\tau}} \qquad \text{(A.1)}$$

Consider the time t and decay time τ in units of time bins and T=40 the number of time bins in a pulse. For clarity the following quantities are introduced:

$$q_1 = \exp(-1/\tau) \; ; \; q = \exp(-T/\tau) = q_1^{40} \; ; \qquad \text{(A.2)}$$

$$s_8 = \frac{1}{8} \sum_{k=0}^{7} q^k \; ; \; s_t = \frac{\sum_{t=T1}^{T2} q_1^t}{T_2 - T_1 + 1} \qquad \text{(A.3)}$$

The average detector over the spin sequence and the average detector voltage at time bin t over all eight pulses in a spin sequence are given by the relations:

$$\bar{D}_d = \frac{1}{T_2 - T_1 + 1} \sum_{t=T_1}^{T_2} \bar{D}_d(t) = f_d \bar{I} + V_d s_8 s_t \tag{A.4}$$

$$\bar{D}_d(t) = \frac{1}{8} \sum_{k=0}^{7} D_d(k,t). \tag{A.5}$$

At time bin t and pulse k, the ratio of the detector signals corrected for the transient is given by the ratio:

$$\frac{D_0(k,t) - V_0 q_1^t q^k}{D_6(k,t) - V_6 q_1^t q^k} = \frac{f_0 I_k(t)(1 + P_{0,t} \cdot s_k)}{f_6 I_k(t)(1 + P_{6,t} \cdot s_k)} \tag{A.6}$$

To cancel the detector gains the ratio of the corrected detector signals (equation A.6) is multiplied with the inverse ratio of sequence-average corrected-detector signals at the same time bin t:

$$\frac{D_0(k,t) - V_0 q_1^t q^k}{D_6(k,t) - V_6 q_1^t q^k} \cdot \frac{\bar{D}_6(t) - V_6 \cdot s_8 q_1^t}{\bar{D}_0(t) - V_0 \cdot s_8 q_1^t} = \frac{f_0 I_k(t)(1 + P_{0,t} \cdot s_k)}{f_6 I_k(t)(1 + P_{6,t} \cdot s_k)} \cdot \frac{f_6 \bar{I}(t)}{f_0 \bar{I}(t)} \tag{A.7}$$

The transient amplitude divided with the pulse average of the transient corrected detector signal, can be written for each detector in the pair:

$$v_{0,6} = \frac{V_{0,6}}{\bar{D}_{0,6}} \tag{A.8}$$

$$\frac{V_{0,6}}{D_{0,6}(k,t)} = v_{0,6} \frac{\bar{D}_{0,6}}{D_{0,6}(k,t)} \approx v_{0,6} \frac{\bar{D}_{0,6}}{\bar{D}_{0,6}(t)} \tag{A.9}$$

Introduce the product of the detector signal ratio and average detector signal ratio, for each time bin:

$$R_{0,6}(k,t) = \frac{D_0(k,t)}{D_6(k,t)} \frac{\bar{D}_6(t)}{\bar{D}_0(t)} \tag{A.10}$$

The product of relative transient voltages is equal with:

$$Q_{0,6}(k,t) = \frac{1 - v_6 q_1^t q^k \frac{\bar{D}_6}{D_6(k,t)}}{1 - v_0 q_1^t q^k \frac{\bar{D}_0}{D_0(k,t)}} \cdot \frac{1 - v_0 q_1^t s_8}{1 - v_6 q_1^t s_8} \tag{A.11}$$

$$Q_{0,6}(k,t) = 1 + v_0 q_1^t \left(q^k \frac{\bar{D}_0}{D_0(k,t)} - s_8 \right) - v_6 q_1^t \left(q^k \frac{\bar{D}_6}{D_6(k,t)} - s_8 \right) \tag{A.12}$$

$$\frac{R_{0,6}(k,t)}{Q_{0,6}(k,t)} = \frac{1 + P_{0,t} \cdot s_k}{1 + P_{6,t} \cdot s_k} \tag{A.13}$$

The asymmetry $P_{0,t} = -P_{6,t}$ in the presence of the transient is calculated from equation A.13:

$$P_{0,t} \cdot s_k = \frac{R_{0,6}(k,t) - Q_{0,6}(k,t)}{R_{0,6}(k,t) + Q_{0,6}(k,t)} \tag{A.14}$$

If the transient is neglected, the uncorrected asymmetry is equal with:

$$A_{0,6}(k,t) = \frac{R_{0,6}(k,t) - 1}{R_{0,6}(k,t) + 1} \tag{A.15}$$

Taking in account the transient signal, the corrected asymmetry can be written as a function of the uncorrected asymmetry:

$$P_{0,t} \cdot s_k = A_{0,6} - v_0 q_1^t \left(\frac{q^k \bar{D}_0}{\bar{D}_0(k,t)} - s_8 \right) \frac{1 - A_{0,6}^2}{2} + v_6 q_1^t \left(\frac{q^k \bar{D}_6}{\bar{D}_6(k,t)} - s_8 \right) \frac{1 - A_{0,6}^2}{2} \tag{A.16}$$

The asymmetry for Al target is smaller than 10^{-6}. Therefore the second order term $A_{0,6} < 10^{-12}$ is negligible compared with the first order terms and can be neglected. There are four pulses with neutron spin up ($s_k = 1$ for k=1, 2, 4, 7) and four pulses with neutron spin down ($s_j = -1$ for j=0, 3, 5,6). It is convenient to calculate the average asymmetry for the two groups of pulses in each spin sequence:

$$P_{\uparrow,t} = \frac{1}{4} \sum_k A_{0,6}(k,t) - \frac{v_0 q_1^t}{8} \sum_k \left(\frac{q^k \bar{D}_0}{D_0(k,t)} - s_8 \right) + \frac{v_6 q_1^t}{8} \sum_k \left(\frac{q^k \bar{D}_6}{D_6(k,t)} - s_8 \right) \tag{A.17}$$

$$P_{\downarrow,t} = \frac{1}{4} \sum_j A_{0,6}(j,t) - \frac{v_0 q_1^t}{8} \sum_j \left(\frac{q^j \bar{D}_0}{D_0(j,t)} - s_8 \right) + \frac{v_6 q_1^t}{8} \sum_j \left(\frac{q^j \bar{D}_6}{D_6(j,t)} - s_8 \right) \tag{A.18}$$

The average corrected asymmetry over all eight pulses in spin sequence, at time bin t is $\bar{P}(t) = (P_{\uparrow,t} - P_{\downarrow,t})/2$. The average uncorrected asymmetry is $\bar{A}(t) = (\sum_j A_{0,6}(j,t) - \sum_k A_{0,6}(k,t))/8$ at each time bin. The sum of the equations A.17 and A.18 is zero because the sum of the asymmetries over all pulses in a spin sequence is expected to be zero. Consider $\bar{E}(t) = (\sum_j A_{0,6}(j,t) + \sum_k A(0,6)(k,t))/8$ and four sums that depend on time bin and the decay parameter:

$$A_0(t) = \frac{1}{8} \sum_k \left(q^k \frac{\bar{D}_0}{D_0(k,t)} - s_8 \right) \; ; \; A_6(t) = \frac{1}{8} \sum_k \left(q^k \frac{\bar{D}_6}{D_6(k,t)} - s_8 \right) \tag{A.19}$$

$$B_0(t) = \frac{1}{8} \sum_j \left(q^j \frac{\bar{D}_0}{D_0(j,t)} - s_8 \right) \; ; \; B_6(t) = \frac{1}{8} \sum_j \left(q^j \frac{\bar{D}_6}{D_6(j,t)} - s_8 \right). \tag{A.20}$$

The relative transient amplitudes v_0 and v_6 of the transient signal can be calculated from the minimization of the χ_1^2 function:

$$\chi_1^2 = \sum_t \left(\bar{E}(t) - \frac{v_0 q_1^t}{2}(A_0(t) + B_0(t)) + \frac{v_6 q_1^t}{2}(A_6(t) + B_6(t)) \right)^2 \quad \text{(A.21)}$$

The fit was done for each accepted spin sequence. The fitting parameters v_0 and v_6 were calculated from the equations $d\chi_1^2/dv_0 = 0$ and $d\chi_1^2/dv_6 = 0$. The transient parameter q_1 was calculated by iterations: q_1 was decreased from 0.98 and 0.94 with a 0.002 step. The decay parameter q_1 and the relative amplitudes v_0 and v_6 were stored in histograms. The average fitting parameter q_1 was about 0.96 for each detector, in agreement with the measurements of the detector signals in the absence of the neutron beam, with SR and DAQ in the beam-on operating condition, and with a battery connected to the 12 ADC inputs for each detector ring. The corrected asymmetry $P(t)$ at each time bin was calculated from the equation:

$$P(t) = A(t) - \frac{1}{2}v_0 q_1(A_0(t) - B_0(t)) + \frac{1}{2}v_6 q_1^t(A_6(t) + B_6(t)) \quad \text{(A.22)}$$

The time average of the corrected and uncorrected asymmetries were calculated at each spin sequence:

$$\bar{P} = \frac{\sum_{t=T_1}^{T_2} P(t)}{T_2 - T_1 + 1} \quad \text{(A.23)}$$

$$\bar{A} = \frac{\sum_{t=T_1}^{T_2} A(t)}{T_2 - T_1 + 1} \quad \text{(A.24)}$$

For opposite detectors the parity terms are equal and opposite $P_6(t) = -P_0(t)$ at each time bin. For each accepted spin-sequence the algorithm calculated the time average corrected detector-pair asymmetry $\bar{P}$ and stored the two corrected detector-asymmetries $\bar{P}_0 = \bar{P}$ and $\bar{P}_6 = -\bar{P}$ in two histograms. For the same spin sequence the uncorrected time average detector-asymmetries $\bar{A}_0 = \bar{A}$ and $\bar{A}_6 = -\bar{A}$ were stored in separate histograms. The calculations were done for all 24 detector pairs and for about 2000 Al runs. At the end of all runs the average and the root mean square (rms(k), k=0 up to 47) of the 48 detector-asymmetry histograms were calculated and used to extract the optimum fitting parameters (A_1, B_1, C) from a second χ_2^2 function that depends on all 48 geometry factors:

$$\chi_2^2 = \sum_{k=0}^{47} \frac{1}{\sigma_k^2} \left(\bar{P}_k - (G_k^{UD} A_1 + G_k^{LR} B_1 + C) \right)^2 \quad \text{(A.25)}$$

The variance is equal with $\sigma_k^2 = N_s/\text{rms(k)}^2$ with N_s the number of accepted spin sequences in all runs. The parity-violating asymmetry A_{UD} and parity-conserving asymmetry A_{LR} are calculated by dividing the fitting parameters A_1 and B_1 with the neutron polarization $P_n = 0.94$ and the efficiency of the Spin Rotator $\epsilon = 0.98$. The calculation of the uncorrected asymmetries was done with the χ_2^2 function in equation A.25 with $\bar{P}_k$ replaced with the uncorrected detector-asymmetry $\bar{A}_k$.

A.3 The Second Geometry Mean

For each accepted spin sequences, and each time bin, the asymmetry can also be calculated from the product of the signal ratio of two opposite detectors in a ring averaged over four pulses with neutron spin up times the inverted signal ratio of the same detectors averaged over the other four pulses with neutron spin down. Consider the two opposite detectors 0 and 6 in the first ring. For a neutron pulse k with spin s_k=+1 the ratio of the signals of a pair for the two opposite is equal with:

$$\frac{D_0(k,t)}{D_6(k,t)} = \frac{f_0 I_k(t)(1 + P_0(t)) + V_0 \cdot e^{-(t+kT)/\tau}}{f_6 I_k(t)(1 + P_6(t)) + V_6 \cdot e^{-(t+kT)/\tau}} \tag{A.26}$$

To cancel the multiplicative detector gains, the above ratio is multiplied with the inverse of the signal ratio for the same pair of detectors for a neutron pulse j with opposite spin:

$$\frac{D_6(j,t)}{D_0(j,t)} = \frac{f_6 I_j(t)(1 - P_6(t)) + V_6 \cdot e^{-(t+kT)/\tau}}{f_0 I_j(t)(1 - P_0(t)) + V_0 \cdot e^{-(t+kT)/\tau}} \tag{A.27}$$

The above ratios can be written in terms of the relative transient amplitudes $v_0 = V_0/\bar{D}_0$ and $v_6 = V_6/\bar{D}_6$. The numerator and denominator are divided with average gamma ray yield at time t.

$$\frac{D_0(k,t)}{D_6(k,t)} = \frac{1 + P_0(t) + \frac{v_0}{f_0 \cdot I_k(t)} e^{-(t+kT)/\tau}}{1 + P_6(t) + \frac{v_6}{f_6 \cdot I_k(t)} e^{-(t+kT)/\tau}} \tag{A.28}$$

$$\frac{D_6(j,t)}{D_0(j,t)} = \frac{1 - P_6(t) + \frac{v_6}{f_6 \cdot I_j(t)} e^{-(t+jT)/\tau}}{1 - P_0(t) + \frac{v_0}{f_0 \cdot I_j(t)} e^{-(t+jT)/\tau}} \tag{A.29}$$

The notation is simplified by introducing the time functions $v_0(t)$ and $v_6(t)$:

$$u_{0,6}(t) = v_{0,6} e^{-t/\tau} \frac{\bar{D}_{0,6}}{f_{0,6} I_k(t)} \tag{A.30}$$

$$q^k = e^{-k \cdot T/\tau} \; ; \; q^j = e^{-j \cdot T/\tau} \tag{A.31}$$

$$\frac{D_0(k,t)}{D_6(k,t)} \cdot \frac{D_6(j,t)}{D_0(j,t)} = \frac{1 + P_0(t) + u_0(t)q^k}{1 + P_6(t) + u_6(t)q^k} \cdot \frac{1 - P_6(t) + u_6(t)q^j}{1 - P_0(t) + u_0(t)q^j} \tag{A.32}$$

The gamma yield in the absence of the asymmetry $I_k(t)$ depends on the pulse number (k) in a spin sequence. For each time bin this term can be approximated with the average gamma yield for the spin sequence $\bar{I}(t)$. The average detector signal $D_0(t)$ in a spin sequence is the average of the eight detector signals $D_0(k,t)$ at the same time bin t:

$$D_0(t) = \frac{1}{8} \sum_{k=0}^{7} D_0(k,t) = \frac{1}{8} \sum_{k=0}^{7} f_0 I_k(t) + V_0 e^{-t/\tau} \frac{1}{8} \sum_k q^k \tag{A.33}$$

The parity term cancel in the sum over the eight pulses in a spin sequence because the term $I_k(t)$ is multiplied with the parity that has opposite signs for pulses with spin up or down. Therefore the term $f_0 I_k(t)$ can be approximated with the average over the eight pulses:

$$f_0 I_k(t) \cong f_0 \bar{I}(t) = D_0(t) - V_0 e^{-t/\tau} q_8 \tag{A.34}$$

$$\frac{\bar{D}_0}{r_0 I_k(t)} \cong \frac{\bar{D}_0}{D_0(t) - V_0 e^{-t/\tau} q_8} \tag{A.35}$$

To decrease the computing time the average detector ratios are calculated for the four pulses and four pulses with spin down:

$$\left\langle \frac{D_{\uparrow,0}(t)}{D_{\uparrow,6}(t)} \right\rangle = 1 + \langle (P_0(t) - P_6(t)) \rangle + u_{0,t} \frac{\sum_{k,\uparrow} q^k}{4} - u_{6,t} \frac{\sum_{k,\uparrow} q^k}{4} \tag{A.36}$$

$$\left\langle \frac{D_{6,\downarrow}(t)}{D_{0,\downarrow}(t)} \right\rangle = 1 - \langle (P_6(t) - P_0(t)) \rangle + u_{6,t} \frac{\sum_{j,\downarrow} q^j}{4} - u_{0,t} \frac{\sum_{j,\downarrow} q^j}{4} \tag{A.37}$$

For opposite detectors $P_6(t) = - P_0(t)$. The second order terms $P_0{}^2$, $u_{0,6}{}^2$ and $P_0 \cdot u_{0,6}$ can be neglected in the product of the two detector signals ratio:

$$\left\langle \frac{D_{\uparrow,0}(t)}{D_{\uparrow,6}(t)} \right\rangle \left\langle \frac{D_{\downarrow,6}(t)}{D_{\downarrow,0}(t)} \right\rangle = 1 + 2(P_0(t) - P_6(t)) + (u_{0,t} - u_{6,t}) \left(\frac{\sum_{k,\uparrow} q^k}{4} - \frac{\sum_{j,\downarrow} q^j}{4} \right) \tag{A.38}$$

For each spin sequence and each time bin, the product of the average detector ratios is calculated:

$$R_{0,6}(t) = \left\langle \frac{D_{0,\uparrow}(t)}{D_{6,\uparrow}(t)} \right\rangle \cdot \left\langle \frac{D_{6,\downarrow}(t)}{D_{0,\downarrow}(t)} \right\rangle \tag{A.39}$$

The asymmetry term P_0 is considered constant over the time bins $[T_1,$ $T_2]$. The transient decay parameter is q_1=exp $(-1/\tau)$ with the decay time in units of time bins. With this notation $T = 40$ is the number of time bins in one pulse and $q = e^{-T/\tau} = q_1{}^{40}$. The asymmetry ratio for each time bin in the time interval $[T_1, T_2]$ is calculated from the ratio $Q(k,t) = (\sqrt{R_{0,6}(t)} - 1)/(\sqrt{R_{0,6}(t)} + 1)$:

$$Q_{0,6}(t) = \frac{P_0(t) - P_6(t)}{2} + \frac{u_0(t) - u_6(t)}{4}\left(\frac{\sum_{k,\uparrow} q^k}{4} - \frac{\sum_{j,\downarrow} q^j}{4}\right) \qquad \text{(A.40)}$$

To calculate the raw asymmetry for each accepted spin sequence the time average of the ratio $Q_{0,6}(t)$ from T_1 to T_2 is saved in a histogram. At the end of the loop over runs, the average and the standard deviation of the four 24 histograms are read. Because the calculated transient amplitude had a gaussian distribution, the asymmetry was calculated at each spin sequence to reduced the contribution of the fluctuations in the transient amplitude.

The corrected asymmetry P_0 , the relative transient amplitudes v_0, v_6, the transient decay rate q_1 , are calculated from the minimization of the χ^2 function for each spin sequence:

$$\chi_e^2 = \sum_{t=T_1}^{t=T_2} \left(Q_{0,6}(t) - P_0(t) - \frac{u_0(t) - u_6(t)}{16}\left(\sum_{k,\uparrow} q^k - \sum_{j,\downarrow} q^j\right)\right)^2 \qquad \text{(A.41)}$$

The time average of each detector pair asymmetry is calculated over the time bins from T_1 to T_2 , for each spin -sequence and saved in a histogram. At the end of all the runs the average and the standard deviation of the 24 histograms are read. The transient contribution is reduced in the asymmetry ratio and the shift in the asymmetry is much smaller than the fitting errors.

If the fit is done only at the end of the runs, the χ^2 function is a sum over all spin sequences and over the time bins.The weights used in this function are the variances of the asymmetry ratio $Q_{0,6}(t)$ and can be calculated at the end of the runs from histograms of the raw asymmetry. All the results presented here were obtained by calculating the asymmetry at each spin sequence and the average asymmetry for each pair was read from histograms at the end of all runs.

$$\chi_e^2 = \sum_{t=t_1}^{t_2} \frac{1}{\sigma_{k,j,t}^2}\left(A_{0,6}(t) - P_0 - (\frac{\bar{D}_0}{D_0(t)}v_0 - \frac{\bar{D}_6}{D_6(t)}v_6)q_1^t \frac{q^k - q^j}{4}\right)^2 \qquad \text{(A.42)}$$

The number of degrees of liberty is $(T_2\text{-}T_1 + 1) - 4$. This procedure was used to calculate the corrected asymmetry for Al and Cl.

APPENDIX B

The Neutron Electric Dipole Moment Experiment at SNS

B.1   Introduction

The neutron has a well known magnetic moment and zero charge. Due to its three quarks structure, the neutron can have an electric dipole moment if the centers of the negative and positive charge distributions do not coincide. However an electric dipole moment of the neutron has not been observed and it is expected to be less than 10^{-33} e $\cdot$ cm in the Standard Model, five orders of magnitude smaller than the current experimental limits. Other theoretical models that extend the Standard Models (the Supersymmetry, Higgs fields and Left-Right Symmetry) predict a neutron Electric Dipole Moment (nEDM) of 10^{-26} to 10^{-28} e$\cdot$ cm that could be measured. A measurement of an nEDM at this level could validate these theoretical models and explain the unbalance of the matter and antimatter in the universe. A non-zero electric dipole moment of the neutron violates both the time reversal invariance and the charge and parity (CP) symmetry. This can be seen by looking to the equation of the potential energy of a neutron placed in the magnetic and electric fields.

$$H = -\vec{E} \cdot \vec{p} - \mu \cdot \vec{B} \cdot \vec{S} \tag{B.1}$$

Here $\vec{p}$ and $\mu\vec{S}$ are the electric and the magnetic dipole moments of the neutron. The electric and magnetic fields are $\vec{E}$ and $\vec{B}$ respectively.

During the experiment the electric and magnetic fields will be aligned in the same direction with very good precision such that the direction of the neutron spin is aligned with the direction of the electric dipole moment. Under a parity transformation the electric dipole moment and the electric fields are reversed but the direction of the neutron magnetic moment and of the magnetic field do not change. Under the time reversal operation both the magnetic field and the magnetic moment change direction but the electric field and dipole moment are conserved. Therefore if there is a change in the neutron potential energy after a change in the direction of the electric fields then it has to be due to a non-zero electric dipole moment if all the other systematic errors are ruled out.

The goal of the neutron electric dipole moment experiment at the SNS is to measure the neutron electric dipole moment or to establish a new limit at the level 10^{-28} e$\cdot$ cm. The experiment has to solve technical problems related with the stability of the high electric field inside the measurement cell, the transport of the polarized ^{3}He, with negligible depolarization, from the Atomic Beam Source (ABS) located outside the nEDM magnetic shields to the injection cell in the Upper Cryostat and finally to the measurement cells in the Lower Cryostat. The systematic errors related with the motion of the neutron spin in non-uniform magnetic field have to be eliminated by reducing the magnetic field gradients inside the measurement cell to less than 10^{-6} (1/cm) [79].

Next sections present the results of the finite-element calculations done in Opera 3D, TOSCA, (Vector Fields) to calculate the attenuation factor of the four Mumetal shields plus one Superconducting shield of the lower cryostat, the three Mumetal shields of the upper cryostat, the calculation of the magnetic field gradient inside the measurement cells and the spin transport of the polarized ^{3}He from the exit of a quadrupole magnet ABS to the center of the injection cell.

B.2   The Design of the Coils

In order to decrease the Earth magnetic field gradients inside the measurement cells, the lower cryostat has five concentric cylnidrical shields: four ferromagnetic shields and one superconducting shields. The cylindrical superconducting shield has radius 69 cm and length 415 cm. The Metglas shield has a radius 67 cm and length 415 cm. The three external Mumetal shields, 80 cm long, have radii 60, 65 and 70 inches.

In the Tosca model there are 40 coils and 8 correction coils placed on the surface of a cylinder 415 cm long, and radius 65 cm surrounded by the cylindrical Metglas shield. Each coil has a saddle shape: there are two straight wires parallel with the axis of the cylinder and two ending arcs bended around the rim of the cylindrical support. The resulting coils, the superconducting, Metglas and Mumetal shields have the same axis.

The position of each coil is given by the angle θ_J (J=1... N/2) and by the coordinates x_J and y_J of their center. The electric current in the straight wires above an below the xz plane is coming out and enters into the page respectively. The direction of the main magnetic field close to the center of the coils is along the x axis. The coil is named cosine theta coil if the angle for the straight wire on the cylindrical surface is given by the formula:

$$\sin\theta_J = \frac{x_J}{R} = \frac{2J-1}{N}, J = 1, 2...N/2 \tag{B.2}$$

B.3   The Calculation of the Magnetic Field of the Upper Cryostat

The beam of ^{3}He atoms is polarized by passing through the ABS quadrupole magnet 128.6 cm long placed outside of the upper cryostat. Only the ^{3}He atoms with the same direction of the spin normal to the ABS axis can pass through the magnet. The axis of the ABS magnet is at $45°$ relative to the axis of the upper cryostat. The polarized ^{3}He atoms have to move from the exit of the ABS to the injection cell, located close to the center of the upper cryostat

cosine theta coils. Along their path the atoms move in the magnetic field of the transport coils. The geometry of these coils and their optimum electric currents were designed with finite-element analysis performed in Opera3D. The calculations allowed to evaluate the change in the magnetic field inside the injection cell due to the ABS quadrupole. The 99% polarized ^{3}He atoms are collected in the injection cell located on the axis and close to the center of the cylindrical coils of the upper cryostat with three Mumetal shields. These coils provide a uniform magnetic field of the injection cell where the polarization of the ^{3}He atoms has to be preserved during the storage time of about 240 seconds. The beam of polarized atoms enters at $45°$ incidence angle on the surface of the super-fluid ^{4}He that fills the Helium injection cell. At the end of the collection time the super-fluid Helium is transferred to the two measurement cells inside the lower cryostat. Inside these cells, the magnetic field gradient along the direction of the main field x has to be smaller than 10^{-6} (G/cm) for a field in the center equal with 10 mG.

The magnetic field of the upper cryostat coils can increase the asymmetry and the field gradients in the two cells of the lower cryostat. Finite-element calculations of a model with upper and lower cryostat were done to estimate the maximum current in the upper cryostat coils for which the field gradient inside the lower cryostat is still within specification. The relaxation time of ^{3}He depends on the magnetic field gradients in the upper cryostat injection cell and was calculated for a temperature equal with 0.35 K inside the injection cell of the upper cryostat coils and transport solenoids. The average field gradient dB_x/dx in the measurement cells was calculated for a range of electric currents the upper cryostat coils. The magnetic field gradients in the region of the He injection cell were calculated in the presence of the ABS magnet, transport solenoids, Mumetal and Metglas shields.

The model considered in this section includes the lower and the upper cosine theta coils, the transport solenoids and the Metglas and Superconducting shields. The model does not have the three external Mumetal shields of the lower cryostat (with radii 106.68 cm, 121.92 cm, 137.16 cm), and the three external Mumetal shields of the upper cryostat (with radii 95.25 cm, 105.41 cm, 115.57 cm). The lower cryostat has 48 modified B_0 coils (R=65 cm, K=0.003, L=416 cm) with the first Metglas shield (R=67 cm, L=416 cm, 0.025 cm thick),and the superconducting shield (R=69 cm, L=416 cm, 0.051 cm thick). The upper cryostat has 24 modified cosine theta coils (R=20.8 cm, K=-0.004) inside a cylindrical Metglas shield (R=21.5 cm, L=134 cm, 0.051 thick, with two gaps 6 cm wide). The center of the 24 coils is on the axis of the cylindrical Metglas shield with two gaps. The axis of the coils coincide with the axis of the Metglas shield. The center of the upper cryostat 24 cosine theta coils and their Metglas shield is located at x_c=41 cm, y_c=137 cm and z_c=50 cm if the origin of the reference system is at the intersection of the vertical axis of

the upper cryostat external shields and the horizontal axis of the external shields of the lower cryostat. The role of the external Mumetal shields is to screen the external magnetic field of the Earth and of the ABS quadrupole magnet. With J the coil number, between 1 and N=20, the angles of the upper cryostat cylindrical coils are given by the relation:

$$\tan \theta_J = \frac{(1 - K_1)^2}{\sqrt{\frac{(2J-1)^2}{N^2} - 1}}$$ (B.3)

Here the angular parameter K_1 is a number between -1 and 1. The magnetic field gradients in the central region of the upper cryostat N=20 and M=4 coils depend on the angular parameters K_1 and K_2 of the N and M coils respectively. The extra M=4 coils are placed on the same cylindrical support like the N=20 coils. Their angular position on the support cylinder is given by the above equation with K_1 replaced by K_2 and N replaced with M.

According to the finite-element calculations done for N=20 cylindrical coils placed inside the cylindrical Metglas shield with two gaps (12 cm wide), the field gradients close to the center of the coils decrease when K_1 is decreased from 0 to less then -0.04. However the parameter K_1 can not be smaller than -0.04 because in this case the distance between the last two pairs of coils become smaller than the gap width (12 cm). For this reason the extra M=4 coils with the same radius like the N=20 coils are introduced in the model. The optimum angular parameter K_2 of the M coils was estimated by computing the field gradients for different values of K_2.

The polarized ^{3}He atoms that exit from the ABS magnet enter the magnetic field of three transport solenoids TR_1, TR_2, TR_3 in Figure B.1. The first transport solenoid TR_1 is 79 cm long. The second solenoid TR_2 (radius R=6.3 cm) and the third solenoids TR_3 (radius R=10.3 cm) are 59 cm long and are coaxial. The solenoids are modeled like one ideal cylindrical coil with the outside radius 0.5 cm bigger than the inner radius.There are 24 cosine theta coils (R=20.8 cm, L=125 cm) inside the Metglas shield of the upper cryostat (R=21.5 cm, L=134 cm, with two gaps 12 cm wide) centered at x_c=41 cm, Y_c=137 cm and z_c=50 cm.The polarized ^{3}He beam coming from ABS quadrupole magnet passes along the axis of the transport solenoids and reaches the injection cell centered at 16 cm above the center of the 24 coils.

In the center of the first transport solenoid TR_1 the field is about equal with the field in the center of the 24 cosine theta coils. In the center of the second transport solenoid TR_2 the field varies between 450 mG and 1000 mG. In order to cancel the external fringe field on the common axis, the current in the third transport solenoid TR_3 flows in the opposite direction to the current in the second transport solenoid TR_2. The common axis of the ABS quadrupole
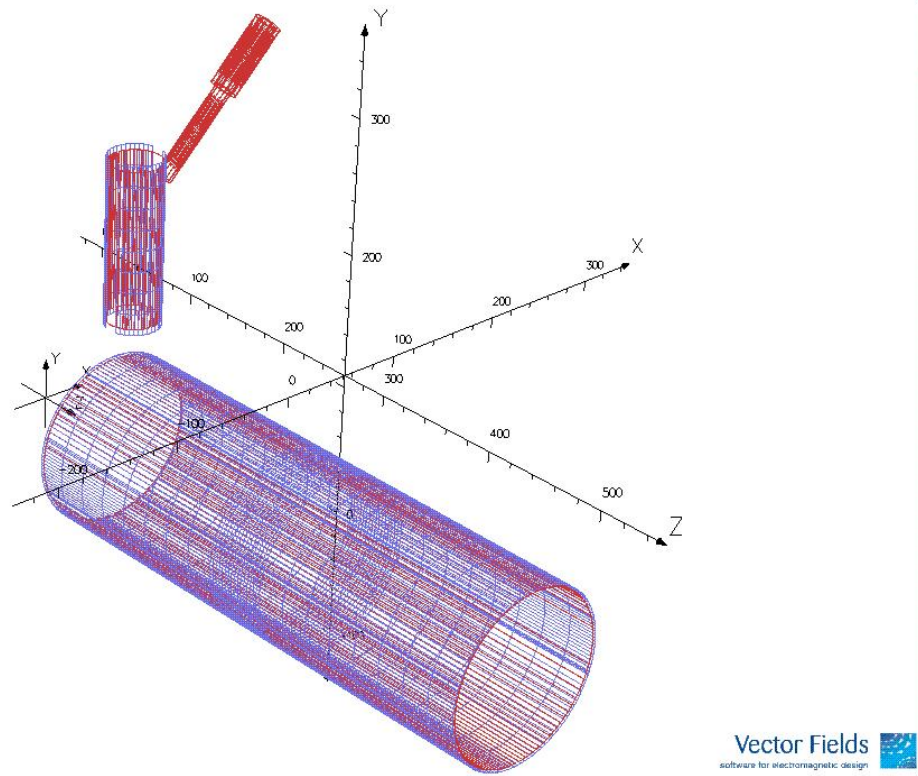
Figure B.1: The coils located inside the magnetic shields of the lower cryostat and upper cryostat.

magnet and transport solenoids makes a $45°$ angle with the axis of the upper cryostat cosine theta coils.

The axes of the two cylindrical shields of the Upper and Lower Cryostat are normal. The model was built in Preprocessor by using three meshes. The base planes of the first and second mesh are parallel with the vertical xy plane normal to the axis z of the lower cryostat . After the base plane was completed the two meshes were extruded in the z direction. The base plane of the third mesh is in the horizontal xz plane. The third mesh was extruded in the vertical y direction to model the cylindrical Metglas shield (R=21.5 cm) with two gaps 12 cm wide. The vertical axis of the third mesh intersects the horizontal xz plane in x=41 cm, y=0 cm,z=-52 cm.

The angular parameter of the lower cryostat N=40 cosine theta coils is K=0.003 and their radius and length are 65 cm and 416 cm respectively. On the same cylinder there are another 4 pairs of gradient coils with the same position and length like the 3rd, 8th , 13th and 18th pairs of B_0 coils. The magnetic field in the two measurement cells was calculated first for a simple model that has only the lower cryostat B_0 coils with the Metglas and

Superconducting shields with no end caps. For this model the magnetic field is normal to the vertical plane yz and tangent to the horizontal planes xz and the plane xy passing through of the center of the B_0 coils. In this case the smallest volume average field gradient $< dB_x/dx > /B_0$ in the measurement cells of the lower cryostat is obtained when the electric current in the 8 gradient coils (I_8) is 1/10 the current in the 40 coils (I_{40}). The magnetic field variation in the measurement cell is the ratio $(B - B_0)/B_0$ (%) where B_0 is the field in the center of the cell. The average relative field variation, calculated along directions parallel with z axis and for three magnetic fields B_1 in the center of the upper cryostat coils is presented in Figure B.2. The average field gradient dB_x/dx calculated on three vertical planes (z=0, 10 , 25 cm and y=0cm, 1cm . . . 5 cm) and for three values of the magnetic field B_1 in the center of the upper cryostat coils and of the transfer solenoids. for the same magnetic fields in the center of the upper cryostat coils is presented in Figure B.3.

In these calculations the magnetic field in the center of the lower cryostat B_0 coils is 22 mG and the electric currents in the lower cryostat 48 coils are I_{40}=60 mA and I_8=10 mA respectively. If the electric currents in the 24 coils of the upper cryostat and in the transport solenoids is switched off, there is still a residual magnetic fields (0.12 mG) in the center of the upper cryostat coils that is due to the 22 mG field in the measurement cells of the lower cryostat. Even for zero currents in the upper cryostat coils and solenoids, the field in the measurement cells has a small asymmetry in the z direction, due to the presence of the upper cryostat Metglas shield. The ratio between the magnetic field B_1 in the center of the injection cell and the fields BR_1, BR_2 in the center of the transport solenoids can be maintained constant if the 24 coils are connected in series with the coils of the transport solenoids.

If the field inside the measurement cells is asymmetric along the z and y direction then the statistical errors related to the geometric phase of the spin precession depends also on the field gradients dB_y/dy and dB_z/dz. The average magnetic field gradients divided with the field in the center of the cell are calculated along directions parallel with the vertical axis in Figure B.4 for the same magnetic fields in the center of the upper cryostat coils B_1 and transport solenoids BR_1, BR_2 considered above. For zero current in the upper cryostat coils and transport solenoids and B_0=22.1 mG in the center of the lower cryostat coils, the fringe fields in the center of the upper cryostat coils and two transport solenoids are B_1=0.2 mG, BR_1=0.033 mG and BR_2=0.0205 mG respectively. The magnetic field in the center of the measurement cells is about 22 mG. For the range of the fields B_1, BR_1, BR_2 considered, the average gradient $< dB_y/dy > /B_0$ increases linearly with the increase in the field of the upper cryostat coils B_1. For B_1=36.8 mG, the field gradients in the two cells are $< dB_y/dy > /B_0$ (left cell) = $1.112 \cdot 10^{-6}$ (1/cm) and $< dB_y/dy > /B_0$ (right cell) = $1.158 \cdot 10^{-6}$ (1/cm).
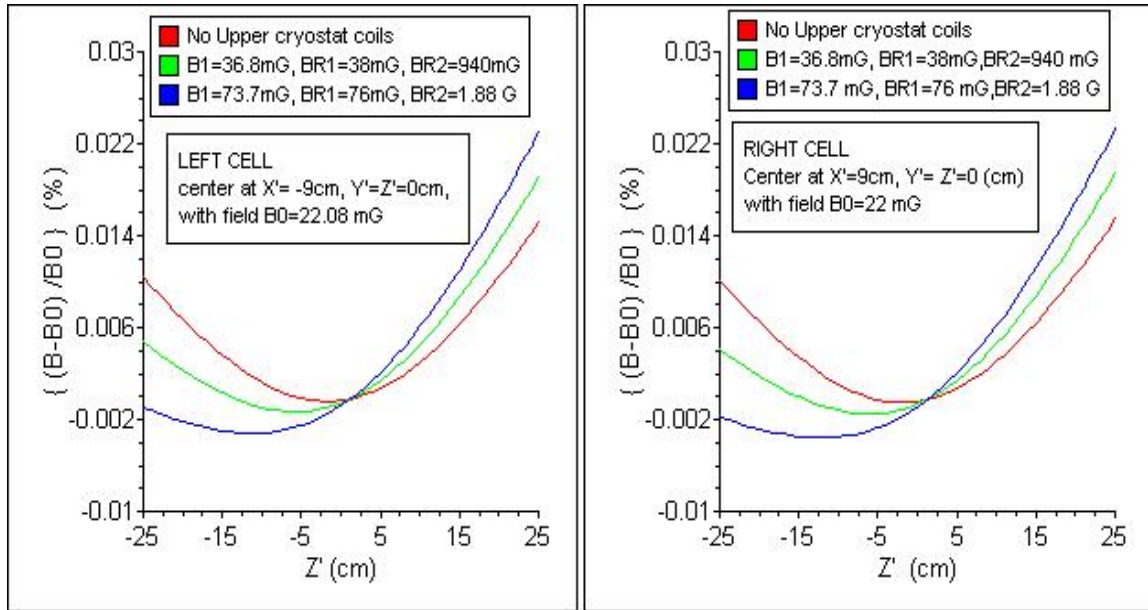
Figure B.2: The magnetic field variation in the two measurement cells are calculated for two magnetic fields B_1 in the center of the upper cryostat shields.
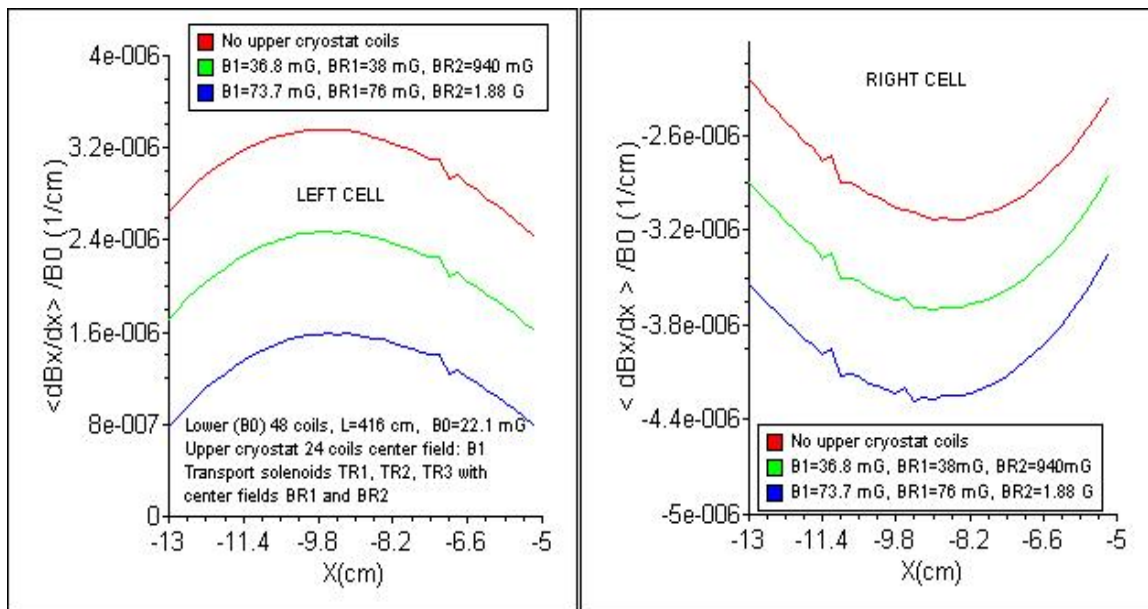

Figure B.3: The average magnetic field gradient $dB_x/dx/B_0$ is calculated in the right and left measurement cells and for three currents in the upper cryostat coils and transfer solenoids.
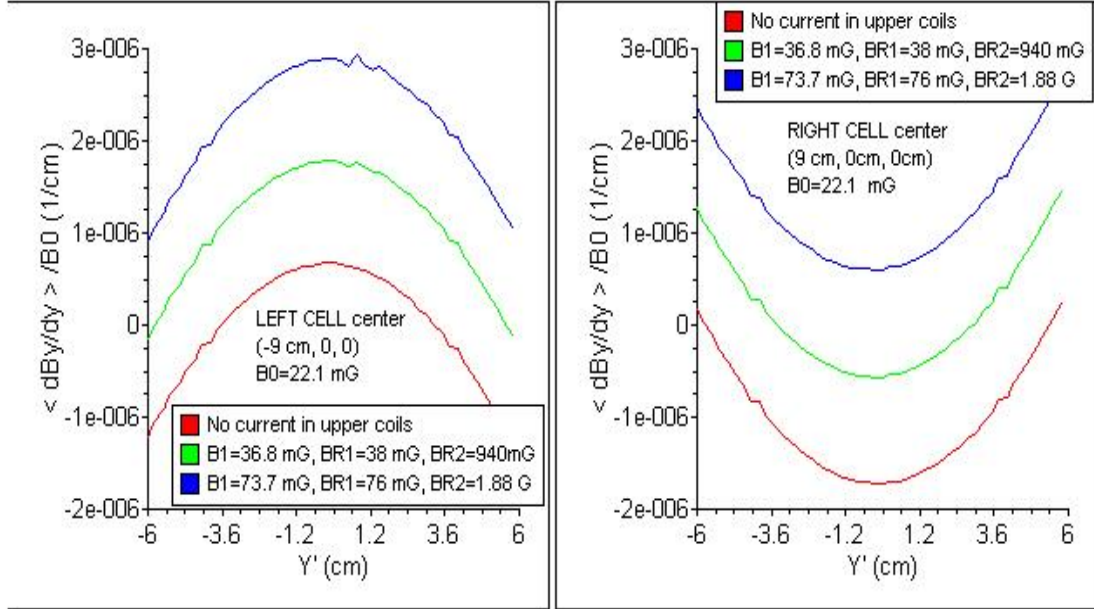
Figure B.4: The average magnetic field gradients $dB_y/dy/B_0$ calculated in the left and right measurement cells for three currents in the upper cryostat coils and transport solenoids.

In contrast to the significant increase of the gradients in the above two figures, the volume average of the magnetic field gradient in the z direction $\{dB_z/dz/B_0\}$ changes less significantly in response to the increase in the B_1 field from 0 to 73.7 mG (Figure B.5). In this figure the average relative field gradient is calculated along directions parallel with the z axis, inside the boundaries of the left and right measurement cells.

The longitudinal relaxation time T_1 of ^{3}He inside the injection cell at 0.35 K and collection volume $AB1$ placed on the axis of the upper cryostat 24 cosine theta coils is calculated in Figure B.6 for a field B_0=22 mG in the center of the lower cryostat coils and two sets of magnetic fields in the upper cryostat (B_1) and transport coils (BR_1, BR_2). The relaxation time is calculated along directions parallel with the vertical axis y_1 and horizontal axis x_1 of the 24 cosine theta coils in the upper cryostat.

The angle parameters for the 20 and 4 coils is K_1 =-0.04 and K_2 = -0.1 respectively. The center of the global reference system xyz is in the center of the upper cryostat Mumetal shields and on the axis of the B_0 coils in the lower cryostat. The origin of the local reference system x_1, y_1, z_1 is in the center of the upper cryostat N=20 cosine theta coils with the x_1, y_1, z_1 axes parallel with the x, y, z axes.
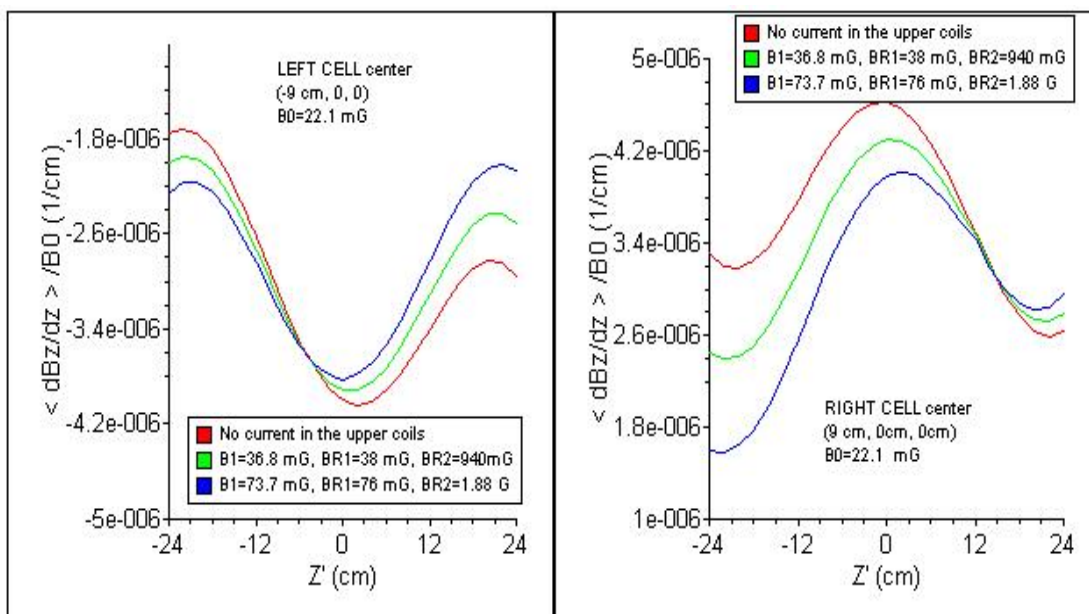
Figure B.5: The average magnetic field gradients $dB_z/dz/B_0$ is calculated inside the left and right measurement cells of the lower cryostat, for three currents in the upper cryostat coils.
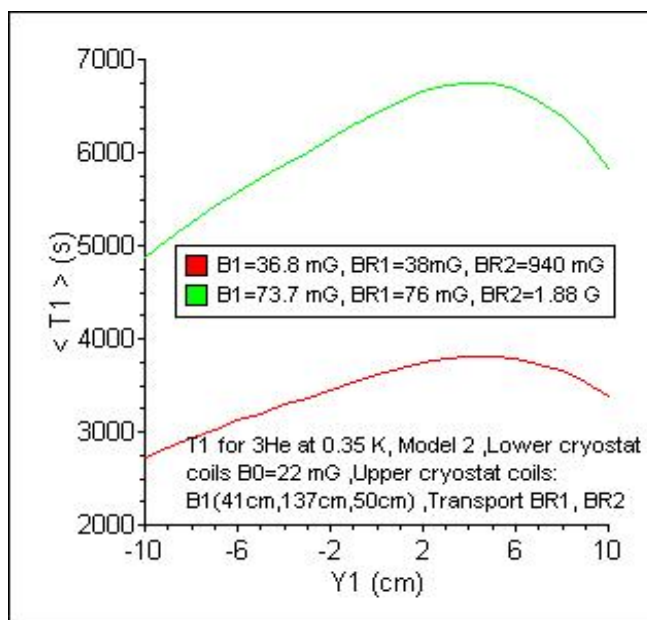

Figure B.6: The longitudinal relaxation time of ^{3}He atoms at 0.25 K is calculated for different currents in the upper cryostat coils and transport solenoids.

The main field inside the upper cryostat coils is in the z direction (parallel with the vertical yz plane). The spin of the polarized ^{3}He atoms at the exit of the ABS magnet is perpendicular to the axis of the quadrupole magnet and parallel with the plane defined by this axis with the vertical axis of the upper cryostat cosine theta coils. Therefore the spin of the ^{3}He atoms has to rotate with $45°$ along their path from the exit of the ABS magnet to the center of the injection cell for both models. The main field inside the Helium injection cell is along the x direction that is also the direction of the main field inside the B_0 coils in the lower cryostat. Because the polarization of the ^{3}He spin has to be preserved during its transport from the injection cell to the two measurement cells there are coils around the transport tube from the injection cell to the measurement cell that make a field uniform field in every point of the tube.

The diagram of the upper cosine theta coils, ferromagnetic shield and injection cell seen in the horizontal plane xz are presented in Figure B.7. The center of the global reference system xyz is at the intersection of the vertical axis of the upper cryostat external shields and the horizontal axis of the B_0 coils of the lower cryostat. The center of the upper cosine theta coils (in red), and their ferromagnetic shield with 2 gaps (12 cm wide) is at x=0 cm, y=137 cm, z=-52 cm at 52 cm distance from the vertical axis y of the Mumetal shields. The local coordinate system x_1, y_1, z_1 is in the center of the upper cosine theta coils and ferromagnetic shield.

The direction of the magnetization vector in each of the four ABS magnets is normal to the axis of the ^{3}He beam. The nominal distance from the exit of the ABS quadrupole and the center of the injection cell is 191 cm measured along the axis. The axis of the ABS quadrupole magnet is coincident with the axis of the ^{3}He transport solenoid.

The magnetic field along the axis of the transport solenoid is calculated from the center of the ^{3}He injection cell to the exit of the ABS quadrupole, for two lengths and electric currents of the transport solenoid (Figure B.8). In the left figure the length of the transport solenoid is 49 cm and the field in its center is 77 mG. In the right figure the length of the transport solenoid is 116 cm, with a field along its axis changing from 77 mG to 1000 mG.

The magnetic field gradients inside the Helium injection cell have to be small such that the relaxation rate of ^{3}He is bigger than 10,000 seconds at T=0.35 K. At this temperature the diffusion coefficient of ^{3}He in ^{4}He is D=$1.8/T^7$ =2797 (cm^2/s). The relaxation rate $1/T_1$ is proportional with the diffusion coefficient D:

$$\frac{1}{T_1} = D \frac{|\nabla B_y|^2 + |\nabla B_z|^2}{B_0^2} \frac{1}{1 + (\omega_0 \tau_c)^2} \qquad (\text{B.4})$$
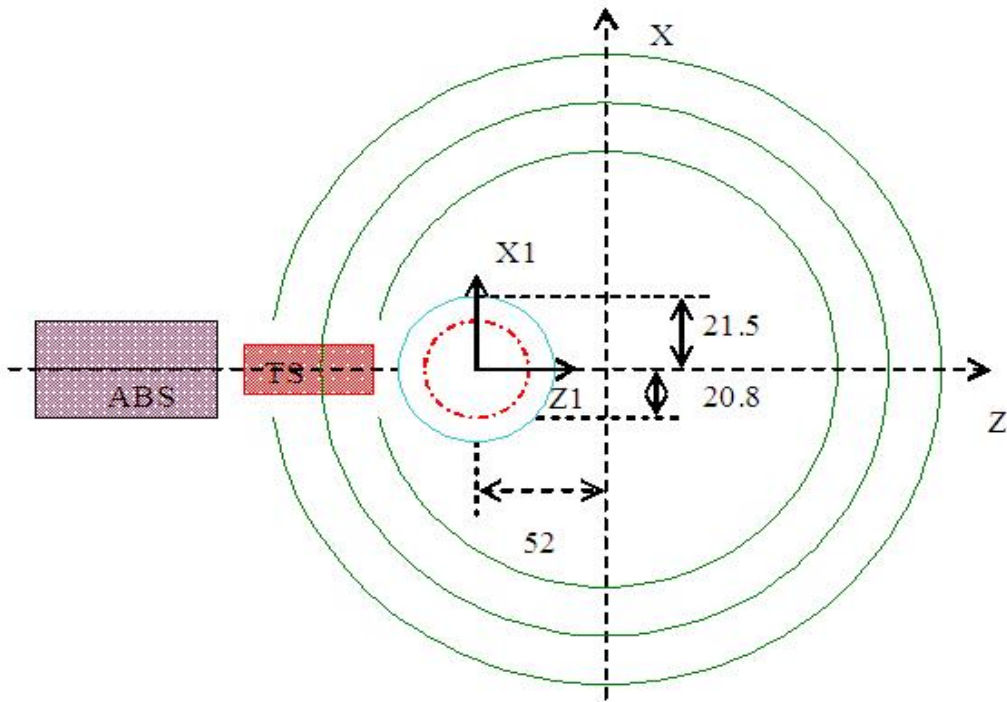
Figure B.7: The model of the upper cryostat external shields, coils, ferromagnetic shield and ABS magnet.
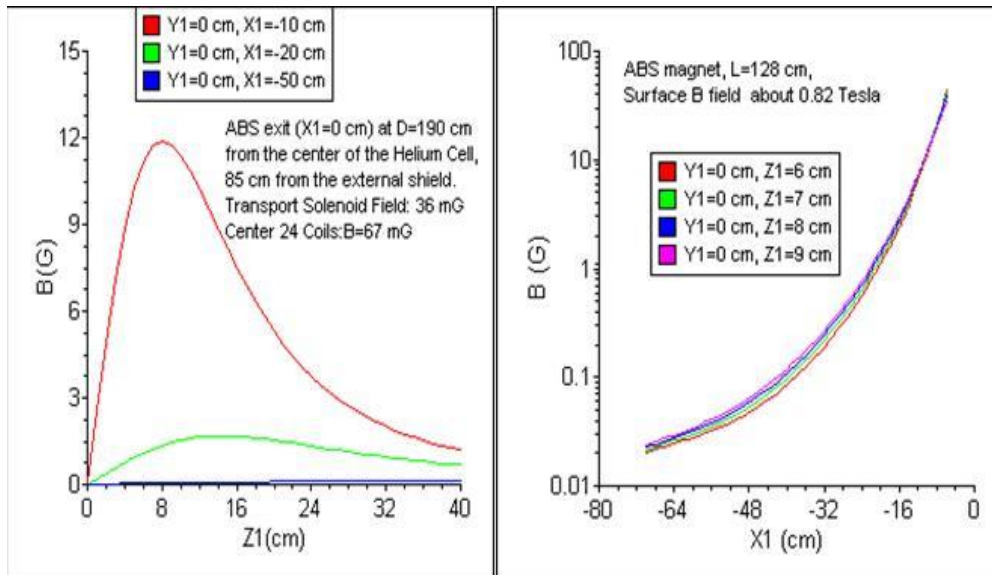

Figure B.8: The magnetic field along the axis of the transport solenoid is calculated for a 49 cm long and a 116 cm long transport solenoid in the left and right figures respectively.

At T=0.35 K the collision time for ^{3}He in super fluid ^{4}He is $\tau = 6.387 \cdot 10^{-4}(s)$. The effective mass of ^{4}He is 2.2 times bigger than the mass of the ^{3}He atoms that is m_{3He}=3.01603 atomic mass units . The Larmour frequency ω_0 of ^{3}He given by:

$\omega_0 = 2.03789 \cdot 10^4 \cdot B$(rad / s). The depolarization of ^{3}He inside the injection cell is smaller than 1% during the collection time, if the relaxation rate is smaller than:

$$\frac{1}{T_1} = D \frac{\left|\vec{\nabla} B_y\right|^2 + \left|\vec{\nabla} B_z\right|^2}{B_0^2} < 10^{-4}(s) \tag{B.5}$$

Therefore there is an upper limit of the transversal spatial field gradients that can be tolerated inside the volume of the ^{3}He injection cell:

$$\frac{\sqrt{\left|\vec{\nabla} B_y\right|^2 + \left|\vec{\nabla} B_z\right|^2}}{B_0} < 1.9 \cdot 10^{-4}(cm^{-1}) \tag{B.6}$$

If the field inside the transport solenoid increases and becomes bigger than the field inside the cylindrical coils of the upper cryostat, the asymmetry of the magnetic field along the vertical y axis and horizontal x of the coils volume also increases. The magnetic field asymmetry along these directions has to be minimized in order to decrease the spatial field gradients and to increase the relaxation time T_1. Therefore the magnetic field along the axis of the transport solenoid has to increase from small values (closer to the Helium injection cell) to about 1000 mG inside the region of the transport solenoid closer to the ABS magnet outside the Mumetal shields.

The magnetic field along the vertical or horizontal axes of the upper cryostat cosine theta coils can also be asymmetric due to the magnetization of the Mumetal shields. The field asymmetry along the horizontal direction due to the magnetic field of the transport solenoid can be decreased by increasing the electric current in two of the M=4 extra coils located on the same cylindrical support like the N=20 coils. The magnetic fields inside the center of the 20 cosine theta coils and transport solenoid are Bc = 53.6 (mG) and Bs=36.6 (mG) respectively. On the surface of the ABS magnet the field is about 0.85 Tesla. The magnetic field of the Earth (500 mG) was not considered in these calculations.

The He atoms can lose their polarization in the regions of very small magnetic field. The transport solenoid has to be longer than 49 cm. Along the axis of the transport solenoid the magnetic field has to vary from about 50 mG close to the injection cell to about 1000 mG close to the ABS magnet. A field
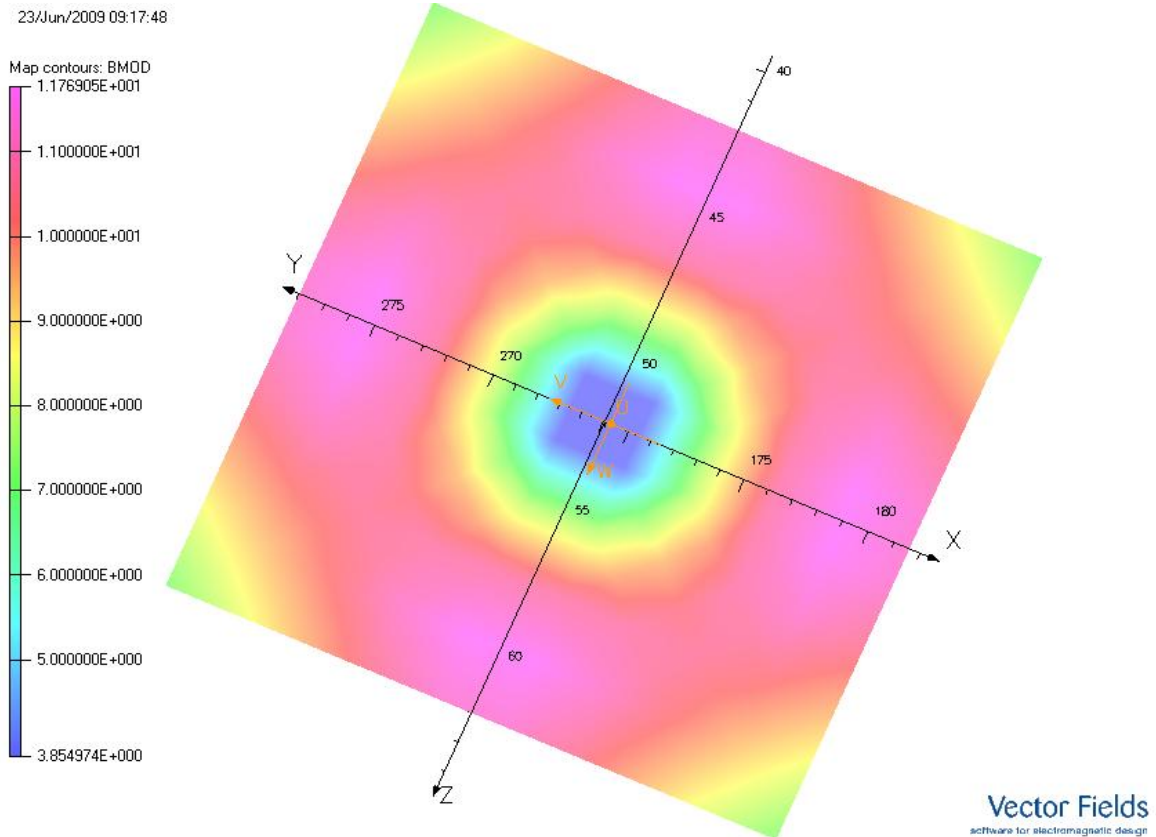
Figure B.9: A two dimensional map of the magnetic field calculated in a plane perpendicular to the axis of the ABS magnet.

map in a plane transversal to the axis of the quadrupole located at 10 cm from the exit face of the quadrupole is presented in Figure B.9. The y and x axes make a +45° and -45° angle with the axis of the ABS magnet that is perpendicular to the plane of the page.

The relative spatial gradients $\left|\vec{\nabla} B_x\right|/B$, $\left|\vec{\nabla} B_y\right|/B$ and $\left|\vec{\nabla} B_z\right|/B$ were calculated along directions parallel with the vertical axis (y_1) of the upper cryostat coils. The center of the local system of reference x_1, y_1, z_1 is located in the center of the cylindrical coils of the upper cryostat. Between y_1=-30 cm and y_1=10 cm the spatial gradients $\left|\vec{\nabla} B_x\right|/B$ and $\left|\vec{\nabla} B_z\right|/B$ are between $1 \cdot 10^{-4}$ (1/cm) and $1 \cdot 10^{-3}$ (1/cm). The spatial gradient $\left|\vec{\nabla} B_y\right|/B$ is about 10^{-4} (1/cm). The longitudinal relaxation time T_1 is calculated at T=0.35 K along the same directions.

To understand the effect of the ABS quadrupole magnet and external Mumetal shields, the longitudinal relaxation time of ^{3}He will be calculated along

181

Figure B.10: The longitudinal relaxation time of ^{3}He along the axis of the upper cryostat coils is calculated at T=0.35 K for two magnetic fields inside the transport solenoid.

the axis of the 20 upper coils for both models, with and without the ABS magnet in the model.

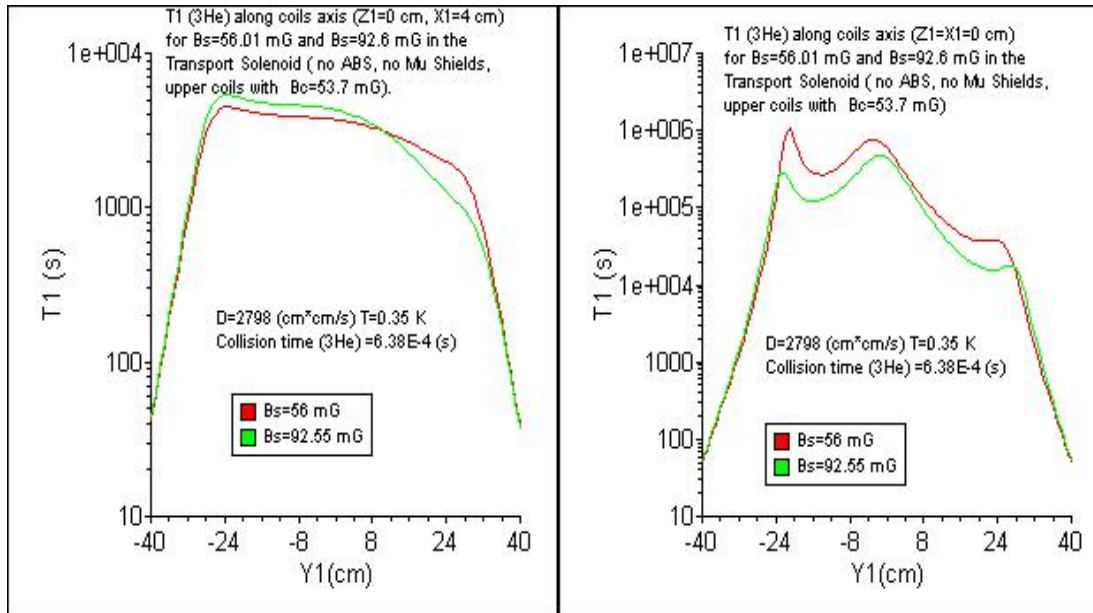The geometry, magnetic field and position of the transport solenoid are the most important factors that determine the value of the relaxation time of ^{3}He inside the injection cell. To prove this point we consider two position of the axis of the transport solenoid. The model has only the ferromagnetic shield with two gaps (12 cm wide), the upper cryostat coils (N=20, M=4) and the transport solenoid 49 cm long with its axis passing through the center of the ^{3}He injection cell. The external Mumetal shields and of the ABS magnet are not built in the model. The relaxation time and the relative field gradients along the axis of the 20 coils remain about the same when the field in the center of the transport solenoid is doubled from 56 mG to 92.6 mG (figure B.10). The electric current in the upper cryostat coils is the same in both cases. Only the current in the transport solenoid (49 cm long) is increased. Therefore the decrease in the relaxation time due to the 100% increase of the field inside the transport solenoid is small when the 49 -cm- long transport solenoid is used.

The fringe field of the same transport solenoid in the ^{3}He cell has to be small (less than 20 mG). At the same time the rate of change in the direction and magnitude of the field has to be small enough to prevent the loss in the ^{3}He polarization. To satisfy these conditions there are three groups of transport

182

solenoids with different currents. The first solenoid (TR1, R=6.3 cm) is close to the ^{3}He injection cell and has a field of 38 mG at its center. The second transport solenoid has two concentric cylindrical solenoids and a field on its axis equal with 470 mG. The inner solenoid (TR2) has a current I_1, radius R_1=6.3 cm. The outer solenoid (TR3) has current I_2 and radius R_2=10.3 cm. The electric currents in the outer and inner solenoids flow in opposite direction to cancel their fringe magnetic fields inside the volume if ^{3}He injection cell.

The longitudinal relaxation time of ^{3}He at 0.35 K is calculated along the horizontal axis x_1 and the vertical axis y_1 of the upper cryostat cylindrical coils in the presence and in the absence of the ABS magnet (Figure B.11. The magnetic fields in the center of the cosine theta coils and transport solenoids B_1=18 mG, BR_1=37 mG and BR_2=470 mG. The ABS magnet does not significantly change the magnetic field gradients and the relaxation time in the volume of the upper cryostat coils. The relaxation time is small because the angular parameter K_2 of the M=4 coils was not optimum and the axis of the transport solenoids passes through the center of the injection cell. The common axis of the transport solenoids passes through the center of the injection cell (x_c =41 cm, y_c =137 cm, z_c =52 cm).
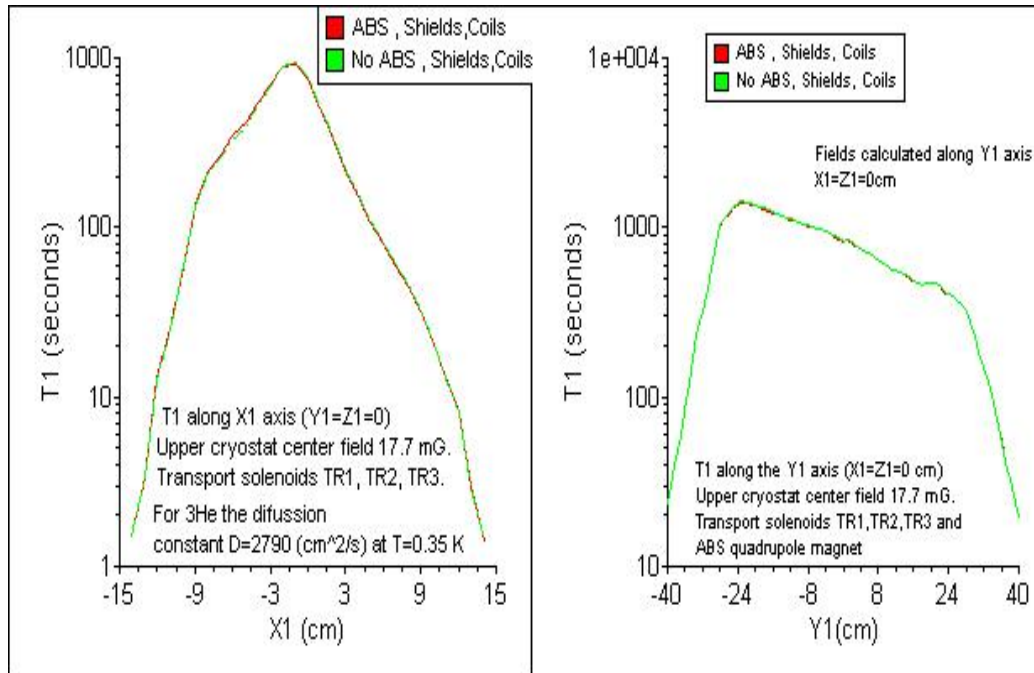

Figure B.11: The longitudinal relaxation time of ^{3}He at 0.35 K is calculated along the vertical axis y_1 and the horizontal axis x_1 of the upper cryostat cosine theta coils.

The relaxation time T_1 is bigger than 10^4 seconds only for a radial distance

smaller than 2.5 cm from the vertical axis y_1 and for $|y_1|<$10 cm. This values of the relaxation time are due to both the asymmetric position of the upper cryostat coils and the particular choice of the electric currents in the 24 upper cryostat coils and transport solenoids. The magnetic field (38 mG) in the center of the first transport solenoid is two times bigger then the field in the center of the upper cryostat coils (17 mG) and the axis of the transport solenoid passes through the center of the upper cryostat coils. The magnetic field asymmetry along the vertical direction increases the spatial field gradients and decreases the relaxation time T_1. The increase in the field gradients are due to the fringe magnetic fields of the transport solenoid inside the ^{3}He cell.

B.4   Conclusion

The relaxation time of ^{3}He inside the injection cell is bigger than 10,000 seconds for the optimum electric currents in the upper cosine theta coils, even in the presence of the ABS quadrupole and for a field of 500 mG on the axis of the transport solenoid and outside the external shield. In this case the asymmetry of the magnetic field inside the He injection cell and the AB1 collection volume is small. The minimum relaxation time in the injection cell is 10,000 seconds. The change in the magnetic field gradients inside the upper cryostat coils due to the 20 mG field in the center of the lower cryostat B_0 coils is negligible.

APPENDIX C

The Nab experiment at SNS

C.1   Introduction

The Nab experiment proposed a precise measurements of a the electron-neutrino correlation parameter and b the Fierz term. The goal accuracy is $\Delta a/a = 10^{-3}$ and $\Delta b = 10^{-3}$. The neutrons will pass through the center volume of a field expansion spectrometer and some will decay in this volume.The proton and electrons originating from the free beta decay of the neutron inside the spectrometer are detected by two Silicon detectors located at the two ends of the spectrometer [80].

The measurement method for a is based on the linear dependence of the cosine of the angle between the electron and neutrino momenta $\cos\theta_{e,\nu}$ and the square of the proton momentum. Consider p_p the momentum of the proton. Due to this linear dependence the slope of the $p_p{}^2$ probability distribution is given by $\beta \cdot a$ where $\beta =$v/c. In the decay volume the field is about 4 Tesla dropping out quickly in order to align the proton momenta along the direction of travel. Two segmented Silicon detectors located at each end of the solenoid can detect the protons and electrons in an effective 4π geometry. The fringe field outside the spectrometer has to be decreased to less than 0.05 Gauss outside the concrete walls of the beam line 13, to meet the SNS requirements. Both active and passive shields are used to meet this requirement. The design of the low carbon steel shield and the calculation of the forces on the the superconducting coils were done in Opera 3D, Tosca, Vector Field.

C.2   The geometry of the Nab coils

The six pairs of the Nab are modeled like simple circular solenoids (Figure C.1). Two solenoids in a pair have the same center on the z axis. The currents in the two solenoids are the same but they flow in opposite direction such that the magnetic fields of the outer and inner solenoids cancel at a certain radial distance from the z axis. The point where the two fields cancel depends on the radii, length and radial thickness of the two solenoids. In addition a passive magnetic shield is located at a radial distance of about 100 cm from the z axis of the spectrometer. In this section the sum of the magnetic fields of the two solenoids of a pair is calculated at 100 cm, 200 cm and 300 cm from the z axis for three values of the electric current densities in the coils.

The two Si detectors of the Nab spectrometer have to be in a small magnetic field. Close to the center of the spectrometer the magnetic field along the z axis is a second power function of z: $B(z) = B_0(1 - \alpha(z - z_c)^2)$ where B_0 is the field at $z = z_c$. The second derivative of the magnetic field divided
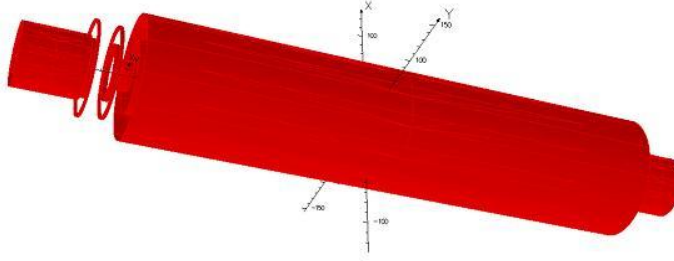
Figure C.1: The model of the six pairs of Nab solenoids is presented in Modeler, Opera 3D

with $-2 \cdot B_0$ is α. The geometry of the inner coils is constrained by the experiment requirement on the magnetic field profile along the z axis. For this reason the radius of the outer solenoid is varied, keeping the radius of the inner solenoids, the radial thickness and the length of the two solenoids fixed. This calculation of the optimum radius of the outer solenoid is done for two values of the current density in the wire.

The magnetic field of the solenoids without magnetic materials was calculated by Biot Savart integration. Each solenoid was modeled like one big coil with rectangular cross section, inner radius R_1 and outer radius R_2 and a radial thickness $\Delta R = R_2 - R_1$. Consider ΔZ the length of the solenoid along z axis. For a total current in the solenoid equal with $n \cdot I$ the current density in TOSCA model is:

$$J_T = \frac{nI}{\Delta R \cdot \Delta Z} \tag{C.1}$$

In the TOSCA the units for ΔR and ΔZ are cm and the units for the current density are A/cm^2. The total current in the solenoid is $n \cdot I$, where n is the number of wires and I is the electric current in the wire. The wire has circular cross section.

The electric current density in the wire can calculated if the diameter d_0 of the wire is known. If the solenoid is made from n loops of wires with diameter d_0 then the total current in the solenoid is equal with

$$nI = J_w \left[n \cdot \frac{\pi d_0^2}{4} \right] = J_w \left[\frac{\Delta R}{d_0} \frac{\Delta Z}{d_0} \frac{\pi d_0^2}{4} \right] = J_w \frac{\Delta R \cdot \Delta Z \cdot \pi}{4} \tag{C.2}$$

$$J_w = \frac{4nI}{\Delta R \cdot \Delta Z \cdot \pi} = \frac{4}{\pi} J_T \tag{C.3}$$

The position of the centers of the solenoids, and the geometry of the solenoids are presented in table C.2.The number of turns N is calculated for a diameter of the wire equal with d_0=0.01 cm. The electric current in a wire is I=3.5 (A).

Table C.1: The position of the solenoid center z_m, the inner radius of the solenoid R_{in}, the radial thickness of the solenoid ΔR, the length of the solenoid ΔZ and the total current in solenoid $n \cdot I$.

Coil	z_m cm	R_{in} cm	ΔR cm	ΔZ cm	$n \cdot I$ kA	J_w kA/cm^2	Nb. loops
C_{1i}	237.5	31.61	0.03	465	488.25	44.56	139500
C_{1o}	237.5	54.6	0.01	465	-162.75	-44.56	46500
C_{2i}	500	15.89	0.21	40	294	44.56	84000
C_{2o}	500	27.18	0.07	40	-98	-44.56	28000
C_{3i}	-61.9	15.90	0.2	56.13	392.91	44.56	112260
C_{3o}	-61.9	26.28	0.07	56.13	-137.52	-44.56	39292
C_{4i}	0	5.23	2.46	4.28	368.51	44.56	105288
C_{4o}	0	12.76	0.31	8.56	-92.88	-44.56	26538
C_{5i}	-11.55	20.44	3.97	3.97	551.63	44.56	157608
C_{5o}	-11.55	37.29	2.29	2.29	-183.54	-44.56	52440
C_{6i}	-31.41	21.65	3.68	3.68	473.98	44.56	135423
C_{6o}	-31.41	39.13	2.12	2.12	-157.3	-44.56	44943

For $J_T = 35$ kA/cm ^{2} the maximum field along the axis of the solenoid is 4 T. The electric current density in the wire is calculated from equation C.3. For a 38 gauge wire (d_0=0.01 cm) the current in the wire is 3.5 (A) and the number of loops for each solenoid is presented in the last column of table C.2.

The Nab solenoids are made from the same wire winded in the same direction $+z$ for the inside coils and in the opposite direction $-z$ for the outside coils. The solenoids are connected in series.

The magnetic field was calculated in the radial direction from the center of each pair of solenoids in the absence of the magnetic shield. For the geometry of the solenoids presented above, the magnetic field at 100 cm from the axis is smaller than 1 Gauss in the planes of the coil pairs 1, 2, 3, 4 but is bigger than 7 Gauss in the plane of the coil pairs 5 and 6. At 200 cm distance from the axis the field is smaller than 1 Gauss for all six pairs of solenoids. The solenoids C_{5i} and C_{6i} have radii 20.44 cm and 21.65 cm, about equal with the distance 19.86 cm between their planes, to provide a uniform field over the active volume of the neutron beam in between their planes.

The magnetic field profile is calculated along the z axis and two other directions parallel with z axis lines in Figure C.2.

Along directions parallel to the z axis, at $R < 3$ cm and -4 cm $< z < 4$ cm the magnetic field has a maximum B_0 and it can be fitted well with a second order polynomial function. The fit for three lines parallel with the z axis at radial distance 0, 1, 2 cm from it is presented in table C.2. The units for α
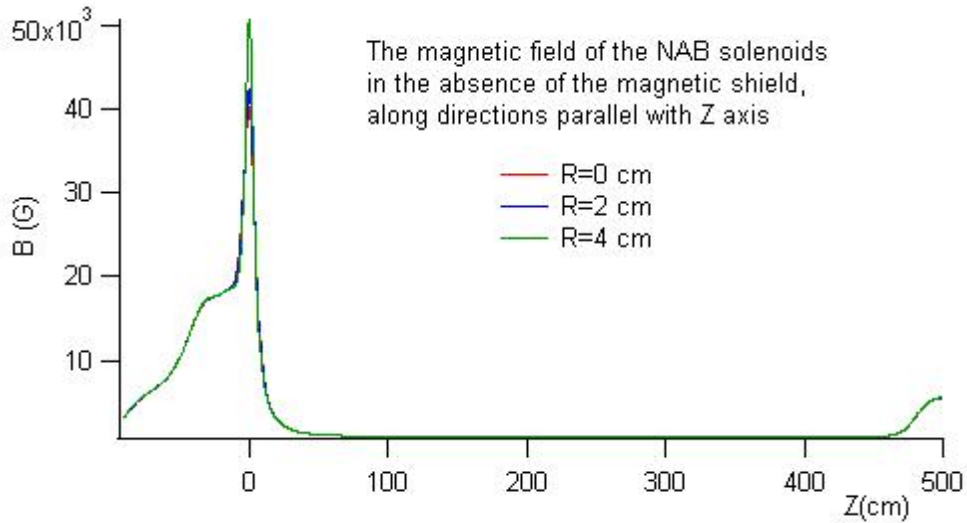
Figure C.2: The magnetic field is calculated along directions parallel with the z axis at three radial distances R=0 , 2 and 4 cm from this axis.

Table C.2: The coefficient α, from the quadratic fit of the magnetic field, along three directions parallel with z axis at 0 cm, 1 cm and 2 cm distance from it.

R(cm)	α^2 coils and shield $1/cm^2$	α^2 coils without shield $1/cm^2$
0	-0.0179	-0.01793
1	-0.0185	-0.01845
2	-0.0203	-0.02026

are 1 /cm^2 while z is measured in cm.

$$B(z)/B_0 = (1 + b \cdot z + \alpha^2 \cdot z^2) \tag{C.4}$$

C.3 The calculation of the forces on the Nab coils.

The closed loop conductors can be modeled with the ideal solenoids provided in Tosca, with uniform current density over their cross section area. The solenoids are read in Post-Processor and the fields are calculated by Biot - Savart integration. To model the real current distribution in the real coils, the current density flow in all the mesh points inside the coils is calculated by solving the current flow problem in Tosca. The outside of the coils is air and is not part of the mesh. After the current flow model is solved the magnetic fields

189

inside the conductors are known and then the forces per unit volume $\vec{J} \times \vec{B}$ can be calculated in any point inside the coil.

One expects that the sum of the forces acting on all the coils is zero because the two forces acting on any pair of coils have opposite directions and their sum is zero. In addition if the solenoids are perfectly centered on the z axis, the radial components of the total force acting on each solenoid is expected to be zero. The maximum number of points (i.e. the order of the Gaussian integration) along the two directions of the cross section and along the direction of the current is 32. Due to numerical errors there are small components of the forces along x or y directions that are not zero. These small errors are related with the Euler angles θ, ϕ, ψ that give the orientation of the solenoids relative to axes. For one pair of solenoids built by reflection of one coil in a plane, the total force is exactly zero. If the pair is not built by reflection of one coil, then there are components of the total force that are not exactly zero. The solution is to rotate the coils with $180°$ about their common axis. The force components for the rotated coils along the radial directions (x, y) have negative sign and almost the same magnitude like the forces for the initial coils. One can consider the average of the corresponding values for each component of the total force. This method was used to calculate the forces on all 12 coils of the Nab spectrometer: only the forces along z were calculated in the presence of the passive shield.

The forces between the coils calculated in the presence of the magnetic shield are presented in table C.3. The number of Gaussian points in the integration of $\vec{J} \times \vec{B}$ over the volume of the coil was 10 along the all three cylindrical coordinates: the radial distance r, the angle ϕ and the coil axis z. The total force along the z axis does not increase the presence of the shield, and is still 0.048 (KN) much smaller than the forces on the coils. The forces are almost not changed in the presence of the steel shield.

The most precise method for the calculation of the forces in Post-Processor in the presence of magnetic materials is the field integration; the magnetic field inside the volume of the coils is calculated by the integration of all the field sources (magnetization and currents in the coils). The precision is increased if the self forces of the coil are omitted and if the number of Gaussian points is increased. The ideal coil is divided in 12 segments with equal length and the forces F_x, F_y, F_z are calculated for each segment. The radial force for each segment is equal with:

$$F_r = \sqrt{F_x^2 + F_y^2} \tag{C.5}$$

The force density per unit coil volume is calculated in the table C.4 along the radial and the axial directions when the axes of the coils and shield

190

Table C.3: The forces acting on each solenoid of the Nab spectrometer in the presence of the shield are compared with the forces in the absence of the shield in the last column.

Coil	F_z kN coils shielded	F_z kN coils not shielded	F_z/V N/cm^3 coils shielded	F_z/V N/cm^3 coils not shielded	V cm^3
C_{1i}	-5.68	-5.68	-2.073	-2.074	2740.389
C_{1o}	0.05	0.045	0.053	0.030	1582.132
C_{2i}	-1.39	-1.39	-1.551	-1.671	834.586
C_{2o}	1.14	1.14	2.855	2.360	482.037
C_{3i}	85.86	85.86	76.701	76.944	1115.912
C_{3o}	-55.38	-55.38	-85.922	-81.862	676.539
C_{4i}	-33.10	-33.10	-45.909	-78.334	422.492
C_{4o}	36.61	36.61	174.614	171.866	213.046
C_{5i}	-188.26	-188.26	66.928	-85.753	2195.437
C_{5o}	5.42	5.41	335.978	4.283	1265.030
C_{6i}	156.03	156.02	-88.723	78.960	1975.996
C_{6o}	-1.33	-1.33	-63.580	-1.170	1135.970
total	0.05	0.05			

coincide (dx=0 cm) and when the coils are moved in the direction of the y axis. The volume density of the radial forces in each coil (for dy=0) is F_{rad}/V. The change in the torque component along x axis with the increase in the distance dy is presented in the last column. To estimate the effect of the misalignment on the axes of the coils and shield, a one half model of the shield was built in Tosca. The field was tangential to the vertical yz plane. The centers of the coils are located on the same vertical axis z_1. The centers of the coils located on z_1 axis were displaced relative to the axis of the shield (z axis) with a distance dy = 0.2, 0.4 ..., 1.6 cm in the direction of the y axis. Therefore the radial forces change more quickly with the distance dy between the two axes. For about 2 cm distance the y component of the total force exerted on the coil is about 0.3 Newton. The force in the axial direction depends very weakly on the distance between the two axes as expected.

The total F_y force on all of the 12 coils depends linearly on the distance dy between the two axes of the coils and of the shield (Figure C.3). The axis of the coils is moved with dy cm relative to the vertical z axis of the shield. The x component of the total force is smaller than 10^{-9} N. The torque in the x direction is calculated for the same displacements dy of the coils center and the vertical axis of the shield in Figure C.3. The total torque acting on the 12 coils is still small (42 N · cm for a displacement dy=1 cm). The y and z

Table C.4: The change rate of the axial force components F_z and F_y (on each of the 12 coils) with the displacement dy of the coils center from the z axis of the shield is calculated from the linear fit.

| Coil	dF_z/dy N/cm 10^{-3}	F_z N $dy=0$	dF_y/dy N /cm 10^{-3}	F_{rad}/V N/cm^3 $dy=0$	$d\tau_x/dy$ N
C_{1i}	1.143	-5680.3	47.874	14.244	-5674.8
C_{1o}	-1.762	44.528	-58.322	1.2399	37.82
C_{2i}	-0.066	-1.671	-0.213	58.814	-1393.6
C_{2o}	0.090	2.359	-0.354	16.502	1136.1
C_{3i}	-0.060	76.940	94.652	40.877	85866
C_{3o}	0.015	-81.855	-101.66	49.108	-55386
C_{4i}	0.274	-33095	-18.068	174.49	-33094
C_{4o}	0.034	171.86	18.282	236.46	36614
C_{5i}	-0.102	-85.751	-411.33	108.15	-188200
C_{5o}	0.165	4.2787	-482.65	115.28	55407.4
C_{6i}	-23.155	156020	-325.28	133.64	1.56E5
C_{6o}	0.426	-1.166	-414.08	95.846	-1307.6
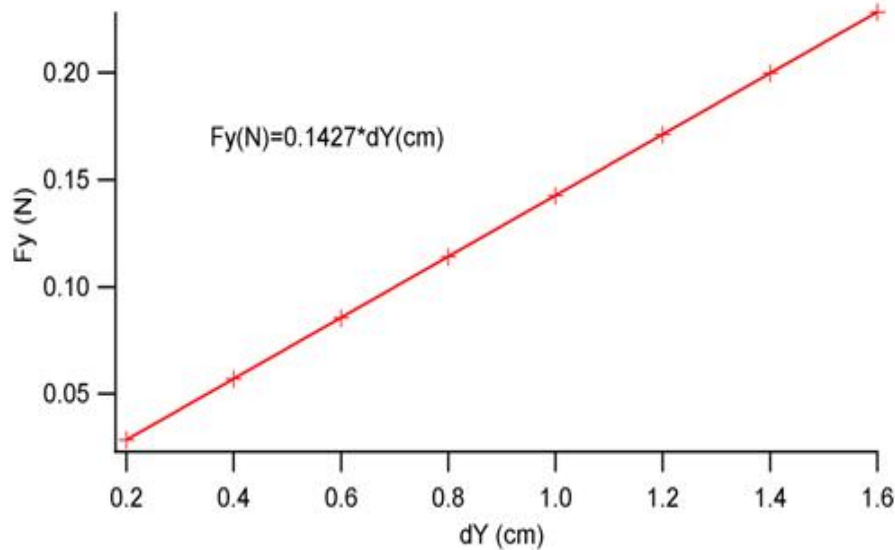
Figure C.3: The total y component of the force acting on the 12 coils of the Nab spectrometer when the centers of the coils are moved with dy cm relative to the vertical axis z of the steel shield.
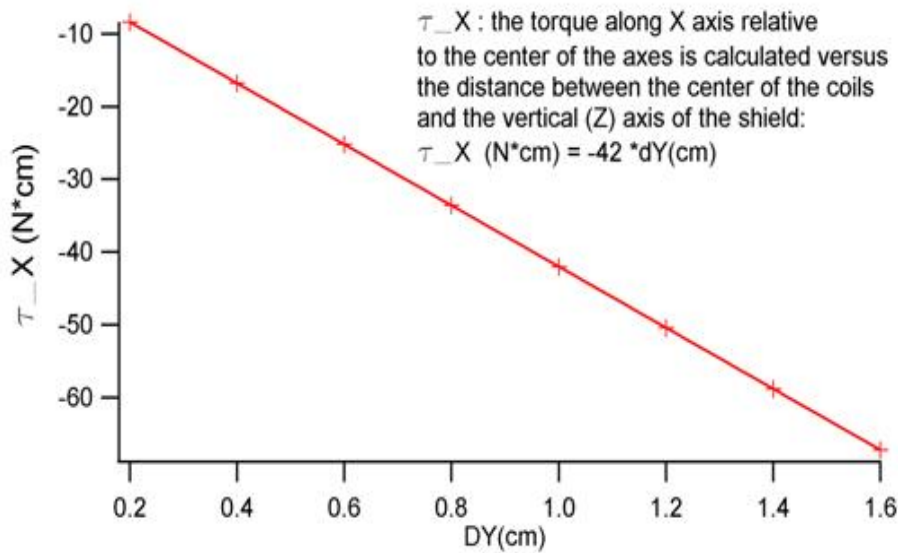
Figure C.4: The x component of the total torque $\vec{\tau} = \vec{r} \times \vec{F}$ on the coils relative to the center of the axes is calculated for different distances dy of the coils center relative to the vertical z axis.

components of the torque are smaller than 10^{-8} N· cm.

The calculation of the rate increase in the force for each coil when the center of the axis is moved in the x direction with a distance dx is presented in the table C.5. Due to the symmetry the F_y component of the force is zero in all cases. The weak dependence of the F_z component on the distance dx is quadratic. For small changes in x the linear fit of Fz versus y is very good.

The x component of the torque on each coil is calculated in Figure C.3 for different values of dy from 0.2 cm up to 1.6 cm. For two coils (C_{5i}, C_{6i}) the increase in the torque $d\tau_x/dy$ is $-1.88 \cdot 10^5$ N and $1.56 \cdot 10^5$ N. For coils C_{3i} and C_{3o} the increase in the x component of the torque is $85.87 \cdot 10^3$ N and $-55.38 \cdot 10^3$ N respectively.

The total force in the x direction is proportional with the displacement dx of the coils center relative to the shield center $F_x(N) = 0.1428$ (cm)

C.4   The magnetic field outside the magnetic shield of the Nab spectrometer

The shield is built from four vertical pairs of plates, 656 cm long and 5.08 cm thick. Two vertical plates in a pair are joined at their corners like in Figure C.6. The shield is symmetric relative to the vertical planes xz and yz. The total volume of the four pair of pillars is 0.998 m^3 and the total mass is 7840 kg. Each corner is made from one plate 34.92 cm wide, 5.08 cm thick

193

Table C.5: The increase in the F_x component of the force with a displacement dx in the center of the coils relative to the center of the shield.

Coil	dF_x/dx N/cm 10^{-3}	$F_x\|dx = 0$ N 10^{-5}	dF_z/dx N/cm 10^{-3}
C_{1i}	48.11	-6.12	17.77
C_{1o}	-58.35	5.91	-2.34
C_{2i}	0.23	-2.49	0.46
C_{2o}	-0.37	2.52	-0.68
C_{3i}	94.82	-23.42	-17.88
C_{3o}	-101.83	23.3	20.11
C_{4i}	-18.09	3.61	13.84
C_{4o}	18.29	-2.06	-9.36
C_{5i}	483.23	-133.5	5.98
C_{5o}	-411.63	43.12	-4.51
C_{6i}	-326.18	54.3	-29.75
C_{6o}	414.58	-54.4	31.31
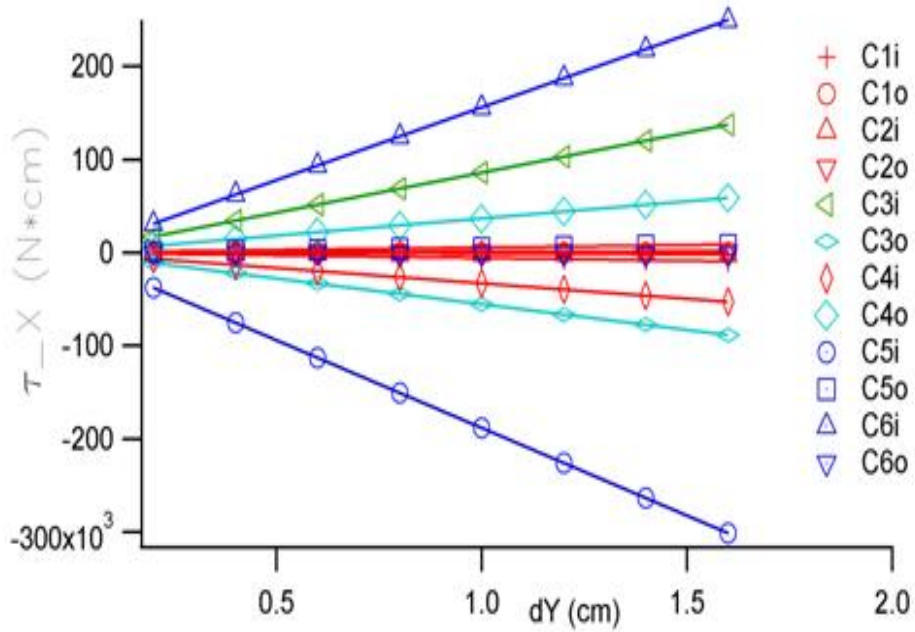
Figure C.5: The x component of the torque acting on each of the 12 coils of the Nab spectrometer is calculated for different distances between the center of the coils and the vertical z axis.
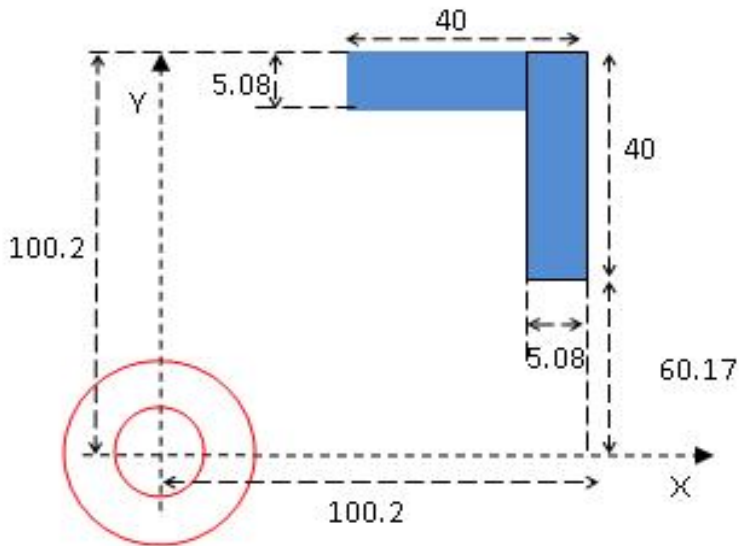
Figure C.6: One quarter of the magnetic shield of the Nab spectrometer is seen in a cross section normal to the axis of the spectrometer.

and a second plate 40 cm wide with the same thickness. The long plates are fixed (by welding or screws) to four steel corners at both the top and the bottom of the shield. The four steel corners (1.27 cm thick) are welded along their short edges into a square and attached with screws (or welded) to a big square plate (200.34×200.34) cm^2 with circular holes with radius 91.44 cm (Figure C.6). Taking in account the thickness of each cap (2.54 cm) the total length of the shield is 662 cm.

Each of the two steel end caps are 2.54 cm thick and are made from two plates (Figure C.7). The total mass of the caps is 528.2 kg. The x and y axes are axes of symmetry for the four corners. The magnetization curve used in the calculations was that for C1010 with composition C (0.08% to 0.13%), Mn (0.3% to 0.5%) and Iron (99%) is presented in figure C.4.

The complete model of the Nab spectrometer and the passive shield is presented in Figure C.9. The center of the coils C4i, C4o is at $z=0$ cm. The steel shield is 662 cm and starts at z_1=-116 cm and ends at z_2= 546 cm.

The magnetic field is calculated along directions parallel with the z axis, in the xz plane, at radial distances bigger than 140 cm from the z axis in Figure C.10. The maximum field is due to the pair of solenoids 5 and 6 centered at -11.55 cm and -31.41 cm. The fringe field is smaller than 1 Gauss at all five radial distances from the z axis. A field smaller than 0.5 Gauss is calculated at a radial distance bigger than 180 cm from the z axis. The field decreases to about 0.1 Gauss between z=230 cm and z=400 cm because the z component
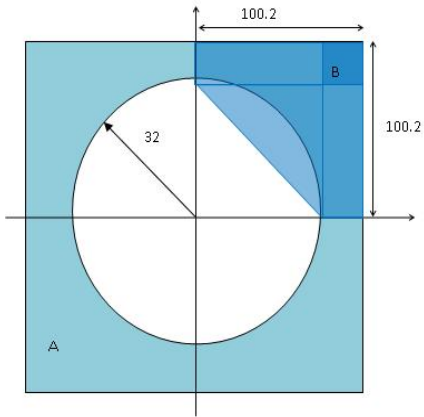
Figure C.7: Each of the two end caps of the magnetic shield of the Nab spectrometer are made from two steel plates with a circular holes (A) and four corners (B). For clarity only one steel corner is presented.
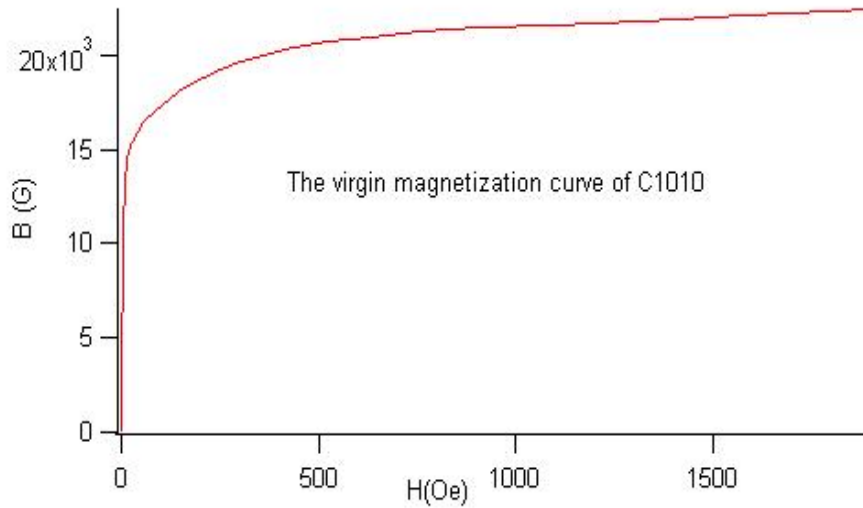

Figure C.8: The magnetization curve of the low carbon steel (C1010) used in the Tosca calculation of the magnetic field of the Nab spectrometer.
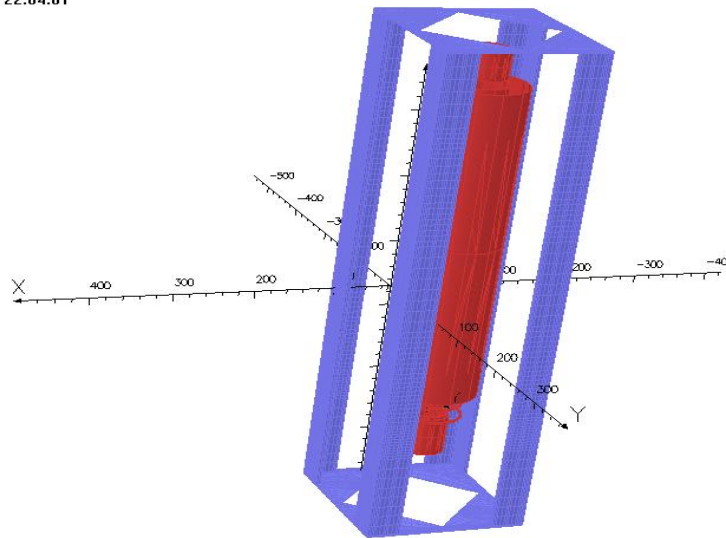
Figure C.9: The magnetic shield and the 6 pairs of coils is presented in Post Processor, Opera 3D.
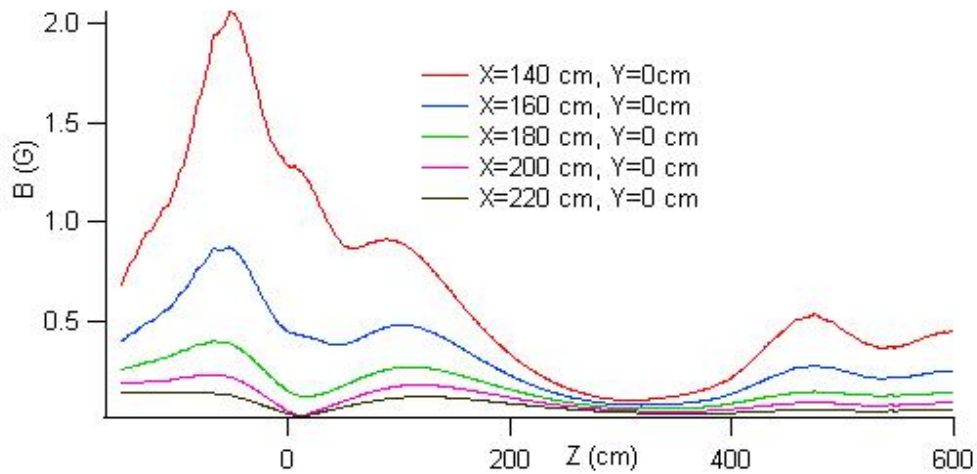

Figure C.10: The magnetic field is calculated along five directions parallel to the z axis at five radial distances from this axis and outside the steel shield, for a 722 cm long shield.
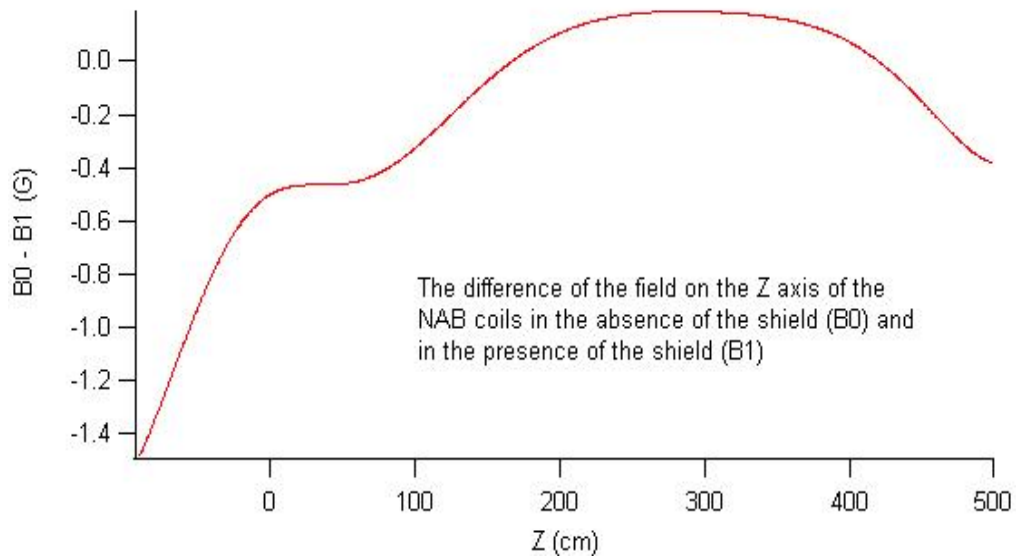
Figure C.11: The difference between the magnetic fields of the Nab coils in the absence and in the presence of the steel shield is calculated along the axis of the Nab coils.
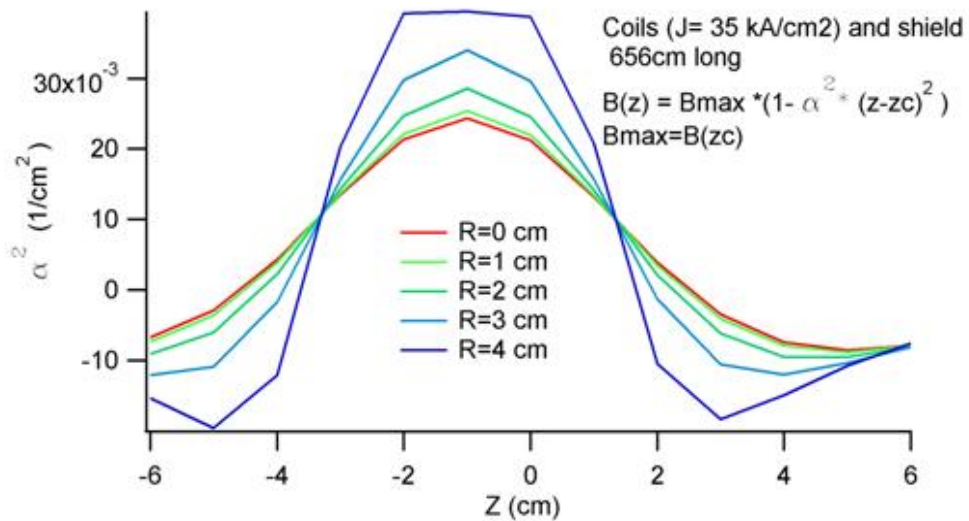

Figure C.12: The coefficient α is calculated along three lines parallel with the z axis at 0 cm, 2 cm and 4 cm distance from this axis, in the presence of the steel shield.

of the field changes sign in this region. The shielding factor is the ratio of the magnetic fields in a point outside the shield in the absence B_0 and in the presence of the steel B_s.

The magnetic field is calculated along three lines parallel with the z axis at x=0, 2, 4 cm and y=0 cm. The difference between the magnetic fields calculated along the z axis in the absence of the steel shield B_0 and in the presence of this shield B_1 is presented in Figure C.11 for a 722 cm long shield. The coefficient α is calculated as a function of z for three lines parallel with the z axis in Figure C.12. In this figure the magnetic field is calculated in Tosca by double integration in the presence of the coils and magnetic shield.

C.5   Conclusion

In the presence of the steel shield the magnetic field along the axis of the six pairs of the Nab solenoids changes with less than 2 Gauss, and the coefficient α is almost the same. The fringe magnetic field is smaller than 0.5 Gauss at a radial distance bigger than 180 cm from the axis of the spectrometer. The sum of the forces on the 12 Nab coils, increases with about 0.5 N for a 1 cm displacement along x and y axis, of the coils center relative to the shield axis.The increase in the sum of the torque component τ_x on all six pairs of Nab coils is 42 (N / cm) for each cm displacement of the coils axis in the radial direction. The increase in the torque on each coil show a much bigger increase: a maximum $1.8 \cdot 10^5$ (N $\cdot$ cm)/cm for coils $C_5 i$ and $C_6 i$.